TiO_2 Based Perovskite and Carbide Nanocomposites to Develop Chemiresistive Sensors for Breath VOC Detection

THESIS

Submitted in the partial fulfillment of the requirements for the degree of

DOCTOR OF PHILOSOPHY

By

Radha Bhardwaj
ID.No. 2019PHXF0031P

Under the supervision of
Dr. Arnab Hazra

BIRLA INSTITUTE OF TECHNOLOGY AND SCIENCE

PILANI

2024

Birla Institute of Technology and Science
Pilani-333031 Rajasthan - India

CERTIFICATE

This is to certify that the thesis entitled "***TiO_2 Based Perovskite and Carbide Nanocomposites to Develop Chemiresistive Sensors for Breath VOC Detection***" submitted by Radha Bhardwaj, ID no 2019PHXF0031P for the award of Ph.D. of the Institute, embodies an original piece of work done by her under my supervision.

Signature of the supervisor ....

Name Dr. Arnab Hazra

Designation Associate Professor

Department of Electrical and Electronics Engineering
BITS Pilani
Pilani Campus
Rajasthan, India

Date:

Birla Institute of Technology and Science
Pilani-333031 Rajasthan - India

DECLARATION

I hereby declare that the work reported in the Ph.D. thesis entitled ***TiO_2 Based Perovskite and Carbide Nanocomposites to Develop Chemiresistive Sensors for Breath VOC Detection*** submitted in the Department of Electrical and Electronics Engineering, Birla Institute of Technology and Science, Pilani, India is an authentic record of my work carried out under the supervision of Dr. Arnab Hazra. I have not submitted this work elsewhere for any other degree or diploma.

I am fully responsible for the content of my Ph.D. thesis.

Radha Bhardwaj

ID.No. 2019PHXF0031P
Department of Electrical and Electronics Engineering
BITS Pilani,
Pilani Campus
Rajasthan

ACKNOWLEDGEMENTS

I hereby express my respect and a deep sense of gratitude to my supervisor Dr. Arnab Hazra, Associate Professor, Department of Electrical and Electronics Engineering, BITS Pilani, Rajasthan, India, for his constant supervision, inspiration and valuable suggestions during the course of the present thesis work. He has always motivated and encouraged me to present my best at every step. Without his support I would not have been able to complete my thesis.

I am grateful to my DAC members Emeritus Prof. Chandra Shekhar, Prof. Navneet Gupta and Prof. Subhasis Gangopadhay for their valuable technical points and advice throughout my Ph.D. work. Their constant support and interactive sessions during my presentations really helped me improve my work.

I would like to cordially thank Prof. Sudhir Kumar Barai, Director BITS Pilani, Pilani Campus, Prof. Navneet Gupta, HoD, EEE Department, BITS Pilani, Pilani Campus and faculties of the EEE Department for their support and valuable guidance throughout my thesis work.

I am very much thankful to all of my respected teachers who always remained a source of inspiration throughout my carrier. I am thankful to my lab partners- Dr. Teena Gakhar, Mr. Uttam Narendar Thakur, and Ms. Divyanshu Rathore.

I wish to convey my sincere regards to my beloved parents for their continuous inspiration. I am also thankful to my siblings and friends for their mental support.

I am very much grateful to the Department of Biotechnology (DBT) and Birla Institute of Technology and Science for providing me financial support and a healthy environment for doing my research work.

Radha Bhardwaj

Preface

The breath analysis is a non-invasive route for the detection and monitoring of a particular disease. This technique involves the study of exhaled breath where a particular gas or VOC is highly correlated to a specific disease and gives insight into the state. Hence, it is a potential replacement for invasive disease monitoring techniques like; blood test, biopsies and colonoscopies etc. which are pain-staking, and expert-dependent. The exhaled breath consists of nitrogen, oxygen, CO_2, humidity (>50%), gases (NH_3, NO, H_2S) and more than three thousand VOCs ranging in concentrations from lower parts per billion (ppb) to parts per million (ppm). Among them, a few breath VOCs with comparatively high concentrations e.g., acetone, isoprene, methanol, ethanol, propanol, acetaldehyde, xylene, etc. act as a breath marker for a disease diagnosis through breath analysis.

Analytical techniques like mass spectroscopy and gas chromatography are considered as the most sensitive techniques for identifying breath VOC markers. Unfortunately, these techniques require expensive equipment, complex working, and expert handling and are relatively time-consuming. Chemiresistive sensors are the best alternative to overcome the limitations of those high-end analytical tools. A chemiresistive sensor is a device that can convert an external stimulant to an electrical signal. Exposure to a certain vapor analyte or change in ambient conditions alters its properties (e.g., resistance, electrical conductivity, capacitance, etc.) in a measurable manner. This technique brings many advantages in breath analysis like cost-friendly production, ease of working, and low power consumption, minimum maintenance.

The chemiresistive sensors should have the following properties to fulfill the requirement of breath VOC sensing. The sensor should be selective towards a particular marker VOC in the presence of large number of interfering analytes. Humidity stability is one of the most concerning factors as the water vapor content in exhaled breath is quite large (Relative humidity: >50%). Other parameters like low concentration (ppb to lower ppm level), high sensitivity and long-term stability still need to be considered.

For breath VOC sensing with chemiresistive sensors, various nanostructured materials have been exploited including metal oxide semiconductors, 2D nanomaterials, perovskites, metal nanoparticles and their hybrids. Litrature confirms that the semiconducting metal oxides are stable and widely explored sensing material for breath VOC detection. Among all of the metal oxides, TiO_2 nanostructures offer a number of advantages for breath VOC sensing. TiO_2 exhibits comparatively low operating temperature, high sensitivity, reliability and stability among other metal oxide semiconductors. However, the low cross-selectivity of these sensors and the high interference of environmental humidity on sensing performance are significant drawbacks in the case of breath VOC detection. Metal carbides possess outstanding sensing properties but they are not much stable as metal oxide semiconductors for vapor sensing. To overcome these drawbacks with the intention of enhancing the sensing performance, hybridization of metal oxide and carbide with semiconducting perovskites and other materials was performed. Perovskites are highly potential materials in terms of morphological stability, good thermal and chemical stability and possess porous morphology making them a desirable candidate for highly stable breath VOC sensing. Later on, hybridization with quantum dots or nanoparticles can further improve the VOC sensing properties of the material for breath analysis application.

This dissertation comprises seven chapters. The **first chapter** describes the introduction, literature survey and scope of work. The first chapter introduces the importance of chemiresistive sensors based volatile organic compound sensing (VOC) for breath analysis application. The first chapter also gives a brief description of the different nanostructured materials utilized for breath VOC sensing. Major emphasis was given to metal oxide semiconductors, semiconducting perovskites and metal carbides and potential for VOC sensing. The literature review reveals the potential of metal oxides, perovskites, metal carbides and their nanocomposite-based VOC sensors in this chapter.

Second chapter is related to the synthesis and characterizations of individual TiO_2 nanostructures, and $Ti_3C_2T_x$ Mxene nanostructures. It also includes the preparation of MoS_2 quantum dots and Pd metal nanoparticles for the hybridization of the material. It describes the techniques to synthesize 0-D TiO_2 nanoparticles, 1-D TiO_2 nanotubes and $Ti_3C_2T_x$ Mxene nanosheets. Various characterization techniques are used to study their morphology, structural and chemical properties.

Third chapter describes the VOC sensing with MoS_2-functionalized TiO_2 nanotubes. This chapter shows the sensing behavior of MoS_2/TiO_2 nanotube-based sensors, fabricated via hydrothermal route. The sensor was tested with various VOCs exists in breath and found to be a highly selective towards xylene at optimum operating temperature. The effect of humidity was also tested in a range of humid conditions.

Fourth chapter concerns the synthesis, characterizations (morphological, structural and chemical) and VOC sensing performance of $SrTiO_3$-TiO_2 nanocomposite. In this chapter, the composite was synthesized by hydrothermal route where $SrTiO_3$ was grown from the TiO_2 nanotubes with the help of Sr precursor. A series of sensors were prepared with different Sr content and tested for the advanced level detection of breath VOCs. The sensitivity and stability amplification by $SrTiO_3$-TiO_2 heterostructured nanotube array sensor has been described in this chapter. This chapter also revealed the humidity-tolerant capabilities of the $SrTiO_3$-TiO_2 nanocomposite.

Fifth chapter is associated with the formation of different nanostructures of $SrTiO_3$ originating from the TiO_2 nanoparticles. Different morphologies like nanograss, nanorods, nanosphere and hollow spheres of $SrTiO_3$ were synthesized by a one-step hydrothermal route by varying the reaction time. A detailed study was executed including their characterization and VOC sensing performances. The sensors were tested in a range of humidity to evaluate their humidity-inactive VOC sensing properties. Later on, the hollow spheres were modified by Pd nanoparticles to enhance the selectivity and sensitivity of the sensor toward ethanol. This chapter describes the selective behavior of $SrTiO_3$ nanostructures toward ethanol with humidity inactive behavior.

Sixth chapter is associated with the formation of an overlayer of hydrophobic $SrTiO_3$ on the 2D $Ti_3C_2T_x$ MXene layer to overcome the limitation of the high humidity interactive nature of MXene material. MXene possesses outstanding VOC sensing capabilities but its hydrophilic nature becomes the major drawback for breath VOC detection. 2D $Ti_3C_2T_x$ MXene was synthesized by a selective chemical etching route. Later an overlayer of $SrTiO_3$ was formed by a one-step hydrothermal followed by the formation of $Ti_3C_2T_x/TiO_2$ using a physical oxidation route. This chapter describes the excellent acetone vapor sensing properties of pure MXene and $Ti_3C_2T_x/TiO_2$ sensors. Further, the overlayer of hydrophobic $SrTiO_3$ on the $Ti_3C_2T_x$ MXene leads to effective vapor sensing with humidity-tolerant nature. The overall stability of the sensor was improved after the controlled oxidation and $SrTiO_3$ modification in the MXene sensing material.

Seventh chapter summarizes the complete work with a general conclusion followed by the future scope of work.

Abstract

The current work primarily aims to develop efficient chemiresistive sensors for VOC detection for breath analysis application. To fulfill the target, emphasis was given to develop selective sensors for particular breath marker VOCs having high sensitivity, stability and humidity tolerant properties. The potential nanomaterials like titanium oxide-based perovskite and carbide nanocomposites are chosen to develop efficient breath VOC sensors. The work was started with the development of two different types of nanostructures of TiO_2 having opposite types of conductivity. First, 1-D TiO_2 nanotubes were developed by electrochemical anodization which exhibited n-type behavior. Secondly, undoped TiO_2 nanoparticles were synthesized by the sol-gel method which exhibited p-type semiconducting behavior. Additionally, $Ti_3C_2T_x$ sheets has been synthesized by selective etching method. TiO_2 nanoparticles were considered as seed material for the formation of a variety of $SrTiO_3$ nanostructures. $Ti_3C_2T_x/SrTiO_3$ nanocomposite was synthesized followed by the formation of TiO_2 nanoparticles. Hybridization of nanomaterials was also developed with MoS_2 quantum dots and Pd nanoparticles. Nanocomposites including the pure nanoforms were subjected to different characterization techniques to study their morphology, chemical composition, structural changes, etc.

Different device structures were fabricated for efficient breath VOC sensing. Two different device structures were proposed on the basis of nanostructures. The 1-D nanostructures (nanotubes) were implemented in Metal Insulator Metal (MIM) sandwiched structured devices. The other 0-D and 2-D nanostructures were implemented in planar structured devices. The proposed device structures were well-matched for the synthesized nanoforms. The prepared different chemiresistive sensors were tested for the sensing of VOCs commonly used as breath markers.

Firstly, a hybrid of MoS_2 quantum dots and TiO_2 nanotubes was synthesized for the selective sensing of xylene marker at low operating temperature. The MoS_2/TiO_2 based chemiresistive sensor showed highest selectivity towards xylene over different interfering VOC components at 75 °C operating temperature. Notably, the highly xylene selective nature was observed over the chemically similar VOCs like benzene and toluene in air.

Later, to improve the sensitivity and long-term stability of the chemiresistive sensors, a $SrTiO_3$-TiO_2 nanotube heterostructure was prepared. $SrTiO_3$-TiO_2 nanotube sensors exhibited an excellent response in the response time of >1 s. Moreover, the sensor showed a low detection

limit of 2.94 ppb towards ethanol which is significantly lower than the ethanol concentration in breath.

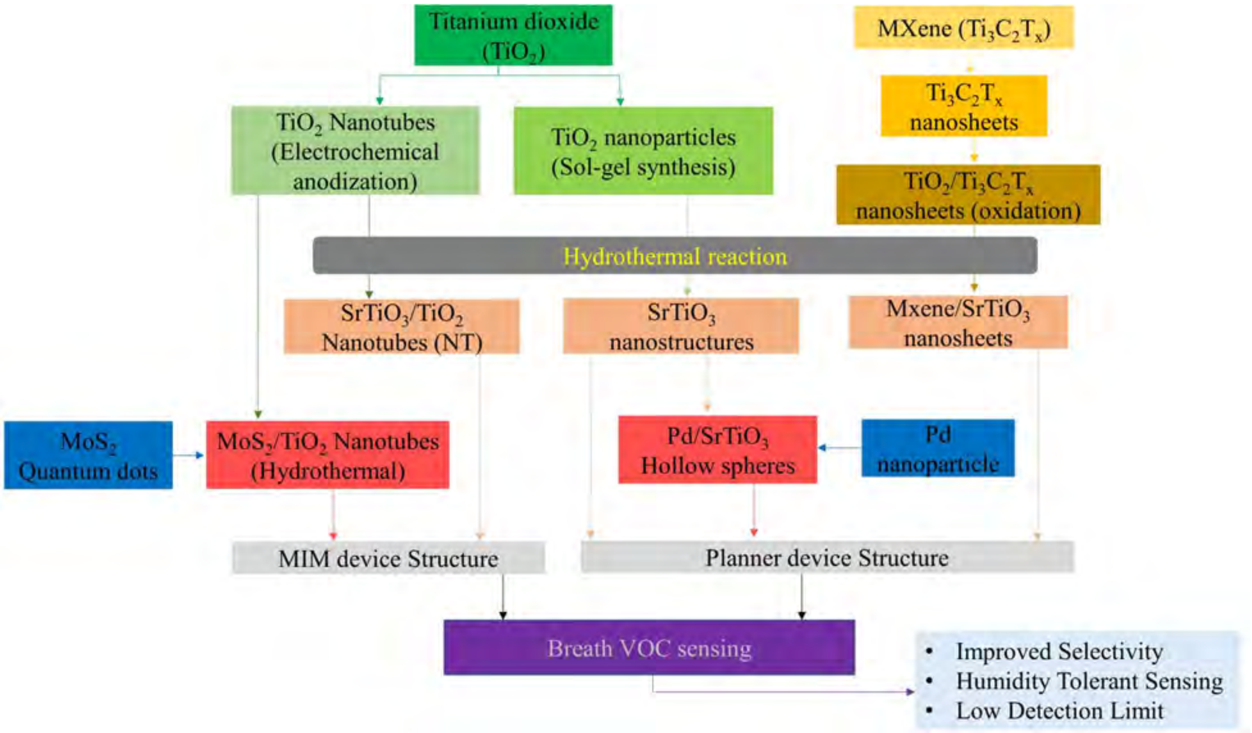

Fig. i. A flow chart presentation of complete thesis work.

A group of $SrTiO_3$ nanostructures with unique nano-architecture have been synthesized to achieve humidity inactive VOC sensing in chemiresistive sensors for breath analysis applications. The $SrTiO_3$ nanoforms showed good ethanol sensing behavior with no attenuation in the sensing properties in 80% RH. $SrTiO_3$ nanostructures displayed superhydrophobic properties with a quite high contact angle in the range of 130-160°. Further Pd modification in $SrTiO_3$ hollow spheres exhibited huge improvement in the response with a natural selectivity towards the ethanol marker.

At last, a $SrTiO_3$ overlayer was formed on hydrophilic 2D $Ti_3C_2T_x$ Mxene sheets to establish a humidity inactive highly sensitive acetone breath marker sensor. $Ti_3C_2T_x$ Mxene sensor coated with a $SrTiO_3$ overlayer exhibited low ppb sensing of acetone marker with humidity-independent sensing characteristics. The sensor showed a quite high response for 100 ppb of acetone which is very low than the concentration of acetone in exhaled breath in 80 % RH.

The flow diagram given in Fig. i indicates all the critical stages.

Table of Contents

1. Literature survey, objectives and scope of work

Abbreviations

0-D	Zero Dimensional
1-D	One Dimensional
2-D	Two Dimensional
3-D	Three Dimensional
AFM	Atomic Force Microscopy
BE	Binding Energy
BET	Brunauer-Emmett-Teller
BTX	Benzene Toluene Xylene
COPD	Chronic Obstructive Pulmonary Disease
CA	Contact Angle
DMSO	Dimethyl Sulfoxide
EDS	Energy Dispersive X-ray Spectroscopy
EG	Ethylene Glycol
FESEM	Field Emission Scanning Electron Microscopy
FET	Field Effect Transistor
GC	Gas Chromatography
GO	Graphene Oxide
HN	Hexagonal Nanosheet
HS	Hollow Spheres
ITO	Indium Tin Oxide
LOD	Limit of Detection
MIM	Metal Insulator Metal
MOS	Metal Oxide Semiconductor
MS	Mass Spectrometry
MX	MXene
NC	Nanocubes
NG	Nanograss
NR	Nanorods
NS	Nanospheres
NF	Nanofibers
NP	Nanoparticle
NT	Nanotube
PPB	Parts Per Billion
PPM	Parts Per Million
PPT	Part per Trillion
PAH	Pulmonary Arterial Hypertension
PTR	Proton Transfer Reaction
PL	Photoluminescence

RH	-	Relative Humidity
RM	-	Response Magnitude
SIFT	-	Selected Ion Flow Tube
SL	-	Single Layer
SOFC	-	Solid Oxide Fuel Cells
STO	-	Strontium Titanate
TBAOH	-	Tetrabutylammonium Hydroxide
TMAOH	-	Tetramethylammonium Hydroxide
TEM	-	Transmission Electron Microscopy
TNT	-	TiO_2 Nanotube
TTIP	-	Titanium (IV) Tetra Iso-propoxide
T1D	-	Type-1 Diabetes
TMDCs	-	Transition Metal Dichalcogenides
VOC	-	Volatile organic compound
XRD	-	X-ray Diffraction
XPS	-	X-ray Photo Spectroscopy

List of Figures

Fig. 5.5. XRD patterns of Nanograss (S1), Nanorods (S2), Nanospheres (S3) and Hollow sphere (S4). and XPS spectra of (b) Ti 2p, (c) Sr 3d and (d) O 1s, respectively.

Fig. 5.6. (a) Ti 2p, (b) Sr 3d and (c) O 1s XPS spectra of Nanograss (S1), Nanorods (S2), Nanospheres (S3) and Hollow sphere (S4), respectively.

Fig. 5.7. The static water contact angles of the sensing film of S1-S4 samples.

Fig. 5.8. (a) Response magnitude; (b) response time; (c) recovery time; as a function of temperature for S1-S4 sensors in 50 ppm of ethanol and 80% constant RH.

Fig. 5.9. (a-d) Dynamic response of nanograss (S1), nanorods (S2), nanospheres (S3) and nano-hollow sphere (S4) to different concentrations of ethanol varying from 500 ppb to 200 ppm; (e) Sensor responses as a function of gas concentration; (f) selectivity behavior of all the four sensors towards various volatile organic compounds at 150 °C in 80% RH.

Fig. 5.10. (a) Reproducibility of the sensor on successive exposure to 50 ppm ethanol pulses for all four sensors at 150 °C in 80% RH; (b) dynamic response curves of sensors in the exposure of 50 ppm ethanol at 150 °C under various humidity conditions (0—80% RH) and corresponding bar chart presentation of the response characteristic of the S1-S4 sensors upon exposure to 50 ppm ethanol from dry air to 80% RH at 150 °C.

Fig. 5.11. Schematic representation of the experimental procedure used to prepare the Pd modified $SrTiO_3$ hollow spheres-based sensing material.

Fig. 5.12. FESEM images of (a) Pd-STO-600 hollow spheres, (b) Size distribution analysis by ImageJ software, (c, d) TEM images at different magnifications; (e) HRTEM images and the inset is showing SEAD pattern and (f) AFM 3D topography images of Pd-STO-600 hollow spheres.

Fig. 5.13. XRD pattern of Pd-STO-600 sensor.

Fig. 5.14. XPS spectra of Pd-STO-600 (a) Ti 2p, (b) O 1s, (c) Sr 3d and (d) Pd 3d.

Fig. 5.15. The static water contact angles of Pd-STO-600 sensing film.

Fig. 5.16. (a) Baseline resistance of the Pd-STO-600 sensor, (b) response of Pd-STO-600 sensor to 50 ppm ethanol at different operating temperatures in 80% RH (generated at 35 ˚C), (c) Response of sensors with different Pd content.

Fig. 5.17. (a) selectivity behavior of all the three sensors towards various volatile organic compounds, (b) Dynamic response to different concentrations of ethanol varying from 500 ppb to 200 ppm, (c) Sensor responses as a function of gas concentration, (d) Reproducibility of the sensor on successive exposure to 50 ppm ethanol pulses, (e) long-term stability of the Pd-STO-600 sensor at 150 ˚C operating temperature in 80% RH (generated at 35 ˚C).

Fig. 5.18. (a) Dynamic response curves of sensors in the exposure of 50 ppm ethanol at 150 ˚C under various humidity conditions, (b) The response and recover characteristics of the Pd-STO-600 sensor upon exposure to 50 ppm ethanol in dry air in 80% RH (generated at 35 ˚C) at 150 ˚C sensor operating temperature.

List of Tables

Chapter 1

Literature survey, objectives and scope of work

1.1 Introduction

The global increase in health problems in humans is a complex and multifaceted issue subject to urbanization, lifestyle and environmental pollutants. Many publicly funded healthcare systems in world found that 73% of individuals aged 65+ have at least one chronic disease such as diabetes, hypertension, heart problems, asthma, etc [1-5]. For instance, International Diabetes Federation approximated that 463 million adults were living with diabetes in 2019 and this number will increase to 700 million if the current trend continues [2]. Continuous monitoring and early-stage diagnosis of these high-risk diseases by using electronics is highly desirable. In recent years, non-invasive breath analysis has held great interest in medical diagnostics and health care [2-5]. The exhaled breath of the human contains traces of some gases (NO_2, CO, H_2S etc.) and VOCs at concentrations ranging from lower parts per billion (ppb) to parts per million (ppm) [5,10]. These trace species reflect many processes occurring in the body. Analysis of breath could potentially provide a non-invasive means to assess a person's health. Moreover, breath analysis is a non-invasive method for detecting or monitoring disease by examining these exhaled breath volatile organic compounds (VOCs) or gases [10]. Hence it can be a potential replacement for traditional disease monitoring tools like; blood test, urine test, etc. which is invasive, pain-staking, and expert-dependent [11]. So, overall breath analysis is a non-invasive, potential, quick and inexpensive technique to detect illnesses [12]. Exhaled breath of humans consists of more than 3000 volatile organic compounds (VOCs) and only a few of them elucidate some practical information about the specific diseases and are identified as a biomarker [13-15]. For instance, Acetone is a breath marker for both type-I and type-II diabetes mellitus and shows a significant variance in concentration in exhaled breath of diabetic (1800 ppb) and healthy individuals (300 to 900 ppb) [16-20]. Some other breath VOCs such as ethanol, pentane, toluene, xylene, and isoprene are the breath markers for intestine and colon-related disease, heart diseases, lung disease, lung cancer and lipid metabolism disorder, respectively [21-27].

To detect breath VOCs, a number of sophisticated techniques are proposed such as laser-absorption spectroscopic techniques, gas chromatography (GC) technique, proton transfer reaction-mass

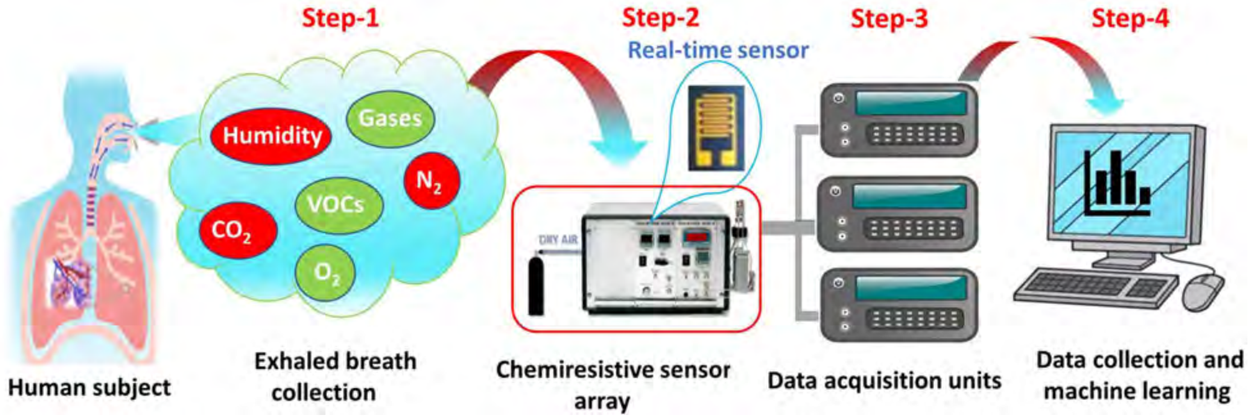

Fig. 1.1. The schematic diagram of exhaled VOC monitoring by chemoresistive sensor array for breath analysis.

spectrometry (MS), selected ion flow tube (SIFT)-MS and ion mobility spectrometry. Unfortunately, these approaches require expensive equipment, time-consuming and high cost [11,28-30]. So, the current state of breath analysis is focusing on the potential use of inexpensive and portable chemiresistive gas/vapor sensors over the more sophisticated spectrometric systems. The schematic diagram is showing necessary steps for exhaled breath VOC analysis by chemiresistive gas/vapor sensors (Fig. 1.1). Firstly, exhaled breath is collected from a human subject and then passed through a chemiresistive sensor array. The sensors show necessary changes in the electrical properties through data acquisition unit and final data was collected from the sensors and then processed through machine learning algorithms. Development of suitable nanomaterial based chemiresistive sensors in the setp-2 of Fig. 1.1 is the primary focus of the current work.

An ideal nanomaterial-based chemiresistive sensor for breath testing should be sensitive to very low concentrations of volatile organic compounds. It should also respond rapidly and highly selective toward a particular breath VOC marker among the high cross-interfering VOCs. Considering all the challenges of the chemo-resistive sensors, a variety of nanomaterials and their nanocomposites-based sensor systems have been explored for the efficient detection of breath markers. In detail, various semiconducting metal oxides such as ZnO [31-34], In_2O_3 [35], WO_3 [36-39], TiO_2 [40-47], and Fe_2O_3 [48,49], etc., semiconducting perovskites i.e. $LaFeO_3$ [50, 51], $ZnSnO_3$ [52], $BaSnO_3$ [53], $LaSrCoO_3$ [54] and $SrTiO_3$ [55,56] and 2D MXenes such as $Ti_3C_2T_x$ [57-60], Ti_3C_2 [61,62], $V_4C_3T_x$ [63,64], and Mo_2CT_x [65,66] have participated in the detection of VOC and gases. These sensing materials with plenty of excellent physicochemical, electronic and mechanical properties provide an opportunity to integrate them with different nanomaterials in a complementary way to attract more research interest in breath VOC sensing applications. Further, the properties of pure nanomaterials were enhanced by synergistic strategies with other materials [21,22,67].

1.2 Breath analysis:

From ancient times it was a known fact that exhaled breath gives insight into the physiological and pathological changes in the human body [68]. Modern breath analysis study started in the 1780s when researchers tried to figure out the chemical composition of human exhaled breath. But the first breath profile was established by Pauling and his coworkers in 1971 by a gas-liquid chromatogram where they reported the existence of 250 VOCs in human breath [69]. With advancements in research technology, this number has increased to more than 300 VOCs and till now, the known number of VOCs in exhaled breath is more than 3500 [11].

In general, breath analysis is a non-invasive route for monitoring or identifying a disease by investigating the specific biomarker and offers many advantages [12, 30]. Exhaled breath of humans is a complex mixture of different components including nitrogen (78.04%), oxygen [16%], carbon dioxide [4%-5%], hydrogen [5%], inert gases [0.9%], thousands of inorganics VOCs and water vapor (>50% RH) referred to as molecular breath signature [11, 70]. The breath signature of a human can vary and is directly related to the age, state of health, lifestyle, gender and smoking habits [29]. The exhaled breath markers are mainly, inorganic gases (NO, CO), volatile organic compounds (VOCs) such as ethane, pentane, acetone, isoprene etc. [12].

1.2.1 Breath VOC markers:

The biochemical processes in the body lead to the release of endogenous substances including inorganic gases, such as NO, CO, volatile organic compounds (VOCs) and other normally nonvolatile substances [71-73]. These substances are responsible for investigating diseased people compared to healthy ones [10,12].

The point of concern is that among all breath marker VOCs, only a few are in the easily detectable range and others are in typical concentration ranges lower than 1 ppb [74]. The most common breath marker VOCs with comparatively high concentrations are acetone (1.2-1880 ppb), isoprene (12-580 ppb), methanol (160-2000 ppb), ethanol (13-1000 ppb), propanol (18 ppb) and acetaldehyde (22 ppb) and gases like; nitrous oxide (1–20 ppb), nitric oxide (20–40 ppb), carbon monoxide (1–5 ppm), ammonia (1.0–2 ppm), xylene (10-200 ppb) [11,12,74]. Table 1.1 is showing the list of prominent VOCs and their related disease.

Acetone with a high concentration in exhaled breath is an effective and renowned breath marker for diabetes Mellitus, particularly for T1D mellitus [75-77]. In a diabetic patient, the concentration of acetone in the breath changes from 0.3 ppm-0.9 ppm to more than 1.8 ppm. Similarly, exhaled carbon monoxide (CO) and nitric oxide (NO) are breath markers for pulmonary diseases such as asthma, chronic obstructive pulmonary disease (COPD) and bronchiectasis [11,78], Hydrogen sulfide (H_2S) for asthma, airway inflammation [11], ammonia (NH_3) for kidney failure, hepatic dysfunction, encephalopathy, brain swelling and type II Alzheimer's disease [79]. Elevated levels of exhaled NO (50 ppb) in untreated asthma patients return close to healthy levels (less than 25 ppb) after corticosteroids inhalation whereas, the exhaled CO is in very high concentration (5–6.2 ppm) in untreated asthma patients and returns close to the healthy levels (1.6–1.8 ppm). Both biomarkers of asthma have significant concentration variations in exhaled breath [11]. A number of pieces of literature have been reported on the study of breath samples from patients with and without lung cancer [80-84]. The lung cancer-related VOCs in concentrations from 50 ppb to 500 ppb are xylene, styrene, isoprene and hexanal and are frequently found in the breath of early-stage smoker lung cancer patients [83,84]. Breath ethane (C_2H_6) is related to lipid peroxidation and oxidative stress [85]. The average concentration of ethanol (C_2H_5OH) in the breath of healthy individuals is high and gets increased to a significant level in the disease-affected person. Excess of ethanol has been related to renal failure, schizophrenia, breast cancer, liver diseases, asthma fatty liver, metabolic syndrome and cardiopulmonary diseases [11,74,79].

Table 1.1. Summarizes the major diseases related to VOC biomarkers [21-27,78].

Breath marker	Healthy (ppm)	Unhealthy (ppm)	Major disease
Acetone	0.3–0.9	>1.8	Type-I and type-II diabetes mellitus
Ethanol	0.013–1	>2.3	Intestine and colon related diseases, schizophrenia, breast cancer, liver diseases, asthma etc.
Pentane	0.038	0.110	Heart diseases
Toluene	0.001-0.02	0.01-0.1	Lung diseases
Xylene	0.001-0.02	0.01-0.1	Lung cancer
Isoprene	0.172	0.255	Lipid metabolism disorder and Lung diseases

Therefore, the efficient detection of these breath VOCs could be the real-time solution for disease identification and monitoring in healthcare applications.

1.2.2 Chemiresistive sensors for breath VOC detection:

Enose technology involves chemiresistive sensor arrays combined with electronic learning algorithms which can put together exhaled molecular fingerprints (breath prints) [11,72]. Chemiresistive sensors are a type of chemical sensor that operate on the changes in its physical properties like mass, resistance, dielectric properties, etc. upon exposure of the specific gases or VOCs in the surrounding environment. These changes are then transformed into an electrical signal whose magnitude is comparable to the target VOC concentration. The fundamental concepts of chemiresistive sensors given in the early 1900s. In 1953, Brattain and coworkers observed a huge change in the resistance of a semiconductor upon adsorption of gas molecules on their surface [86]. Onwards in 1970, SnO_2 was the first semiconducting material extensively studied for gas sensing [87].

The basic structure of chemiresistive sensor consists of a sensing material or film that interacts with the target VOC. The sensing material is typically a semiconductor that show a change in electrical properties in the exposure of gaseous analyte. The sensing material is usually deposited onto a insulating substrate i.e., SiO_2/Si, glass, alumina and metal electrodes are attached to measure the resistance change [21,22,75]. The basic mechanism of chemiresistive sensor involves the adsorption/desorption of gas molecules on the surface of sensing film. The adsorption led to change in free charge carrier concentration and corresponding modulation of the resistance or conductance of the material [92]. This change in the resistance is proportional to the concentration of the analyte in the environment. The resistance change is then converted into electrical signal which can be further processed. Several parameters like; sensitivity, selectivity, response/recovery time, operating temperature and detection of limit are used to characterize a sensor [21,75,92]. These sensor properties can be modulated by changing the sensing material and its characteristics.

The common semiconducting materials used as sensing element in chemiresistive sensors include metal oxides (SnO_2, ZnO, TiO_2, WO_3), carbon nanomaterials (graphene, carbon nanotubes), chalcogenides, perovskites and carbides etc [40-44,21,52-54,57-60,75,92]. These materials have extraordinary physical, chemical and electrical properties which make them suitable for sensing application. Not only this, these materials have been explored in different morphologies like; nanoparticles, nanotubes, nanoflowers, nanosheets to improve the sensing characteristics [40-44,52-54,57-60,75,92]. Certainly, the field of sensors development is continuously evolving and with researchers exploring new material and their hybridization possibilities [52-54, 44,45,63,64].

In case of breath marker detection by the chemiresistive sensor, two main ways can be implemented [11, 81]. The first selective mechanism where the sensor is highly selective towards a particular VOC and secondly the fabrication of an array of cross-reactive sensors and data discrimination was done by a pattern recognition algorithm [88]. In principle, sensor arrays were exposed to a mixture of VOCs and which caused a change in their electrical resistance resulting in the production of a breath print and recognition patterns was employed to differentiate between different disease states [81]. The current state of the research is focusing on the development of inexpensive and portable chemiresistive gas/vapor sensors that are already used for food quality monitoring [89,90], air-quality monitoring [91,92], alcohol breath analyzers, etc [14,93]. The new-age sensor system should detect small changes in concentration and provide a consistent rapid output specific to a given breath volatile organic compound.

1.2.3 Challenges in chemiresistive sensors for breath analysis:

The careful evaluation of chemiresistive sensors showing some elementary problems that should be addressed for efficient and reliable detection of VOC markers for breath analysis applications. The real time implementation of sensors is limited by poor selectivity towards a target VOC over other interfering VOCs, high operating temperature, high detection limit, poor long-term stability and significant deterioration in sensing properties under the humid atmosphere [11,88,94-96]. One of the most fundamental problems is significant influence of humidity which always remains a major barrier and less focused constrain in the chemiresistive sensors [96,97].

1. The restricted selectivity is yet the most limiting factor, especially for trace concentrations (lower ppb) of target analytes in chemiresistive sensor [11,74]. The selectivity of the chemiresistive sensor is a relative phenomenon where the selectivity towards a particular gas or VOC directly depends on the other cross-interfering VOCs in the sensing environment. In the case of the breath VOC detection, the cross interference is high from the other chemically similar VOCs so we need the highly selective chemiresistive sensor system. Enhanced selectivity of a sensor system can be achieved in two ways. Either selecting a highly sensitive sensing material to that particular VOC

analyte or discrimination between analytes in a mixture of VOCs [88]. Several strategies in addition to tailoring the material properties, addition of dopants, morphology variations, vacancy modulation, optimization of operating temperature and composite formation, etc. have been used to improve the selectivity. But the strategies are insufficient to overcome realistic problems of accurate breath VOC detection [88, 94].

2. The operating temperature of the different components in a breath VOC testing system also has an impactful aspect that must be cautiously considered. Chemo-resistive sensors show high sensitivity at higher operating temperatures. But high-temperature operation makes the sensors unstable for long-time measurements. The average operating temperature of the reported metal oxide sensor is very high (200-500 ºC) which is responsible for sensor instability with baseline drift [94].
3. The sensitivity of the sensors should be very high towards a particular VOC due to the presence of many chemically similar VOCs in exhaled breath [11,95]. The concentration range of the VOC markers in exhaled human breath as low as ppm, ppb or ppt level encourages the fabrication of chemo-resistive sensors with a low detection limit (LOD) for faithful detection.
4. The high relative humidity (RH) in the breath samples (>50% RH − equivalent to >25 000 ppm of water vapor at 1 atm and 25 °C) limits the accuracy of the sensor data [70]. In chemiresistive sensors, humidity influence on the sensor properties can be categorized in different ways. Firstly, during the competitive adsorption of the water molecule and gas molecule, the charge transfer between water molecules and sensing materials leads to a significant change in the conductive channel. Secondly, the type of adsorption of water molecules on sensing film. Physical adsorption leads to the adsorption of water molecules in the form of ions, such as H^+, rather than electron transfer to the sensing layer in chemical adsorption [96]. In the case of hydrophilic sensing film, huge water adsorption may block the adsorption of gas molecules. Therefore, humidity limitation is serious and causes drifts in sensor properties, over time drift in sensors, such as aging, or incomplete release of absorbed chemical species [70,95]. Many strategies such as the conductivity modulation of sensing materials [56,97,98], surface functionalization [99,100], noble metals addition [6,101,102], operating temperature [102], enhancement of porosity/roughness [7,99,103,104] and variations in the measurement parameters like

operating temperature [105] have been introduced to minimize the effect of environmental humidity on the performance chemiresistive sensors.

The above-mentioned requirements for VOC detection for breath analysis applications encourage researchers to fabricate advanced nanomaterials and composite-based chemiresistive sensors. In this regard, various advanced nanomaterials like metal oxides, carbon nanomaterials, chalcogenides, perovskites, metal carbides, and metal nanoparticles, etc. have been explored by researchers for VOC detection. Detailed analysis and futuristic outcomes of these nanomaterials for VOC sensors have been incorporated in the next section.

1.3 Nanomaterials for breath VOC detection:

Nanomaterials are showing a great potential as sensing layer on gas or VOC sensing due to their peculiar physical and chemical properties and high surface area to volume ratio with respect to their bulk counterparts [21,22]. Tunable properties of nanomaterials like; size, shape, composition and surface chemistry provide a wide spectrum for modulating the sensing characteristics in chemiresistive sensors. A variety of nanomaterials like metal oxides [106-127], carbon nanomaterials [21,67,75], chalcogenides [114, 125], perovskites [128-132] and metal nanoparticles [6, 21] have been introduced by the researchers as a sensing layer for chemiresistive sensors. Among them, pristine metal oxides are the oldest and most widely used sensing material but high operating temperature and poor selectivity are the major drawbacks of these sensors [32-39]. Similarly, carbon nanomaterials like; graphene, carbon nanotubes etc. are low temperature sensing material but poor stability and incomplete sensing response are major shortcoming of this material. Most of the carbon nanomaterial and chalcogenides-based sensors are reported on the hybridization with other nanomaterials to achieve expected outcomes [21,67,75]. However, metal nanoparticles ae famous for their functionalization capabilities with other sensing material to enhance the sensing properties of chemiresistive sensors. But in the pristine form they are not an appropriate candidate for the gas sensing [6,21,102]. On the other hand, perovskites are less explored material in chemiresistive gas sensors but their outstanding stability properties and robust nature make them a suitable candidate [128,129]. On the basis of detailed survey on different sensing materials we have discussed the most suitable one in the details.

1.3.1 Metal Oxides:

Metal oxides are usually represented as M_xO_y, where M represents a metal such as Sn, W, Fe, Zn, Ti, etc. and O represents oxygen. Metal and oxygen exist as ionic compounds in metal oxide having positive (x) and negative (y) charges, respectively [21,22]. For many decades metal oxide semiconductors have been established materials in solid-state gas sensors in both practical and scientific manner. The attractive profits of metal oxide sensors include minimum cost, flexibility, easy fabrication, and high congruence with silicon microfabrication made researchers explore them more in diversifying way. Moreover, the mechanical stability and environmental friendly nature make the metal oxides more promising for real-time detection of gases and VOCs [21,22]. Metal oxide sensors are employed in numerous applications like; environmental monitoring, food quality monitoring, indoor air quality, industrial applications, and so on. However, the employment of metal oxide-based sensors for breath VOC detection under breath analysis application is not been explored much. Very few detailed reports focused on breath VOC detection have been published and showed desirable outcomes expecting a high scope of advanced studies in the near future. In detail, various semiconducting metal oxides such as ZnO [31-34], In_2O_3 [35], WO_3 [36-39], TiO_2 [40-42], and Fe_2O_3 [48,49], etc. have participated in the sensing of breath acetone for diabetes mellitus detection. A number of MOS such as TiO_2, SnO_2, WO_3, NiO-based ethanol and xylene sensors are reported [44,106,107]. Among them, very few are focused on the sensing of xylene and ethanol markers for breath analysis applications [84,108-116].

The sensing capabilities of metal oxide sensors depends on many factors like composition of sensing material, type of morphology, size of resulting nanostructures, porosity and the type of conductivity (n- or p-type) [22]. The modulation in any of these properties can significantly change the sensing behavior [67]. Additionally, the employment of pristine metal oxides gives the major advantage of having the capability to be synthesized in different nanoforms like nanotubes, nanosphere, thin films, nanorods, nanoclusters, nanofibers and nanoplates [21]. As a consequence, a variety of nano morphologies like 0-D (nanoparticles), 1-D (nanotubes, nanowires, nanorods) 2-D (nanosheets and nanofibers, etc.) and 3-D (nanospheres and nanoflowers) of various metal oxides like SnO_2, ZnO, WO_3, Fe_2O_3, $CuFe_2O_4$, In_2O_3 and TiO_2, etc. have been synthesized and investigated for VOC sensing as shown in Fig. 1.2 [11,21,22,33,39,44-48]. For instance, one-dimensional Fe_2O_3 oxide possesses a high specific surface area with fast charge transfer while preserving adequate chemical reactive groups and thermal stability with minimal energy consumption provide it improved acetone sensing capabilities [48,117]. The morphological variations in metal oxides are mostly controlled by the synthesis method [67].

The typical methods applied for the synthesis of nanostructures are electrochemical anodization [48], sol-gel [40,49], hydrothermal method [32,34,36-38], template-assisted synthesis [33], electrospinning [39,42] and matrix-assisted pulsed laser evaporation [117]. On the basis of type of conductivity, semiconducting metal oxides display different sensing outcomes and interaction behavior. Metal oxides such as ZnO [31-34], In_2O_3 [35], WO_3 [36-39], TiO_2 [40-43], and Fe_2O_3 [48,49] are n-type semiconductors and explored more frequently than p-type materials like CuO, Co_3O_4 and NiO [75]. The n-type semiconductors have been found most interactive for ammonia (NH_3), acetone (CH_3COCH_3), ethanol (CH_3CH_2OH), and formaldehyde (HCHO) whereas p-type are more promising for H_2S and NO_2 [21,22,75].

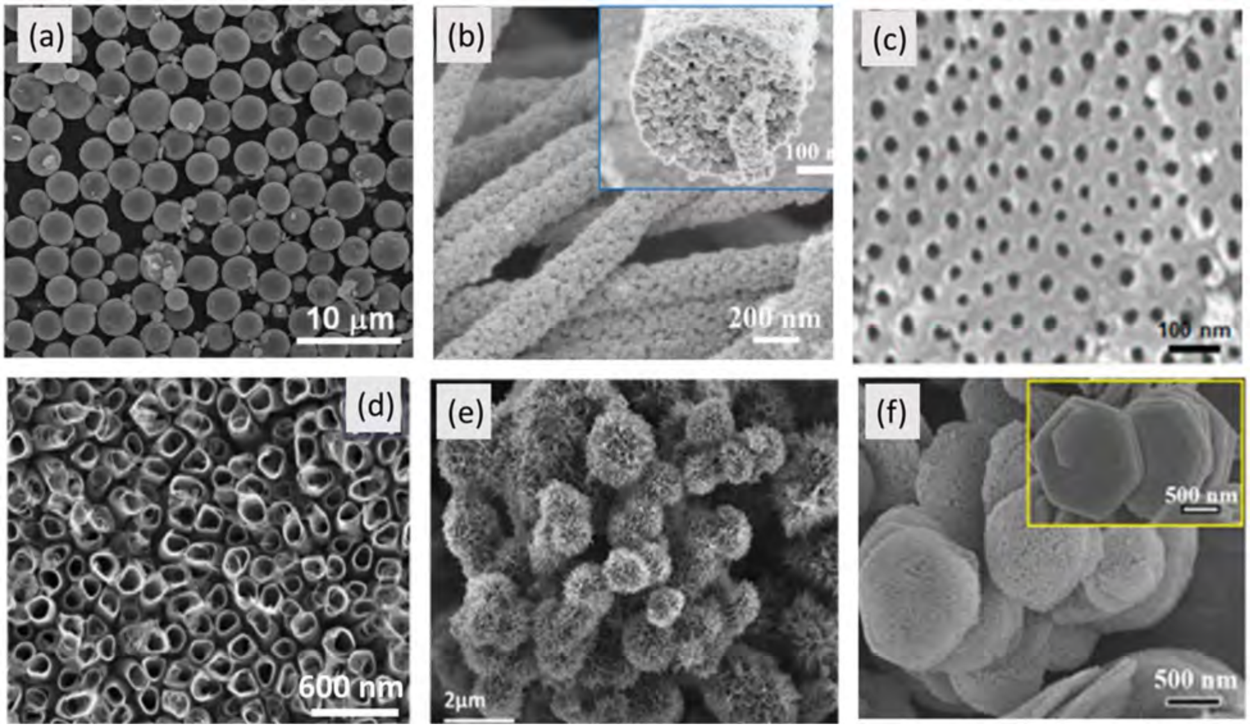

Fig. 1.2. FESEM images of various metal oxide nanostructures: (a) ZnO microspheres [33], (b) WO_3 nanofibers [39], (c) Fe_2O_3 nanotubes [48], (d) TiO_2 nanotubes [44], (e) TiO_2 spheres [45] and (f) TiO_2 nanosheets [47].

The sensing mechanism plays a key role in the understanding of sensing behavior which varies with the type of conductivity. The dangling bonds on the surface of metal oxide semiconductors are the primary factor that participates in forming ionized oxygen species via adsorption on the surface of metal oxide in the air ambient [22]. The electrical resistance of the MOS (n-type) in the air is increased due to the reduced free electron concentration available on the surface of metal oxide. On exposure to the reducing VOC, the resistance of MOS is thereby decreased due to the release of free electrons during the interaction of vapors and adsorbed oxygen species [22,117]. This phenomenon is reversed in p-type MOS where holes are the majority carrier concentration and the resistance increases in exposure to reducing VOC [117].

Table 1.2. Summarizes the metal oxide-based breath VOC sensors.

Metal oxide	**morphology**	**Target VOC**	**Sensitivity**	**Cross-interfering VOCs/gases**	**Humidity study (RH)**	**Op. tem.**	**Ref.**
ZnO	Hierarchical	Acetone	42 ^{a} (100 ppm)	Methanol, ethanol, toluene, ammonia, CO	No	425	32
ZnO	Hollow microspheres	Acetone	101.1 ^{b} (100 ppm)	Methanol, ethanol, benzene, xylene	30%-90%	300	33
ZnO	Nanorods	Acetone	30 ^{b} (100 ppm)	Ethanol, toluene, NH_3, CO, NO_2, H_2S, ethyne, methane, chlorine, benzene, formaldehyde	No	300	34
ZnO	Thin film	Acetone	50 ^{b} (25 ppm)	Ethanol, acetaldehyde	No	RT	31
ZnO	Nanowires	Ethanol	78 ^{b} (100 ppm)	Methanol, acetone, acetaldehyde	No	RT	118
WO_3	Nanosheets	Acetone	3.8 ^{b} (0.25 ppm)	-	No	320	36
WO_3	Microsphere	Acetone	3.53 ^{b} (0.25 ppm)	Methanol, ethanol, n-butanol, ammonia, benzene	No	230	37
WO_3	Nanoplates	Acetone	4.1 ^{b} (10 ppm)	Ethanol, ammonia, formaldehyde	No	300	38
WO_3	Nanofibers	Acetone	22.1 ^{b} (50 ppm)	Toluene, Ethanol, ammonia, formaldehyde	No	350	39
SnO_2	Nanoparticles	Xylene, Benzene	27.9 ^{b} (100 ppm)	N_2O, CH_4, CO_2, C_2H_4, CO, NO_2	0-80%	350	119
SnO_2	Thin film	xylene	-	Benzene, toluene, cyclohexane, oligomer, propene	10-100%	50	109
Fe_2O_3	Nanotubes	Acetone	84 ^{b} (50 ppm)	Ethanol, NH^3, CO, Benzene, toluene, H_2, Methane	No	350	48
Fe_2O_3	Foam	Acetone	11 ^{b} (100 ppm)	-	No	49	49
NiO	Thin film	xylene	1 ^{b} (100 ppm)	Toluene, Benzene, o-xylene, m-xylene	No	300	26
TiO_2	nanorods	Acetone	21 ^{b} (500 ppm)	ethanol, NH_3, DMF, formaldehyde	No	500	42

TiO_2	Fractals	Acetone	98% ^{c} (12.5 ppm)	NO, CO_2, H_2O, C_2H_4O	yes	325	43
TiO_2	Nanotubes	Methanol	95.8% ^{c} (200 ppm)	Ethanol, acetone, 2-propanol	Dry-85%	RT	44
TiO_2	Nanosheets	Acetone	21.6 ^{b} (200 ppm)	Ethanol, formaldehyde, NH_3	32-91.9%	400	47
TiO_2	Spheres	Toluene	13.6 ^{b} (100 ppm)	NO_2, Benzene, xylene	10-90%	150	45
TiO_2	Nanowires	Xylene	10 ^{b} (40 ppm)	Toluene, CO, CH_4, NH_3	10-50%	150	46
TiO_2	Nanoparticles	Acetone	2.22 ^{b} (20 ppm)	Methanol, Formaldehyde, Ethanol, Isopropanol, Butanol	-	370	120
TiO_2	Thin film	Acetone	115% ^{c} (50 ppm)	Xylene, toluene, methanol	Dry-75%	150	40

*a= $(I_g-I_a)/I_a$, b= R_a/R_g, c= $(\Delta R/R_a)$ x 100

Table 1.2 illustrates different metal oxide semiconductors (p-type and n-type) based on breath VOC sensors operating in the resistive mode. Among the reported metal oxides for breath VOC detection, ZnO, WO_3, and TiO_2, etc. are the conventional and most investigated metal oxide semiconductors [11, 21, 109-115]. Additionally, ZnO has been widely explored and established sensing material since the 1960s [21]. TiO_2 is most comparatively more explored for breath ethanol sensing [114,115]. Pan et al. [114] and Tian et al. [115] synthesized TiO_2 thin film and nanospheres, respectively for fast and sensitive ethanol detection. MOS semiconductors are employed for breath xylene detection and found that discrimination of Xylene from BTX is quite difficult and require a highly selective sensing material [84,110,111]. Some metal oxides mainly, ZnO, SnO_2, etc were operated at high temperatures (200 to 425 °C) making the sensors electrically unstable and complex for real time breath testing [32-34, 36,42,47,48,119]. The humidity-active nature of metal oxides results in deteriorated sensing properties such as response, response and recovery time of the sensor [11]. Only a few numbers of reported sensors for breath VOC detection optimized their sensors in the presence of sufficient humidity level ($\geq$ 50% RH) [33,40,44-47,109,119,120]. The low selectivity of metal oxides leads to false results during cross-sensing study [11, 75]. Poor long-term stability of sensors causes the problems such as uncertain results, non-repeatability and false readings [75]. There have been numerous reports of metal oxide semiconductor sensors having detection limits higher than 300 ppm, which is not particularly helpful for the majority of real-time applications [11,21,75].

Among all of the metal oxides, TiO_2 nanostructures offer a number of advantages for breath VOC sensing. TiO_2 possesses outstanding qualities such as non-toxicity, environment friendly, photostability, and corrosion-free nature [121]. TiO_2 is a wide bandgap (~3.2 eV) metal-semiconductor that exists in three crystalline phases; anatase, rutile, and brookite [122]. TiO_2 is an n-type semiconducting material due to the presence of higher oxygen vacancies and can be easily transformed into any of the phases which can be exploited in the modulation of the sensing properties [123]. However, the type of conductivity of TiO_2 can be altered from n- to p-type by varying the concentration of Ti vacancies with respect to oxygen vacancies. Thus, the type and magnitude of conductivity of TiO_2 can be changed by controlling these defect densities. Among all three forms, rutile is the most stable crystalline state of TiO_2 and is utilized in many applications. Interestingly, anatase TiO_2 has a more active structure than its counterparts like rutile and brookite [122]. The surface of anatase TiO_2 has a large number of free charge carriers, which lowers the activation energy needed by the analyte molecules to react on the surface which promotes the low-temperature sensing of the VOCs [124]. Other metal oxides (like ZnO, SnO_2, WO_3, etc.) sensors are fabricated by transferring or depositing them on some foreign substrates like SiO_2/Si, ITO, alumina, etc. which degrades the stability and repeatability of the sensors [21,22,75,113]. However, most of the TiO_2 nanostructures grow over the metallic Ti substrate which increases the overall stability of the material [44]. Apart from this, TiO_2 can be synthesized in a variety of nanoforms like 0-D (nanoparticles, Quantum dots) [125], 1-D (nanotubes, nanorods) [44], 2-D (thin films, nanofibers) [126] and 3-D (nanospheres) [45]. The variation in morphology of TiO_2 consequences in the change in specific surface area and reactive sites of gaseous analytes [123]. 1-D morphologies of TiO_2 are more favorable compared to thin films and other nanostructures because they provide both an inner and an exterior surface for the adsorption-desorption of VOCs, which improves the response magnitude of the sensor [44]. Additionally, 1-D nanostructure-like nanotubes electrodes were placed vertically between TiO_2 nanotubes where electrons do not need to cross the intergranular potential barrier and consequently reduce the operating temperature [44]. Apart from this, Zero-dimensional (0-D) nanomaterials are also promising with their unique nature. They are superior to other nanomaterials due to their excessively small size, highly functional edge sites per unit mass, and edge and quantum confinement effect [127].

From the above discussion, 1-D and 0-D TiO_2 nanostructures can be considered promising materials for chemiresistive sensors. Comparatively low operating temperature, high sensitivity, reliability and stability are the key factors for choosing this material among other metal oxide semiconductors. However, the low cross-selectivity of these sensors and the high interference of environmental humidity on sensing performance are major drawbacks in the case of breath VOC detection [123].

1.3.2 Perovskites:

Perovskites materials gained wide attention in past few years due to their outstanding properties like; high charge carrier mobility, morphological stability, good thermal and chemical stability, tunable semiconducting bandgap and porous morphology, good reliability and long-term sensor performance are employed in a variety of applications like photocatalytic reactions, Li-ion batteries, switching devices and gas/VOC sensors [128-132]. Generally, perovskites are represented by the general formula of; ABX_3, where A and B are two cations of very dissimilar groups and X is often oxygen and other big anions most probably halides, sulfides, and nitrides [133,134]. A is a monovalent organic or inorganic cation and its functionally sizable and its size, shape and charge distribution are vital factors for the stability of the perovskite structure [133]. B as a metallic cation has a smaller size [135]. The semiconducting nature of perovskites offers high charge carrier mobility and relatively high conductivity even at room temperature offering a potential use in gas or VOC sensing applications [133, 136]. A variety of perovskites $LaFeO_3$

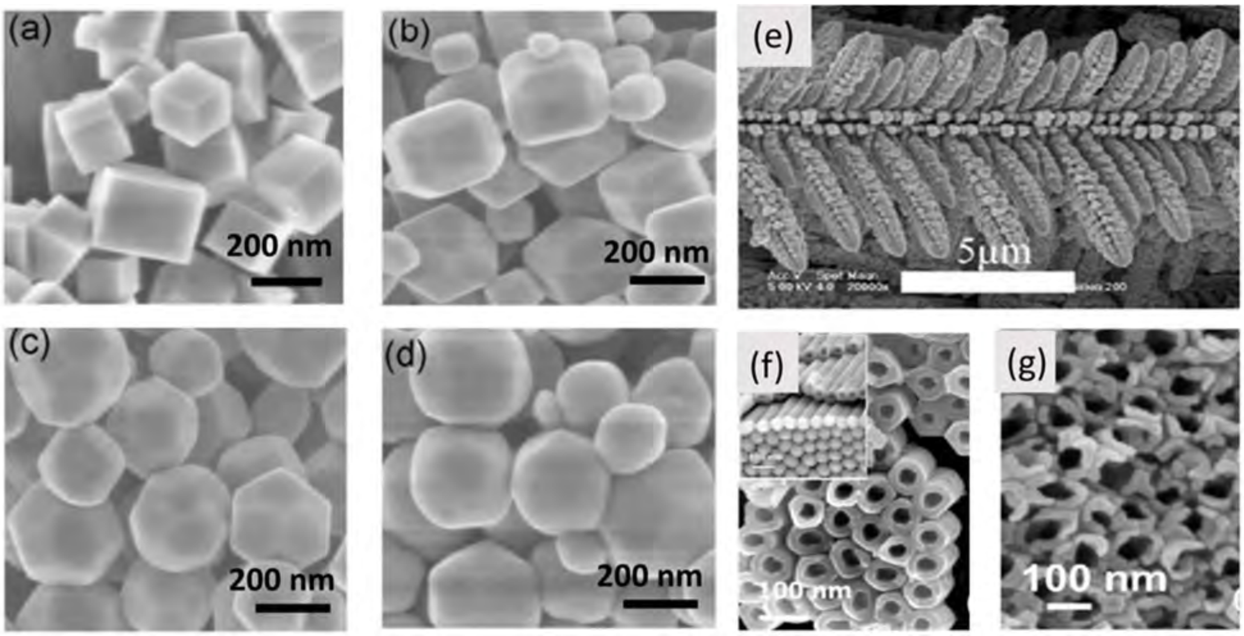

Fig. 1.3. FESEM images of various morphologies of $SrTiO_3$ perovskites: (a-d) four typical shapes of $SrTiO_3$ submicro/nanocrystals, share one scale bar (200 nm, as shown in (a)) [134], (e) Three-dimensional microscale superstructures [149] and (f, g) $SrTiO_3$ nanotubes at different reaction times [138].

[50, 51], $ZnSnO_3$ [52], $BaSnO_3$ [53], $LaSrCoO_3$ [54] and $SrTiO_3$ [55,56] for a variety of breath VOCs. For example, the $LaFeO_3$ (LFO) hollow porous sphere, prepared by the hydrothermal method, exhibited a rapid response and high sensitivity toward 143 ppm ethanol at 300 °C [51]. Trabelsi et al. reported oxygen vacancies modulated $SrTiO_{3-\delta}$ for effective ethanol sensing study at room temperature. The data concluded that sensors with optimized oxygen vacancy content showed good semiconducting and ethanol sensing properties [55].

Table 1.3 is showing the VOC sensing characteristics of different perovskite-based chemiresistive sensors. In summary, the sensing behavior of perovskite-based gas chemiresistive sensors depend upon the morphology and crystalline structure of the perovskites. Compared to primitive metal oxides their operating temperature is low with a highly stable sensing characteristic. However, most of the sensors are not optimized in the range of humid environments and the selectivity of pristine perovskites lacking towards a particular target breath VOC in the presence of other cross-interfering VOCs and gases.

Table 1.3. Summarizes the perovskites-based breath VOC sensors.

Perovskite	**Morphology**	**Target VOC**	**Sensitivity**	**Cross-interfering VOCs/gases**	**Humidity study (RH)**	**Op. Temp.**	**Ref.**
$ZnSnO_3$	Spheres	Acetone	37^{a} (80 ppm)	Ethanol, toluene, H_2, CO, NO_2	10%, 30%	270	52
$BaSnO_3$	Nanorods	Acetone	45.85^{a} (50 ppm)	Ethanol, methanol, acetaldehyde, CO_2, ammonium hydroxide	No	80	53
$LaSrCoO_3$	Nanoparticles	Acetone	$20\%^{b}$ (50 ppm)	Ethanol, ammonia, methane	45%	25	54
$LaFeO_3$	Film	Acetone	19.3^{a} (500 ppm)	Methanol, formaldehyde, CH_4, LPG	No	240	50
$LaFeO_3$	Hollow spheres	Ethanol	14.5^{a} (143 ppm)	Acetone, LPG, ammonia	No	300	51
$ZnCr_2O_4$	Mesoporous film	xylene	26.8^{a} (1 ppm)	-	No	270	24
$SrTiO_{3-\delta}$ (δ= 0.125)	Sheets	Ethanol	$1600\%^{b}$ (100 ppm)	-	No	66	56
$SrTiO_{3-\delta}$	Sheets	Ethanol	- (500 ppm)	-	No	56-366	55
$(C_4H_9NH_3)_2PbI_4$	-	xylene	11.8^{a} (1 ppm)	Benzene, ethanol, toluene, formaldehyde, dichloromethane, acetone	-	140	137

*a= R_a/R_g, b= $(\Delta R/R_a)$x100

Strontium titanate ($SrTiO_3$) exhibits an ideal model perovskite structure with outstanding physical properties [55,138-140]. The physical properties of $SrTiO_3$, to adopt the specific application can easily be modified by changing the nature and concentration of lattice defects through doping and controlling the oxygen stoichiometry [55,56,141]. Regardless of whether it is used as a single reactive material or combined with other semiconductors to form heterojunction composites, $SrTiO_3$ is an integral part of determining the overall performance of devices for various applications [142-148]. Additionally, shape-construction of $SrTiO_3$ sensing material in various morphological nanostructures has been achieved by the different research groups to improve the specific surface area, variated surface properties (porosity, surface roughness) and defect density which results in high stability and superior gas-sensing properties as shown in Fig. 1.3 [134,138,149]. Especially, symmetric dimensional $SrTiO_3$ morphologies such as faceted crystals, nanorods, nanotubes, nanowires, nanosheets etc. have been explored and expected to have significantly higher efficiency than conventional nanoparticle-based Films [149]. A wide variety of morphologies of $SrTiO_3$ like nanocubes (NC), nanoparticle (NP), nanosphere (NS), nanofiber (NF), nanotubes (NT) etc. are developed by hydrothermal treatment and employed in various applications such as solid oxide fuel cells (SOFCs), multiferroic materials, water splitting, catalysts, medical devices, and photonic devices [142-146]. Ha et al. reported morphology-controlled $SrTiO_3/TiO_2$ nanocubes (NC), nanoparticle (NP), nanosphere (NS), and nanofiber (NF) heterostructures, by facile hydrothermal process and examined for photocatalytic performance. The most conventional route for the synthesis of $SrTiO_3$ is a hydrothermal reaction [141]. However, other routes like sol-gel, molten salt, template-assisted chemical methods, mechanochemical, combustion, etc. have also been reported extensively for the synthesis of $SrTiO_3$ [141]. Real-time detection of gases and volatile organic compounds (VOCs) is one such application where $SrTiO_3$ is preferred due to its good thermal, chemical and microstructural stability, high reliability and low processing cost [55, 145-147]. $SrTiO_3$ also provides high defect density at its interface which significantly influences its sensing characteristics [145,147].

1.3.3 Metal carbides (MXene): MXenes are relatively younger members of the 2D materials family and attracted significant attention for multiple applications due to their extraordinary physical, chemical, and electronic properties. MXenes are early-transition metal carbide/carbonitride and nitrides with general formula $M_{n+1}X_nT_X$, where M is transition metals (like Sc, Ti, V, Cr, Zr, Nb, Mo, and Ta), X is C or N and T is surface terminal groups (like O, F, OH, etc.) [57,150,151]. Mxenes are mostly synthesized from the parent MAX phases which are generally formulated with $M_{n+1}AX_n$ where the A element (Al, Si, P, S, Ga, etc.) are from group 13 or 14 of the periodic table [58]. MXenes are synthesized by selective etching of A element from the MAX phase [58]. Till now, the following MXenes i.e., M_2X type, M_3X_2 type, and M_4X_3 type have been synthesized and employed in a variety of applications. HF (hydrofluoric acid) is the most commonly used etchant for MXene synthesis but later some mild etchants like LiF+ HCl, NaF+HCl [59, 152,153], and fluoride-free alkaline etchant [154] were also found suitable for MXene synthesis. In some cases, intercalation and delamination of MXene sheets have also been used for the synthesis of single-layered MXene by using suitable agents like DMSO (dimethyl sulfoxide) [61], tetrabutylammonium hydroxide (TBAOH) [63], tetramethylammonium hydroxide (TMAOH) [65] with attractive properties participate in sensing [155].

The attractive properties of MXenes such as large specific surface area, abundant functional groups (–OH, –O, or –F), porous structure, tunable surface chemistry, good chemical and thermal

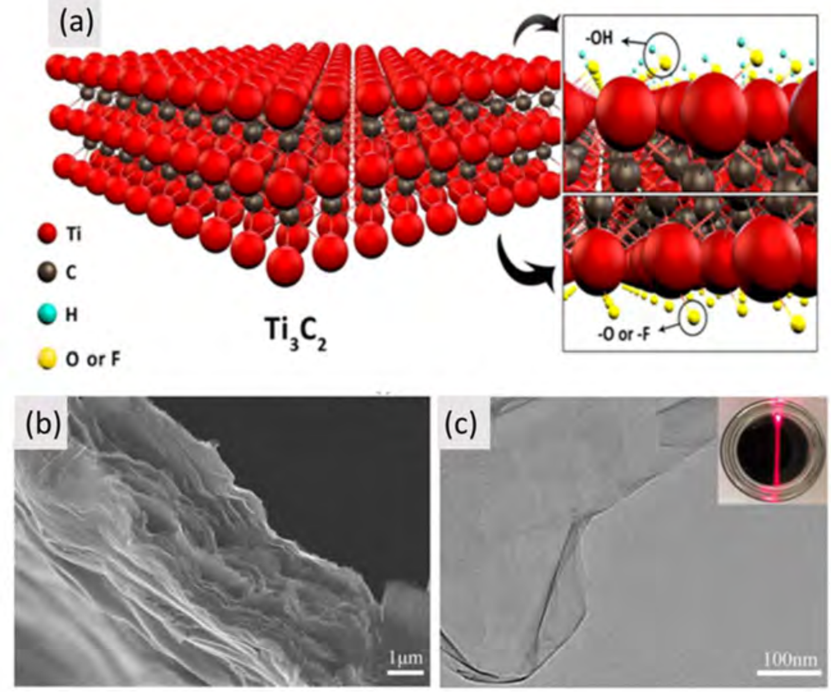

Fig. 1.4. (a) Schematic representation of $Ti_3C_2T_x$ structure and different functional groups on the surface of $Ti_3C_2T_x$ nanosheets [59], (b) SEM image of the cross-section view of the SL-Ti_3C_2 film and (d) TEM image of SL-Ti_3C_2 nanosheets [61].

stability, high metallic conductivity, fast electron transfer ability and easy solution processability provide much applicability in gas or VOC sensing as shown in Fig. 1.4 [60,150,151]. Herein, gases and VOCs sensing behavior of MXene has been reported by different research groups. Pristine MXene such as $Ti_3C_2T_x$ [57-60], Ti_3C_2 [61,62], $V_4C_3T_x$ [27,42], and Mo_2CT_x [65,66] are used for the detection of various gases, and VOCs. Among all of these MXenes, $Ti_3C_2T_x$ is most widely implemented as the gas sensing material and found highly sensitive towards acetone [63,156] and ethanol [157-159] compared to other breath VOCs. Eunji Lee et al. reported the first MXene-based gas sensor where they tested ethanol, methanol, acetone and ammonia on the surface of 2D $Ti_3C_2T_x$ sheets. They claimed that the sensing response of *p*-type $Ti_3C_2T_x$ was due to the active defective sites and interaction with surface functional groups with the highest response for ammonia (~0.21/100 ppm) because of its large adsorption energy as shown in Fig. 1.4(a) [59]. MXene with *p*-type semiconducting behavior showed a positive gas response where the resistance of the device gets increased with the addition of reducing one [63,60,158]. The thickness of the MXene film dramatically affect the sensing performance. With increase of the thickness of MXene sheets, the sensor response gets declined for both reducing and oxidizing gases. The composition, morphology and synthesis route of MXene significantly affect the gas sensing properties. Variation in carbon precursors (graphite, TiC, lampblack) [58] and $Ti_3C_2T_x$ flakes size [60] directly influence the NH_3 sensing response at room temperature and found that small size flakes show better response than the larger one because it produced shorter gas diffusion path [58,60]. $Ti_3C_2T_x$ film as a metallic channel was used to provide good electrical conductivity to yield low noise and high signals induced by tremendous adsorption sites for ethanol sensing reported by Kim et al [158]. A virtual sensor array based on MXene was fabricated for the selective detection of ethanol in the concentration range of 100-800 ppm and principal component analysis (PCA) was used to discriminate the VOCs. The resulting data concluded ~93.4% accuracy for the ethanol concentration showing the potential for the detection of particular VOC in complex interfering VOCs mixture for breath analysis application [160].

Table 1.4. Summarizes the MXenes based breath VOC sensors.

MXene	Other specification	Target gas	Sensitivity	Cross interfering VOCs	Humidity study	Op. tem.	Ref.
$V_4C_3T_x$	48% HF	CH_3COCH_3	0.65 [a] (8ppm)	-	10%	RT	63
Mo_2CT_x	25 wt % HF	$C_6H_5CH_3$	2.65 % [b] (100 ppm)	Methanol, ethanol, benzene, acetone	No	RT	65

$Ti_3C_2T_x$	LiF+HCl	C_2H_5OH	6% ^{b} (20 ppm)	Ethylene, hexane, octane, benzene, acetone, toluene	water	RT	159
$Ti_3C_2T_x$	LiF/HCl	CH_3COCH_3	0.97% ^{b} (100 ppm)	acetone, ethanol, NH_3, propanal, NO_2, SO_2, CO_2	No	RT	158
Mo_2C	Carburization	C_2H_5OH	6% ^{b} (1000 ppm)	NO_2, SO_2, NH_3, acetone, propanal, ethanol, hexane, toluene	No	RT	66
$Ti_3C_2T_x$	LiF+HCl+HF	$C_7H_6O+C_7H_6N_2O_4+C_8H_7N$	-(100 ppm)	Indole, DNT	No	RT	161

*a=R_a/R_g, c= $(\Delta R/R_a)$x100

*a=R_a/R_g, b= $(\Delta R/R_a)$x100

Pristine MXenes such as $Ti_3C_2T_x$ [158,161], $V_4C_3T_x$ [63] and Mo_2CT_x [65,66] are used for the detection of breath VOCs. Interestingly most of the reported 2D MXene was sensed at room temperature as shown in Table 1.4. Among all of these MXenes, $Ti_3C_2T_x$ is most widely implemented as the gas sensing material (Table 1.4) due to its outstanding properties. Sensing possibilities of MXene towards different gases/VOCs was tested and found that it was highly sensitive towards acetone [63], and ethanol [158,66,159]. On the other hand, MXene was less explored for some other gases/VOCs as discussed in Table 3 [65,161]. $Ti_3C_2T_x$ is more widely preferred for reducing gas sensing as compare to the oxidizing one because it gets easily oxidized in TiO_2 in oxidizing ambient [63,161].

Moreover, the selectivity of a sensor towards a particular gas/VOC was a major concern in MXene-based sensors as shown in Table 1.4. Pure MXenes suffer from other shortcomings like high humidity interactive nature due to hydrophilic behavior, low flexibility, high metallic conductivity, and low thermal and chemical stability of MXene in aqueous solution. On the other hand, MXene-based sensors also faced some major obstacles like high recovery time and drift in baseline resistance, etc. which encouraged us to think about its composites fabrication to overcome these limitations. The literature concluded that MXene-based sensors provided improved properties after the composite formation with other sensing materials.

1.3.4 Hybridization of sensing material:

As we discussed earlier each sensing material has certain limitations in its pristine form and to overcome these problems many solutions have been proposed by the researchers. The following best-known strategies have been used by the researchers are (i) use of temperature cycling [21],

(ii) doping in nanomaterials [21], (iii) formation of composite [21, 28, 29, 162-175], (iv) surface functionalization [21,145,176-182], (v) morphological variations [21,22], (vi) use of multi-sensor array and pattern recognition [21,22]. To improve a particular sensing characteristic of the sensor, optimization of the parameters could be different. In this case, the sensitivity of a sensor depends on factors like nanostructure or morphology, specific surface area, the composition of the participating materials and porosity of the sensing material [22]. The composite formation includes the formation of heterostructures between two efficient semiconducting sensing materials is one of the most common interests of the researchers.

Research data envisaged that hybridization of TiO_2 with different sensing materials like; metal oxides (WO_3 [162,163], SnO_2 [115, 164], Co_3O_4 [165]), carbon nanomaterials (GO [166]) and chalcogenides (MoS_2 [125], WSe_2 [114]) exhibit enhanced breath VOC sensing performance and overcome the limited response and high operating temperature issues of sensor significantly. The morphology of participating composite materials also plays a key role in further improving the sensing properties. Zhang et. al. reported TiO_2 nanofibers coated with WO_3 nanospheres for efficient xylene sensing characteristics. It was noted that WO_3 nanocubes on the TiO_2 nanofibers are helpful in achieving high surface area and enhancing the gas-sensing catalytic process [163]. The addition of chalcogenides like MoS_2, WSe_2, WS_2 etc. with the TiO_2 metal oxide improves the selectivity, sensitivity and operating temperature of the resulting sensor device [114,125,167]. Specifically, 2D chalcogenides are famous materials for their low-temperature sensing and selective nature towards a particular gas or VOC among a number of other interfering VOCs [167]. Pan et. al. synthesized an ethanol selective sensor system based on the TiO_2/WSe_2 nanocomposite. The hydrothermal route was used to synthesize TiO_2 nanospheres (NSs) and WSe_2 hexagonal nanosheets (HNs). The sensor attained high response (42.8/100 ppm ethanol), extremely short response/recovery time (2 s/1 s for 30 ppm), and excellent selectivity at 25 °C operating temperature [114]. Apart from this, doping or surface functionalization by noble metal nanoparticles such as Ag [176], Au [35,119], Pd [177, 178,179], Pt [179], Sn [180], Nb [112] and Sr [23] are the most suitable technique for overcoming the certain limitations of MO sensing material [21]. These sensitization effects increase the sensitivity, improve selectivity and decrease the overall operating temperature of the sensors [178].

$SrTiO_3$ perovskite has been functionalized and hybridized with other materials to improve its sensing properties. Hybridization with other materials [28,29,146], nanoparticle [145] and oxygen functionalization [55,56]. A number of reports have been published on hybridized $SrTiO_3$ sensors for the detection of different VOCs and gases such as H_2 [146], ethanol [55,56,145], O_2 [128,139] and ozone [130]. Trabelsi et al reported oxygen vacancy modulated $SrTiO_3$ for effective ethanol sensing at room temperature. The data concluded that sensors with optimized oxygen vacancy content showed good semiconducting and ethanol sensing properties [55]. Meng et al. reported that the p-type Au-$LaRhO_3/SrTiO_3$ sensor showed good ethanol sensing characteristics based on the change of resistance caused by the interaction between adsorbed ethanol molecules on the surface of the sensor [145]. The incorporation of metal nanoparticles in sensing material dominates the electronic exchange between the sensing film and the ambient by generating new O^{2-} adsorption sites [6,101,102].

The hybridization of metal oxides and metal nanoparticle with 2D MXene can overcome the poor selectivity and low stability issues of MXenes [54,55,62,153,168,169]. $Ti_3C_2T_x$ MXene composite with different metal oxides such as Co_3O_4 [168], TiO_2 [170-172], CuO [173], SnO-SnO_2 [174], and $W_{18}O_{49}$ [175] have been extensively studied by the researchers. $W_{18}O_{49}$ nanorods/$Ti_3C_2T_x$ composite was synthesized by solvothermal method and sensing performance revealed that $Ti_3C_2T_x$ with 2% concentration showed the highest response (11.6% at 20 ppm) for acetone and beyond this concentration response get decreased with 0.17 ppm LOD on the cost of operating temperature (300 ˚C) [175]. TiO_2 was the most frequently used metal oxide in composition with MXene for the detection of reducing gases at room temperature. Partially oxidized $Ti_3C_2T_x$ at 350 ˚C [170] and oxygen plasma-treated $Ti_3C_2T_x$ [171] resulted in the formation of inbuilt TiO_2 nanoparticles and showed a significantly high response toward ethanol (22.47% at 100 ppm) and acetone (180 % at 2 ppm), respectively due to the defects and oxygen functional groups [170,171]. A Ternary MXene composite based on TiO_2 was synthesized (TiO_2-C/g(graphene)-$C_3N_4/Ti_3C_2T_x$) and showed outstanding sensitivity (91 % at 10 ppm) towards ethanol but the selectivity of the sensor was not attractive enough for real-time study [172]. MXenes [181,182] based sensors showed improved sensing properties through electronic and chemical sensitization effects of noble metal nanoparticles.

Apart from these, reports claim that the use of metal functionalization (Ag [6], Pd/Sn [102]) or the addition of overlayer (CeO_2 on CuBr [100], trimethylacetic anhydride [159]) blocks the interaction between moisture and sensing layer to improve the robustness of the sensors towards humidity. Metal nanoparticles act as a hydroxyl absorber drastically decreasing the response toward humidity [102]. Li et. al. reported reduced hydrophilicity while improving the VOCs sensitivity of $Ti_3C_2T_x$ MXene towards ethanol by introducing hydrocarbon terminations. The trimethylacetic anhydride functionalized $Ti_3C_2T_x$ MXene showed a reduced response of 71% against water vapor compared with pristine $Ti_3C_2T_x$ [159]. Nanoporous materials act as "breathable" materials where gas molecules can diffuse through the pores and show a negligible influence on humidity [7].

1.4 Gaps in existing research:

The detailed literature review envisaged that most of the chemiresistive sensors suffer with several limitations. After introduction of nanostructured materials, efficiency of chemoresistive sensors have been increased significantly. A sufficient improvement is still remained to make nanomaterials based chemiresistive sensors suitable for advanced application like breath analysis. A few research gaps have been identified from breath VOC sensing perspective and listed below.

- Chemiresistive sensors are mostly operated at high temperatures (300-500 °C) that significantly influence the long-term stability of sensor. Metal oxide and perovskite-based sensors are the most common example where extra activation energy is essential for gas or VOC detection.
- Poor selectivity is also a major concern. No systematic study was performed to make the sensor selective. The sensors are not selective for long chain VOCs.
- The detection limit of the sensors is very high for a breath VOC detection. For breath analysis application, the detection limit should be in the lower ppb or ppt level.
- Humidity is the less focused area for gas or VOC sensing. Humidity study is essential for any real time applications like breath VOC detection.

After considering all these shortcomings of the breath VOC sensor research, titanium oxide based perovskite and carbide nanocomposite sensors have been proposed in the present research proposal. The nanocomposites of these materials have been chosen to develop advanced breath VOC sensors. The major objective is to develop a humidity-tolerant sensor that detects the ppb level of VOC. Also, the emphasis is on developing first responding devices for different VOC to develop naturally selective sensors.

1.5 Objectives:

- ✓ Synthesis of titanium oxide and their perovskite and carbide composites in nanoscale dimension.
- ✓ Hybridization of the above materials with nanoparticles of metal and chalcogenides.
- ✓ Structural, morphological and chemical characterizations of developed nanomaterials and their nanocomposites.
- ✓ Fabrication of vertical or MIM, and planar type sensors by using the developed nanomaterials.
- ✓ Testing and characterizations of sensors in the exposure of volatile organic compounds (VCOs), mostly considered as the potential breath marker associated with different diseases.
- ✓ Optimization of sensor performance in terms of low-level (ppb) detection, humidity tolerant sensing with long term stability to make them suitable for breath analysis application.

References:

[1] R. Schnabel, R. Fijten, A. Smolinska, J. Dallinga, and F. J. Van Schooten, "Analysis of volatile organic compounds in exhaled breath to diagnose ventilator-associated pneumonia," *Nat. Publ. Gr.*, no. July, pp. 1–10, 2015, doi: 10.1038/srep17179.

[2] X. Lin *et al.*, "Global, regional, and national burden and trend of diabetes in 195 countries and territories: an analysis from 1990 to 2025," *Sci. Rep.*, vol. 10, no. 1, pp. 1–11, 2020, doi: 10.1038/s41598-020-71908-9.

[3] R. P. Arasaradnam, J. A. Covington, C. Harmston, and C. U. Nwokolo, "Alimentary Pharmacology and Therapeutics Review article : next generation diagnostic modalities in gastroenterology – gas phase volatile compound biomarker detection," 2014, doi: 10.1111/apt.12657.

[4] C. Di, R. Paolesse, E. Martinelli, and R. Capuano, "Analytica Chimica Acta Solid-state gas sensors for breath analysis : A review," *Anal. Chim. Acta*, vol. 824, pp. 1–17, 2014, doi: 10.1016/j.aca.2014.03.014.

[5] J. S. Kim, H. W. Yoo, H. O. Choi, and H. T. Jung, "Tunable volatile organic compounds

sensor by using thiolated ligand conjugation on MoS_2," *Nano Lett.*, vol. 14, no. 10, pp. 5941–5947, 2014, doi: 10.1021/nl502906a.

[6] Y. Qin, X. Wang, and J. Zang, "Sensors and Actuators : B . Chemical Ultrasensitive ethanol sensor based on nano-Ag & ZIF-8 co-modified SiNWs with enhanced moisture resistance," *Sensors Actuators B. Chem.*, vol. 340, no. 92, p. 129959, 2021, doi: 10.1016/j.snb.2021.129959.

[7] P. Zhu, S. Li, C. Zhao, Y. Zhang, and J. Yu, "3D synergistical rGO Eu(TPyP)(Pc) hybrid aerogel for high-performance NO_2 gas sensor with enhanced immunity to humidity," *J. Hazard. Mater.*, vol. 384, no. October 2019, p. 121426, 2020, doi: 10.1016/j.jhazmat.2019.121426.

[8] W. Yan, X. Zeng, H. Liu, C. Guo, M. Ling, and H. Zhou, "Highly reliable and selective ethanol sensor based on α-Fe_2O_3 nanorhombs working in realistic environments," *Chinese Phys. B*, vol. 28, no. 10, p. 106801, Sep. 2019, doi: 10.1088/1674-1056/ab3af1.

[9] N. Roy *et al.*, "Paper Based Enzymatic Chemiresistor for POC Detection of Ethanol in Human Breath," vol. 20, no. 5, pp. 2278–2286, 2020.

[10] A. Physics, "Current status of clinical breath analysis 1," vol. 426, pp. 421–426, 2006, doi: 10.1007/s00340-006-2280-4.

[11] S. Das and M. Pal, "Review—Non-Invasive Monitoring of Human Health by Exhaled Breath Analysis: A Comprehensive Review," *J. Electrochem. Soc.*, vol. 167, no. 3, p. 037562, 2020, doi: 10.1149/1945-7111/ab67a6.

[12] B. De Lacy Costello *et al.*, "A review of the volatiles from the healthy human body," *J. Breath Res.*, vol. 8, no. 1, 2014, doi: 10.1088/1752-7155/8/1/014001.

[13] V. Saasa, T. Malwela, M. Beukes, M. Mokgotho, C.-P. Liu, and B. Mwakikunga, "Sensing Technologies for Detection of Acetone in Human Breath for Diabetes Diagnosis and Monitoring," *Diagnostics*, vol. 8, no. 1, p. 12, 2018, doi: 10.3390/diagnostics8010012.

[14] X. Zhou *et al.*, "Nanomaterial-based gas sensors used for breath diagnosis," *J. Mater. Chem. B*, vol. 8, no. 16, pp. 3231–3248, 2020, doi: 10.1039/c9tb02518a.

[15] S. J. Kim, S. J. Choi, J. S. Jang, H. J. Cho, and I. D. Kim, "Innovative Nanosensor for Disease Diagnosis," *Acc. Chem. Res.*, vol. 50, no. 7, pp. 1587–1596, 2017, doi: 10.1021/acs.accounts.7b00047.

[16] R. Unnikrishnan, R. M. Anjana, and V. Mohan, "Diabetes mellitus and its complications in India," *Nat. Rev. Endocrinol.*, vol. 12, no. 6, pp. 357–370, 2016, doi: 10.1038/nrendo.2016.53.

[17] S. Zhang *et al.*, "An acetone gas sensor based on nanosized Pt-loaded Fe_2O_3 nanocubes," *Sensors Actuators, B Chem.*, vol. 290, no. July 2018, pp. 59–67, 2019, doi: 10.1016/j.snb.2019.03.082.

[18] S. J. Choi *et al.*, "Selective diagnosis of diabetes using Pt-functionalized WO_3 hemitube networks as a sensing layer of acetone in exhaled breath," *Anal. Chem.*, vol. 85, no. 3, pp. 1792–1796, 2013, doi: 10.1021/ac303148a.

[19] M. Righettoni and A. Tricoli, "Toward portable breath acetone analysis for diabetes detection," *J. Breath Res.*, vol. 5, no. 3, 2011, doi: 10.1088/1752-7155/5/3/037109.

[20] J. Kwak *et al.*, "Evaluation of Bio-VOC sampler for analysis of volatile organic compounds in exhaled breath," *Metabolites*, vol. 4, no. 4, pp. 879–888, 2014, doi: 10.3390/metabo4040879.

[21] M. Ahmadipour *et al.*, "Detection of breath acetone by semiconductor metal oxide nanostructures-based gas sensors: A review," *Mater. Sci. Semicond. Process.*, vol. 149, no. November 2021, p. 106897, 2022, doi: 10.1016/j.mssp.2022.106897.

[22] D. Yang, R. A. Gopal, T. Lkhagvaa, and D. Choi, "Metal-oxide gas sensors for exhaled-breath analysis: A review," *Meas. Sci. Technol.*, vol. 32, no. 10, 2021, doi: 10.1088/1361-6501/ac03e3.

[23] L. Song *et al.*, "Sr-Doped Cubic In_2O_3/Rhombohedral In_2O_3 Homojunction Nanowires for Highly Sensitive and Selective Breath Ethanol Sensing : Experiment and DFT Simulation Studies," pp. 2–11, 2020, doi: 10.1021/acsami.9b15928.

[24] R. Guo *et al.*, "Ordered large-pore mesoporous $ZnCr_2O_4$ with ultrathin crystalline frameworks for highly sensitive and selective detection of ppb-level p-xylene," *Sensors*

Actuators B Chem., vol. 365, no. March, 2022, doi: 10.1016/j.snb.2022.131964.

[25] G. Peng *et al.*, “Diagnosing lung cancer in exhaled breath using gold nanoparticles,” *Nat. Nanotechnol.*, vol. 4, no. 10, pp. 669–673, 2009, doi: 10.1038/nnano.2009.235.

[26] M. Phillips *et al.*, “Volatile organic compounds in breath as markers of lung cancer: A cross-sectional study,” *Lancet*, vol. 353, no. 9168, pp. 1930–1933, 1999, doi: 10.1016/S0140-6736(98)07552-7.

[27] D. Poli *et al.*, “Exhaled volatile organic compounds in patients with non-small cell lung cancer: Cross sectional and nested short-term follow-up study,” *Respir. Res.*, vol. 6, pp. 1–10, 2005, doi: 10.1186/1465-9921-6-71.

[28] W. Cao, Y. Duan, W. Cao, and Y. Duan, “Critical Reviews in Analytical Chemistry Current Status of Methods and Techniques for Breath Analysis Current Status of Methods and Techniques for Breath Analysis,” vol. 8347, pp. 2–13, 2007, doi: 10.1080/10408340600976499.

[29] A. Sharma, R. Kumar, and P. Varadwaj, “Smelling the Disease : Diagnostic Potential of Breath Analysis,” *Mol. Diagn. Ther.*, no. 0123456789, 2023, doi: 10.1007/s40291-023-00640-7.

[30] A. Amann and D. Smith, “Breath Analysis : The Approach Towards Clinical Applications,” pp. 115–129, 2007.

[31] K. Muthukrishnan *et al.*, “Studies on acetone sensing characteristics of ZnO thin film prepared by sol–gel dip coating,” *J. Alloys Compd.*, vol. 673, pp. 138–143, 2016, doi: 10.1016/j.jallcom.2016.02.222.

[32] M. R. Alenezi, S. J. Henley, N. G. Emerson, and S. R. P. Silva, “From 1D and 2D ZnO nanostructures to 3D hierarchical structures with enhanced gas sensing properties,” *Nanoscale*, vol. 6, no. 1, pp. 235–247, 2014, doi: 10.1039/c3nr04519f.

[33] Y. Li, S. Wang, P. Hao, J. Tian, H. Cui, and X. Wang, “Soft-templated formation of double-shelled ZnO hollow microspheres for acetone gas sensing at low concentration/near room temperature,” *Sensors Actuators, B Chem.*, vol. 273, no. April, pp. 751–759, 2018, doi: 10.1016/j.snb.2018.06.110.

[34] Y. Zeng *et al.*, “Growth and selective acetone detection based on ZnO nanorod arrays,” *Sensors Actuators, B Chem.*, vol. 143, no. 1, pp. 93–98, 2009, doi: 10.1016/j.snb.2009.08.053.

[35] R. Xing *et al.*, “Preparation and gas sensing properties of In_2O_3/Au nanorods for detection of volatile organic compounds in exhaled breath,” *Sci. Rep.*, vol. 5, no. October 2014, pp. 1–14, 2015, doi: 10.1038/srep10717.

[36] J. Lu, C. Xu, L. Cheng, N. Jia, J. Huang, and C. Li, “Acetone sensor based on WO_3 nanocrystallines with oxygen defects for low concentration detection,” *Mater. Sci. Semicond. Process.*, vol. 101, no. May, pp. 214–222, 2019, doi: 10.1016/j.mssp.2019.05.038.

[37] Q. Q. Jia, H. M. Ji, D. H. Wang, X. Bai, X. H. Sun, and Z. G. Jin, “Exposed facets induced enhanced acetone selective sensing property of nanostructured tungsten oxide,” *J. Mater. Chem. A*, vol. 2, no. 33, pp. 13602–13611, 2014, doi: 10.1039/c4ta01930j.

[38] H. Zhang, Z. Liu, J. Yang, W. Guo, L. Zhu, and W. Zheng, “Temperature and acidity effects on WO_3 nanostructures and gas-sensing properties of WO_3 nanoplates,” *Mater. Res. Bull.*, vol. 57, pp. 260–267, 2014, doi: 10.1016/j.materresbull.2014.06.013.

[39] H. Xu *et al.*, “Mesoporous WO_3 nanofibers with crystalline framework for high-performance acetone sensing,” *Front. Chem.*, vol. 7, no. APR, pp. 1–11, 2019, doi: 10.3389/fchem.2019.00266.

[40] B. Bhowmik, K. Dutta, A. Hazra, and P. Bhattacharyya, “Low temperature acetone detection by p-type nano-titania thin film: Equivalent circuit model and sensing mechanism,” *Solid. State. Electron.*, vol. 99, pp. 84–92, 2014, doi: 10.1016/j.sse.2014.04.023.

[41] L. L. Deng, C. X. Zhao, Y. Ma, S. S. Chen, and G. Xu, “Low cost acetone sensors with selectivity over water vapor based on screen printed TiO_2 nanoparticles,” *Anal. Methods*, vol. 5, no. 15, pp. 3709–3713, 2013, doi: 10.1039/c3ay40373d.

[42] H. Bian *et al.*, “Characterization and acetone gas sensing properties of electrospun TiO_2 nanorods,” *Superlattices Microstruct.*, vol. 81, pp. 107–113, 2015, doi:

10.1016/j.spmi.2015.01.022.

[43] Y. M. Sabri *et al.*, “Sensors and Actuators B : Chemical Soot template TiO_2 fractals as a photoactive gas sensor for acetone detection,” *Sensors Actuators B. Chem.*, vol. 275, no. August, pp. 215–222, 2018, doi: 10.1016/j.snb.2018.08.059.

[44] P. Bindra and A. Hazra, “Selective detection of organic vapors using TiO_2 nanotubes based single sensor at room temperature,” *Sensors Actuators, B Chem.*, vol. 290, no. April, pp. 684–690, 2019, doi: 10.1016/j.snb.2019.03.115.

[45] Z. P. Tshabalala, T. P. Mokoena, K. T. Hillie, H. C. Swart, and D. E. Motaung, “Sensors and Actuators : B . Chemical Improved BTEX gas sensing characteristics of thermally treated TiO_2 hierarchical spheres manifested by high-energy { 001 } crystal facets,” *Sensors Actuators B. Chem.*, vol. 338, no. February, p. 129774, 2021, doi: 10.1016/j.snb.2021.129774.

[46] Z. P. Tshabalala *et al.*, “TiO 2 Nanowires for Humidity-Stable Gas Sensors for Toluene and Xylene,” 2021, doi: 10.1021/acsanm.0c02963.

[47] W. Ge, S. Jiao, Z. Chang, X. He, and Y. Li, “Ultrafast Response and High Selectivity toward Acetone Vapor Using Hierarchical Structured TiO 2 Nanosheets,” 2020, doi: 10.1021/acsami.9b23181.

[48] D. H. Kim *et al.*, “Vertically ordered hematite nanotube array as an ultrasensitive and rapid response acetone sensor,” *ACS Appl. Mater. Interfaces*, vol. 6, no. 17, pp. 14779–14784, 2014, doi: 10.1021/am504156w.

[49] D. Han and M. Zhao, “Facile and simple synthesis of novel iron oxide foam and used as acetone gas sensor with sub-ppm level,” *J. Alloys Compd.*, vol. 815, p. 152406, 2020, doi: 10.1016/j.jallcom.2019.152406.

[50] P. Song, H. Zhang, D. Han, J. Li, Z. Yang, and Q. Wang, “Sensors and Actuators B : Chemical Preparation of biomorphic porous $LaFeO_3$ by sorghum straw biotemplate method and its acetone sensing properties,” *Sensors Actuators B. Chem.*, vol. 196, pp. 140–146, 2014, doi: 10.1016/j.snb.2014.02.006.

[51] T. To *et al.*, “Sensors and Actuators : B . Chemical Hierarchically structured $LaFeO_3$ with

hollow core and porous shell as efficient sensing material for ethanol detection," *Sensors Actuators B. Chem.*, vol. 354, no. November 2021, p. 131195, 2022, doi: 10.1016/j.snb.2021.131195.

[52] P. M. Ba *et al.*, "Gas Sensors Based on Porous Ceramic Bodies of $MSnO_3$ Perovskites (M = Ba, Ca, Zn): Formation and Sensing Properties towards Ethanol, Acetone, and Toluene Vapours," 2022.

[53] A. Verma, D. Yadav, A. Singh, M. Gupta, K. B. Thapa, and B. C. Yadav, "Sensors and Actuators : B . Chemical Detection of acetone via exhaling human breath for regular monitoring of diabetes by low-cost sensing device based on perovskite $BaSnO_3$ nanorods," *Sensors Actuators B. Chem.*, vol. 361, no. January, p. 131708, 2022, doi: 10.1016/j.snb.2022.131708.

[54] H. Liu, Y. Guo, R. Xie, T. Peng, G. Ma, and Y. Tang, "Sensors and Actuators B : Chemical Novel acetone sensing performance of $La_{1-x}Sr_xCoO_3$ nanoparticles at room temperature," *Sensors Actuators B. Chem.*, vol. 246, pp. 164–168, 2017, doi: 10.1016/j.snb.2017.02.072.

[55] H. Trabelsi, M. Bejar, E. Dhahri, M. P. F. Grac, and M. A. Valente, "Applied Surface Science Raman, EPR and ethanol sensing properties of oxygen-Vacancies $SrTiO_{3-ı}$ compounds," vol. 426, pp. 386–390, 2017, doi: 10.1016/j.apsusc.2017.07.128.

[56] Hp. E. : L. S. and N. O. giant permittivity and ethanol sensing response in Trabelsi, M. Bejar, E. Dhahri, M. A. Valente, and M. P. F. Graça, "Physica E : Low-dimensional Systems and Nanostructures Oxygen-vacancy-related giant permittivity and ethanol sensing response in $SrTiO_{3-\delta}$ ceramics," *Phys. E Low-dimensional Syst. Nanostructures*, vol. 108, no. December 2018, pp. 317–325, 2019, doi: 10.1016/j.physe.2018.12.025.

[57] Y. Chae *et al.*, "An investigation into the factors governing the oxidation of two-dimensional Ti_3C_2 MXene," *Nanoscale*, vol. 11, no. 17, pp. 8387–8393, 2019, doi: 10.1039/c9nr00084d.

[58] C. E. Shuck *et al.*, "Effect of Ti_3AlC2 MAX Phase on Structure and Properties of Resultant $Ti_3C_2T_x$ MXene," *ACS Appl. Nano Mater.*, vol. 2, no. 6, pp. 3368–3376, 2019,

doi: 10.1021/acsanm.9b00286.

[59] E. Lee, A. Vahidmohammadi, B. C. Prorok, Y. S. Yoon, M. Beidaghi, and D. J. Kim, "Room Temperature Gas Sensing of Two-Dimensional Titanium Carbide (MXene)," *ACS Appl. Mater. Interfaces*, vol. 9, no. 42, pp. 37184–37190, 2017, doi: 10.1021/acsami.7b11055.

[60] S. J. Kim *et al.*, "Interfacial assembly of ultrathin, functional mxene films," *ACS Appl. Mater. Interfaces*, vol. 11, no. 35, pp. 32320–32327, 2019, doi: 10.1021/acsami.9b12539.

[61] M. Wu *et al.*, "Ti_3C_2 MXene-Based Sensors with High Selectivity for NH_3 Detection at Room Temperature," *ACS Sensors*, vol. 4, no. 10, pp. 2763–2770, 2019, doi: 10.1021/acssensors.9b01308.

[62] E. S. Muckley, M. Naguib, and I. N. Ivanov, "Multi-modal, ultrasensitive, wide-range humidity sensing with Ti_3C_2 film," *Nanoscale*, vol. 10, no. 46, pp. 21689–21695, 2018, doi: 10.1039/c8nr05170d.

[63] W. N. Zhao, N. Yun, Z. H. Dai, and Y. F. Li, "A high-performance trace level acetone sensor using an indispensable $V_4C_3T_X$ MXene," *RSC Adv.*, vol. 10, no. 3, pp. 1261–1270, 2020, doi: 10.1039/c9ra09069j.

[64] E. Lee, A. Vahidmohammadi, Y. S. Yoon, M. Beidaghi, and D. J. Kim, "Two-Dimensional Vanadium Carbide MXene for Gas Sensors with Ultrahigh Sensitivity Toward Nonpolar Gases," *ACS Sensors*, vol. 4, no. 6, pp. 1603–1611, 2019, doi: 10.1021/acssensors.9b00303.

[65] W. Guo *et al.*, "Selective Toluene Detection with Mo_2CT_xMXene at Room Temperature," *ACS Appl. Mater. Interfaces*, vol. 12, no. 51, pp. 57218–57227, 2020, doi: 10.1021/acsami.0c16302.

[66] S. Y. Cho, J. Y. Kim, O. Kwon, J. Kim, and H. T. Jung, "Molybdenum carbide chemical sensors with ultrahigh signal-to-noise ratios and ambient stability," *J. Mater. Chem. A*, vol. 6, no. 46, pp. 23408–23416, 2018, doi: 10.1039/C8TA07168C.

[67] A. K. Pathak *et al.*, "Recent Advances in Sensing Materials Targeting Clinical Volatile Organic Compound (VOC) Biomarkers: A Review," *Biosensors*, vol. 13, no. 1, 2023, doi:

10.3390/bios13010114.

[68] B. Buszewski, K. Martyna, T. Ligor, and A. Amann, "Human exhaled air analytics : biomarkers of diseases," vol. 566, pp. 553–566, 2007, doi: 10.1002/bmc.

[69] L. Pauling, A. B. Robinson, R. O. Y. Teranishit, and P. Cary, "Quantitative Analysis of Urine Vapor and Breath by Gas-Liquid Partition Chromatography," vol. 68, no. 10, pp. 2374–2376, 1971, doi: 10.1073/pnas.68.10.2374.

[70] G. Konvalina and H. Haick, "Effect of Humidity on Nanoparticle-Based Chemiresistors: A Comparison between Synthetic and Real-World Samples," 2012.

[71] T. A. Popov, "Human exhaled breath analysis," *ANAI*, vol. 106, no. 6, pp. 451–456, 2011, doi: 10.1016/j.anai.2011.02.016.

[72] K. D. G. van de Kant, L. J. T. M. van der Sande, Q. Jöbsis, O. C. P. van Schayck, and E. Dompeling, "Clinical use of exhaled volatile organic compounds in pulmonary diseases: A systematic review," *Respir. Res.*, vol. 13, 2012, doi: 10.1186/1465-9921-13-117.

[73] F. Buljubasic and G. Buchbauer, "The scent of human diseases : a review on specific volatile organic compounds as diagnostic biomarkers," no. March, 2014, doi: 10.1002/ffj.3219.

[74] J. D. Fenske and S. E. Paulson, "Human breath emissions of VOCs," *J. Air Waste Manag. Assoc.*, vol. 49, no. 5, pp. 594–598, 1999, doi: 10.1080/10473289.1999.10463831.

[75] M. Masikini, M. Chowdhury, and O. Nemraoui, "Review—Metal Oxides: Application in Exhaled Breath Acetone Chemiresistive Sensors," *J. Electrochem. Soc.*, vol. 167, no. 3, p. 037537, 2020, doi: 10.1149/1945-7111/ab64bc.

[76] A. Rydosz, "A Negative Correlation Between Blood Glucose and Acetone Measured in Healthy and Type 1 Diabetes Mellitus Patient Breath," 2015, doi: 10.1177/1932296815572366.

[77] A. A. Karyakin, S. V Nikulina, D. V Vokhmyanina, E. E. Karyakina, E. K. H. Anaev, and A. G. Chuchalin, "Electrochemistry Communications Non-invasive monitoring of diabetes through analysis of the exhaled breath condensate (aerosol)," *Electrochem.*

commun., vol. 83, no. September, pp. 81–84, 2017, doi: 10.1016/j.elecom.2017.09.005.

[78] A. Mashir and R. A. Dweik, “Exhaled breath analysis : The new interface between medicine and engineering,” *Adv. Powder Technol.*, vol. 20, no. 5, pp. 420–425, 2009, doi: 10.1016/j.apt.2009.05.003.

[79] L. A. Spacek *et al.*, “Breath ammonia and ethanol increase in response to a high protein challenge,” *Biomarkers*, vol. 00, no. 00, pp. 1–8, 2015, doi: 10.3109/1354750X.2015.1040840.

[80] P. J. Mazzone *et al.*, “with a colorimetric sensor array,” pp. 565–569, 2007, doi: 10.1136/thx.2006.072892.

[81] D. Hashoul and H. Haick, “Sensors for detecting pulmonary diseases from exhaled breath,” 2019, doi: 10.1183/16000617.0011-2019.

[82] A. Ulanowska, T. Kowalkowski, E. Trawińska, and B. Buszewski, “The application of statistical methods using VOCs to identify patients with lung cancer,” *J. Breath Res.*, vol. 5, no. 4, 2011, doi: 10.1088/1752-7155/5/4/046008.

[83] A. Sponring, W. Filipiak, C. Ager, and J. Schubert, “Analysis of volatile organic compounds (VOCs) in the headspace of NCI-H1666 lung cancer cells,” vol. 7, pp. 153–161, 2010, doi: 10.3233/CBM-2010-0182.

[84] S. Zhao *et al.*, “A colorimetric detector for lung cancer related volatile organic compounds based on cross-response mechanism,” *Sensors Actuators, B Chem.*, vol. 256, pp. 543–552, 2018, doi: 10.1016/j.snb.2017.10.091.

[85] C. M. F. Kneepkens, A. G. U. Y. Lepage, and C. C. Roy, “MEASURE OF LIPID PEROXIDATION,” vol. 17, no. 2, pp. 127–160, 1994.

[86] W.H. Brattain, J. Bardeen, "Surface properties of germanium," *Bell System Technical Journal*, vol. 32 pp. 1–41, 1953.

[87] N. Taguchi, "Gas detecting device," *U.S.Patent*, 3, 631, patent no. 436, 1971.

[88] P. Barik and M. Pradhan, “developments , challenges , and future perspectives,” no. i, pp. 1024–1054, 2022, doi: 10.1039/d1an02070f.

[89] Z. Yuan *et al.*, “Trace-Level , Multi-Gas Detection for Food Quality Assessment Based on Decorated Silicon Transistor Arrays,” vol. 1908385, pp. 1–8, 2020, doi: 10.1002/adma.201908385.

[90] A. Ponzoni *et al.*, “Issues Addressed at the SENSOR Lab, Brescia (Italy),” doi: 10.3390/s17040714.

[91] R. Baron, “Amperometric Gas Sensors as a Low Cost Emerging Technology Platform for Air Quality Monitoring Applications: A Review,” pp. 1553–1566, 2017, doi: 10.1021/acssensors.7b00620.

[92] N. Masson, R. Piedrahita, and M. Hannigan, “Sensors and Actuators B : Chemical Approach for quantification of metal oxide type semiconductor gas sensors used for ambient air quality monitoring,” *Sensors Actuators B. Chem.*, vol. 208, pp. 339–345, 2015, doi: 10.1016/j.snb.2014.11.032.

[93] E. Comini, G. Faglia, G. Sberveglieri, Z. Pan, and Z. L. Wang, “Stable and highly sensitive gas sensors based on semiconducting oxide nanobelts Stable and highly sensitive gas sensors based on semiconducting oxide nanobelts,” vol. 1869, no. May 2014, pp. 28–31, 2008, doi: 10.1063/1.1504867.

[94] S. Mahajan and S. Jagtap, “Metal-oxide semiconductors for carbon monoxide (CO) gas sensing: A review,” *Appl. Mater. Today*, no. xxxx, p. 100483, 2019, doi: 10.1016/j.apmt.2019.100483.

[95] G. Konvalina and H. Haick, “Sensors for Breath Testing : From Nanomaterials to Comprehensive Disease Detection,” vol. 47, no. 1, 2014.

[96] Z. Yuan, Q. Zhao, Z. Duan, C. Xie, X. Duan, and S. Li, “Sensors and Actuators : B . Chemical Ag 2 Te nanowires for humidity-resistant trace-level NO 2 detection at room temperature,” *Sensors Actuators B. Chem.*, vol. 363, no. 2, p. 131790, 2022, doi: 10.1016/j.snb.2022.131790.

[97] H.-R. Kim, A. Haensch, I. Kim, N. Barsan, U. Weimar, and J. Lee, “The Role of NiO Doping in Reducing the Impact of Humidity on the Performance of SnO_2-Based Gas Sensors: Synthesis Strategies, and Phenomenological and Spectroscopic Studies,” *Adv.*

Funct. Mater., vol. 21, no. 23, pp. 4456–4463, Dec. 2011, doi: 10.1002/adfm.201101154.

[98] L. Qiu *et al.*, “Sensors and Actuators : B . Chemical Enhanced , stable , humidity-tolerant xylene sensing using ordered macroporous NiO/ZrO_2 nanocomposites,” *Sensors Actuators B. Chem.*, vol. 324, no. February, p. 128648, 2020, doi: 10.1016/j.snb.2020.128648.

[99] F. Qu *et al.*, “Surface Functionalized Sensors for Humidity-Independent Gas Detection,” *Angew. Chemie - Int. Ed.*, vol. 60, no. 12, pp. 6561–6566, 2021, doi: 10.1002/anie.202015856.

[100] H. Li, C. Lee, D. H. Kim, and J. Lee, “Flexible Room-Temperature NH_3 Sensor for Ultrasensitive , Selective , and Humidity-Independent Gas Detection,” 2018, doi: 10.1021/acsami.8b09169.

[101] G. Rahamim *et al.*, “Sensors and Actuators B : Chemical Hydrogen sensors with high humidity tolerance based on indium-tin oxide colloids,” *Sensors Actuators B. Chem.*, vol. 310, no. December 2019, p. 127845, 2020, doi: 10.1016/j.snb.2020.127845.

[102] K. Suematsu, M. Sasaki, M. Yuasa, and K. Shimanoe, “Antimony-Doped Tin Dioxide Gas Sensors Exhibiting High Stability in the Sensitivity to Humidity Changes,” 2016, doi: 10.1021/acssensors.6b00323.

[103] K. D. Esmeryan, T. A. Yordanov, L. G. Vergov, Z. G. Raicheva, and E. I. Radeva, “Humidity Tolerant Organic Vapor Detection Using a Superhydrophobic Quartz Crystal Microbalance,” vol. 15, no. 11, pp. 6318–6325, 2015.

[104] R. L. Wilson *et al.*, “Humidity-Tolerant Ultrathin NiO Gas-Sensing Films,” 2020, doi: 10.1021/acssensors.0c00172.

[105] A. Heilig, N. Bârsan, U. Weimar, M. Schweizer-Berberich, J. W. Gardner, and W. Göpel, “Gas identification by modulating temperatures of SnO_2-based thick film sensors,” *Sensors Actuators B Chem.*, vol. 43, no. 1–3, pp. 45–51, Sep. 1997, doi: 10.1016/S0925-4005(97)00096-8.

[106] G. Dharmalingam, R. Sivasubramaniam, and S. Parthiban, “Quantification of Ethanol by Metal-Oxide-Based Resistive Sensors: A Review,” *J. Electron. Mater.*, vol. 49, no. 5, pp. 3009–3024, 2020, doi: 10.1007/s11664-020-08039-4.

[107] S. Yang, G. Lei, H. Xu, Z. Lan, Z. Wang, and H. Gu, “Metal oxide based heterojunctions for gas sensors: A review,” *Nanomaterials*, vol. 11, no. 4, pp. 1–26, 2021, doi: 10.3390/nano11041026.

[108] A. Staerz, U. Weimar, and N. Barsan, “Understanding the potential of WO_3 based sensors for breath analysis,” *Sensors (Switzerland)*, vol. 16, no. 11, 2016, doi: 10.3390/s16111815.

[109] G. Gregis *et al.*, “Detection and quantification of lung cancer biomarkers by a micro-analytical device using a single metal oxide-based gas sensor,” *Sensors Actuators, B Chem.*, vol. 255, pp. 391–400, 2018, doi: 10.1016/j.snb.2017.08.056.

[110] H. Yamagiwa *et al.*, “Detection of volatile organic compounds by weight-detectable sensors coated with metal-organic frameworks,” *Sci. Rep.*, vol. 4, pp. 1–6, 2014, doi: 10.1038/srep06247.

[111] H. Liu *et al.*, “Discriminating BTX Molecules by the Nonselective Metal Oxide Sensor-Based Smart Sensing System,” *ACS Sensors*, vol. 6, no. 11, pp. 4167–4175, 2021, doi: 10.1021/acssensors.1c01704.

[112] T. H. Kim, S. Y. Jeong, Y. K. Moon, and J. H. Lee, “Dual-mode gas sensor for ultrasensitive and highly selective detection of xylene and toluene using Nb-doped NiO hollow spheres,” *Sensors Actuators, B Chem.*, vol. 301, no. July, p. 127140, 2019, doi: 10.1016/j.snb.2019.127140.

[113] X. Zhou *et al.*, “Synergetic p+n Field-Effect Transistor Circuits for ppb-Level Xylene Detection,” *IEEE Sens. J.*, vol. 18, no. 9, pp. 3875–3882, 2018, doi: 10.1109/JSEN.2018.2818710.

[114] W. Pan, Y. Zhang, and D. Zhang, “Self-assembly fabrication of titanium dioxide nanospheres-decorated tungsten diselenide hexagonal nanosheets for ethanol gas sensing application,” *Appl. Surf. Sci.*, vol. 527, no. April, p. 146781, 2020, doi: 10.1016/j.apsusc.2020.146781.

[115] X. Tian, Z. Hu, T. Wang, H. Wang, Q. Zhang, and X. Wei, “Influence of multi-layer TiO_2/SnO_2 heterojunctions on fast and sensitive ethanol detection,” *Vacuum*, vol. 207, no. May 2022, 2023, doi: 10.1016/j.vacuum.2022.111620.

[116] M. Z. Ahmad, J. H. Kang, A. Z. Sadek, A. Moafi, G. Sberveglieri, and W. Wlodarski, "Synthesis of WO_3 nanorod based thin films for ethanol and H_2 Sensing," *Procedia Eng.*, vol. 47, pp. 358–361, 2012, doi: 10.1016/j.proeng.2012.09.157.

[117] B. Saruhan, R. Lontio Fomekong, and S. Nahirniak, "Review: Influences of Semiconductor Metal Oxide Properties on Gas Sensing Characteristics," *Front. Sensors*, vol. 2, no. April, pp. 1–24, 2021, doi: 10.3389/fsens.2021.657931.

[118] P. Shankar and J. B. B. Rayappan, "Monomer: Design of ZnO Nanostructures (Nanobush and Nanowire) and Their Room-Temperature Ethanol Vapor Sensing Signatures," *ACS Appl. Mater. Interfaces*, vol. 9, no. 43, pp. 38135–38145, 2017, doi: 10.1021/acsami.7b11561.

[119] D. J. Yu, W. Oum, A. Mirzaei, K. Y. Shin, E. B. Kim, and H. M. Kim, "Pr ep pe er r Pr ep rin t n ot pe ed."

[120] N. Chen *et al.*, "Sensors and Actuators B : Chemical Acetone sensing performances based on nanoporous TiO_2 synthesized by a facile hydrothermal method," *Sensors Actuators B. Chem.*, vol. 238, pp. 491–500, 2017, doi: 10.1016/j.snb.2016.07.094.

[121] C. A. Grimes, "Synthesis and application of highly ordered arrays of TiO_2 nanotubes," pp. 1451–1457, 2007, doi: 10.1039/b701168g.

[122] K. Herrington, B. Y. D. O. N. T. Cromer, and K. Herrington, "The Structures of Anatase and Rutile," vol. 605, no. 9, pp. 12–13, 1954.

[123] O. Tio, "Insights in the Application of Stoichiometric and Non-Stoichiometric Titanium Oxides for the Design of Sensors for the Determination of Gases and VOCs," 2020.

[124] H. Zhang and J. F. Banfield, "Thermodynamic analysis of phase stability of nanocrystalline titania," *J. Mater. Chem.*, vol. 8, no. 9, pp. 2073–2076, 1998, doi: 10.1039/a802619j.

[125] T. Gakhar and A. Hazra, "C_{60} -encapsulated TiO_2 nanoparticles for selective and ultrahigh sensitive detection of formaldehyde," 2021.

[126] S. Singh and S. Sharma, "Temperature dependent selective detection of ethanol and

methanol using MoS_2/TiO_2 composite," *Sensors Actuators B Chem.*, vol. 350, no. August 2021, 2022, doi: 10.1016/j.snb.2021.130798.

[127] Z. Wang, T. Hu, R. Liang, and M. Wei, "Application of Zero-Dimensional Nanomaterials in Biosensing," vol. 8, no. April, pp. 1–19, 2020, doi: 10.3389/fchem.2020.00320.

[128] A. M. Schultz, T. D. Brown, M. P. Buric, S. Lee, K. Gerdes, and P. R. Ohodnicki, "High temperature fiber-optic evanescent wave hydrogen sensors using La-doped $SrTiO_3$ for SOFC applications," *Sensors Actuators, B Chem.*, vol. 221, pp. 1307–1313, 2015, doi: 10.1016/j.snb.2015.07.046.

[129] H. Deng *et al.*, "Nanolayered Ti_3C_2 and $SrTiO_3$ Composites for Photocatalytic Reduction and Removal of Uranium(VI)," *ACS Appl. Nano Mater.*, vol. 2, no. 4, pp. 2283–2294, 2019, doi: 10.1021/acsanm.9b00205.

[130] V. R. Mastelaro *et al.*, "Ozone gas sensor based on nanocrystalline $SrTi_{1-x}Fe_xO_3$ thin films," *Sensors Actuators B Chem.*, vol. 181, pp. 919–924, May 2013, doi: 10.1016/j.snb.2013.02.068.

[131] K. Kacem, J. Casanova-Chafer, S. Ameur, M. F. Nsib, and E. Llobet, "Gas sensing properties of graphene oxide loaded with $SrTiO_3$ nanoparticles," *J. Alloys Compd.*, vol. 941, p. 169011, 2023, doi: 10.1016/j.jallcom.2023.169011.

[132] S. Supriya, "A critical review on crystal structure mechanisms, microstructural and electrical performances of $Bi_{0.5}Na_{0.5}$TiO3—$SrTiO_3$ perovskites," *J. Electroceramics*, vol. 49, no. 2, pp. 94–108, 2022, doi: 10.1007/s10832-022-00295-6.

[133] P. V Shinde, "A review on the sensing mechanisms and recent developments on metal halide-based perovskite gas sensors," pp. 10196–10223, 2022, doi: 10.1039/d2tc01980a.

[134] L. Dong, H. Shi, K. Cheng, Q. Wang, W. Weng, and W. Han, "Shape-controlled growth of $SrTiO_3$ polyhedral submicro / nanocrystals," vol. 7, no. 9, pp. 1311–1318, 2014, doi: 10.1007/s12274-014-0495-y.

[135] C. C. Stoumpos and M. G. Kanatzidis, "The Renaissance of Halide Perovskites and Their Evolution as Emerging Semiconductors," no. Figure 1, 2015, doi: 10.1021/acs.accounts.5b00229.

[136] E. Abdul and R. Assirey, “Perovskite synthesis , properties and their related biochemical and industrial application,” *Saudi Pharm. J.*, vol. 27, no. 6, pp. 817–829, 2019, doi: 10.1016/j.jsps.2019.05.003.

[137] M. Zhu, L. Zhang, J. Yin, J. Chen, L. Bie, and B. D. Fahlman, “Sensors and Actuators B : Chemical Physisorption induced p -xylene gas-sensing performance of ($C_4H_9NH_3)_2PbI_4$ layered perovskite,” *Sensors Actuators B. Chem.*, vol. 282, no. November 2018, pp. 659–664, 2019, doi: 10.1016/j.snb.2018.11.124.

[138] H. Amani Hamedani, J. A. Khaleel, K. H. Dahmen, and H. Garmestani, “Surface controlled growth of thin-film strontium titanate nanotube arrays on silicon,” *Cryst. Growth Des.*, vol. 14, no. 10, pp. 4911–4919, 2014, doi: 10.1021/cg500374m.

[139] X. Zhou, T. Smensen, and Y. Xu, “Defect structure and oxygen sensing properties of Mg-doped SrTiO , thick film sensors,” vol. 41, pp. 177–182, 1997.

[140] N. Y. Chan *et al.*, “Palladium nanoparticle enhanced giant photoresponse at LaAlO 3/SrTiO3 two-dimensional electron gas heterostructures,” *ACS Nano*, vol. 7, no. 10, pp. 8673–8679, 2013, doi: 10.1021/nn4029184.

[141] G. Canu, “Hydrothermal synthesis of strontium titanate : thermodynamic considerations , morphology control and crystallisation mechanisms morphological and structural,” pp. 3867–3891, 2017, doi: 10.1039/c7ce00834a.

[142] H. Che *et al.*, “Construction of $SrTiO_3/Bi_2O_3$heterojunction towards to improved separation efficiency of charge carriers and photocatalytic activity under visible light,” *J. Alloys Compd.*, vol. 688, pp. 882–890, 2016, doi: 10.1016/j.jallcom.2016.07.311.

[143] M. Y. A. Rahman, S. A. M. Samsuri, and A. A. Umar, “TiO_2–$SrTiO_3$ composite photoanode: effect of strontium precursor concentration on the performance of dye-sensitized solar cells,” *Appl. Phys. A Mater. Sci. Process.*, vol. 125, no. 1, p. 0, 2019, doi: 10.1007/s00339-018-2344-4.

[144] R. Tao, X. Li, X. Li, C. Shao, and Y. Liu, “$TiO_2/SrTiO_3/g\text{-}C_3N_4$ ternary heterojunction nanofibers: gradient energy band, cascade charge transfer, enhanced photocatalytic hydrogen evolution, and nitrogen fixation,” *Nanoscale*, vol. 12, no. 15, pp. 8320–8329,

2020, doi: 10.1039/D0NR00219D.

[145] Z. Meng *et al.*, "Au nanoparticle modified single-crystalline p-type $LaRhO_3/SrTiO_3$ heterostructure for high performing VOCs sensor," *Ceram. Int.*, vol. 46, no. 14, pp. 22140–22145, Oct. 2020, doi: 10.1016/j.ceramint.2020.05.290.

[146] N. Y. Chan *et al.*, "Highly sensitive gas sensor by the $LaAlO_3/SrTiO_3$heterostructure with Pd nanoparticle surface modulation," *Adv. Mater.*, vol. 26, no. 47, pp. 5962–5968, 2014, doi: 10.1002/adma.201401597.

[147] H. Tai, Z. Duan, Y. Wang, S. Wang, and Y. Jiang, "Paper-Based Sensors for Gas , Humidity , and Strain Detections : A Review," 2020, doi: 10.1021/acsami.0c06435.

[148] B. Szafraniak and Ł. Fu, "Semiconducting Metal Oxides: $SrTiO_3$, $BaTiO_3$ and $BaSrTiO_3$ in Gas-Sensing Applications: A Review," pp. 1–22, 2021.

[149] X. Yuan *et al.*, "Self-assembly of three-dimensional $SrTiO_3$ microscale superstructures and their photonic effect," *Inorg. Chem.*, vol. 52, no. 5, pp. 2581–2587, 2013, doi: 10.1021/ic302585g.

[150] N. Li *et al.*, "A fully inkjet-printed transparent humidity sensor based on a Ti_3C_2/Ag hybrid for touchless sensing of finger motion," *Nanoscale*, vol. 11, no. 44, pp. 21522–21531, 2019, doi: 10.1039/c9nr06751e.

[151] B. Sun *et al.*, "Co_3O_4@PEI/$Ti_3C_2T_x$MXene nanocomposites for a highly sensitive NOxgas sensor with a low detection limit," *J. Mater. Chem. A*, vol. 9, no. 10, pp. 6335–6344, 2021, doi: 10.1039/d0ta11392a.

[152] L. Yang *et al.*, "SnO_2-Ti_3C_2 MXene electron transport layers for perovskite solar cells," *J. Mater. Chem. A*, vol. 7, no. 10, pp. 5635–5642, 2019, doi: 10.1039/c8ta12140k.

[153] Z. Yang *et al.*, "Flexible resistive NO_2 gas sensor of three-dimensional crumpled MXene $Ti_3C_2T_x$/ZnO spheres for room temperature application," *Sensors Actuators, B Chem.*, vol. 326, no. 2, p. 128828, 2021, doi: 10.1016/j.snb.2020.128828.

[154] T. Li *et al.*, "Fluorine-Free Synthesis of High-Purity $Ti_3C_2T_x$ (T=OH, O) via Alkali Treatment," *Angew. Chemie - Int. Ed.*, vol. 57, no. 21, pp. 6115–6119, 2018, doi:

10.1002/anie.201800887.

[155] A. Lipatov, M. Alhabeb, M. R. Lukatskaya, A. Boson, Y. Gogotsi, and A. Sinitskii, "Effect of Synthesis on Quality, Electronic Properties and Environmental Stability of Individual Monolayer Ti_3C_2 MXene Flakes," *Adv. Electron. Mater.*, vol. 2, no. 12, 2016, doi: 10.1002/aelm.201600255.

[156] J. Wang, R. Xu, Y. Xia, and S. Komarneni, "Ti_2CT_x MXene: A novel p-type sensing material for visible light-enhanced room temperature methane detection," *Ceram. Int.*, no. July, Aug. 2021, doi: 10.1016/j.ceramint.2021.08.357.

[157] Y.-U. Haq *et al.*, "Synthesis and characterization of 2D MXene: Device fabrication for humidity sensing," *J. Sci. Adv. Mater. Devices*, no. xxxx, 2021, doi: 10.1016/j.jsamd.2021.08.003.

[158] S. J. Kim *et al.*, "Metallic $Ti_3C_2T_x$ MXene Gas Sensors with Ultrahigh Signal-to-Noise Ratio," *ACS Nano*, vol. 12, no. 2, pp. 986–993, 2018, doi: 10.1021/acsnano.7b07460.

[159] X. Li *et al.*, "Room Temperature VOCs Sensing with Termination-Modified $Ti_3C_2T_x$ MXene for Wearable Exhaled Breath Monitoring," vol. 2100872, pp. 1–12, 2022, doi: 10.1002/admt.202100872.

[160] D. Li *et al.*, "Virtual sensor array based on MXene for selective detections of VOCs," *Sensors Actuators, B Chem.*, vol. 331, no. November 2020, p. 129414, 2021, doi: 10.1016/j.snb.2020.129414.

[161] K. Yang *et al.*, " $Ti_3C_2T_x$ MXene-Loaded 3D Substrate toward On-Chip Multi-Gas Sensing with Surface-Enhanced Raman Spectroscopy (SERS) Barcode Readout ," *ACS Nano*, vol. 15, no. 8, pp. 12996–13006, 2021, doi: 10.1021/acsnano.1c01890.

[162] N. Chen, D. Deng, Y. Li, X. Xing, and X. Liu, "RSC Advances The xylene sensing performance of WO_3 decorated anatase TiO_2 nanoparticles as a sensing material for a gas sensor at a low operating temperature †," pp. 49692–49701, 2016, doi: 10.1039/c6ra09195d.

[163] N. Zhang *et al.*, "Materials Science & Engineering B Gas sensor based on TiO_2 nanofibers decorated with monodispersed WO_3 nanocubes for fast and selective xylene detection,"

Mater. Sci. Eng. B, vol. 263, no. October 2020, p. 114901, 2021, doi: 10.1016/j.mseb.2020.114901.

[164] T. Wang and L. Cheng, "Sensors and Actuators : B . Chemical Hollow hierarchical TiO_2 - SnO_2-TiO_2 composite nanofibers with increased active-sites and charge transfer for enhanced acetone sensing performance," *Sensors Actuators B. Chem.*, vol. 334, no. February, p. 129644, 2021, doi: 10.1016/j.snb.2021.129644.

[165] J. Wang *et al.*, "Sensors and Actuators B : Chemical Stabilized zirconia-based acetone sensor utilizing Fe_2TiO_5-TiO_2 sensing electrode for noninvasive diagnosis of diabetics," *Sensors Actuators B. Chem.*, vol. 321, no. June, p. 128489, 2020, doi: 10.1016/j.snb.2020.128489.

[166] R. Kalidoss, S. Umapathy, and Y. Sivalingam, "An investigation of GO-SnO_2 -TiO_2 ternary nanocomposite for the detection of acetone in diabetes mellitus patient's breath," *Appl. Surf. Sci.*, vol. 449, pp. 677–684, 2018, doi: 10.1016/j.apsusc.2017.12.090.

[167] S. Kumar, V. Pavelyev, P. Mishra, N. Tripathi, P. Sharma, and F. Calle, "Materials Science in Semiconductor Processing A review on 2D transition metal di-chalcogenides and metal oxide nanostructures based NO_2 gas sensors," *Mater. Sci. Semicond. Process.*, vol. 107, no. November 2019, p. 104865, 2020, doi: 10.1016/j.mssp.2019.104865.

[168] D. Zhang, Q. Mi, D. Wang, and T. Li, "MXene/Co_3O_4 composite based formaldehyde sensor driven by ZnO/MXene nanowire arrays piezoelectric nanogenerator," *Sensors Actuators, B Chem.*, vol. 339, no. January, p. 129923, 2021, doi: 10.1016/j.snb.2021.129923.

[169] J. Choi *et al.*, "In Situ Formation of Multiple Schottky Barriers in a Ti_3C_2 MXene Film and its Application in Highly Sensitive Gas Sensors," *Adv. Funct. Mater.*, vol. 30, no. 40, pp. 1–9, 2020, doi: 10.1002/adfm.202003998.

[170] H. Pazniak *et al.*, "Partially Oxidized $Ti_3C_2T_x$ MXenes for Fast and Selective Detection of Organic Vapors at Part-per-Million Concentrations," *ACS Appl. Nano Mater.*, vol. 3, no. 4, pp. 3195–3204, 2020, doi: 10.1021/acsanm.9b02223.

[171] M. Hou *et al.*, "Improvement of gas sensing property for two-dimensional $Ti_3C_2T_x$ treated

with oxygen plasma by microwave energy excitation," *Ceram. Int.*, vol. 47, no. 6, pp. 7728–7737, 2021, doi: 10.1016/j.ceramint.2020.11.117.

[172] M. Hou, J. Gao, L. Yang, S. Guo, T. Hu, and Y. Li, "Room temperature gas sensing under UV light irradiation for $Ti_3C_2T_x$ MXene derived lamellar TiO_2-C/g-C_3N_4 composites," *Appl. Surf. Sci.*, vol. 535, no. August 2020, 2021, doi: 10.1016/j.apsusc.2020.147666.

[173] A. Hermawan *et al.*, "CuO Nanoparticles/$Ti_3C_2T_x$ MXene Hybrid Nanocomposites for Detection of Toluene Gas," *ACS Appl. Nano Mater.*, vol. 3, no. 5, pp. 4755–4766, 2020, doi: 10.1021/acsanm.0c00749.

[174] Z. Wang *et al.*, "SnO-SnO_2 modified two-dimensional MXene $Ti_3C_2T_x$ for acetone gas sensor working at room temperature," *J. Mater. Sci. Technol.*, vol. 73, pp. 128–138, 2021, doi: 10.1016/j.jmst.2020.07.040.

[175] S. Sun *et al.*, "$W_{18}O_{49}$/$Ti_3C_2T_x$ Mxene nanocomposites for highly sensitive acetone gas sensor with low detection limit," *Sensors Actuators, B Chem.*, vol. 304, no. August 2019, p. 127274, 2020, doi: 10.1016/j.snb.2019.127274.

[176] A. K. Pathak and C. Viphavakit, "VOC Biomarker Monitoring for Diabetes through Exhaled Breath Using Ag/P-TiO_2 Composite Plasmonic Sensor," *IEEE Sens. J.*, vol. 21, no. 20, pp. 22631–22637, 2021, doi: 10.1109/JSEN.2021.3104766.

[177] P. Bindra and A. Hazra, "Electroless deposition of Pd/Pt nanoparticles on electrochemically grown TiO_2 nanotubes for ppb level sensing of ethanol at room temperature," *Analyst*, vol. 146, no. 6, pp. 1880–1891, 2021, doi: 10.1039/d0an01757d.

[178] J. H. Lee, A. Mirzaei, J. Y. Kim, J. H. Kim, H. W. Kim, and S. S. Kim, "Optimization of the surface coverage of metal nanoparticles on nanowires gas sensors to achieve the optimal sensing performance," *Sensors Actuators, B Chem.*, vol. 302, no. September 2019, p. 127196, 2020, doi: 10.1016/j.snb.2019.127196.

[179] M. S. Barbosa, P. H. Suman, J. J. Kim, H. L. Tuller, and M. O. Orlandi, "Sensors and Actuators B : Chemical Investigation of electronic and chemical sensitization e ff ects promoted by Pt and Pd nanoparticles on single-crystalline SnO nanobelt-based gas sensors," *Sensors Actuators B. Chem.*, vol. 301, no. August, p. 127055, 2019, doi:

10.1016/j.snb.2019.127055.

[180] X. Zhang *et al.*, “Gas response enhancement of VOCs sensor based on Sn doped nanoporous anatase TiO_2 nanoparticles at a relative low operating temperature Gas response enhancement of VOCs sensor based on Sn doped nanoporous anatase TiO_2 nanoparticles at a relative low operating temperature,” 2017.

[181] S. N. Shuvo, A. M. Ulloa Gomez, A. Mishra, W. Y. Chen, A. M. Dongare, and L. A. Stanciu, “Sulfur-Doped Titanium Carbide MXenes for Room-Temperature Gas Sensing,” *ACS Sensors*, vol. 5, no. 9, pp. 2915–2924, 2020, doi: 10.1021/acssensors.0c01287.

[182] Z. Zhu *et al.*, “Flexible and lightweight $Ti_3C_2T_x$ MXene@Pd colloidal nanoclusters paper film as novel H_2 sensor,” *J. Hazard. Mater.*, vol. 399, no. March, p. 123054, 2020, doi: 10.1016/j.jhazmat.2020.123054.

Chapter-2

Synthesis and characterization of base materials

2.1 Introduction

Various semiconducting metal oxides have been employed for gas or VOC sensing, showing good sensing properties with several benefits. They have iconic electronic exchange characteristics, suitable semiconductor properties, and stability to work in harsh environments [1-7]. Metal oxides are mainly divided by their type of conductivity (n-, p-type). TiO_2 is a comparatively stable (chemically and thermally), non-toxic, corrosion-resistant, and biodegradable material, making it a promising material for sensing applications [6,8-10]. TiO_2 possesses a variety of nano morphologies like 0-D (nanoparticles) [9], 1-D (nanotubes, nanowires, nanorods) [11, 12], 2-D (nanosheets and nanofibers etc.) [6,13] and 3-D (nanospheres) [8] which could play a noteworthy role in sensing behavior. The most common methods for TiO_2 synthesis are electrochemical anodization [7], sol-gel [6, 16], hydrothermal method [17-19], and electrospinning [5, 12].

Nowadays, MXenes are also gathering immense attention in gas sensing applications due to their large specific surface area, abundant functional groups ((–OH, –O, or –F), porous structure, tunable surface chemistry [20-24]. Among several MXenes, $Ti_3C_2T_x$ is most widely studied for the gas or VOC sensing application [25-30]. 2D $Ti_3C_2T_x$ sheets were formed by the chemical exfoliation or removal of A element by a selective etching [31,32]. A variety of etchants like HF [31], fluoride-containing reagents with HCl (LiF+HCl, NaF+ HCl) [20,21] leave the MXene surface terminated by different functional groups (-OH, -F, and -O) and represented as $M_{n+1}X_nT_x$, where x is the number of functional groups [32]. However, some Intercalating and delaminating agents like DMSO (dimethyl sulfoxide) [33], tetrabutylammonium hydroxide (TBAOH) [26], Tetramethylammonium hydroxide (TMAOH) [34] are also used to obtain MXene with high specific surface area.

This chapter includes the detailed synthesis procedure and characterization of titanium oxide in the form of 1-D nanotubes and 0-D nanoparticles, carbide ($Ti_3C_2T_x$), MoS_2 quantum dots and Pd nanoparticles. 1-D TiO_2 nanotubes were fabricated by electrochemical anodization and 0-D TiO_2

nanoparticles were fabricated by sol-gel method. $Ti_3C_2T_x$ MXene was synthesized by the selective chemical etching route. Morphological (FESEM, TEM/HRTEM), structural (Raman, XRD), and chemical (XPS) characterizations were performed to analyze the nanostructures. Device fabrication and gas sensing and humidity setup were also discussed in detail.

2.2 TiO_2 nanostructures

2.2.1 1-D TiO_2 nanotubes array

2.2.1.1 Synthesis

TiO_2 nanotube array was synthesized by a simple electrochemical anodization method. A 2 cm × 2 cm Ti Foil (0.25 mm thickness, purity > 99.9%) was cleaned thoroughly by sonication, followed by 10 minutes of dipping in each of the following solvents: acetone, ethanol, and deionized water. Lastly, a 2 M of HF (48% purity, Sigma–Aldrich) etching was done to provide suitable roughness for better growth of nanotubes. Anodization was done in two steps; the first step was carried out for 90 min at 40 V using a power supply in a two-electrode system with a graphite counter electrode. 1.5 cm × 1.5 cm (thickness: 1 mm) counter graphite electrode was maintained at a constant distance of 3.5 cm during the reactions. The second anodization step was maintained for 1 min at 60 V constant voltage. The anodic reaction was carried out at room temperature. Both reactions were carried out simultaneously in different electrolyte solutions containing a prefix ratio of 0.589 g ammonium fluoride (NH_4F), 9 ml deionized water, and 171 ml ethylene glycol. This tow step procedure leads to the completely open-pores structure of TiO_2 nanotubes. Thermal annealing was performed in the air at 450 °C for 4 h, making the samples mechanically robust and the amorphous nanotubes to anatase.

2.2.1.2 Characterization

Morphological characterization

The morphological and structural analysis were performed with field emission scanning electron microscopy (FESEM, Apreo LoVac) with an acceleration voltage of 15 kV and high-resolution transmission electron microscopy (HRTEM, Tecnai G2 20 S-TWIN [FEI]) with an acceleration voltage of 200 kV. Highly arranged and oriented TiO_2 nanotube arrays were synthesized from the electrochemical anodization route. The average length of nanotubes varied from 1.5 - 2 µm (Fig. 2.1 (a)). The average outer diameter of the TiO_2 nanotubes was ∼110 nm with an inner pore diameter of ∼ 79 nm (Fig. 2.1 (b)). The average pore size of the nanotube was around 74 nm as shown in Fig. 2.1 (c). The detailed morphology of a single nanotube in the array was studied by TEM results (Fig. 2.1 (d)). From the TEM results, the wall thickness and the inner diameter of anodically grown TiO_2 nanotubes are not homogenous and enhanced in the bottom direction resulting in a smaller inner radius. Consequently, the inner diameter of the tube near the top and bottom part was determined to be 45 nm and 85 nm, respectively to maintain the outer diameter of the nanotube nearly constant around 135 nm throughout the length (fig. 2.1 (d)). Later, the inset of Fig. 2.1 (d) shows the high-resolution TEM (HRTEM) image of the TiO_2 nanotube array. The 0.346 nm lattice spacing was indexed to the (101) crystal plane of A-TiO_2 in Fig. 2.1 (d) [8,35].

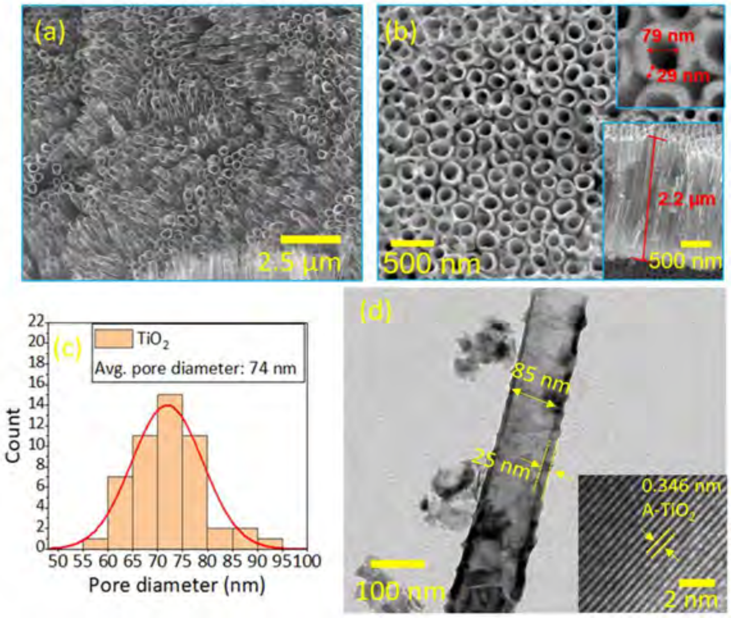

Fig. 2.1. FESEM image of TiO_2 nanotubes:(a) overall view of TiO_2 nanotubes (b) top view and inset side view. (c) pore size distribution analysis of TiO_2 nanotube array by ImageJ software. (d) TEM image of the nanotube and the inset is showing the HRTEM image of the TiO_2 nanotube.

Structural characterization

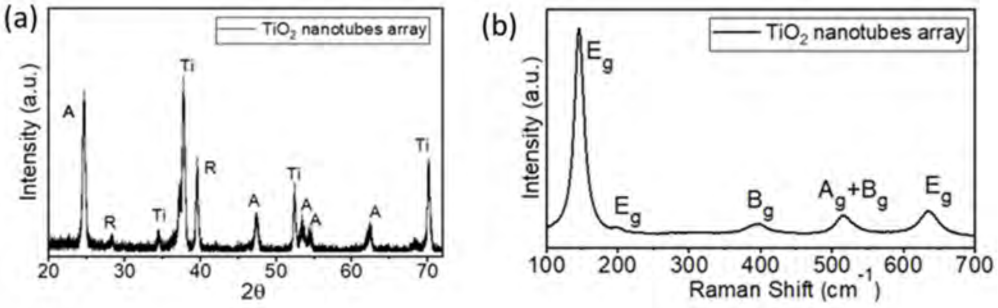

Fig 2.2. (a) XRD spectra and (b) Raman spectra of TiO_2 nanotubes.

Fig. 2.2 (a) shows the X-ray diffraction data (XRD, Bruker AXS D2 PHASER) using CuKα radiation (1.5418 Å) which discloses the crystalline nature of the TiO_2 nanotube arrays. The sharp and highest intensity (101) peak at 24.5° is related to anatase TiO_2, and a few low intensity anatase peaks are observed in pure TiO_2 samples (JCPDS File No. 21- 1272) [8]. The peak at 27.4° and 36.1° are related to the rutile (110) and (200) crystallinity observed in the sample (Fig. 2.2 (a)) [12]. Other anatase crystallinity peaks of (200), (105), (211) and (118) were observed at 47.6◦, 53.5◦ 54.61◦ and 62.2◦, respectively [9,12]. The Ti substrate peaks were also observed in the XRD spectra of TiO_2 nanotubes.

The Raman spectra (Raman Spectroscopy, Labram HR Evolution, Omega Scope) of pure TiO_2 nanotubes were noted using a 532 nm laser at room temperature (Fig. 2.2 (b)). The TiO_2 nanotube array showed five peaks defining the different Raman active modes. Five bands at 145 cm^{-1} (Eg), 195.4 cm^{-1} (Eg), 395.2 cm^{-1} (Bg), 514.6 cm^{-1} (Ag + Bg), and 634.4 cm^{-1} (Eg) (Figure 3b) signifies the presence of anatase phase of TiO_2 [35].

Chemical characterization

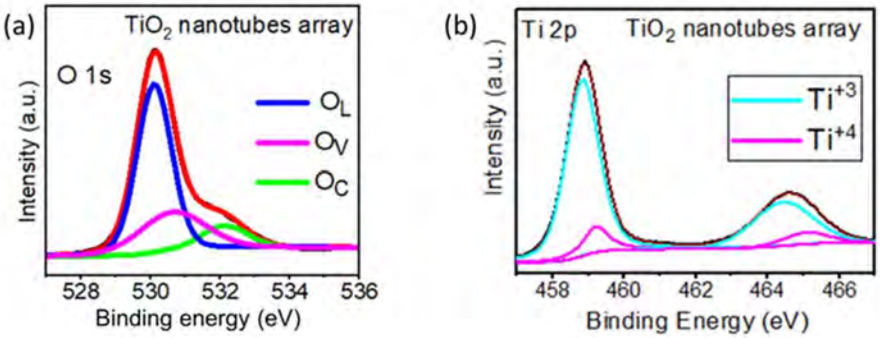

Fig. 2.3. XPS spectra of TiO_2 nanotubes (a) O1s, (b) Ti 2p.

The XPS spectra (XPS, Thermo Fisher Scientific, K-Alpha) of Ti 2p and O 1s are shown in Fig. 2.3(a, b) to identify the chemical states of the samples. The O 1s spectra of pure TiO_2 nanotubes array were deconvoluted into three peaks related to the lattice oxygen (O_L), oxygen vacancies (O_V), and surface-chemisorbed oxygen (O_C) at 530.3, 531.7, and 533 eV, respectively, as shown in Fig. 2.3(a) [35]. The O_L, O_V, and O_C components percentages are 69, 20.6, and 10.4%, respectively, concluding the less oxygen functionalized surface of the pure TiO_2 nanotubes (Fig. 2.3(a)). In the Ti 2p spectra, two peaks centered at 458.8 and 464.6 eV are related to Ti $2p_{3/2}$ and

Ti $2p_{1/2}$, respectively (Fig. 2.3 (b)). These two peaks are further deconvoluted into four mountains, which are Ti^{3+} $2p_{3/2}$ (458.7 eV), Ti^{4+} $2p_{3/2}$ (459.6 eV), Ti^{3+} $2p_{1/2}$ (464 eV), and Ti^{4+} $2p_{1/2}$ (465.1 eV) [36,37]. In pure TiO_2 nanotubes, the intensity and area of Ti^{+3} peaks are significantly higher than those of Ti^{+4} peaks, confirming the oxygen-deficient nature of the pure TiO_2 nanotube array.

2.2.2 0-D TiO_2 nanoparticles

2.2.2.1 Synthesis

The Undoped p-type, anatase-TiO_2 nanoparticles were synthesized from the titanium (IV) isopropoxide (TTIP, 99.99% pure from Sigma Aldrich), acetic acid (CH_3COOH) by the sol-gel method. Firstly, 25 ml acetic acid was maintained at 0 ˚C in an ice bath under a vigorous stirring state. Next 5 ml of TTIP precursor was added dropwise to the reaction chamber. Finally, 100 ml of deionized (DI) water was added slowly into the mixture of TTIP and CH_3COOH. The resulting opaque solution then underwent a continuous stirring state for 90 mins and the color of the solution became utterly transparent and restored in a cool dry place for further reactions.

2.2.2.2 Characterization

Morphological characterization

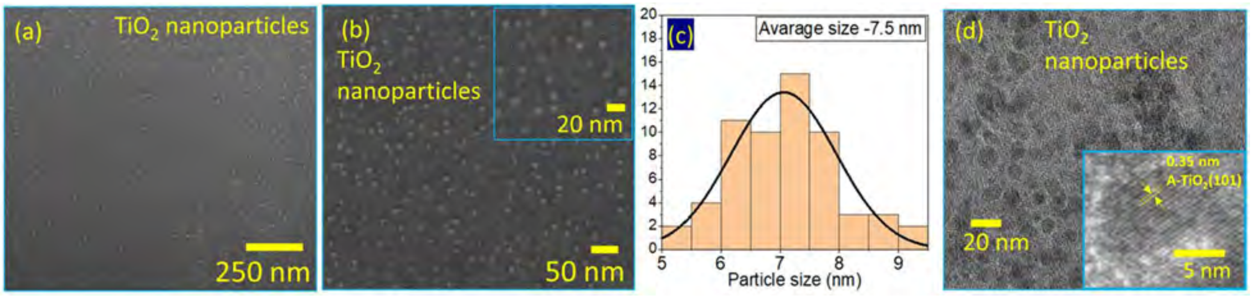

Fig. 2.4. Undoped p-type TiO_2 nanoparticles (a, b) FESEM, (c) average size distribution analysis by ImageJ software, (d) TEM image of TiO_2 nanoparticles and inset is showing HRTEM image representing the lattice fringes.

The pure TiO_2 nanoparticles distribution is shown in Fig. 2.4(a, b). The distribution was uniform, continuous, and compact throughout the substrate. The spherical nanoparticles ranging in size from 6-9 nm with an average size of 7.5 nm were estimated from the FESEM image (Fig. 2.4 (b)) using ImageJ analysis (Fig. 2.4 (c)). The distribution was also analyzed by TEM analysis where no such aggregation of the nanoparticles was observed (Fig. 2.4 (d)). The HRTEM image in the inset of Fig. 2.4 (d)) shows a lattice spacing of 0.352 nm confirming the formation of anatase (101) crystallinity in the TiO_2 nanoparticles [35].

Structural characterization

The XRD measurement was done to identify the dominant crystallinity of the undoped TiO_2 nanoparticles (Fig. 2.5 (a)). The highest intensity peak was observed at 24.45 ° referring to the anatase (101) crystal plane into TiO_2 nanoparticles. Other anatase crystallinity peaks were also pointed at 2θ values of 47.7° and 53.9° corresponding to the anatase (200) and (105) respectively [8,9]. The XRD peaks for anatase TiO_2 was well matched with JCPDS file No. 21-1272.

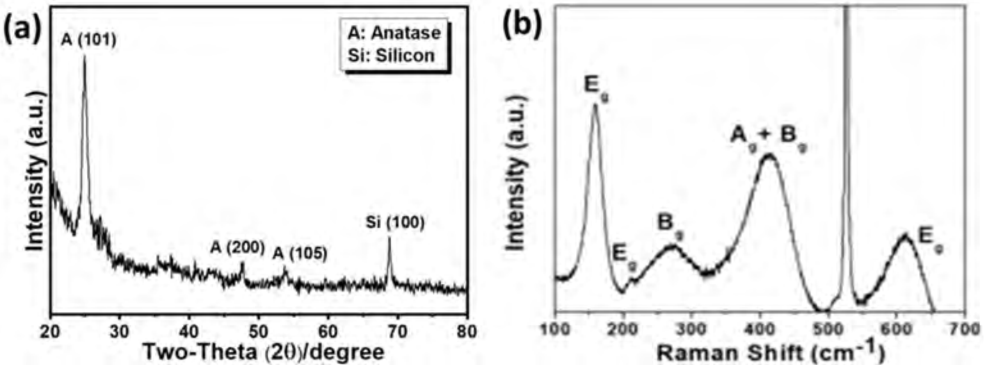

Fig. 2.5. (a) XRD and (b) Raman spectrum of undoped p-type TiO_2 nanoparticle.

The Raman spectra of undoped TiO_2 nanoparticles are shown in Fig. 2.5 (b)). The anatase crystallinity in TiO_2 NPs was established by six Raman active modes like E_g (144 cm^{-1}), E_g (199 cm^{-1}), B_g (399 cm^{-1}), $A_g + B_g$ (516 cm^{-1}) and E_g (639 cm^{-1}) Fig. 2.5 (b)).

Chemical characterization

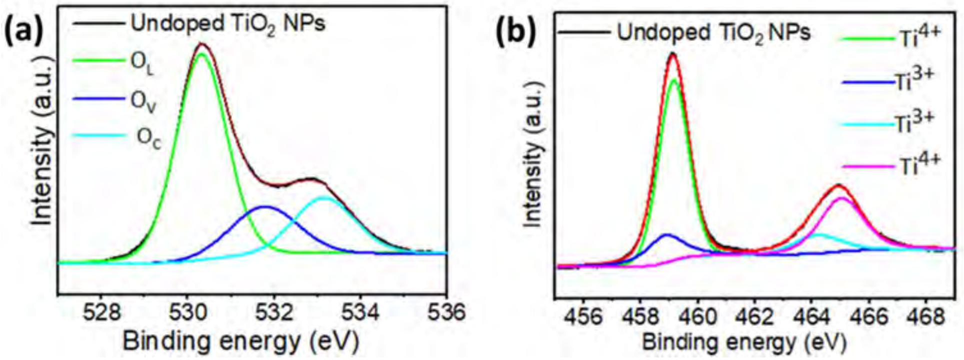

Fig. 2.6. XPS spectra of undoped p-type TiO_2 nanoparticles (a) O 1s, (b) Ti 2p.

O 1s spectra of TiO_2 nanoparticles deconvoluted into three major peaks assigned to lattice oxygen (O_L), oxygen vacancies (O_V) and chemisorbed oxygen (O_C) in TiO_2 nanoparticles (Fig. 2.6(a)). The high specific surface area of TiO_2 nanoparticles eventually increased the number of surface oxygen originating from Ti-OH, adsorbed oxygen species, etc. which eventually increased the intensity and area of O_C peak [35]. The Ti 2p spectra centered at 459.1 and 465.2 eV are related to Ti $2p_{3/2}$ and Ti $2p_{1/2}$, respectively (Fig. 2.6(b)). The peaks were deconvoluted into Ti^{3+} $2p_{3/2}$ (459.1 eV), Ti^{4+} $2p_{3/2}$ (459.4 eV), Ti^{3+} $2p_{1/2}$ (464 eV), and Ti^{4+} $2p_{1/2}$ (465.2 eV) as visible in Fig. 2.6(b). The separation of Ti^{+4} peaks in Ti $2p_{3/2}$ and Ti $2p_{1/2}$ was 5.9 eV, validating anatase TiO_2 [36,37].

2.3 $Ti_3C_2T_x$ MXene

2.3.1 Synthesis

$Ti_3C_2T_x$ MXene was synthesized by the selective etching of Al from Ti_3AlC_2 (sigma aldrich) or MAX phase precursor. The synthesis of MXene was a two-stage process, firstly 1 g of Ti_3AlC_2 was added in 10 ml of HF (48% v/v) solution while stirring for 20 h at room temperature. Ti_3AlC_2 was added to the solution slowly to avoid initial overheating. As the etching was done, the mixture was rinsed multiple times with distilled water until a pH of 6 was achieved. The product was then collected by centrifuge at 3500 rpm for 10 min and dried in a vacuum desiccator at 80 °C for 18 h. In the second step, intercalation and delamination of $Ti_3C_2T_x$ MXene sheets were done where 10 ml DMSO was added to the 0.2 g of powder under a nitrogen-protected environment for 18 h with a continuous stirring state at room temperature. The final solution was washed multiple times and centrifuged at 3500 rpm for 5 mins to remove DMSO. A sonication of 6 h was maintained and ended up with a centrifuge process at 1000 rpm for 15 mins.

2.3.2 Characterization

Morphological characterization

The FESEM analysis was done to understand the morphological changes in the MXene sheets with the different compositional changes (Figure 2.7(a, b)). Fig. 2.7(a) shows the tightly bounded sheets in the unetched MAX phase (Ti_3AlC_2). The Unetched MAX phase was further treated with suitable etchants and delaminating agents resulting in a typical accordion-like multilayer structure with a smooth surface of $Ti_3C_2T_x$ MXene (Fig. 2.7(b)). The exfoliated sheets with a

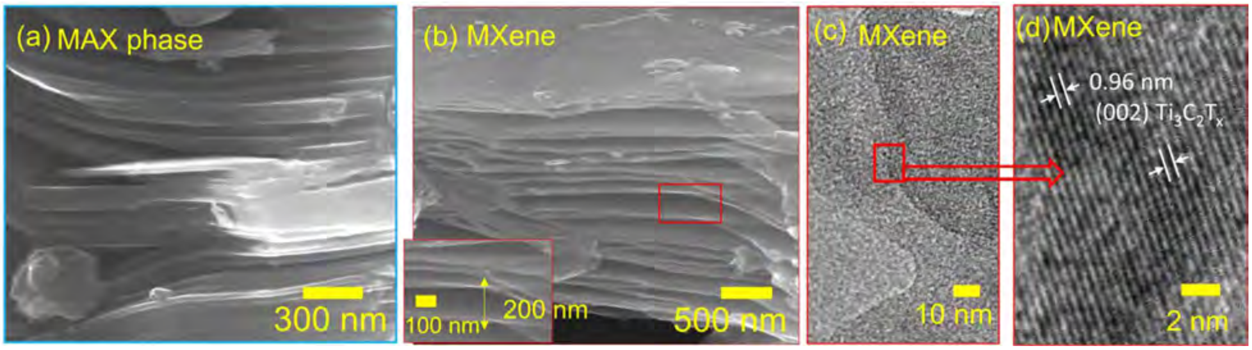

Fig. 2.7. FESEM images of (a) MAX phase of Ti_3AlC_2, (b) $Ti_3C_2T_x$ MXene after etching, (c) TEM image of $Ti_3C_2T_x$ MXene sheets and (d) HRTEM image representing the lattice fringes.

wide separation indicated the successful removal of Al from the MAX phase as shown in Fig. 2.7(b). The inset image (Fig. 2.7(b)) shows a close view of the spaced layer with average interlamination spacing of 200 nm.

TEM and HRTEM analysis show a detailed analysis of structural changes in MXene and composites. Fig. 2.7(c) shows the TEM image of MXene sheets lying on each other and identified by the contrast change. Moreover, the HRTEM image of a selected area from the TEM image (Fig. 2.7(d)) showed the coexistence of lattice fringes of MXene. The estimated lattice fringes spacing for MXene was observed to be 0.96 nm, which is attributed to the (002) crystal plane [23].

Structural characterization

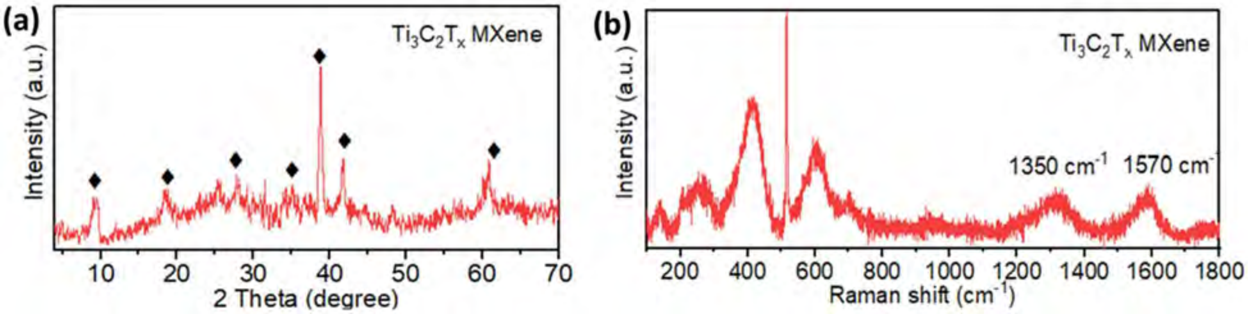

Fig. 2.8. (a) XRD and (b) Raman spectrum of $Ti_3C_2T_x$ MXene sheets.

The XRD spectra in the Fig. 2.8(a) show the diffraction peaks for MXene. The Pure $Ti_3C_2T_x$ MXene has several diffraction peaks at 9.34°, 18.6° and 27.9° and contributed to the typical peaks of (002), (004) and (006) planes of 2D $Ti_3C_2T_x$ MXene which are also consequences from the Al etching from the Ti_3AlC_2 MAX phase [38,39]. The series of MXene peaks confirms a layered structure of stacked sheets with an interplanar distance of 0.96 nm [40].

Raman spectra were recorded to identify the structural modifications in the material (Fig. 2.8(b)). In pure $Ti_3C_2T_X$, the peaks at 390 and 620 cm^{-1} belong to the A1g signals arising from the presence of –OH, –O, and–F functional groups on the surface. The vibration modes for Ti-Al were missing in the resulting spectrum, confirming the successful etching [41,42]. The two broad peaks at 1350 and 1570 cm^{-1} were observed corresponding to the D and G peaks resulting from the formation of graphitic carbon during the etching process [41,42].

Chemical characterization

Fig. 2.9(a) shows the Ti 2p peaks for the pristine MXene sample with four doublets for Ti $2p_{1/2}$ and Ti $2p_{3/2}$ whereas each doublet is separated by 5.9 eV. The pristine $Ti_3C_2T_x$ Ti $2p_{3/2}$ was deconvoluted into four peaks centered at 455.2, 456.6, 458.4 and 459.3 eV corresponding to the Ti–C (Ti^+), Ti–X (Ti^{2+}), Ti_xO_y (Ti^{3+}), and TiO_2 (Ti^{4+}), respectively [38,39]. The O 1S spectra (Fig. 2.9(b)) were deconvoluted into three peaks at 530.5, 532.5, and 533.8 eV credited to Ti-OH, Ti-O-Ti, and C-OH, respectively [40]. In pristine MXene, plentiful oxygen functional groups are present on the surface and edges which are beneficial for gas or VOC sensing. Fig. 2.9(c) shows the C 1s spectra fitted into four peaks corresponding to C-Ti, C=C, C-O, and C-F positioned at binding energies of 281.9, 285, 286.4 and 289.1 eV, respectively.

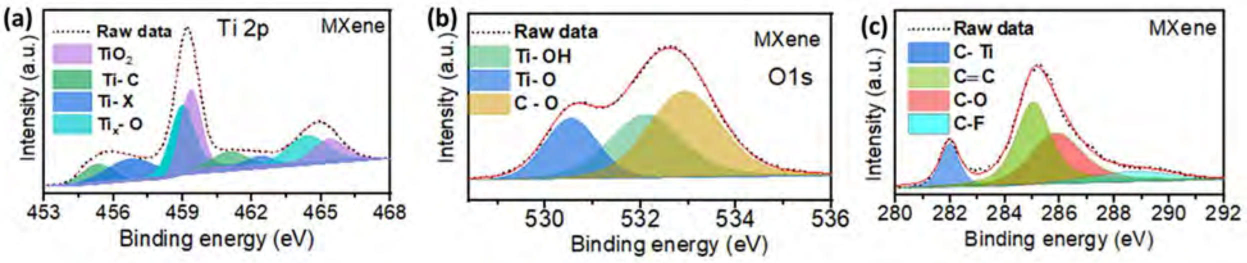

Fig. 2.9. XPS spectra of $Ti_3C_2T_x$ MXene sheets (a) Ti 2p, (b) O 1s and (c) C 1s spectra.

2.4 MoS_2 Quantum dots (QDs)

2.4.1 Synthesis

MoS_2 was purchased from Sigma Aldrich and further proceeded without any purification. 2 ml of MoS_2 suspension was dispersed into 100 ml of MQ water and sonicated for 1 h. The resulting sonicated suspension was then centrifuged at 4500 rpm for 10 min. the resulting supernatant was collected and then used further for composite formation.

2.4.2 Characterization

Morphological characterization

MoS_2 QDs were uniformly distributed on the substrate as visible in the lower magnification image (Fig. 2.10(a, b)). At higher magnification, it was noted that quantum dots aggregated and formed small clusters of different dimensions (Fig. 2.10(a)). The discrete quantum dots with spherical shape are visible with a diameter ranging between 10-15 nm and after the aggregation, the cluster size ranges between 50-80 nm as shown in Fig. 2.10(b). The TEM image shows the cluster of aggregated QDs with many MoS_2 quantum dots Fig. 2.10(c). The inset of Fig. 2.10(c) is leading the individual MoS_2 quantum dot with spherical morphology. The lattice fringes in Fig. 2.10(c) showing an inter-planer distance of 0.75 nm corresponds to the (002) crystal plane of MoS_2 concluding less crystalline and non-homogenous lattice arrangement of the resulting QDs which is in good agreement with the previously reported works [43].

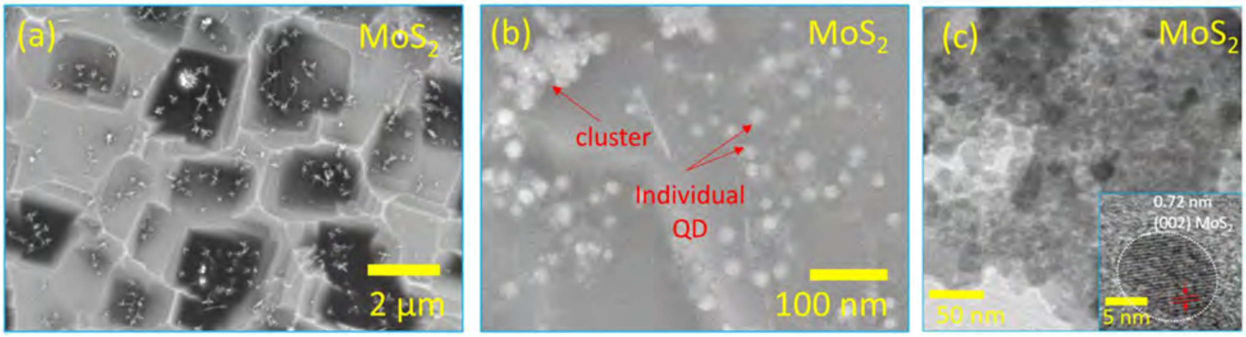

Fig. 2.10. (a, b) FESEM images of MoS_2 quantum dots at different magnifications, (C) TEM image of MoS_2 quantum dots and inset representing the lattice fringes of single quantum dot.

Structural characterization

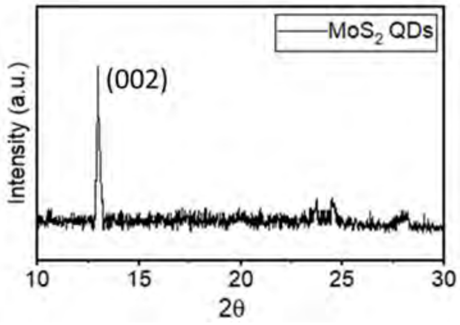

Fig. 2.11. (a) XRD spectrum of MoS_2 quantum dots.

To understand the crystalline nature of MoS_2, a powder X-ray diffraction study was performed in Fig. 2.11(a). The sharpest and most intense peak at 14.2° of MoS_2 in the resulting material was confirmed by the Mo (002) orientation [43].

Chemical characterization

X-ray photoelectron spectroscopy (XPS) was conducted on MoS_2 samples to examine their chemical state and surface compositions. The two characteristic peaks (S^{2-} $2p_{3/2}$ and S^{2-} $2p_{1/2}$) of S 2s spectra were merged into one and observed at 162.9 eV. At a higher binding energy of 169.7 eV a significant peak was observed for S^{+4}, further confirming the +6-oxidation state of Mo (Fig. 2.12(a)). The highly oxidized surface of MoS_2 contains a huge number of reactive sites [44]. The Mo 3d signal comes from the peaks around 229.2, 231.1, 233.2 and 235.1 eV matching with Mo^{4+} $3d_{5/2}$, Mo^{4+} $3d_{3/2}$, Mo^{6+} $3d_{5/2}$ and Mo^{5+} $3d_{3/2}$ of MoS_2, respectively (Fig. 2.12(b)) [44]. The attachment of unstable oxygen functional groups or partial oxidation on the surface of MoS_2 QDs generates Mo^{+6} states which help during the gaseous interaction [44].

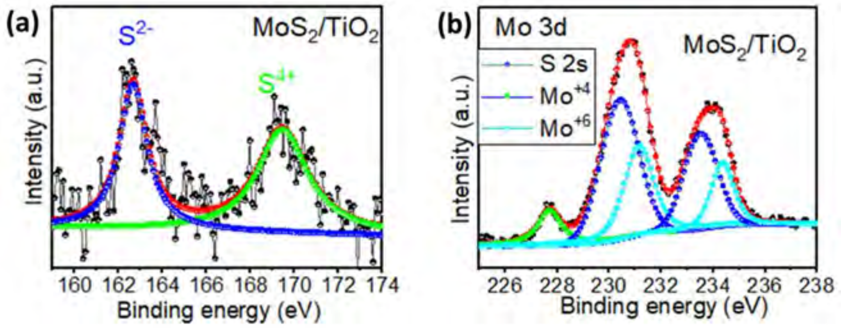

Fig. 2.12. XPS spectra of MoS_2 quantum dots (a) S 2s, (b) Mo 3d spectra.

2.5 Pd nanoparticles

2.5.1 Synthesis

All the chemicals were analytic grade and palladium chloride ($PdCl_2$) (CAS: 7647101) was purchased from Molychem and used without further purifications. 1 mM of palladium chloride ($PdCl_2$) was dissolved in 1 L of deionized water and then sonicated for one hour at room temperature. The prepared nanoparticle solution was stabilized by adding diluted HCl dropwise with continuous sonication.

2.5.2 Characterization

Morphological characterization

The FESEM image shows a uniform decoration of spherical Pd nanoparticles with negligible aggregation (Fig. 2.13(a)). The TEM images of Pd (Fig. 2.13(b)) also show the detailed morphology and distribution of nanoparticles. TEM data revealed that metal nanoparticles were compact, uniform and well-distributed. The distribution of nanoparticles was uniform in the case of Pd nanoparticles (Fig. 2.13(b)). The HRTEM image (Fig. 2.13(c)) shows the lattice spacing measurements of Pd metallic nanoparticles give a recurrent value of 0.22 nm which corresponds to the (111) plane of the metallic Pd phase which is in agreement with the previously reported works [45,46]. The size distribution of noble Pd metal nanoparticles was calculated from TEM images (Fig. 2.13(d)) using ImageJ software. Pd nanoparticles were small and contained high surface energy with an average of particle ~3.4 nm.

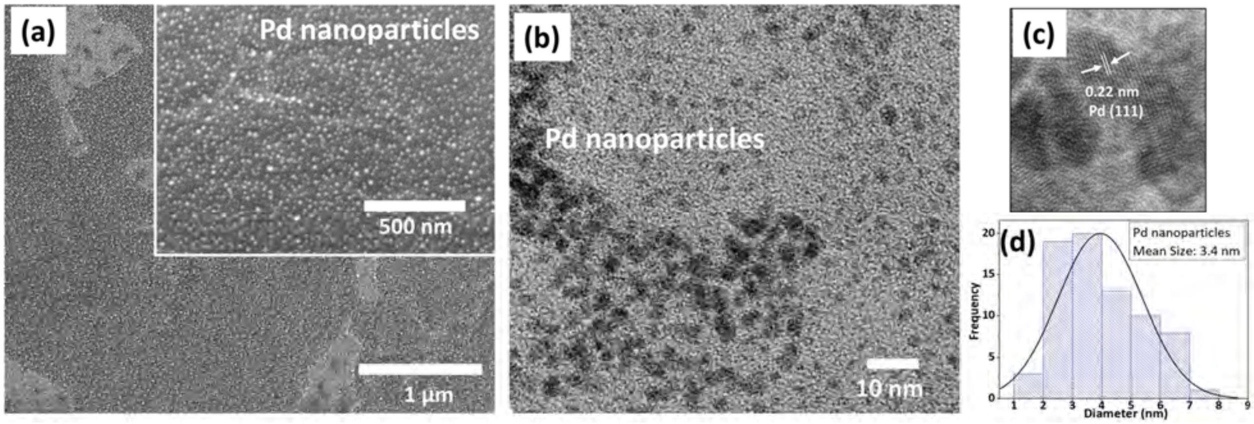

Fig. 2.13. (a) FESEM image of Pd nanoparticles, (b) TEM image of Pd nanoparticles, (c) representing the lattice fringes of Pd nanoparticles, and (d) the average size of Pd nanoparticles by ImageJ software.

Chemical characterization

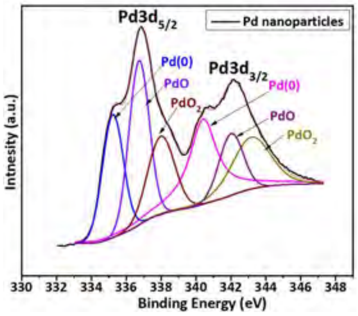

Fig. 2.14. XPS spectra of Pd 3d spectra of Pd nanoparticles.

The Pd 3d spectrum was deconvoluted into four doublets (Fig. 2.14). These four doublets for Pd $3d_{5/2}$/Pd $3d_{3/2}$ centered at binding energy values of 335.1/340.1, 336.9/340.2 and 338.2/343.6 corresponding to Pd(0), PdO and PdO_2, respectively [47,48]. The formation of four different oxidation states confirms that the Pd nanoparticles are highly reactive to the environmental oxygen species and attributed to the increase in surface oxygen of the sensing layer.

2.6 Device fabrication

Two types of device structures were considered according to the morphology as well known that the proper device structure for different nanostructures is essential for desired sensing outcomes. In a planar structure, electrodes are taken from the same plane of the sensing layer (Fig. 2.15(a)). 0-D, 2D and 3D nanostructures like nanoparticles, nanoflowers and spheres are deposited over the substrate like Si/SiO_2, glass, etc. On the other hand, for 1-D nanostructures like nanotubes, nanorods, etc. vertical or metal-insulator-metal (MIM) devices can be fabricated where highly aligned and oriented nanostructures are sandwiched between electrodes. The vertically aligned TiO_2 nanotubes on the Ti substrate where Ti substrate was considered the bottom electrode. Au top electrodes of thickness ~150 nm was deposited on the top surface of TiO_2 nanotubes by the electron beam evaporation technique, maintaining a 10^6 mbar vacuum. The Au top electrode was deposited using an aluminum metal mask with a 1 mm × 1 mm opening as shown in Fig. 2.15(b).

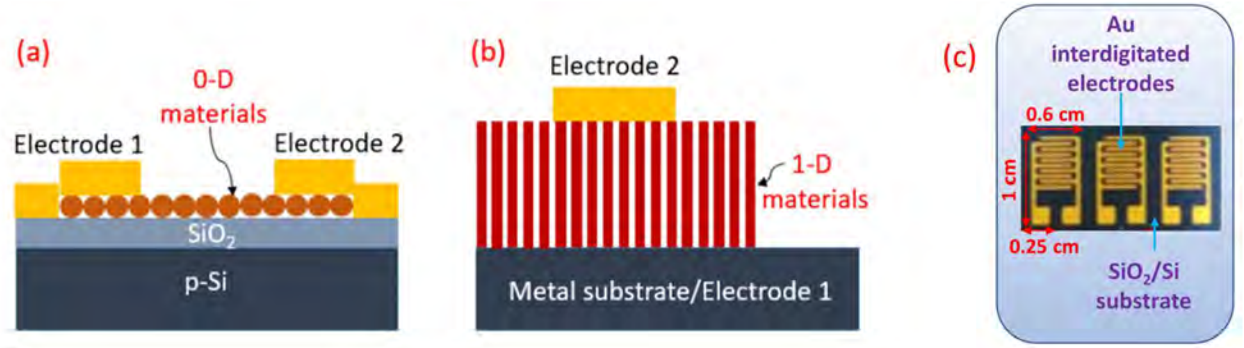

Fig. 2.15. Device structures; (a) Planar structured sensor, (b) Vertical structured sensor. (c) Schematic view of interdigitated Au electrodes on SiO_2/Si substrate.

In detail, the powder sample was dispersed in deionized water (5 mg/1 ml) and sonicated for 1 h. The Interdigitated Au (150 nm) planner electrodes were deposited on 90 nm SiO_2 coated Si (⟨100⟩) substrate by vacuum coating technique where a customized molybdenum shadow mask was used to create the desired electrode pattern as shown in (Fig. 2.15(c)). Thereafter, 30 µl dispersions of the solution were spray coated on Au/SiO_2/Si substrate placed on a hot plate heated at 75 °C.

2.7 Sensing and humidity setup

The sensing properties of the devices were examined by a gas flow apparatus having a sealed glass chamber with a volume of 600 ml. VOCs were injected through a syringe pump system and the flow rate of the gases was controlled with mass flow controllers. The syringe pump contains different types of micro syringes (Hamiltonian, range: 0.2−1000 μl) for different concentrations of VOC. The concentration (C) of VOCs was calculated by the formula C (ppm) = $2.46 \times (V_1D/VM) \times 10^3$, where D (gm/ml), M (gm/mol) and V (Lit) represent the density of the VOC, molecular weight of the VOC and volume of vaporization chamber respectively [35,49]. A data acquisition module (Keithley 6487) was used to provide a constant voltage (1V) and to measure the resistance change toward different VOCs. The response magnitude was measured as R_g/R_a or R_a/R_g, where R_a is the resistance in humid air and R_g is the resistance under exposure to the VOCs. Response and recovery time were calculated considering 90% of the maximum change in the current value of the sensor. Schematic of the sensor setup (Fig. 2.16). The theoretical detection limit was calculated by using the formula LOD (ppm) = 3 x RMS/S, where standard

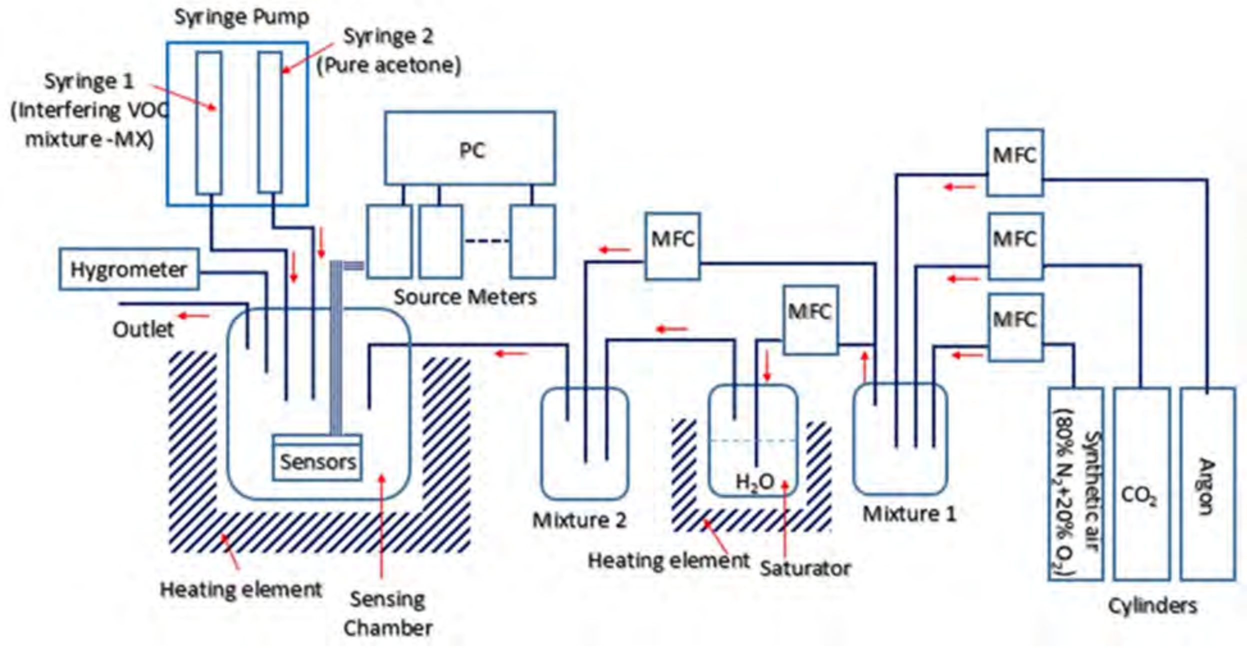

Fig. 2.16. Schematic of the sensor characterization setup and the humidity setup for breath VOC detection.

deviation of the response (RMS) of the curve and the slope of the calibration curve (S) approximating the LOD of the sensor [50,51].

In the humidity study, the humid air was used as the reference gas, and the total flow rate for the reference gas was maintained at 450 sccm and controlled by a mass flow controller (MFC, ALICAT Scientific). Humidity levels were maintained using a flow-through setup where synthetic air (N_2:O_2—4:1) was passed through a bubbler (saturator) and a mixer and finally to the sensing chamber. The maximum of 80% ± 2 relative humidity value was set and humid air flowed into the gas-sensing chamber. The humidity level was measured in the sensing chamber. The different humidity levels were achieved by varying the humid air to dry air ratio. The desired humidity level was monitored during the study using the high-accuracy hygrometer (± 2 RH) (Fig. 2.16).

2.8 Conclusion

TiO_2 nanotubes and undoped TiO_2 nanoparticles were synthesized by simple electrochemical anodization and sol-gel method, respectively. These two methods are simple, cost-effective and don’t use toxic chemicals. Different morphological, structural and chemical characterizations of prepared metal oxide nanoforms were done to analyze the properties. FESEM established the formation of highly orientated and organized nanotubes and the compact and uniform distribution of nanoparticles. XRD confirmed the dominant anatase crystallinity of TiO_2 in both nano forms. All the Raman active modes corresponding to the anatase crystallinity of TiO_2 were observed. X-ray photo spectroscopy was performed to study the composition of TiO_2.

In the same way, 2D MXene sheets were exfoliated by a chemical etching route using a suitable etchant. Characterization techniques authenticate the formation of exfoliated $Ti_3C_2T_X$ MXene sheets. Pure MoS_2 quantum dots solution (Sigma Aldrich, 99 %) and Pd nanoparticle solution from $PdCl_2$ salt (MolyChem) was synthesized in aqueous form for further use. Both of the aqueous solutions obtained were highly stable, uniform and active. Both nanostructures were analyzed using different characterization techniques.

Titanium oxide, and carbide nanomaterials have been widely utilized to detect a variety of breath volatile organic compounds (VOCs). Different researchers have adopted different ways to improve the sensing performance of these material-based devices. The most common ways of improving the properties per the requirements are forming the nanocomposite of sensing materials and surface functionalization by different semiconducting and metallic nanoparticles.

References

[1] M. Masikini, M. Chowdhury, and O. Nemraoui, “Review—Metal Oxides: Application in Exhaled Breath Acetone Chemiresistive Sensors,” *J. Electrochem. Soc.*, vol. 167, no. 3, p. 037537, 2020, doi: 10.1149/1945-7111/ab64bc.

[2] K. Muthukrishnan *et al.*, “Studies on acetone sensing characteristics of ZnO thin film prepared by sol–gel dip coating,” *J. Alloys Compd.*, vol. 673, pp. 138–143, 2016, doi: 10.1016/j.jallcom.2016.02.222.

[3] S. Salehi, E. Nikan, A. A. Khodadadi, and Y. Mortazavi, “Highly sensitive carbon nanotubes-SnO_2 nanocomposite sensor for acetone detection in diabetes mellitus breath,” *Sensors Actuators, B Chem.*, vol. 205, pp. 261–267, 2014, doi: 10.1016/j.snb.2014.08.082.

[4] R. Xing *et al.*, “Preparation and gas sensing properties of In_2O_3/Au nanorods for detection of volatile organic compounds in exhaled breath,” *Sci. Rep.*, vol. 5, no. October 2014, pp. 1–14, 2015, doi: 10.1038/srep10717.

[5] H. Xu *et al.*, “Mesoporous WO_3 nanofibers with crystalline framework for high-performance acetone sensing,” *Front. Chem.*, vol. 7, no. APR, pp. 1–11, 2019, doi: 10.3389/fchem.2019.00266.

[6] B. Bhowmik, K. Dutta, A. Hazra, and P. Bhattacharyya, “Low temperature acetone detection by p-type nano-titania thin film: Equivalent circuit model and sensing mechanism,” *Solid. State. Electron.*, vol. 99, pp. 84–92, 2014, doi: 10.1016/j.sse.2014.04.023.

[7] D. H. Kim *et al.*, “Vertically ordered hematite nanotube array as an ultrasensitive and rapid response acetone sensor,” *ACS Appl. Mater. Interfaces*, vol. 6, no. 17, pp. 14779–14784, 2014, doi: 10.1021/am504156w.

[8] W. Pan, Y. Zhang, and D. Zhang, “Self-assembly fabrication of titanium dioxide nanospheres-decorated tungsten diselenide hexagonal nanosheets for ethanol gas sensing application,” *Appl. Surf. Sci.*, vol. 527, no. April, p. 146781, 2020, doi: 10.1016/j.apsusc.2020.146781.

[9] X. Tian, Z. Hu, T. Wang, H. Wang, Q. Zhang, and X. Wei, “Influence of multi-layer

TiO_2/SnO_2 heterojunctions on fast and sensitive ethanol detection," *Vacuum*, vol. 207, no. May 2022, 2023, doi: 10.1016/j.vacuum.2022.111620.

[10] A. Hazra, S. Das, J. Kanungo, C. K. Sarkar, and S. Basu, "Studies on a resistive gas sensor based on sol–gel grown nanocrystalline p-TiO2 thin film for fast hydrogen detection," *Sensors Actuators B Chem.*, vol. 183, pp. 87–95, Jul. 2013, doi: 10.1016/j.snb.2013.03.113.

[11] T. Gakhar and A. Hazra, "Oxygen vacancy modulation of titania nanotubes by cathodic polarization and chemical reduction routes for efficient detection of volatile organic compounds," *Nanoscale*, vol. 12, no. 16, pp. 9082–9093, 2020, doi: 10.1039/c9nr10795a.

[12] H. Bian *et al.*, "Characterization and acetone gas sensing properties of electrospun TiO_2 nanorods," *Superlattices Microstruct.*, vol. 81, pp. 107–113, 2015, doi: 10.1016/j.spmi.2015.01.022.

[13] L. L. Deng, C. X. Zhao, Y. Ma, S. S. Chen, and G. Xu, "Low cost acetone sensors with selectivity over water vapor based on screen printed TiO_2 nanoparticles," *Anal. Methods*, vol. 5, no. 15, pp. 3709–3713, 2013, doi: 10.1039/c3ay40373d.

[14] M. Ahmadipour *et al.*, "Detection of breath acetone by semiconductor metal oxide nanostructures-based gas sensors: A review," *Mater. Sci. Semicond. Process.*, vol. 149, no. November 2021, p. 106897, 2022, doi: 10.1016/j.mssp.2022.106897.

[15] A. K. Pathak *et al.*, "Recent Advances in Sensing Materials Targeting Clinical Volatile Organic Compound (VOC) Biomarkers: A Review," *Biosensors*, vol. 13, no. 1, 2023, doi: 10.3390/bios13010114.

[16] D. Han and M. Zhao, "Facile and simple synthesis of novel iron oxide foam and used as acetone gas sensor with sub-ppm level," *J. Alloys Compd.*, vol. 815, p. 152406, 2020, doi: 10.1016/j.jallcom.2019.152406.

[17] J. Lu, C. Xu, L. Cheng, N. Jia, J. Huang, and C. Li, "Acetone sensor based on WO_3 nanocrystallines with oxygen defects for low concentration detection," *Mater. Sci. Semicond. Process.*, vol. 101, no. May, pp. 214–222, 2019, doi: 10.1016/j.mssp.2019.05.038.

[18] Q. Q. Jia, H. M. Ji, D. H. Wang, X. Bai, X. H. Sun, and Z. G. Jin, "Exposed facets induced enhanced acetone selective sensing property of nanostructured tungsten oxide," *J. Mater. Chem. A*, vol. 2, no. 33, pp. 13602–13611, 2014, doi: 10.1039/c4ta01930j.

[19] Y. Zeng *et al.*, "Growth and selective acetone detection based on ZnO nanorod arrays," *Sensors Actuators, B Chem.*, vol. 143, no. 1, pp. 93–98, 2009, doi: 10.1016/j.snb.2009.08.053.

[20] A. Hermawan *et al.*, "CuO Nanoparticles/$Ti_3C_2T_x$ MXene Hybrid Nanocomposites for Detection of Toluene Gas," *ACS Appl. Nano Mater.*, vol. 3, no. 5, pp. 4755–4766, 2020, doi: 10.1021/acsanm.0c00749.

[21] C. E. Shuck *et al.*, "Effect of Ti_3AlC_2 MAX Phase on Structure and Properties of Resultant $Ti_3C_2T_x$ MXene," *ACS Appl. Nano Mater.*, vol. 2, no. 6, pp. 3368–3376, 2019, doi: 10.1021/acsanm.9b00286.

[22] L. Yang *et al.*, "SnO_2-Ti_3C_2 MXene electron transport layers for perovskite solar cells," *J. Mater. Chem. A*, vol. 7, no. 10, pp. 5635–5642, 2019, doi: 10.1039/c8ta12140k.

[23] N. Li *et al.*, "A fully inkjet-printed transparent humidity sensor based on a Ti_3C_2/Ag hybrid for touchless sensing of finger motion," *Nanoscale*, vol. 11, no. 44, pp. 21522–21531, 2019, doi: 10.1039/c9nr06751e.

[24] B. Sun *et al.*, "Co_3O_4@PEI/$Ti_3C_2T_x$ MXene nanocomposites for a highly sensitive NO_x gas sensor with a low detection limit," *J. Mater. Chem. A*, vol. 9, no. 10, pp. 6335–6344, 2021, doi: 10.1039/d0ta11392a.

[25] E. Lee, A. Vahidmohammadi, B. C. Prorok, Y. S. Yoon, M. Beidaghi, and D. J. Kim, "Room Temperature Gas Sensing of Two-Dimensional Titanium Carbide (MXene)," *ACS Appl. Mater. Interfaces*, vol. 9, no. 42, pp. 37184–37190, 2017, doi: 10.1021/acsami.7b11055.

[26] W. N. Zhao, N. Yun, Z. H. Dai, and Y. F. Li, "A high-performance trace level acetone sensor using an indispensable $V_4C_3T_X$ MXene," *RSC Adv.*, vol. 10, no. 3, pp. 1261–1270, 2020, doi: 10.1039/c9ra09069j.

[27] W. Guo *et al.*, "Selective Toluene Detection with Mo_2CT_x MXene at Room Temperature,"

ACS Appl. Mater. Interfaces, vol. 12, no. 51, pp. 57218–57227, 2020, doi: 10.1021/acsami.0c16302.

[28] S. Y. Cho, J. Y. Kim, O. Kwon, J. Kim, and H. T. Jung, "Molybdenum carbide chemical sensors with ultrahigh signal-to-noise ratios and ambient stability," *J. Mater. Chem. A*, vol. 6, no. 46, pp. 23408–23416, 2018, doi: 10.1039/C8TA07168C.

[29] E. Lee, A. Vahidmohammadi, Y. S. Yoon, M. Beidaghi, and D. J. Kim, "Two-Dimensional Vanadium Carbide MXene for Gas Sensors with Ultrahigh Sensitivity Toward Nonpolar Gases," *ACS Sensors*, vol. 4, no. 6, pp. 1603–1611, 2019, doi: 10.1021/acssensors.9b00303.

[30] K. Yang *et al.*, " $Ti_3C_2T_x$ MXene-Loaded 3D Substrate toward On-Chip Multi-Gas Sensing with Surface-Enhanced Raman Spectroscopy (SERS) Barcode Readout ," *ACS Nano*, vol. 15, no. 8, pp. 12996–13006, 2021, doi: 10.1021/acsnano.1c01890.

[31] D. Wang, D. Zhang, P. Li, Z. Yang, Q. Mi, and L. Yu, "Electrospinning of Flexible Poly(vinyl alcohol)/MXene Nanofiber-Based Humidity Sensor Self-Powered by Monolayer Molybdenum Diselenide Piezoelectric Nanogenerator," *Nano-Micro Lett.*, vol. 13, no. 1, pp. 1–13, 2021, doi: 10.1007/s40820-020-00580-5.

[32] S. H. Lee *et al.*, "Room-Temperature, Highly Durable $Ti_3C_2T_x$ MXene/Graphene Hybrid Fibers for NH_3 Gas Sensing," *ACS Appl. Mater. Interfaces*, vol. 12, no. 9, pp. 10434–10442, 2020, doi: 10.1021/acsami.9b21765.

[33] S. Sun *et al.*, "$W_{18}O_{49}$/$Ti_3C_2T_x$ Mxene nanocomposites for highly sensitive acetone gas sensor with low detection limit," *Sensors Actuators, B Chem.*, vol. 304, no. August 2019, p. 127274, 2020, doi: 10.1016/j.snb.2019.127274.

[34] H. Tai *et al.*, "Enhanced ammonia response of $Ti_3C_2T_x$ nanosheets supported by TiO_2 nanoparticles at room temperature," *Sensors Actuators, B Chem.*, vol. 298, no. July, p. 126874, 2019, doi: 10.1016/j.snb.2019.126874.

[35] T. Gakhar, Y. Rosenwaks, and A. Hazra, "Fullerene (C60) functionalized TiO_2 nanotubes for conductometric sensing of formaldehyde," *Sensors Actuators B Chem.*, vol. 364, no. April, 2022, doi: 10.1016/j.snb.2022.131892.

[36] J. Dhanalakshmi, S. Iyyapushpam, S. T. Nishanthi, M. Malligavathy, and D. P. Padiyan, “Investigation of oxygen vacancies in Ce coupled TiO_2 nanocomposites by Raman and PL spectra,” *Adv. Nat. Sci. Nanosci. Nanotechnol.*, vol. 8, no. 1, 2017, doi: 10.1088/2043-6254/aa5984.

[37] J. Liu *et al.*, “In situ green oxidation synthesis of Ti^{3+} and N self-doped $SrTiO_xN_y$ nanoparticles with enhanced photocatalytic activity under visible light,” *RSC Adv.*, vol. 8, no. 13, pp. 7142–7151, 2018, doi: 10.1039/C7RA13523H.

[38] H. Deng *et al.*, “Nanolayered Ti_3C_2 and $SrTiO_3$ Composites for Photocatalytic Reduction and Removal of Uranium(VI),” *ACS Appl. Nano Mater.*, vol. 2, no. 4, pp. 2283–2294, 2019, doi: 10.1021/acsanm.9b00205.

[39] A. Lipatov, M. Alhabeb, M. R. Lukatskaya, A. Boson, Y. Gogotsi, and A. Sinitskii, “Effect of Synthesis on Quality, Electronic Properties and Environmental Stability of Individual Monolayer Ti_3C_2 MXene Flakes,” *Adv. Electron. Mater.*, vol. 2, no. 12, 2016, doi: 10.1002/aelm.201600255.

[40] Y. Wei, P. Zhang, R. A. Soomro, Q. Zhu, and B. Xu, “Advances in the Synthesis of 2D MXenes,” *Adv. Mater.*, vol. 2103148, pp. 1–30, 2021, doi: 10.1002/adma.202103148.

[41] T. Su *et al.*, “Sulfur Vacancy and Ti3C2Tx Cocatalyst Synergistically Boosting Interfacial Charge Transfer in 2D/2D $Ti_3C_2T_x/ZnIn_2S_4$ Heterostructure for Enhanced Photocatalytic Hydrogen Evolution,” *Adv. Sci.*, vol. 9, no. 4, pp. 1–16, 2022, doi: 10.1002/advs.202103715.

[42] L. Jin, L. Chai, W. Yang, H. Wang, and L. Zhang, “Two-Dimensional Titanium Carbides ($Ti_3C_2T_x$) Functionalized by Poly (m-phenylenediamine) for Efficient Adsorption and Reduction of Hexavalent Chromium.”

[43] S. R. Ahmed and S. Neethirajan, “ Chiral MoS_2 Quantum Dots: Dual-Mode Detection Approaches for Avian Influenza Viruses ,” *Glob. Challenges*, vol. 2, no. 4, p. 1700071, 2018, doi: 10.1002/gch2.201700071.

[44] S. Singh and S. Sharma, “Temperature dependent selective detection of ethanol and methanol using MoS_2/TiO_2 composite,” *Sensors Actuators B Chem.*, vol. 350, no. August

2021, 2022, doi: 10.1016/j.snb.2021.130798.

[45] J. Huang *et al.*, “Enhanced acetone-sensing properties to ppb detection level using Au/Pd-doped ZnO nanorod,” *Sensors Actuators, B Chem.*, vol. 310, no. September 2019, 2020, doi: 10.1016/j.snb.2019.127129.

[46] Y. Xiao *et al.*, “Highly enhanced acetone sensing performances of porous and single crystalline ZnO nanosheets: High percentage of exposed (100) facets working together with surface modification with pd nanoparticles,” *ACS Appl. Mater. Interfaces*, vol. 4, no. 8, pp. 3797–3804, 2012, doi: 10.1021/am3010303.

[47] C. Liu, Q. Kuang, Z. Xie, and L. Zheng, “The effect of noble metal (Au, Pd and Pt) nanoparticles on the gas sensing performance of SnO_2-based sensors: a case study on the {221} high-index faceted SnO_2 octahedra,” *CrystEngComm*, vol. 17, no. 33, pp. 6308–6313, 2015, doi: 10.1039/c5ce01162k.

[48] J. X. Tang *et al.*, “Screw-like PdPt nanowires as highly efficient electrocatalysts for methanol and ethylene glycol oxidation,” *J. Mater. Chem. A*, vol. 6, no. 5, pp. 2327–2336, 2018, doi: 10.1039/c7ta09595c.

[49] P. Bindra and A. Hazra, “Selective detection of organic vapors using TiO_2 nanotubes based single sensor at room temperature,” *Sensors Actuators, B Chem.*, vol. 290, no. January, pp. 684–690, 2019, doi: 10.1016/j.snb.2019.03.115.

[50] J. Y. Jeon, B. C. Kang, Y. T. Byun, and T. J. Ha, “High-performance gas sensors based on single-wall carbon nanotube random networks for the detection of nitric oxide down to the ppb-level,” *Nanoscale*, vol. 11, no. 4, pp. 1587–1594, 2019, doi: 10.1039/c8nr07393g.

[51] D. Han, X. Li, F. Zhang, F. Gu, and Z. Wang, “Ultrahigh sensitivity and surface mechanism of gas sensing process in composite material of combining In_2O_3 with metal-organic frameworks derived Co_3O_4,” *Sensors Actuators, B Chem.*, vol. 340, no. April, p. 129990, 2021, doi: 10.1016/j.snb.2021.129990.

Chapter-3

MoS_2 functionalized TiO_2 nanotubes for selective detection of xylene at low temperature

3.1 Introduction

xylene is an efficient breath marker for lung cancer and in the exhaled breath of a patient, the concentration gets increased from 20 ppb to 100 ppb [1-5]. The selective detection of xylene breath marker among the complex chemically similar VOCs is a significant concern. BTX (benzene, toluene and xylene) aromatic hydrocarbons are found in exhaled breath and very difficult to detect a particular xylene marker among the chemically similar other VOCs [1-3].

Various semiconducting metal oxides have been employed for VOC sensing and found a suitable material with many benefits [1,2,6,7]. Specifically, TiO_2 has been recognized as a promising gas-sensing semiconductor in the present-day scenario [8-10]. The anodically grown 1-D TiO_2 has more catalytic activity and is suitable for the gas or VOC sensing [11,13,14]. Gakhar et.al explored the oxygen vacancy modulation of TiO_2 nanotubes by cathodic polarization and chemical reduction routes for efficient VOC sensing. Doped nanotubes presented high response magnitudes of 99.64% and 60% under exposure to 100 ppm of ethanol at 200 °C and 50 °C, respectively [15]. However, low selectivity and high operating temperature remain challenging for the TiO_2 sensors [15,16]. The improvement in these properties is essential to work as a potential breath marker sensor.

From the literature survey, it was evident that transition metal dichalcogenides (TMDs) are the more acceptable and demanding nanomaterial [17-21]. The presence of electronic bandgaps in TMDCs makes them suitable semiconducting gas-sensing materials and till now MoS_2 [17,18,22-24], WS_2 [25-27], $MoSe_2$ [28], and WSe_2 [29] have been employed. TMDs are famous for their low temperature sensing capabilities and selective detection of VOCs [30-33]. Most of the TMDs are reported in the 2-D morphologies like nanoflowers, nanosheets, etc. [23,24,26,27] but their employment in 0-D form for the hybridization with other materials simulating more attention in gas sensing field [25,28]. 0-D TMDs hold more specific surface area and surface reactive sites than other proposed 2-D morphologies [25,28]. Among all TMDs, MoS_2 can be chosen in 0-D form due to their markable number of reactive sites, high sensitivity, and easy surface functionalization [17,18,23,24,30-32]. Kim et. al. synthesized mercaptoundecanoic acid (thiolated ligand)- conjugated MoS_2 sensor to achieve high reactivity towards the target VOC [30].

Combining two materials can be implemented to modulate the characteristics of the sensing device. In this regard, the functionalization of materials with 0-D (dimensional) nanoparticles results in chemical and electrical sensitization in the material [33,34,35,25,28]. The electrical sensitization leads to the formation of discrete Schottky junctions due to their work function differences [34,35]. Singh et. al. synthesized a highly sensitive, and stable sensor based on the thin film of MoS_2/TiO_2 composite. The device has shown a 100% response for ethanol with a superior signal-to-noise ratio at 240 °C [8].

In this chapter, we have prepared a MoS_2 functionalized TiO_2 nanotubes composite to overcome the issue of poor selectivity and higher operating temperature. The composite was prepared for highly stable and selective xylene sensing among chemically similar compounds like benzene and toluene. Specifically, we synthesized a MoS_2/TiO_2-based composite via a low-cost hydrothermal method. The metal insulator metal (MIM) type sensor device from composite has displayed excellent xylene selectivity lower 75 °C operating temperature. The highly selective detection of Xylene over other chemically similar VOCs by MoS_2/TiO_2-based sensor shows a potential applicability in breath VOC detection. The sensor showed good response behavior with outstanding long-term and signal stability in air and 75 °C.

3.2 Synthesis of MoS_2/TNTs Heterostructured nanotube array

MoS_2 QDs coated TiO_2 nanotubes were synthesized by using a one-step hydrothermal reaction at 180 °C and 18 h. The annealed TNTs were placed in a Teflon-lined autoclave containing 2.8 mg MoS_2 in 100 ml MQ water. The resulting sample was washed with absolute ethanol and DI water to remove excess MoS_2 and dried in the air. MoS_2/TiO_2 heterostructure nanotubes array was thermally treated at 250 °C for 3 h in the air to provide thermal stability to the heterostructure.

3.3 Characterization

Morphological characterization

The surface morphology of the prepared TiO_2 nanotube array before and after the hydrothermal treatment with MoS_2 QDs was analyzed by the FESEM technique. The nanotube morphology was intact after the MoS_2 deposition but significantly decreased pore diameters and the average pore diameter decreased from 95 nm for pristine TNTs to 70 nm for MoS_2/TNTs as shown in Fig. 3.1(a). MoS_2 QDs were aggregated, formed small clusters of different dimensions, and decorated on the TiO_2 nanotubes. The distribution of MoS_2 QDs. It was anticipated that the surface roughness of the TNTs would be enhanced due to the decorating of individual and aggregated MoS_2 (Fig. 3.1(b)). However, the decoration of MOS_2 on the sidewall of the TiO_2 nanotubes is not meaningfully evident from the FESEM image (Fig. 3.1(c)). Consequently, a detailed TEM analysis was performed to determine the decoration of small and individual MoS_2 QDs on the top of the TiO_2 nanotube surface as shown in Fig. 3.1(d, e). The uniform decoration of MOS_2 QDs was observed on the top and side walls of the nanotube as displayed in Fig. 3.1(d, e). Interestingly, the TEM analysis showed that MOS_2 QDs have relatively small dimensions (5-10 nm) compared to the average cluster size (Fig. 3.1(d)). The side wall of the nanotube is fully decorated with the MoS_2 QDs in Fig. 3.1(e). The high-resolution TEM (HRTEM) image in Fig. 3.1(f) shows the MoS_2/TNTs side wall interface where the inter-planer distance of 0.375 nm corresponds to the (101) crystal plane of anatase [13,15] and 0.75 nm corresponds to the (002)

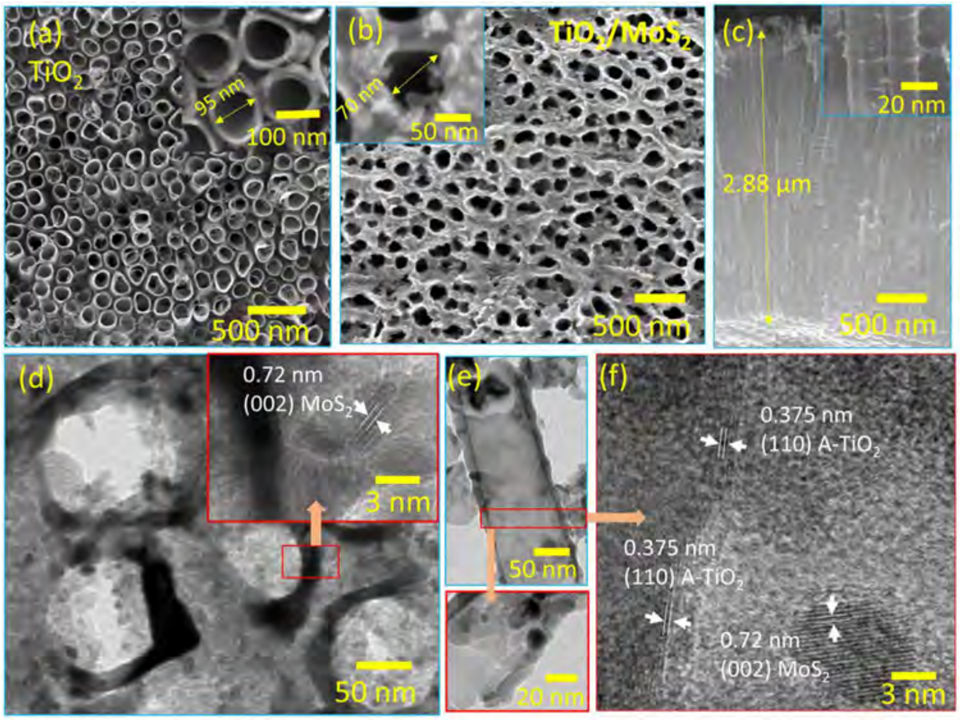

Fig. 3.1. SEM micrographs of (a) pure TiO_2 nanotube arrays, (b,c) MoS_2/TiO_2 composite, (d,e) TEM image of MoS_2/TiO_2 composite and (e) HRTEM image of MoS_2/TiO_2.

crystal plane of MoS_2 showing less crystalline and non-homogenous lattice arrangement of the resulting QDs which is in good agreement of the previously reported works [37,38].

Structural characterization

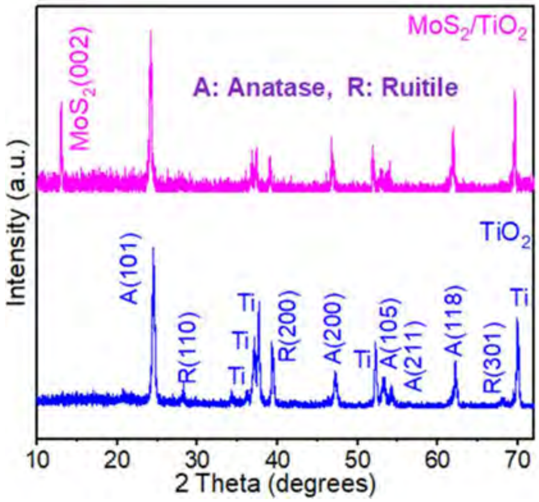

Fig. 3.2. XRD spectra of MoS_2/TiO_2 composite of MoS_2/TiO_2 nanocomposite.

To understand the crystalline nature of TiO_2 and MoS_2/TiO_2 NTs composites was performed using powder X-ray diffraction and represented in Fig. 3.2. The sharpest and most intense peak at 24.7° confirmed the significant contribution of anatase (101) crystallinity in both samples [13,15]. However, Fig. 3.2 illustrates a few small peaks of rutile crystallinity following the hydrothermal and heating treatment in both samples (Fig. 3.2). A small rutile (110) peak was observed near 28.8° [15, 35]. The other low-intensity peaks at 38.7° and 68.2° in pure TiO_2 sample correspond to rutile (200) and (301) crystallinity, respectively. Some other low-intensity anatase peaks of (200), (105), (211) and (118) were observed at 46°, 53.5°, 54.61° and 62.2°, respectively. Some peaks of Ti substrate were also observed in both samples (Fig. 3.2). The existence of MoS_2 in the nanocomposites is confirmed by the MO (002) orientation at 14.2°, ensuring the coexistence of both the materials [38].

Chemical characterization

X-ray photoelectron spectroscopy (XPS) was carried out on pure TiO_2 and MoS_2/TiO_2 composite samples to examine their chemical state and surface compositions. Ti 2p peaks were found at 459.3 and 465.2 eV with a spin-orbital doublet separated by 5.9 eV, which infers two oxidation states into the resulting material (Fig. 3.3(a)). The peaks were deconvoluted based on oxidations into the resulting samples and observed at respective binding energies corresponding to the Ti^{3+} 2p$_{3/2}$, Ti^{4+} 2p$_{3/2}$, Ti^{3+} 2p$_{1/2}$ and Ti^{4+} 2p$_{1/2}$, respectively as shown in Table 3.1. The intensity and the area of Ti^{+3} peaks are significantly lower than those of Ti^{+4} peaks in the MoS$_2$/TiO$_2$ composite compared to the pure TNTs confirming the improved surface oxygen in TiO$_2$ nanotube array after the MOS$_2$ functionalization (Fig. 3.3(a)). The O 1s spectra in Fig. 3.3(b) showed three peaks at 530.6, 531.9, and 533.5 eV corresponding to the O^{2-} (lattice oxygen), O$^-$ (oxygen vacancies), and O$^-_2$ (chemisorbed oxygen), respectively [35]. The higher area of chemisorbed oxygen peak compared to the lattice oxygen and oxygen vacancy in MoS$_2$/TiO$_2$ composite could arise due to highly chemically sensitized MoS$_2$ QDs which helps in the more gaseous analyte interaction during the sensing experiments (Table 3.2) [40]. The Mo 3d signal comes from the peaks around 229.2, 231.1, 233.2 and 235.1 eV matching with Mo^{4+} 3d$_{5/2}$, Mo^{4+} 3d$_{3/2}$, Mo^{6+} 3d$_{5/2}$ and Mo^{5+} 3d$_{3/2}$ of MoS$_2$, respectively (Fig. 3.3(c)) [8, 39]. The adsorption of surface oxygen functional groups or partial oxidation on the surface of MoS$_2$ QDs generates Mo^{+6} states which help during the gaseous interaction (Table 3.2) [8, 40]. It should be pointed out that both Mo and S peaks were observed in the Mo 3d spectrum of the MoS$_2$/TiO$_2$ composite, suggesting its origin from the MoS$_2$ component [40]. The two characteristic peaks (S^{2-} 2p$_{3/2}$ and S^{2-} 2p$_{1/2}$) of S 2s spectra were merged into one and observed at 162.9 eV originating from the edge-located S$_2^{2-}$ which are recognized as the active sites of MoS$_2$ (Fig. 3.3(d)) [40]. At a higher binding energy of 169.7 eV a significant peak was observed for S^{+4}, further confirming the +6-oxidation state of

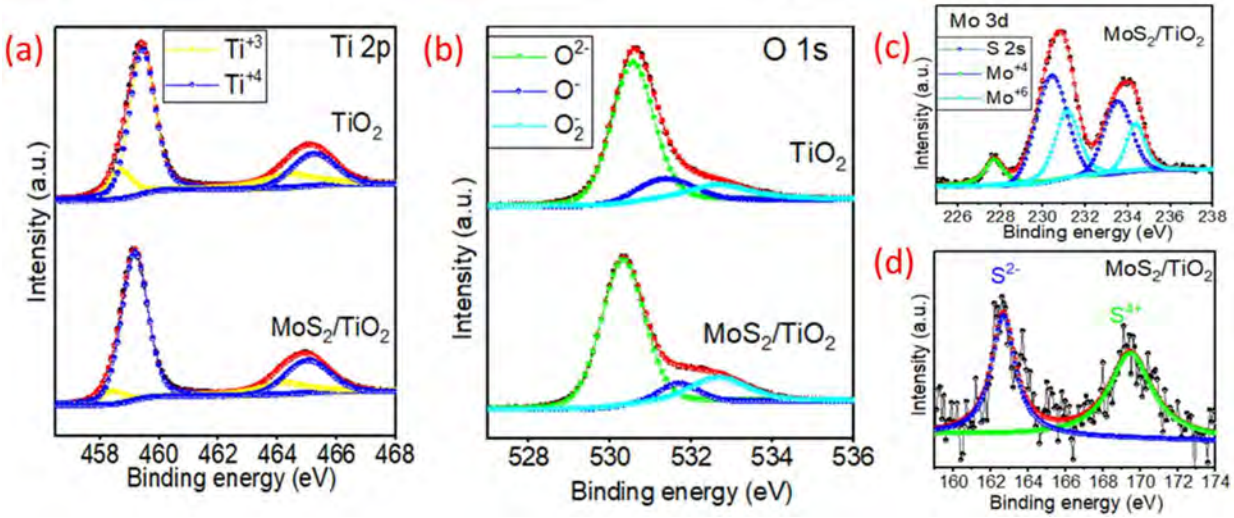

Fig. 3.3. High-resolution XPS spectra and peak positions of (a) Ti 2p, (b) O 1s, (c) Mo 3d and (d) S 2s spectrum of MoS$_2$/TiO$_2$ nanocomposite.

Table 3.1. Binding energy (eV) of the deconvoluted peaks of TiO_2 and MoS_2/TiO_2 spectra.

Sample	**Ti^{+3} ($2p_{3/2}$, $2p_{1/2}$)**	**Ti^{+4} ($2p_{3/2}$, $2p_{1/2}$)**	**O^{2-}, O^{-}, O_2^{-}**	**Mo^{+4} ($3d_{5/2}$, $3d_{3/2}$)**	**Mo^{+6} ($3d_{5/2}$, $3d_{3/2}$)**	**S 2s**	**S^{2-}**	**S^{+4}**
TiO_2	458.3, 464.1	459.1, 464.9	530.3, 531.4, 532.6	-	-	-	-	-
MoS_2/TiO_2	458.4, 464.2	459.3, 465.1	530.5, 531.3, 532.6	230.4, 233.5	231.1, 234.3	227.7	162.6	169.4

Table 3.2. Relative area (%) estimation of the deconvoluted peaks of TiO_2 and MoS_2/TiO_2 spectra.

Sample	**Ti^{+3} ($2p_{3/2}$, $2p_{1/2}$)**	**Ti^{+4} ($2p_{3/2}$, $2p_{1/2}$)**	**O^{2-}, O^{-}, O_2^{-}**	**Mo^{+4} ($3d_{5/2}$, $3d_{3/2}$)**	**Mo^{+6} ($3d_{5/2}$, $3d_{3/2}$)**	**S 2s**	**S 2p S^{2-}**	**S 2p S^{+4}**
TiO_2	24.7	75.3	72,13,15	-	-	-	-	-
MoS_2/TiO_2	16	84	73,8,19	59	33	8	43	57

Mo (Table 3.1). The highly oxidized surface of MoS_2 contains many reactive sites [8]. Additionally, MoS_2/TiO_2 heterostructure formation will lead to more defect sites and as the defects are increased, it induces the change of the local electron distribution of Mo and S in heterojunction which provides electronic sensitization in the resulting composite

Surface wettability study

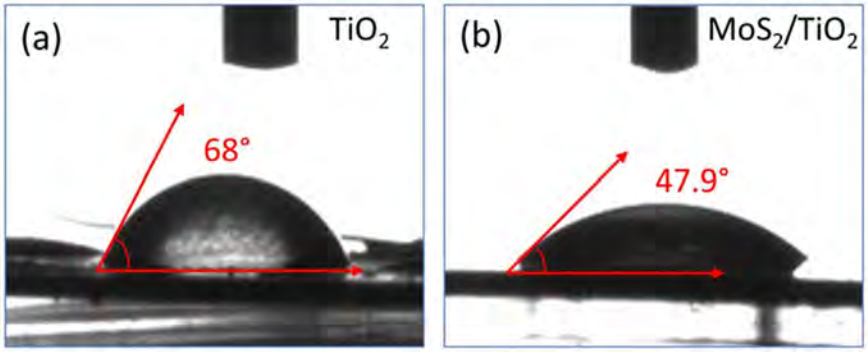

Fig. 3.4. Water contact angle of (a) TiO_2 nanotubes array and (b) MoS_2/TiO_2 nanocomposite.

sensor [40]. In particular, we examined the surface wettability of pure TiO_2 nanotubes and MoS_2/TiO_2 nanotubes array composite (Fig. 3.4(a, b)). The static water contact angles (CAs) of a deionized water droplet (8 µl) on the surface STO film were measured using a contact angle measurement device.

The static contact angle of these two films was measured (Fig. 3.4(a-b)) and found to be 68°, and 47.9° for TiO_2 and MoS_2/TiO_2, respectively. However, the result was very close to the previously reported contact angle data for pure TiO_2 nanotube array [41,42]. The modification of MoS_2 decreases the water contact angle and improves the hydrophilicity in the results composite as visible in Fig. 3.4(b) [43,44]. The poor contact angle makes the water molecules faster to adsorb to the surface of the sensing film, and the predicted hindrance to the sensing performance is due to humidity [44].

3.4 Sensor study

VOC sensing

To optimize the best-suited working temperature, the gas sensing behavior of prepared sensors was analyzed at a range of temperatures from 45- 90 °C. The baseline resistance decreased abruptly with the increase in temperature from 45 °C to 90 °C and showed a saturation tendency confirming the low-temperature stability of MoS_2 in the sensors (Fig. 3.5(a)) [33,34]. The

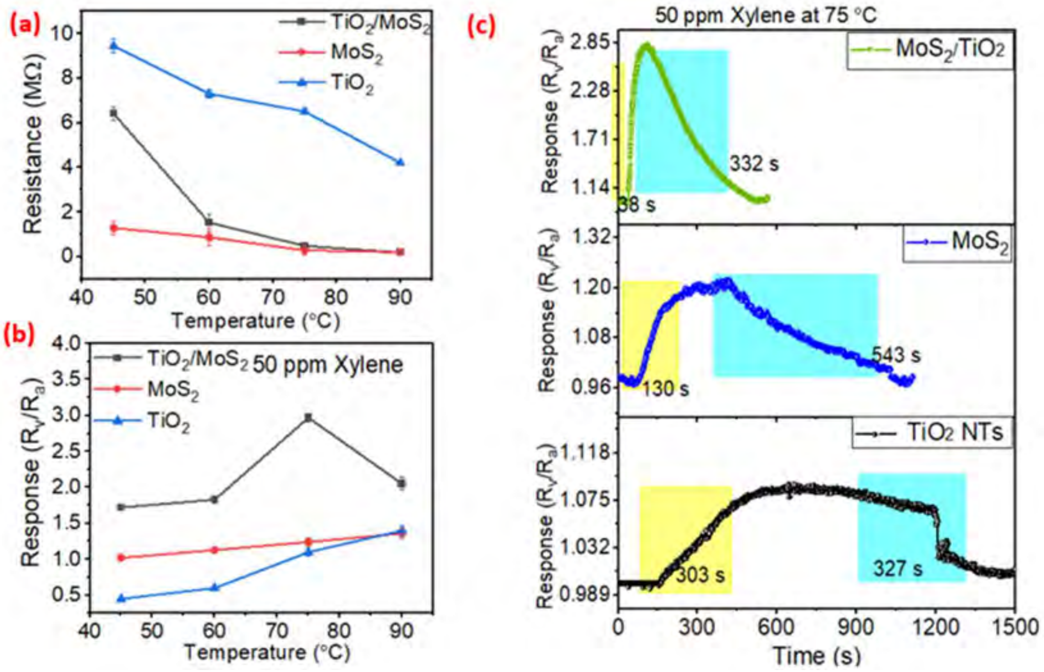

Fig. 3.5. (a) Baseline resistance change vs temperature and (d) corresponding response magnitude (R_v/R_a) vs temperature for all three sensors and (c) response characteristics of all three sensors at optimized 75 °C temperature.

response of MoS_2, TiO_2 and MoS_2/TiO_2 sensors were evaluated with 50 ppm of xylene in air at different temperatures shown in Fig. 3.5(b). The response curve exhibited a dip tendency beyond 75 °C, displaying a volcano-shaped curve (Fig. 3.5(b)). For MoS_2/TiO_2 NTA sensors (Fig. 3.5(b)), response magnitude increased linearly from 45 °C to 90 °C and showed an excellent sharp increment in response magnitude at 75 °C. Moreover, the MoS_2/TiO_2 sensor showed a pretty high response, i.e., 2.85, which is many times higher than the pure MoS_2 and TiO_2 sensors at the 75 °C temperature. Fig. 3.5(c) contains the response and response /recovery time characteristics of all three sensors at 75 °C optimized temperature in the air atmosphere.

The response time and recovery time for the MoS_2/TiO_2 sensor are 35 s and 335 s with an excellent response (2.85) to 50 ppm xylene, which is much faster than the pure TiO_2 and MoS_2 sensors at 75 °C temperature (Fig. 3.5(c)). The quick response and recovery are mainly attributed to the fast electron transfer kinetics of pure MoS_2 and TiO_2 nanotubes combined throughout the composite [13, 34]. It should be noted that previously reported pure TiO_2 sensors require a relatively high operating temperature for VOC adsorption or desorption [15]. Therefore, the MoS_2 modification on the TiO_2 NT surface reduces the operating temperature of the sensors

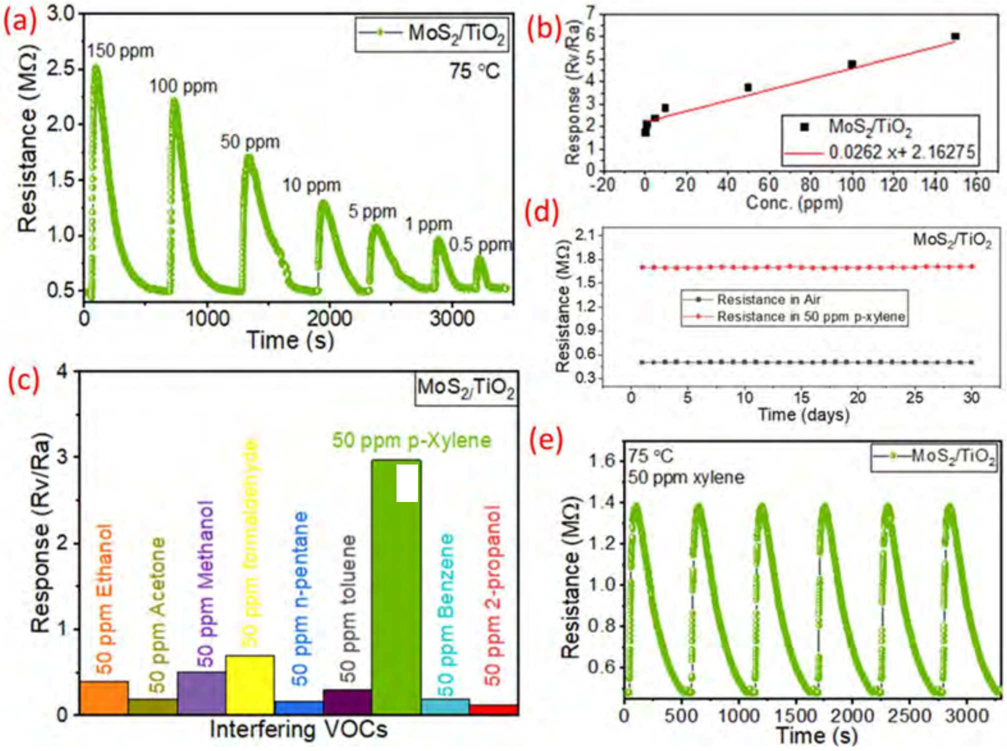

Fig. 3.6. (a) MoS_2/TiO_2 Sensor resistance change for different xylene concentrations (in ppm). (b) Corresponding absolute response magnitude vs xylene concentration (in ppm). (c) selectivity study of xylene over other interfering VOCs, (d) long-term stability study of the sensor for 30

days with an interval of 1 day, and (e) repeatability test for continuous six cycles for 50 ppm concentration. All measurement was performed at an optimized 75 °C temperature.

significantly. The results were better than those obtained previously with MoS_2/TiO_2 thin film-based composites at 240 °C operating temperature [8]. The 1D nature of TiO_2 nanotubes also played a significant role by offering both inner and outer surfaces for adsorption-desorption, which increases the reactivity of the sensor compared to the thin film of TiO_2 [8,13].

To further evaluate the sensing response functional relation with different concentrations of xylene ranging from 150 ppm to 0.5 ppm at optimum 75 °C temperature in air. From the results, initially, the response characteristics show massive changes, and beyond 100 ppm of xylene a slow variation with increasing xylene concentration was observed (Fig. 3.6(a)). The high response magnitude of 1.73 even at a lower concentration of 500 ppb of xylene might arise due to the availability of the effective surface area developing an intimate contact between two different heterostructured materials [40]. The MoS_2/TiO_2 sensor processed a nearly linear response to xylene ($R^2 > 0.971$) with a lower detection limit (LOD) of 33 ppb (Fig. 3.6(b)), suggesting the most excellent linearity and reproducibility favorable to more extensive detection range and lower limit of detection for real-time xylene sensing. The selectivity of the MoS_2/TiO_2 sensor was also measured by comparing it with various VOCs (e.g., acetone, methanol, ethanol, 2-propanol, formaldehyde, n-pentane benzene, toluene and xylene), as shown in Fig. 3.6(c). Results indicated that the MoS_2/TiO_2 sensor exhibits a focused selectivity towards xylene. The sensor showed excellent selectivity towards the xylene (aromatic) among chemically different VOCs like; methanol (alcohol), acetone (ketone), n-pentane (hydrocarbons) and formaldehyde (aldehyde) (Fig. 3.6(c)). Additionally, interfering aromatic VOCs with identical chemical properties like benzene and toluene showed negligible response compared to the xylene. This result should be ascribed to the abundant active sites with highly oxidizing functional groups and superficial electrons in MoS_2 and the catalytic action of Mo-based material which benefit the selective adsorption of aromatic molecules like xylene [40, 45,46]. Benzene with maximum resonance behavior required a huge dissociation energy for the interaction and toluene has less electron-donating capacity than xylene making the composite more favorable for xylene selective sensing [45]. The repeatability and long-term stability of the composite sensor are crucial parameters for a practical environment. The sensor showed remarkable consistency in a 30 days study with an interval of one day (Fig. 3.6(d)). The repeatable nature of the sensor was tested for 6 consecutive cycles and a variation of less than ± 0.4 in relative response magnitude was recorded (Fig. 3.6(e)).

Humidity study

The sensing characteristics of a sensor in the presence of humidity estimated the environmental stability of a sensor. Consequently, to understand the stability of the sensor, the sensing characteristics at different humidity levels range from 20% to 80% (Fig. 3.7(a-f)). The measurements include changes in transient characteristics, baseline resistance, response/recovery time and response magnitude of the sensor. Its visible, the base resistance decreases abruptly with rising RH level due to the removal of adsorbed oxygen species on the sensing surface (Fig. 3.7(f)). The response magnitude also decreased significantly when RH changed from 20% to 80% in the composite sensor. The response/recovery time also varies with the change of different humidity levels (Fig. 3.7(a-e)). In the presence of humidity, the water poisoning effect dominates the sensor, and the adsorption of gas molecules becomes competitive with the water molecule, resulting in a decreased response magnitude [8].

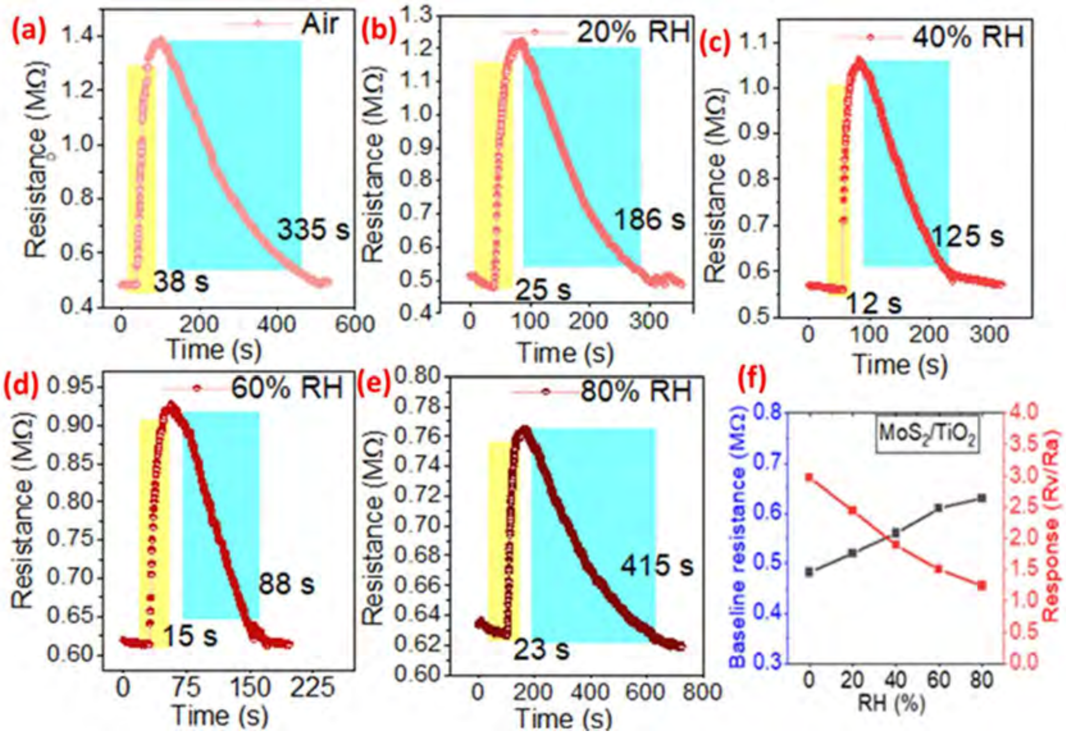

Fig. 3.7. (a-e) MoS_2/TiO_2 sensor resistance variation with different relative humidity levels (air, 20-80% RH) at a fixed xylene concentration of 50 ppm at 75 °C and (f) change in baseline resistance and response magnitude of the MoS_2/TiO_2 sensor at different humidity levels.

Moreover, gas sensing characteristics and stability, the excellent xylene selective sensing performance of the MoS_2/TiO_2 sensor was mainly attributed to the following: (i) controlled 1D morphology and introducing defect structures and oxygen functionality introduced by sufficient active sites, (ii) building the p–n heterojunctions and forming discrete Schottky junctions, (iii) unique structural and electronic properties are contributed to higher recoverability and durability of the sensor [40].

The sensing mechanism of composite involves the synergistic effect of both the participating materials. MoS_2 is one of the most promising nanomaterials with a tuneable natural bandgap and high carrier mobility, which provide a direct conduction path for carrier transportation [9,18]. MoS_2 quantum dots possess remarkable number of reactive sites at the edges in the form of S^{-2}, S_2^{-2}, and SH^- groups [19]. MoS_2 quantum dots plays a key role in significantly good sensing properties at relatively low operating temperature. The very high specific surface area, and chemical sensitization of MoS_2 dots on TiO_2 nanotubes facilitate fast and huge electron transfer due to the more significant number of VOC analyte interaction [24,36]. On the other side, 1-D TiO_2 nanotubes are provide both an inner and an exterior surface for the adsorption-desorption of VOCs, which improves the response magnitude of the sensor [14-16]. Enhanced sensing properties of MoS_2/TiO_2 sensor over pure-TiO_2 might be due to the catalytic effect of the quantum dots and the semiconductor discrete Schottky junctions [24,36]. When the TiO_2 nanotubes were functionalized with MoS_2 dots, surface area and the possibility for gas diffusion were increased tremendously.

3.5 Conclusion

In exhaled breath, xylene concentration is 10-200 ppb with a high interference and a saturated humidity (>50% RH) level. For real-time xylene sensing, a sensor system should have a low detection limit and a highly selective nature towards xylene. In this construction, we have established a one-step hydrothermal strategy to synthesize MoS_2/TiO_2 heterostructured nanocomposite. TiO_2 nanotube arrays were first synthesized by an electrochemical anodization route. The excess specific surface area and many heterointerfaces endow MoS_2/TiO_2 with many VOC interactive sites. Owning to the improved surface and electronic properties, the MoS_2/TiO_2 composite showed a high response magnitude of 1.73 for 500 ppb of xylene at 75 °C operating temperature. The sensor achieved a lower detection limit (LOD) of 33 ppb which is very similar to the concentration of xylene in exhaled breath. Most importantly, high xylene selectivity was observed in the cross interference of chemically similar VOCs like benzene and toluene. These research outcomes are fulfilling the requirements of xylene sensing for breath analysis application in terms of selectivity and low ppb detection at a low operating temperature. On the other hand, the sensor was significantly affected by the humidity and sensing properties get deteriorate at high humidity levels.

Humidity interference still remains a challenge in MoS_2/TiO_2 sensor. Metal oxides are well-known

gas/VOC sensing material but are still affected by the humidity. The addition of an overlayer with a highly porous and physically and chemically stable material can act as a breathable and humidity-tolerant material where gas molecules can diffuse through the pores and show a negligible influence on the humidity. In this regard, composite formation with chemically and physically stable and robust materials like perovskites can be the best solution to develop humidity-tolerant VOC sensors for breath analysis application.

References

[1] X. Liu, F. Xu, Z. Li, Z. Liu, W. Yang, Y. Zhang, H. Fan, H.Y. Yang, Design strategy for MXene and metal chalcogenides/oxides hybrids for supercapacitors, secondary batteries and electro/photocatalysis, Coord. Chem. Rev. 464 (2022) 214544.

[2] S. Yang, G. Lei, H. Xu, Z. Lan, Z. Wang, H. Gu, Metal oxide based heterojunctions for gas sensors: A review, Nanomaterials. 11 (2021) 1–26. https://doi.org/10.3390/nano11041026.

[3] H. Liu, G. Meng, Z. Deng, K. Nagashima, S. Wang, T. Dai, L. Li, T. Yanagida, X. Fang, Discriminating BTX Molecules by the Nonselective Metal Oxide Sensor-Based Smart Sensing System, ACS Sensors. 6 (2021) 4167–4175. https://doi.org/10.1021/acssensors.1c01704.

[4] C. Feng, C. Wang, H. Zhang, X. Li, C. Wang, P. Cheng, J. Ma, P. Sun, Y. Gao, H. Zhang, Y. Sun, J. Zheng, G. Lu, Enhanced sensitive and selective xylene sensors using W-doped NiO nanotubes, Sensors Actuators, B Chem. 221 (2015) 1475–1482. https://doi.org/10.1016/j.snb.2015.07.114.

[5] R. Guo, X. Shang, C. Shao, X. Wang, X. Yan, Q. Yang, X. Lai, Ordered large-pore

mesoporous $ZnCr_2O_4$ with ultrathin crystalline frameworks for highly sensitive and selective detection of ppb-level xylene, Sensors Actuators B Chem. 365 (2022). https://doi.org/10.1016/j.snb.2022.131964.

[6] G. Gregis, J.B. Sanchez, I. Bezverkhyy, W. Guy, F. Berger, V. Fierro, J.P. Bellat, A. Celzard, Detection and quantification of lung cancer biomarkers by a micro-analytical device using a single metal oxide-based gas sensor, Sensors Actuators, B Chem. 255 (2018) 391–400. https://doi.org/10.1016/j.snb.2017.08.056.

[7] H. Yamagiwa, S. Sato, T. Fukawa, T. Ikehara, R. Maeda, T. Mihara, M. Kimura, Detection of volatile organic compounds by weight-detectable sensors coated with metal-organic frameworks, Sci. Rep. 4 (2014) 1–6. https://doi.org/10.1038/srep06247.

[8] S. Zhao, J. Lei, D. Huo, C. Hou, X. Luo, H. Wu, H. Fa, M. Yang, A colorimetric detector for lung cancer related volatile organic compounds based on cross-response mechanism, Sensors Actuators, B Chem. 256 (2018) 543–552. https://doi.org/10.1016/j.snb.2017.10.091.

[9] S. Singh, S. Sharma, Temperature dependent selective detection of ethanol and methanol using MoS_2/TiO_2 composite, Sensors Actuators B Chem. 350 (2022). https://doi.org/10.1016/j.snb.2021.130798.

[10] P. V. Kamat, TiO_2 nanostructures: Recent physical chemistry advances, J. Phys. Chem. C. 116 (2012) 11849–11851. https://doi.org/10.1021/jp305026h.

[11] A.N. Enyashin, G. Seifert, Structure, stability and electronic properties of TiO_2 nanostructures, Phys. Status Solidi Basic Res. 242 (2005) 1361–1370. https://doi.org/10.1002/pssb.200540026.

[12] H. Zhang, J.F. Banfield, Thermodynamic analysis of phase stability of nanocrystalline titania, J. Mater. Chem. 8 (1998) 2073–2076. https://doi.org/10.1039/a802619j.

[13] T. Gakhar, A. Hazra, C_{60} -encapsulated TiO_2 nanoparticles for selective and ultrahigh sensitive detection of formaldehyde, Nanotechnology. 32 (2021) 505505. https://doi.org/10.1088/1361-6528/ac23f9.

[14] P. Bindra, A. Hazra, Selective detection of organic vapors using TiO_2 nanotubes based

single sensor at room temperature, Sensors Actuators, B Chem. 290 (2019) 684–690. https://doi.org/10.1016/j.snb.2019.03.115.

[15] M.A. Einarsrud, T. Grande, 1D oxide nanostructures from chemical solutions, Chem. Soc. Rev. 43 (2014) 2187–2199. https://doi.org/10.1039/c3cs60219b.

[16] T. Gakhar, A. Hazra, Oxygen vacancy modulation of titania nanotubes by cathodic polarization and chemical reduction routes for efficient detection of volatile organic compounds, Nanoscale. 12 (2020) 9082–9093. https://doi.org/10.1039/c9nr10795a.

[17] M.M. Arafat, A.S.M.A. Haseeb, S.A. Akbar, A selective ultrahigh responding high temperature ethanol sensor using TiO_2 nanoparticles, Sensors (Switzerland). 14 (2014) 13613–13627. https://doi.org/10.3390/s140813613.

[18] J.S. Kim, H.W. Yoo, H.O. Choi, H.T. Jung, Tunable volatile organic compounds sensor by using thiolated ligand conjugation on MoS2, Nano Lett. 14 (2014) 5941–5947. https://doi.org/10.1021/nl502906a.

[19] K. Lee, R. Gatensby, N. McEvoy, T. Hallam, G.S. Duesberg, High-performance sensors based on molybdenum disulfide thin films, Adv. Mater. 25 (2013) 6699–6702. https://doi.org/10.1002/adma.201303230.

[20] S. Anantharaj, S. Kundu, S. Noda, Progress in nickel chalcogenide electrocatalyzed hydrogen evolution reaction, J. Mater. Chem. A. 8 (2020) 4174–4192. https://doi.org/10.1039/c9ta14037a.

[21] J. Huang, Y. Jiang, T. An, M. Cao, Increasing the active sites and intrinsic activity of transition metal chalcogenide electrocatalysts for enhanced water splitting, J. Mater. Chem. A. 8 (2020) 25465–25498. https://doi.org/10.1039/d0ta08802a.

[22] W.Y. Lee, K. Kim, S.H. Lee, J.H. Bae, I.M. Kang, M. Park, K. Kim, J. Jang, Room-Temperature High-Detectivity Flexible Near-Infrared Photodetectors with Chalcogenide Silver Telluride Nanoparticles, ACS Omega. 7 (2022) 10262–10267. https://doi.org/10.1021/acsomega.1c06870.

[23] X. Chen, X. Chen, Y. Han, C. Su, M. Zeng, N. Hu, Y. Su, Z. Zhou, H. Wei, Z. Yang, Two-dimensional $MoSe_2$ nanosheets via liquid-phase exfoliation for high-performance

room temperature NO_2 gas sensors, Nanotechnology. 30 (2019) 445503. https://doi.org/10.1088/1361-6528/ab35ec.

[24] W. Zhao, R. Yan, H. Li, K. Ding, Y. Chen, D. Xu, Highly sensitive NO_2 gas sensor with a low detection limit based on Pt-modified MoS2 flakes, Mater. Lett. 330 (2023) 133386. https://doi.org/10.1016/j.matlet.2022.133386.

[25] N. Yue, J. Weicheng, W. Rongguo, D. Guomin, H. Yifan, Hybrid nanostructures combining graphene-MoS_2 quantum dots for gas sensing, J. Mater. Chem. A. 4 (2016) 8198–8203. https://doi.org/10.1039/c6ta03267b.

[26] J.H. Kim, A. Mirzaei, H.W. Kim, S.S. Kim, Flexible and low power CO gas sensor with Au-functionalized 2D WS2 nanoflakes, Sensors Actuators, B Chem. 313 (2020) 128040. https://doi.org/10.1016/j.snb.2020.128040.

[27] J.H. Kim, A. Mirzaei, H.W. Kim, S.S. Kim, Realization of Au-decorated WS_2 nanosheets as low power-consumption and selective gas sensors, Sensors Actuators, B Chem. 296 (2019) 126659. https://doi.org/10.1016/j.snb.2019.126659.

[28] Y. Sun, B. Wang, S. Liu, Z. Zhao, W. Zhang, W. Zhang, K. Suematsu, J. Hu, WS_2 quantum dots modified In_2O_3 hollow hexagonal prisms for conductometric NO_2 sensing at room-temperature, Sensors Actuators B Chem. 380 (2023) 133341. https://doi.org/10.1016/j.snb.2023.133341.

[29] S.Y. Choi, Y. Kim, H.S. Chung, A.R. Kim, J.D. Kwon, J. Park, Y.L. Kim, S.H. Kwon, M.G. Hahm, B. Cho, Effect of Nb doping on chemical sensing performance of two-dimensional layered $MoSe_2$, ACS Appl. Mater. Interfaces. 9 (2017) 3817–3823. https://doi.org/10.1021/acsami.6b14551.

[30] W.Y. Chen, X. Jiang, S.N. Lai, D. Peroulis, L. Stanciu, Nanohybrids of a MXene and transition metal dichalcogenide for selective detection of volatile organic compounds, Nat. Commun. 11 (2020) 1–10. https://doi.org/10.1038/s41467-020-15092-4.

[31] C. Zhao, X. Gan, Q. Yuan, S. Hu, L. Fang, J. Zhao, High-Performance Volatile Organic Compounds Microsensor Based on Few-Layer MoS2-Coated Photonic Crystal Cavity, Adv. Opt. Mater. 6 (2018) 1–7. https://doi.org/10.1002/adom.201700882.

[32] P. Dwivedi, S. Das, S. Dhanekar, Wafer-Scale Synthesized MoS_2/Porous Silicon Nanostructures for Efficient and Selective Ethanol Sensing at Room Temperature, ACS Appl. Mater. Interfaces. 9 (2017) 21017–21024. https://doi.org/10.1021/acsami.7b05468.

[33] M. Barzegar, M. Berahman, A.I. Zad, Sensing behavior of flower-shaped MoS_2 nanoflakes: Case study with methanol and xylene, Beilstein J. Nanotechnol. 9 (2018) 608–615. https://doi.org/10.3762/bjnano.9.57.

[34] J.W. Yoon, J.H. Lee, Toward breath analysis on a chip for disease diagnosis using semiconductor-based chemiresistors: Recent progress and future perspectives, Lab Chip. 17 (2017) 3537–3557. https://doi.org/10.1039/c7lc00810d.

[35] C. Liu, Q. Kuang, Z. Xie, L. Zheng, The effect of noble metal (Au, Pd and Pt) nanoparticles on the gas sensing performance of SnO_2-based sensors: a case study on the {221} high-index faceted SnO_2 octahedra, CrystEngComm. 17 (2015) 6308–6313. https://doi.org/10.1039/c5ce01162k.

[36] S. Liu, Z. Wang, Y. Zhang, Z. Dong, T. Zhang, Preparation of zinc oxide nanoparticle-reduced graphene oxide-gold nanoparticle hybrids for detection of NO_2, RSC Adv. 5 (2015) 91760–91765. https://doi.org/10.1039/c5ra18680c.

[37] D. Zhang, Z. Yang, P. Li, M. Pang, Q. Xue, Flexible self-powered high-performance ammonia sensor based on Au-decorated $MoSe_2$ nanoflowers driven by single layer MoS2-flake piezoelectric nanogenerator, Nano Energy. 65 (2019). https://doi.org/10.1016/j.nanoen.2019.103974.

[38] S.J. Panchu, K. Raju, H.C. Swart, B. Chokkalingam, M. Maaza, M. Henini, M.K. Moodley, Luminescent MoS_2 Quantum Dots with Tunable Operating Potential for Energy-Enhanced Aqueous Supercapacitors, ACS Omega. 6 (2021) 4542–4550. https://doi.org/10.1021/acsomega.0c02576.

[39] R. Abinaya, J. Archana, S. Harish, M. Navaneethan, S. Ponnusamy, C. Muthamizhchelvan, M. Shimomura, Y. Hayakawa, Ultrathin layered MoS_2 nanosheets with rich active sites for enhanced visible light photocatalytic activity, RSC Adv. 8 (2018) 26664–26675. https://doi.org/10.1039/c8ra02560f.

[40] V. Fominski, M. Demin, V. Nevolin, D. Fominski, R. Romanov, M. Gritskevich, N. Smirnov, Reactive pulsed laser deposition of clustered-type mosx (X ~ 2, 3, and 4) films and their solid lubricant properties at low temperature, Nanomaterials. 10 (2020). https://doi.org/10.3390/nano10040653.

[41] Z. Liu, H. Lv, Y. Xie, J. Wang, J. Fan, B. Sun, L. Jiang, Y. Zhang, R. Wang, K. Shi, A 2D/2D/2D $Ti_3C_2T_x$@TiO_2@MoS_2 heterostructure as an ultrafast and high-sensitivity NO2 gas sensor at room-temperature, J. Mater. Chem. A. 10 (2021) 11980–11989. https://doi.org/10.1039/d1ta09369j.

[42] M. Terracciano, V. Galstyan, I. Rea, M. Casalino, L. De Stefano, G. Sbervegleri, Chemical modification of TiO_2 nanotube arrays for label-free optical biosensing applications, Appl. Surf. Sci. 419 (2017) 235–240. https://doi.org/10.1016/j.apsusc.2017.05.029.

[43] L. A, W. Xu, J. Zhao, C. Li, M. Qi, X. Li, L. Wang, Y. Zhou, Surface functionalization of TiO_2 nanotubes with minocycline and its in vitro biological effects on Schwann cells, Biomed. Eng. Online. 17 (2018) 1–20. https://doi.org/10.1186/s12938-018-0520-6.

[44] A. Kozbial, X. Gong, H. Liu, L. Li, Understanding the Intrinsic Water Wettability of Molybdenum Disulfide (MoS_2), Langmuir. 31 (2015) 8429–8435. https://doi.org/10.1021/acs.langmuir.5b02057.

[45] J. Guo, Y. Li, B. Jiang, H. Gao, T. Wang, P. Sun, F. Liu, X. Yan, X. Liang, Y. Gao, J. Zhao, G. Lu, Xylene gas sensing properties of hydrothermal synthesized SnO_2-Co_3O_4 microstructure, Sensors Actuators, B Chem. 310 (2020) 127780. https://doi.org/10.1016/j.snb.2020.127780.

[46] G. Yang, C. Cao, H. Zhong, Y. Cheng, W. Zhang, D. Wang, Construction of SnO_2 nanofibers @ MoS_2 nanosheets core-shell nanocomposites for high efficiency xylene detection, Colloids Surfaces A Physicochem. Eng. Asp. 659 (2023) 130813. https://doi.org/10.1016/j.colsurfa.2022.130813.

Chapter-4

$SrTiO_3$-TiO_2 heterostructured nanotube arrays for ultrafast ethanol sensing

4.1 Introduction

Ethanol is a breath marker for a variety of diseases like renal failure, schizophrenia, breast cancer, cardiopulmonary diseases and lung cancer etc. and change in the concentration of ethanol in exhaled breath give insight information about these diseases [1-3]. The reported mean concentration of ethanol in healthy people ranging from 0.013–1 ppm gets increased to >2.3 ppm in a disease affected person [2,3]. The concentration of ethanol in exhaled breath varies and depends upon the type of disease in a person [1]. As we know lower concentration of ethanol in breath is in ppb range with a huge number of interfering VOCs/gases and a significant amount of humidity (>50% RH) [3]. So, the detection of ethanol vapor for breath analysis application requires a highly sensitive, low ppb, low humidity interference and stable chemiresistive sensor system.

Conventional metal oxides are widely employed for the volatile organic compounds (VOCs) detection [4-10]. The fascinating physical and chemical properties of TiO_2 make it the most promising VOC sensing material [4-6]. TiO_2 has been explored in chemiresistive sensors for VOC like; ethanol [10, 11], acetone [12-15], heptane [16], and formaldehyde [17] for breath analysis application. Tian et al. synthesized sensing film [11] and Pan et al. synthesized [10] nanospheres based on TiO_2 fast and sensitive ethanol marker detection but the response and baseline resistance were significantly decreased from in the humidity ranging from 0% to 97% RH [11]. moreover, limited time stability, high working temperature (200–400 ˚C) and humidity interference inhibit the sensing characteristics [2-4,11,18,19]. In this regard, to overcome the effect of humidity different composites materials with TiO_2 such as MoS_2/TiO_2 [2], Au/TiO_2 [3], $TiO_2/CoTiO_3$ [4], and $Ti_3C_2T_x$-TiO_2 [19] have been explored but no significant improvement was observed in humidity tolerant properties of the sensors.

In this scenario, perovskite semiconductor oxides (ABO_3) can be a potential composite material for long-term sensing performance because of their stability in thermal and chemical atmospheres, high reaction temperature and superior reliability [6,7,18,20-22]. A range of perovskite materials (ABO_3) like $LaFeO_3$ [18], $ZnSnO_3$ [7,23,24], $LaRhO_3$ [22], $SrTiO_3$ [20,22, 25-28] have been widely explored in ethanol sensing application. Among various perovskite oxides, the strontium titanate ($SrTiO_3$) with the advantages of low-cost synthesis, easy defect modulation, wide bandgap, physicochemical stability and non-toxicity became a popular candidate for variety of applications [20, 28-32]. The high chemical and thermal stability of $SrTiO_3$ makes it a robust material for gas or VOC sensing [20-22, 25-28, 29-32]. Till now $SrTiO_3$ and its composites have been employed for the detection of different VOCs and gases such as H_2 [21, 26], ethanol [20, 22], O_2 [25,27] and ozone [33]. The studies reveal that the high sensitivity and fast response/ recovery time of $SrTiO_3$-based ethanol sensors could be due to the high defect density (oxygen vacancy) and high carrier mobility in $SrTiO_3$. Studies reveal that $SrTiO_3$ is a good candidate for coupling with TiO_2 and improves the electronic properties [32].

The hybrid of $SrTiO_3$ with TiO_2 nanotube array results in the replacement of Ti^{4+} by Sr^{+2} ions and leads to different type of defects in the resulting heterostructure [34,35]. These defects (oxygen vacancies) are possibly due to the insertion of Sr^{+2} on the Ti^{4+} octahedral site to balance the electric charge. The incorporation of a controlled amount of strontium can creates a relatively large number of defects which will significantly improve the ethanol sensing properties [33].

Motivated by these experimental findings and the theoretical predictions, we have fabricated $SrTiO_3$-TiO_2 heterostructured nanotube array, in order to trigger the humidity tolerant gas sensing ability of the TiO_2 nanotube array. TiO_2 nanotubes array was synthesized by using an electrochemical anodization route and $SrTiO_3$ heterojunction was grown on TiO_2 nanotubes by facial hydrothermal technique. The sensors based on $SrTiO_3$-TiO_2 heterostructured nanotube arrays with different concentrations of strontium (0.25- 25 mM) exhibited ultrafast response (0.4–3 s) towards ethanol under high humid ambient (80% RH) at 150 ˚C operating temperature. The sensor showed remarkable long-term stability with lower detection limit of 2.94 ppb, which makes it suitable for ethanol sensing for breath analysis application.

4.2 synthesis of $SrTiO_3$-TiO_2 heterostructured nanotube array

Annealed TiO_2 nanotubes/Ti sample was added in an aqueous solution of $Sr(OH)_2 \cdot 8H_2O$ under a Teflon-lined autoclave and underwent a hydrothermal reaction. In the current study, three different aqueous solutions of $Sr(OH)_2$, i.e., 0.25 mM, 2.5 mM, and 25 mM, were prepared and used for hydrothermal synthesis. During the synthesis, other reaction parameters like reaction time (18 h) and temperature (180 ˚C) were marked as a constant. The resulting samples were washed multiple times with water and absolute ethanol to remove impurities and dried in the air. Three sets of $SrTiO_3$-TiO_2 nanotubes (i.e., ST-0.25, ST-2.5 and ST-25), treated under different molarity of $Sr(OH)_2$ were thermally treated at 450 °C for 3 h in air. A schematic representation is provided in Fig. 4.1. indicating the fabrication steps of the $SrTiO_3$-TiO_2 heterostructured nanotube array sensors (S0-S3).

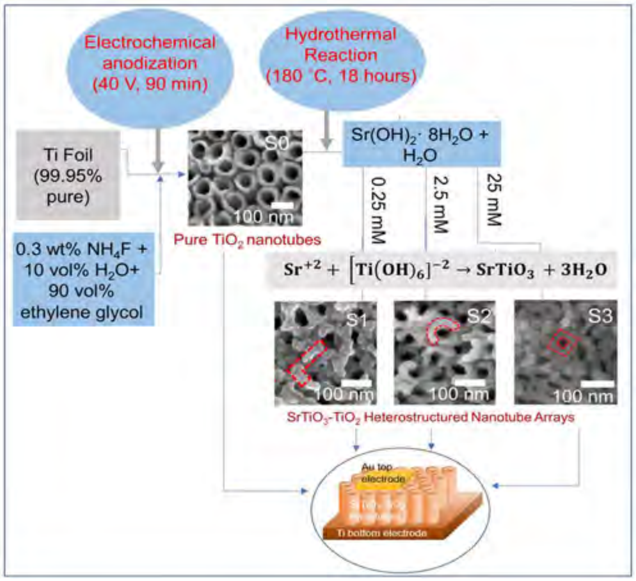

Fig. 4.1. Schematic illustration for the synthesis of $SrTiO_3$-TiO_2 heterostructured nanotube array and fabrication of metal-insulator-metal (MIM) structured sensors.

4.3 Synthesis mechanism

Electrochemical anodization reaction resulting from a combined effect of growth and dissolution of oxide for a long duration resulting in pits formation due to the fluoride complex $[TiF_6^{-2}]$. Reaction parameters like Ti metal, H_2O (acidic medium) and applied voltage (40 V) directly influence the growth of resulting oxide. And the insufficient supply of oxygen, defective or oxygen vacancy-rich TiO_2 nanotubes were formed. The detailed TiO_2 nanotube array (TNTA) growth mechanism based on the defects (oxygen and Ti vacancies) distribution model is discussed in our reported works [36,37].

The dissolution-precipitation mechanism explains the formation of $SrTiO_3$ on TiO_2 nanotube where the nanotubes are not only used as a precursor of titanium ions but also act as growth points for $SrTiO_3$ [34,35,38]. The process involves breaking the Ti-O bonds by the hydrolytic attack and

forming a soluble $[Ti(OH)_6]^{-2}$ intermediatory complex [34,35] as mentioned in Eq. 4.1.

$$TiO_2 + 2OH^- + 2H_2O \rightarrow [Ti(OH)_6]^{-2} \qquad (4.1)$$

Then, the Sr^{+2} ions interact with this reactive complex and result in the precipitation of $SrTiO_3$ (Eq. 4.2).

$$\mathrm{Sr^{+2} + [Ti(OH)_6]^{-2} \rightarrow SrTiO_3 + 3H_2O} \qquad (4.2)$$

The simultaneous dissolution of TiO_2 and precipitation of $SrTiO_3$ takes place in the vicinity of the tubes because the free $[Ti(OH)_6]^{-2}$ complex is absent away from the area. Therefore, the nucleation of $SrTiO_3$ mostly takes place on the top surface of the TiO_2 nanotubes. Initially, the porous and loosely packed $SrTiO_3$ layer is formed that cannot block the transportation of Sr^{+2} and OH^- completely. Later, the reaction elapsed due to thicker $SrTiO_3$ at the top of the nanotubes that eventually restrict the transportation and diffusion of ions to the reaction sites. This leads to a gradual decrease in the Sr concentration with depth revealed by the characterization results [38]. A thick layer of $SrTiO_3$ reduces the pore diameter of the nanotubes at the top.

The increase in the concentration of Sr precursor results in more Sr^{+2} production during the reaction showing a significant variation in morphology of the $SrTiO_3$-TiO_2 heterostructured nanotube array which is evidenced by FESEM results (Fig. 4.2(a-d)). When Sr concentration is increased, rapid dissolution and precipitation take place and more $SrTiO_3$ is preferentially and spontaneously nucleated and formed a thicker layer on the top surface and sidewall of nanotubes. The high rate of nucleation at the top surface totally blocks the transportation of reactive ions (Sr^{+2} and OH^-) towards the lower region of TiO_2 nanotubes which results in a gradient in $SrTiO_3$ concertation from the top to the bottom of the nanotubes.

4.4 Characterization

Morphological characterization

A highly oriented TiO_2 nanotubes array of inner pore diameter ~79 nm and length ~2.2 μm was synthesized by anodic oxidation (Fig. 4.2(a)). After hydrothermal treatment, the original nanotube array architecture was retained but the structure of individual nanotubes was changed as denoted in Fig. 4.2(b-d). The inner pore diameter of the $SrTiO_3$-TiO_2 heterostructured nanotube array decreased from 79 nm to 29 nm when moving from S0 to S3 and on the other hand, outer wall thickness increased significantly from 29 nm to 109 nm (inset of Fig. 4.2(a-d)). This was probably due to the volume expansion during the growth of $SrTiO_3$ on TiO_2 nanotubes [38]. The amount of $SrTiO_3$ growth on TiO_2 nanotube arrays was readily tuned by varying the $Sr(OH)_2{\cdot}8H_2O$ concentration at a steady reaction time (18 h) and temperature (180 ˚C) during hydrothermal treatment. Fig. 4.2(b) is showing the formation of small buds or "L" shape structured $SrTiO_3$ at the exterior of TiO_2 nanotubes showing the partial growth of $SrTiO_3$ due to template effects [35]. In

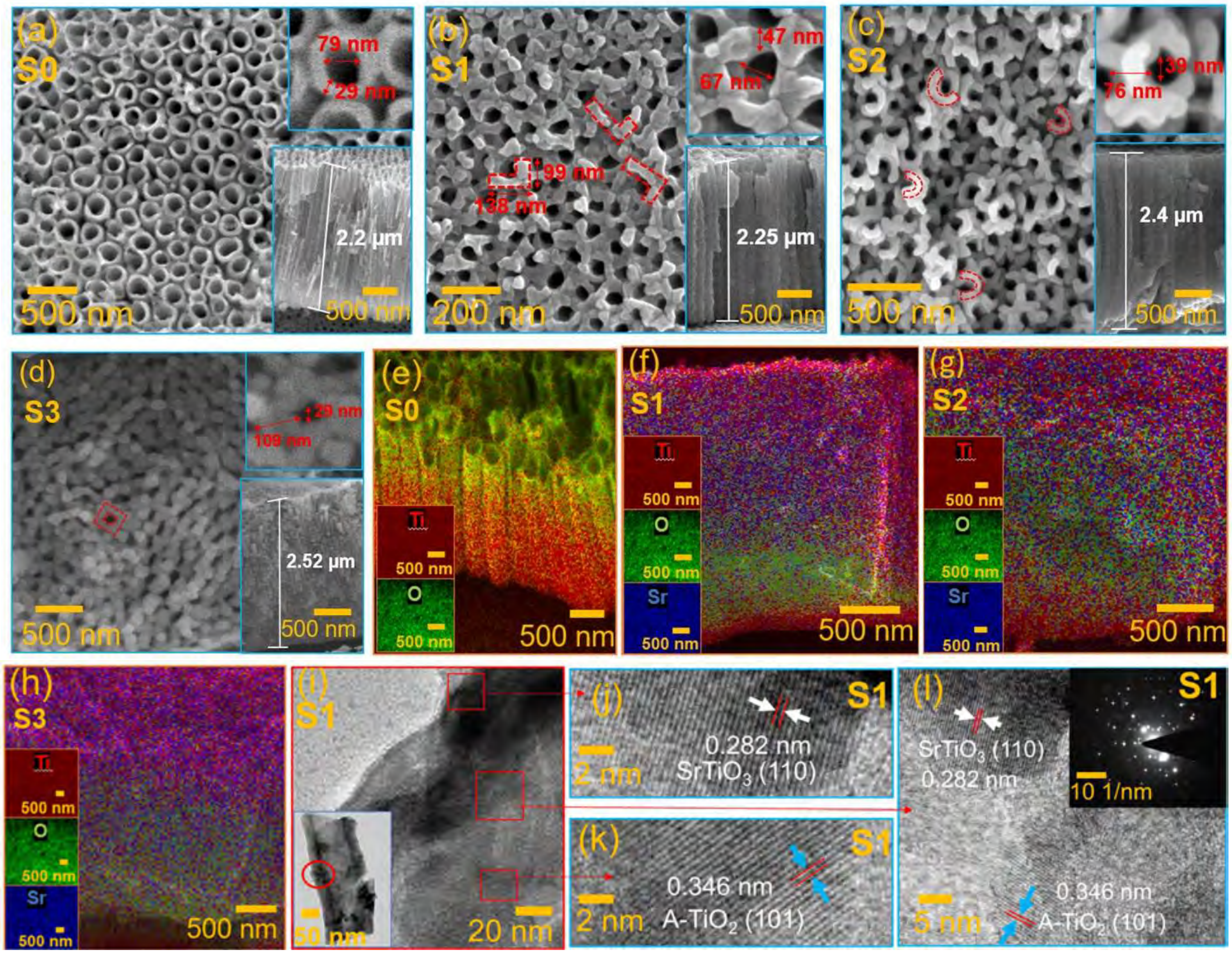

Fig. 4.2. FESEM images of (a) pure TiO_2 nanotube array, $SrTiO_3$-TiO_2 heterostructured nanotube array synthesized with (b) 0.25 mM, (c) 2.5 mM and (d) 25 mM $Sr(OH)_2$ solution. The side view of the nanotubes is shown in the inset of Fig. 4.2(a-d). EDS elemental analysis of (e) S0, (f) S1, (g) S2 and (h) S3. HRTEM and TEM image (inset) of (i) S1 and the lattice spacing of (j) anatase TiO_2, (k) $SrTiO_3$ and (l) both anatase and $SrTiO_3$ in a single sample to justify the existence of $SrTiO_3$-TiO_2 heterostructured nanotube array. SAED pattern is shown in the inset of Fig. 4.2(l).

EDS data of S0-S3 samples showing the non-uniform distribution of Ti, Sr and O to the length of S2, the self-alignment of L-shaped STO takes place which results in the semi-circle nanocubes formation on the surface of the nanotubes (Fig. 4.2(c)). Finally, in S3, the STO crystals become the larger enough to comparable the nanotube curvature and formed the self-aligned nanocubes (Fig. 4.2(d)). Fig. 4.2(b-d) showing the enough nucleation and different type of STO growth on defect sites of the TiO_2 surfaces depending on the $Sr(OH)_2{\cdot}8H_2O$ concentration. the nanotubes (Fig. 4.2(e-h)). The maximum Strontium and oxygen contents are found at the top of the nanotubes and gradually decrease towards the bottom (i.e., Ti substrate). The Sr content is also improved with an increase in the Sr concentration from samples S1-S3 (Fig. 4.2(f-h)). Therefore, the Sr and oxygen deficiency levels were increased towards the bottom of the tubes (Fig. 4.2(e-h)).

Fig. 4.2(i) shows the HRTEM image and the inset image shows the TEM image of a part of $SrTiO_3$-TiO_2 heterostructured nanotube (S1). The HRTEM images show the side wall and inner part of the tube which is signifying the presence of both $SrTiO_3$ and TiO_2 in the nanotube (Fig. 4.2(i)). Later on, Fig. 4.2(j-l) show high-resolution TEM (HRTEM) images and the selected area electron diffraction (SEAD) pattern (inset of Fig. 4.2(g)) of the $SrTiO_3$-TiO_2 heterostructured nanotube array (S_1). The 0.346 nm lattice spacing was indexed to (101) crystal plane of A-TiO_2 in Fig. 4.2(j). Fig. 4.2(k) shows the lattice fringes of $SrTiO_3$ nanocubes with a lattice spacing of 0.282 nm which corresponds to the (110) crystal plane of cubic phase $SrTiO_3$. Fig. 4.2(l) reveals the existence both $SrTiO_3$ and TiO_2 crystallinity in a single sample and it confirms the formation of $SrTiO_3$-TiO_2 heterostructured nanotube array. The SEAD pattern in the inset o Fig. 4.2(l) is showing the discrete spots for $SrTiO_3$-TiO_2 heterostructured nanotube array that authenticates the superior crystalline nature after the growth of $SrTiO_3$ on TiO_2 nanotubes.

Structural characterization

Fig. 4.3(a) showing XRD data which disclose the crystalline nature of the TiO_2 and $SrTiO_3$-TiO_2 heterostructured nanotube array. The highest intensity (101) peak at 24.5° is related to anatase TiO_2 and a few low-intensity anatase peaks are observed in all the samples (S0–S3) (JCPDS File No. 21-1272) [1,5]. The peak at 27.4° is related to rutile (110) crystallinity observed in S0-S2 samples and disappears in the highest strontium concentrated sample (S3) (Fig. 4.3(a)). The Ti substrate peaks were also observed in all S0-S3 samples. The strong peak for cubic $SrTiO_3$ is observed at 32° indicating the crystal plane of (110) (JCPDS File No. 89-4934) [20,38]. A few low-intensity peaks originated from $SrTiO_3$ are observed at 38.6°, 46.6°, 53°, 57.7° and 67° indicating the (111), (200), (210), (211) and (220) planes (JCPDS File No. 89-4934), respectively [20,38]. The intensity

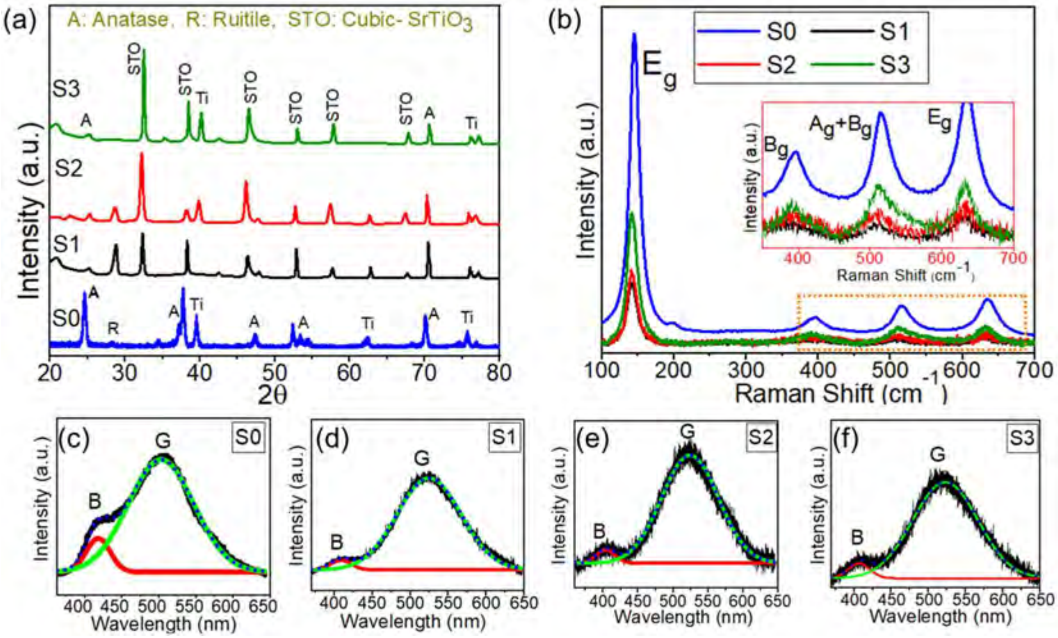

Fig. 4.3. (a) XRD, (b) Raman spectra of four different samples with different levels of Sr content and PL spectra of all four samples i.e. (c) S0 (as grown); (d) S1 (0.25 mM Sr content); (e) S2 (2.5 mM Sr content) and (f) S3 (25 mM Sr content).

of anatase (101) peak gets reduced and the intensity of STO (110) peak gets increased with increase of Sr concentration in samples (Fig. 4.3(a)). The increase in $SrTiO_3$ peaks intensity relative to TiO_2 peaks confirms the high rate of Sr^{2+} exchange and formation of more crystalline $SrTiO_3$ [32,38].

The Raman spectra of pure TiO_2 nanotubes (S0) showed four bands at 145 cm^{-1} (E_g), 395.2 cm^{-1} (B_g), 514.6 cm^{-1} ($A_g + B_g$) and 634.4 cm^{-1} (E_g) (Fig. 4.3(b)). In $SrTiO_3$-TiO_2 samples, due to the interaction of Sr^{+2} with TiO_2 lattice, E_g peak was shifted towards the lower wavenumbers [5, 39]. The redshift in E_g confirms better crystallinity in $SrTiO_3$-TiO_2 heterostructured nanotube arrays which is in good agreement with the XRD results. The enlarged Raman spectra in the inset of Fig. 4.3(b), show the broadening of the band at 395.2, 514.6 cm^{-1} and 634.4 cm^{-1} due to the overlapping of $SrTiO_3$ first-order Raman-active modes [39]. The Raman modes i.e., E_g, B_g and $A_g + B_g$ (inset of Fig. 4.3(b)) in $SrTiO_3$-TiO_2 samples (S1-S3) showed a slight increase in Raman intensity because of the strain effect of the oxygen vacancies in $SrTiO_3$ [39].

The PL spectra in Fig. 4.3(c-f) were used to identify the defect density in $SrTiO_3$ modified TiO_2 nanotube samples. The two main peaks; one in the UV region centered at ~410 nm and the second one at ~505 nm are related to the band gap emission (B) and deep level emissions (G), respectively [5,40]. The first peak is related to the electronic transition from the conduction band to the valence band and the second peak in the green region is attributed to the band-edge free excitons and bound excitons that represent the surface defects and oxygen vacancies related trap assisted Recombination [5,40]. The results are clearly showing the improvement in oxygen vacancies content in Sr modified samples (S1-S3) compared to the pure TiO_2 nanotube array sample (S0). The relative area of both B and G- peaks were calculate by using Gaussian fitting and summarized in Table 4.1 for all the four samples (S0–S3).

Table 4.1. Comparison of relative area change in O 1s spectra of the S0-S3 samples by XPS and photoluminescence study.

	XPS			Photoluminescence	
Sample	%Area (O_L)	%Area (O_V)	%Area (O_C)	% Area (B)	% Area (G)
S0	69	20.6	10.4	9.8	90.2
S1	46	25.2	28.8	3.2	96.8
S2	52	17.5	30.5	3.9	96.1
S3	70	11	19	4.9	95.1

Chemical characterization

The XPS spectra of Ti 2p, Sr 3d and O 1s in Fig. 4.4(a-c) are given to identify the chemical states of the samples. In Ti 2p spectra, two peaks centered at 458.8 eV and 464.6 eV are related to Ti $2p_{3/2}$ and Ti $2p_{1/2}$, respectively (Fig. 4.4(a)). These two peaks were then further deconvoluted into 4 peaks which are Ti^{3+} $2p_{3/2}$ (458.7 eV), Ti^{4+} $2p_{3/2}$ (459.6 eV), Ti^{3+} $2p_{1/2}$ (464 eV) and Ti^{4+}

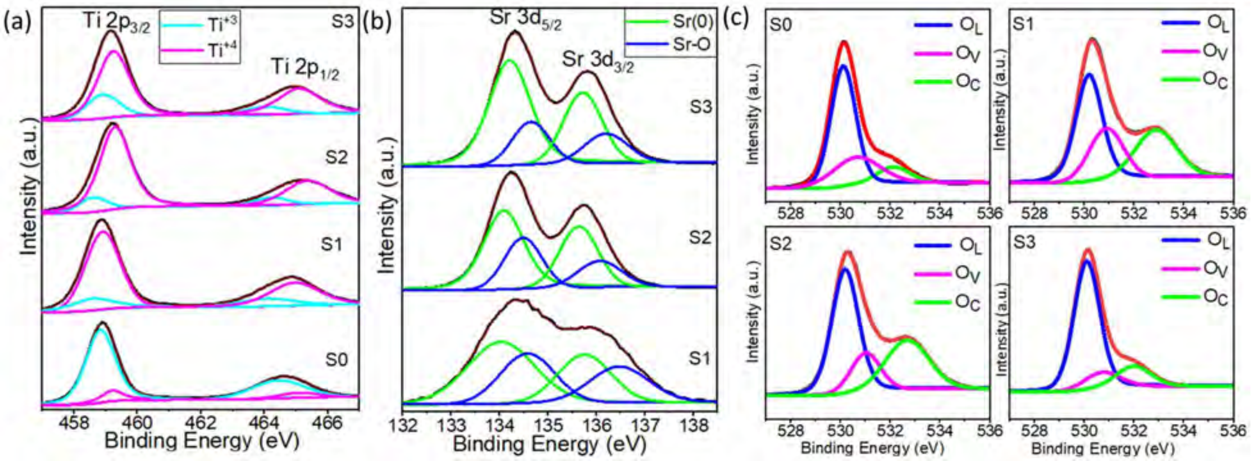

Fig. 4.4. XPS spectra of S0-S3 samples; (a) deconvoluted Ti(2p) spectra; (b) deconvoluted Sr 3d spectra; (c) deconvoluted fitted peaks of XPS O(1s) spectra.

$2p_{1/2}$ (465.1 eV) [40,41]. In S0, the intensity and area of Ti^{+3} peaks are significantly higher than Ti^{+4} peaks confirming the oxygen-deficient nature of the pure TiO_2 nanotube array. Whereas, in $SrTiO_3$-TiO_2 heterostructured nanotube array samples, oxygen deficiency is diminished and Ti^{4+} peaks are dominated over Ti^{+3} (Fig. 4.4(a)). Among all the $SrTiO_3$ modified samples, S1 showed the lowest oxygen vacancy and S3 showed the highest oxygen vacancy as evidenced by Ti 2p spectra. The Sr 3d spectra (Fig. 4.4(b)) showed two major peaks of Sr $3d_{5/2}$ and Sr $3d_{3/2}$ at 133.6 eV and 135.3 eV, respectively. They are showing the bonding of Sr atoms in the $SrTiO_3$ perovskite structure. The Sr $3d_5$ peaks are de-convoluted into four peaks as Sr-0 $3d_{5/2}$ (133.9 eV), Sr -O $3d_{5/2}$ (134.4 eV), Sr-0 $3d_{3/2}$ (135.5 eV), Sr-O $3d_{3/2}$ (136.3 eV), which demonstrate the existence of perovskite and non-perovskite bonding in $SrTiO_3$ [42,43]. The intensity and area of non-perovskite bonding (Sr- OH, Sr-Sr, and Sr-O) of $SrTiO_3$ were highest in S1 and minimum in the S3 sample as shown in Fig. 4.4(b). The O 1s spectra in Fig. 4.4(c) was deconvoluted into three peaks related to the lattice oxygen (O_L), oxygen vacancies (O_V) and surface-chemisorbed oxygen (O_C) at 530.3 eV, 531.7 eV and 533 eV respectively, as shown in Fig. 4.4(c). The relative percentage of three peaks for S0-S3 is summarized later in the sensing mechanism section [44].

Surface wettability study

The static contact angle of all four sensing layers was measured (Fig. 4.5(a-d)) and found to be 68°, 76.5°, 84° and 108° for S0-S3, respectively. However, the results confirm the improvement of the hydrophobic nature as the Sr content increased from the sample S1-S3. The enhanced

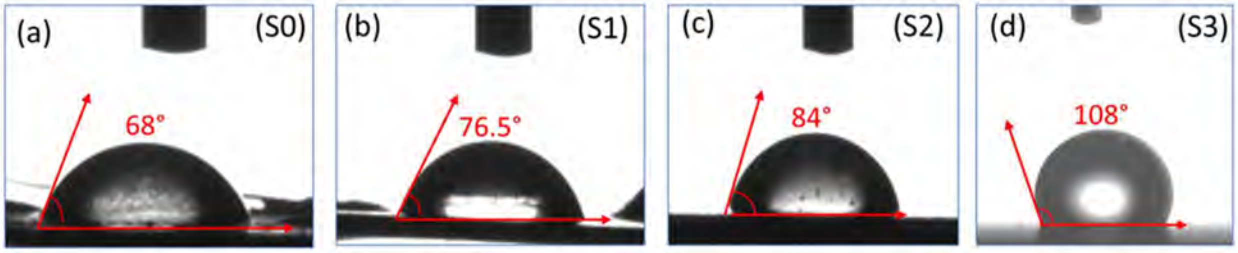

Fig. 4.5. The static water contact angles of the sensing film of S0-S3 samples.

water contact angle might be attributed to the $SrTiO_3$ addition on TiO_2 nanotubes. The high contact angle makes the water molecules harder to adsorb to the surface of the sensor and the hindrance of sensing performance due to humidity is minimized.

4.5 Sensor study

VOC sensing

To optimize the effective working temperature, we have compared the response of S0-S3 sensors for a range of temperatures (50- 250 ˚C) towards 50 ppm of ethanol and at 80% RH (Fig. 4.6(a)).

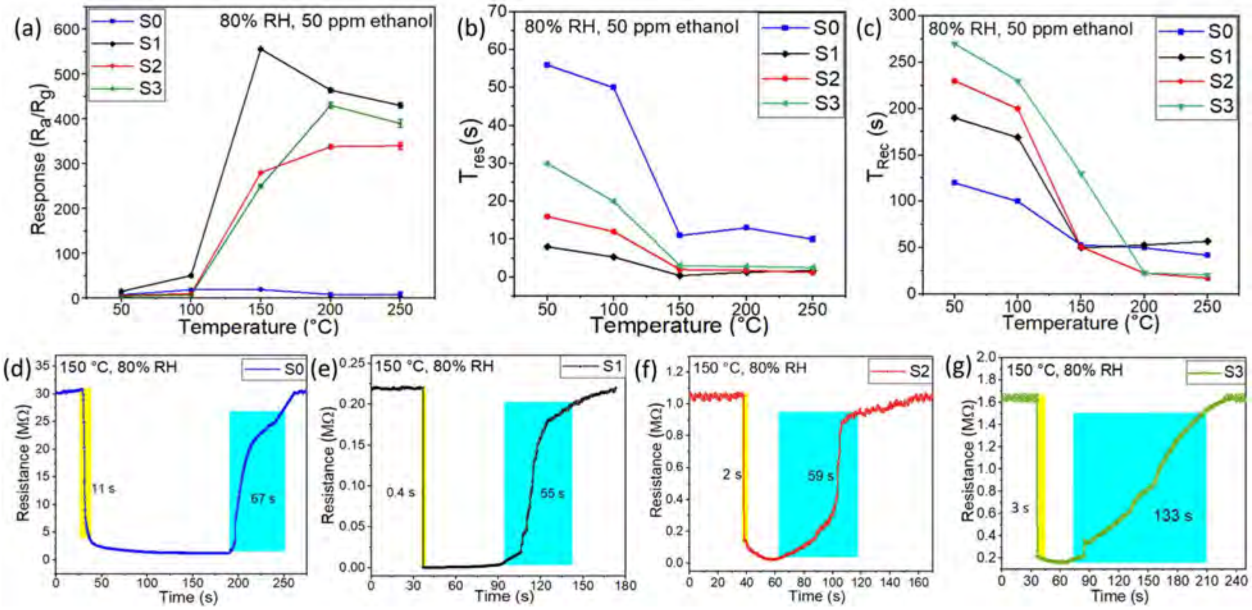

Fig. 4.6. (a) Response magnitude; (b) response time; (c) recovery time; as a function of temperature in 50 ppm of ethanol for all four sensors; response and recovery curves of sensors based on (d) S0 (as grown); (e) S1 (0.25 mM Sr content); (f) S2 (2.5 mM Sr content) and (g) S3 (25 mM Sr content) to 50 ppm ethanol at 150 ℃ and 80% RH.

All the sensors showed an increment in response magnitude with an increase in temperature (Fig.4.6(a)). Overall, the Sr modified sensors showed the best response values at a relatively higher temperature than S0 (Fig. 4.6(a)) possibly due to the high thermal stability nature of perovskite semiconductors. Among all the sensors, S1 exhibited the highest response magnitude of 556 at 150 ˚C which is approximately 29 times higher than the S0 sensor. Apart from S1 and S2, S3 showed a significantly higher response magnitude of 280 and 250 at 150 ˚C, respectively than the S0 sensor (Fig. 4.6(a)). This higher sensitivity in S1-S3 is possibly due to the improved specific surface area and abundant surface defects contributed by the Sr modification on TiO_2 nanotubes (Fig. 4.6(a)).

The response/recovery time is a critical parameter that can be affected significantly by the temperature condition. Fig. 4.6(b, c) show the response and recovery times of the S0-S3 sensors towards 50 ppm ethanol under the temperature range of 50-250 ˚C at 80% RH. At high operating temperatures, the availability of sufficient energy enables easy dissociation of VOC analytes that makes the surface adsorption and desorption faster which results in the quick response and recovery for all the sensors (Fig. 4.6(b, c)). S1 with the highest response showed the shortest response time whereas S0 showed the highest response time at all temperature conditions (Fig. 4.6(b)). S2 and S3 showed relatively high response time than S1 but faster than S0 (Fig. 4.6(b)). At high temperatures (150-250 ˚C), recovery of the S2 and S3 was faster than the S1 and S0 (Fig. 4.6(c)). The ultrafast response of the strontium-modified sensor (S1-S3) is mainly attributed to the high surface oxygen functionality and the porous structure of the resulting tubes. At 150 ˚C, all the sensors achieved almost equal recovery times (Fig. 4.6(c)). After considering, all three parameters i.e. response magnitude, and response/recovery time, 150 °C was considered the optimized temperature for studying other sensing characteristics like repeated cycle, transient response, selectivity, and humidity study.

Fig. 4.6(d-g) shows the ultra-fast response characteristics of the sensors towards 50 ppm ethanol at 150 °C and 80% RH. The response/recovery time was measured s for pure TiO_2 nanotubes (S0) as 11 s/ 67 s which was then improved significantly in case of $SrTiO_3$-TiO_2 heterostructured nanotube array (0.4 s/ 55 s) as shown in Fig. 4.6(d, e). Response time was appreciably fast in the case of S2 (2 s) and S3 (3 s) but the recovery time was measured maximum for S3 (133 s) (Fig. 4.6(f, g)). Undoubtedly, the formation of the $SrTiO_3$ layer on TiO_2 nanotubes improved the response characteristics of the sensors. The excess use of $SrTiO_3$ (2.5 mM and 25 mM $Sr(OH)_2$) on TiO_2 nanotubes slower the response/recovery time as compared to the S1. The large amount of $SrTiO_3$, may change the conduction properties of the composite or hinder the interaction between the composite and ethanol molecules. A significant reduction of the porosity of the tubes

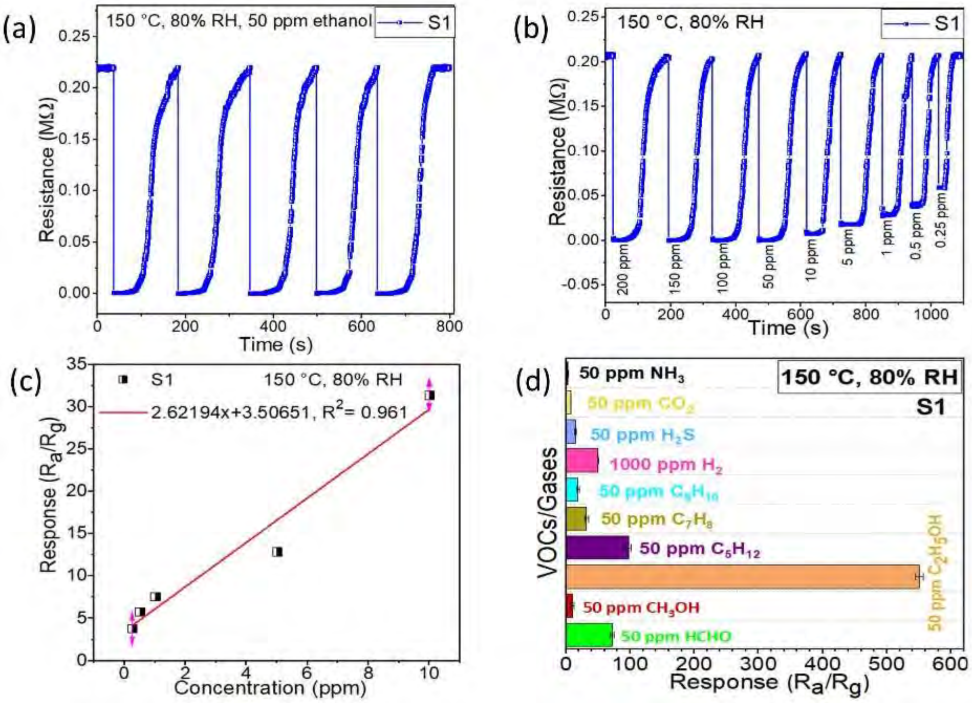

Fig. 4.7. (a) Five response and recovery curves of the S1 sensor based on 0.25mM Sr content at 50 ppm ethanol, and 150 °C and 80% RH; the dynamic response curves of S1 sensor versus ethanol concentration in the range of (b) 0.25 – 200 ppm; (c) response-concentration fitting curve of the S1 sensor at 0.5 – 10 ppm ethanol; (d) gas responses of S1 sensor for various target VOCs/gases of 50 ppm at 150 °C and 80% RH.

eventually increases the response/recovery time of the S2 and S3. Therefore, the S1 sensor is used for further discussion in the following section due to its highest response and ultra-fast response and recovery time among all the samples.

As depicted in Fig. 4.7(a), the S1 sensor showed good repeatability with several cycles of response-recovery curves in 50 ppm ethanol at 150 ˚C and 80% RH. The response toward 50 ppm ethanol exhibited a rapid decrement in resistance that corresponds to a typical n-type semiconductor behavior. The presence of the $SrTiO_3$ improved the conductivity, thermal and chemical stability of the composite and additionally the porous and functionalized surface facilitate the reaction with ethanol [20,33,45].

The dynamic characteristics of the S1 sensor towards different concentrations (0.25– 200 ppm) of ethanol were measured at 150 ˚C with 80% RH and shown in Fig. 4.7(b). The response of the S1 sensor was increased linearly with the increase in ethanol concentration and was found to be saturated between 100 ppm to 200 ppm. S1 showed a promising response at the sub-ppm level of ethanol vapor. The minimum concentration of 250 ppb was detected by S1 with an appreciably high response of ~3.79 (Fig. 4.7(c)). With an increase in ethanol concentration, the response magnitude was increased almost linearly and the response magnitude of ~12.9 was measured at 5 ppm. Sensor (S1) response was increased further from ~31.4 (10 ppm) to ~550 (50 ppm) and saturated at the response magnitude of 552 for ≥ 100 ppm (Fig. 4.7(b, c)). Notably, the response values are in a good linear relation with ethanol concentrations varying from 10 to 0.25 ppm ($R^2 = 0.961$, $y = 2.62194x+3.50651$) (Fig. 4.7(c)). The limit of detection (LOD) for the S1 sensor was 2.94 ppb ethanol which was calculated from an improved IUPAC method [46].

The cross-sensitivity of the S1 sensor was also measured by testing the sensor in 50 ppm of various gases/VOCs (e.g., HCHO, CH_3OH, C_2H_5OH, C_5H_{12}, C_7H_8, C_8H_{10}, H_2S, CO_2, NH_3 and 1000 ppm H_2 at 150 ˚C in presence of 80% RH, as shown in Fig. 4.7(d). The selectivity results confirmed the extremely high selectivity of the S1 sensor towards ethanol compared to other analytes. The result ascribed to the abundant active sites and oxygen functionalized surface of the $SrTiO_3$-TiO_2 heterostructured nanotube array, which was beneficial to the adsorption of ethanol molecules [20]. The required dissociation energy, acidity, size of the molecules, sticking coefficients, etc. played a significant role in showing the natural selectivity of S1 sensors towards ethanol [5]. The selectivity towards ethanol of the S1 sensor was attributed to the increase in oxidation states due to $SrTiO_3$ modification on the TiO_2 nanotube array. These states actively participate in the different catalytic activities and results in more oxidation of ethanol vapor. Additionally, abundant active sites or defects and oxygen functionalized surface of $SrTiO_3$-TiO_2 heterostructured nanotube array is beneficial to the adsorption of ethanol molecules [20]. The required dissociation energy, acidity, size of the molecules, sticking possibilities of ethanol was in favor with $SrTiO_3$-TiO_2 heterostructured nanotube array that played a significant role to show the natural selectivity towards ethanol [5]. Apart from this, the lowest selectivity towards the larger sized VOCs like C_5H_{12}, C_7H_8 and C_8H_{10} is due to the hindrance during entering and diffusion on sensing layer [5, 20].

Humidity and long-term stability study

The effect of different levels of relative humidity (dry air- 80% RH) on response characteristics of the S1 sensor in the exposure of 50 ppm ethanol is shown in Fig. 4.8(a). Response/recovery time for S1 was measured as 0.4s/44s, 0.4s/50s, 0.4s/52s, 0.4s/53s and 0.4s/ 55s in the presence

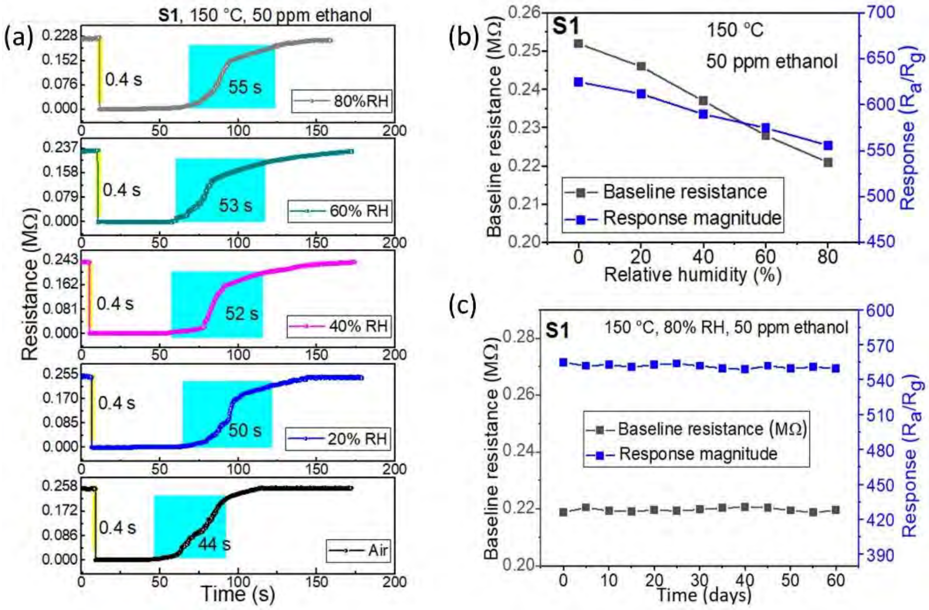

Fig. 4.8. (a) Dynamic resistance changes of S1 sensor toward 50 ppm ethanol at a range of humid environments; (b) change of baseline resistance and response magnitude with an increase of relative humidity at 150 ˚C; (c) long-term stability of S1 sensor in high humid atmosphere (80% RH) toward 50 ppm ethanol at 150 ˚C.

of 20%, 40%, 60% and 80% RH in 50 ppm ethanol at 150°C (Fig. 4.8(a)). Moreover, no significant change in response and recovery time was noticed due to the change in RH levels. The humidity mechanism involves the competitive adsorption between water molecules and ethanol molecules on the interaction sites of the sensor. The water molecules interact with the chemisorbed oxygen species and block the number of ethanol interaction sites which results in a decrease in baseline resistance and as well response magnitude [47, 48]. The effect of environmental humidity on the response and baseline resistance of the S1 sensor was investigated (Fig. 4.8(b)). The baseline resistance was decreased from 0.252 MΩ to 0.221 MΩ and the response magnitude was reduced from ~625 to 556 with an increase of RH from 0 (dry air) to 80% RH air. So, a 1% RH change can show a 0.862 change in response magnitude (Fig. 4.8(b)). This amount of change in response comes when the ethanol concentration is 0.0775 ppm. Moreover, 1% RH has a similar effect which comes with 0.0775 ppm ethanol for the sensor S1.

In order to further examine the long-term stability of the S1 sensor in high humidity conditions, the sensor undergoes a response test for 60 days and the response was measured at an interval of 5 days in 80% RH. The baseline resistance and response towards 50 ppm ethanol at 150 ˚C with 80% RH as shown in Fig. 4.8(c). The baseline resistance and response magnitude of S1 sensor showed a negligible attenuation. The results indicate good stability with the promising thermal and chemical stability of $SrTiO_3$ material [45, 49].

4.6 Sensing mechanism

The rapid response of the $SrTiO_3$-TiO_2/Ti heterostructured nanotube array benefited from the combined effect of defect modulation by $SrTiO_3$ and $SrTiO_3$-TiO_2 heterojunction. The response/recovery time of the sensor is strongly influenced by the adsorption/desorption behavior of gas molecules on the sensing layer and the Langmuir model also explains the adsorption rate of analytes in proportion to the number of vacant sites [50-52]. In $SrTiO_3$-TiO_2/Ti heterostructured nanotube array, $SrTiO_3$ increases the defects in terms of oxygen vacancies and chemisorbed oxygen (Table 4.1) that significantly modulate the activation energy and results in faster adsorption of ethanol on the sensing layer [50, 51]. The surface reaction is also dependent on the oxidation states of the sensing layer which directly influences the sensing performance [48]. In the current study, modification of TiO_2 nanotubes with $SrTiO_3$ caused a significant change in the defects density (such as oxygen vacancies) which dominantly modified the electronic properties of the composite material. $SrTiO_3$ was capable of modulating the chemical and physical properties of TiO_2 by introducing defective crystal structures with oxygen vacancy-type defects [47, 49].

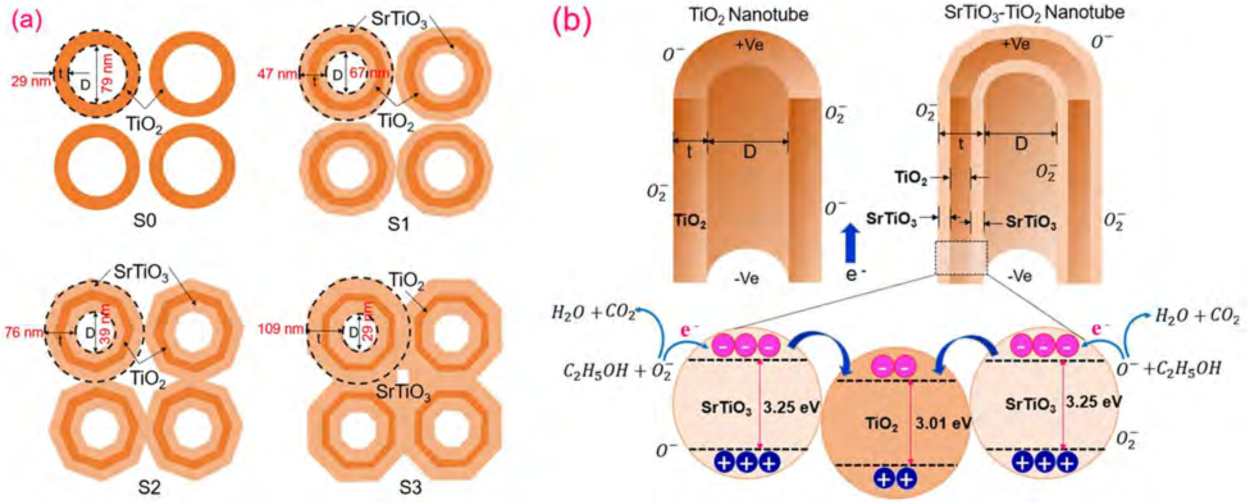

Fig. 4.9. A schematic representation of (a) change in pore size and wall thickness of four different nanotubes (S0-S3), (b) band structure of $SrTiO_3$-TiO_2 heterojunction and proposed charge transfer mechanism in the exposure of ethanol.

Therefore, the surface of the $SrTiO_3$-TiO_2 composites had more adsorbed oxygen that actively participated in the gas-sensing reaction and improved the VOC sensing characteristics.

The O 1s spectra (XPS scan in Fig. 4.4(c)) were studied in detail to estimate the enhancement in the surface oxygen and oxygen vacancy in TiO_2 nanotube arrays after the $SrTiO_3$ modification in sensors. The Gaussian component O_L (lattice oxygen) is attributed to O^{2-} ions in the TiO_2-$SrTiO_3$ bulk region, the middle peak for oxygen vacancies (O_V) is associated with O^- ions in oxygen-deficient regions due to the surface defects and the peak at higher binding energy for chemisorbed oxygen species (O_C) attributed to surface adsorbed oxygen ions (O_2^-) and dissociated oxygen species as mentioned in characterization results [48,53,54]. The percentages of O_L, O_V, and O_C components are 69 %, 20.6 %, and 10.4 %, respectively, in the pure TiO_2 nanotubes, while the O_V and O_C are enhanced in all the $SrTiO_3$ modified TiO_2 nanotubes as shown in Table 4.1. Among all the four samples, S1 exhibited the lowest bulk oxygen (46%) and highest area for the combined peaks of oxygen vacancy (25.2 %) and chemisorbed oxygen (28.7 %). On the other hand, S2 showed 52% bulk oxygen and the highest amount of surface oxygen (30.5%). However, S3 was lacking in terms of surface (19%) and oxygen vacancy (11%) components but still showed better than the pure TiO_2 nanotube sample. Similar results were also observed in photoluminescence spectra after calculating the percentage area of two fitted peaks i.e., B-peak and G-peak (Table 4.1). Pure TiO_2 nanotube exhibited the highest band-to-band recombination (9.8%) and lowest defect-assisted recombination (90.2%). The defect-assisted recombination was maximum in S1 (96.8%) and decreased gradually in S2 (96.1%) and S3 (95.1%). So, the PL results support the finding from XPS spectra and indicate the highest defective nature of the S1 sample. The mechanism behind higher oxygen vacancies as well as surface defects in $SrTiO_3$-modified samples is due to the substitution of some Ti^{4+} by Sr^{2+} ions that yield mobile oxygen vacancies (Vö) in order to balance the electric charge on the surface [34,35]. The optimization concluded that controlled Sr modification is responsible for improved surface defects in pure TiO_2 nanotube array that increased the O_V and O_C components which could provide more active sites for the interaction of targeting VOCs on the surface of the $SrTiO_3$-TiO_2 composites and thus lead to an ultrafast gas sensing performance.

The FESEM image in Fig. 4.2 confirms the gradual decrease of pore size and increase of wall thickness due to the incremental growth of $SrTiO_3$ in S1 to S3 and the same observation is represented in Fig. 4.9(a). The effective surface area was reduced from S1 to S3 due to the excess growth of $SrTiO_3$ on the TiO_2 nanotube. Pure TiO_2 nanotubes are wall separated in nature that makes the outer surface exposed to the ambient. Horizontal growth of $SrTiO_3$ on the TiO_2 nanotube diminishes the wall separation as well as the pore size (Fig. 4.2(b-d)). On the other hand, the growth of $SrTiO_3$ on TiO_2 nanotubes formed heterojunctions that improved the ethanol sensing behavior [5, 21]. The electron affinity of TiO_2 and $SrTiO_3$ is 5.1 eV [5] and 4.0 eV [21], respectively and the optical bandgap of $SrTiO_3$ (~3.3 eV) [31] is slightly higher than the TiO_2 (~3.2 eV) [2]. So, the conduction band electrons must be transferred from $SrTiO_3$ to TiO_2 to reach equilibrium. The highly defective surface of $SrTiO_3$ enhanced the dissociative adsorption of the ambient oxygen which further interacted with ethanol molecules during sensing. The oxidation of ethanol by the chemisorbed oxygen species (O_2^-, O^-etc.) is responsible for the injection of the additional electron to the conduction band of $SrTiO_3$ and the extra electron are then transferred to the conduction band of TiO_2 as shown in Fig. 4.9(b). The core portion of the TiO_2 is mostly taking part in vertical electron transport between two electrodes [5,37]. The conductivity of the TiO_2 core is altered significantly in air and in reducing ambient showing the overall change in sensor resistance. So, the formation of $SrTiO_3$-TiO_2 heterojunction enhanced the electron exchange in the core part of the TiO_2 nanotubes that eventually enhance the sensitivity of the sensors. Effective surface area also plays a pivotal role in gas/VOC sensing and due to excess growth of $SrTiO_3$ on TiO_2 nanotubes restricts the exposure of the outer and inner surface of the nanotube to the ambient. So, the formation of $SrTiO_3$-TiO_2 heterojunction enhances ethanol sensing. But, horizontal growth of $SrTiO_3$ on TiO_2 nanotubes reduces the effective surface area reducing the interaction with the target species. Due to the combined effect of both the phenomenon, S1 sensor, with moderate growth of $SrTO_3$ exhibited an exceptionally high response towards ethanol. The response was reduced gradually in S2 and S3 possibly due to the excess growth of $SrTiO_3$ on TiO_2 nanotubes. So, the current study confirms that the growth of an appropriate amount of $SrTiO_3$ can improve the sensing capabilities of the material.

4.7 Conclusion

In the current chapter, ultrafast and highly stable sensors were developed by establishing $SrTiO_3$-TiO_2 nanostructures-based composite for the detection of ethanol till ppb level for breath analysis application. An anodic growth of anatase TiO_2 nanotubes array on Ti substrate which was then treated with one-step hydrothermal by using aqueous solution of $Sr(OH)_2 \cdot 8H_2O$ precursors (0.25-25 mM) to synthesized $SrTiO_3$-TiO_2 heterostructured nanotube arrays. The surface morphology and growth of the grains at the exterior wall of the TiO_2 nanotube arrays were found to be different for each concentration of the $Sr(OH)_2 \cdot 8H_2O$ precursors. The addition of $SrTiO_3$, a high number of defects was generated due to the substitution of some Ti^{4+} by Sr^{+2} ions that ultimately assisted in more absorption and fast capture of ethanol analytes. Owning to the advantages in the structure and electronic characteristics, the $SrTiO_3$-TiO_2 sensor showed extraordinary sensing properties towards ethanol 150 ˚C optimum temperature and 80% RH. Overall, $SrTiO_3$-TiO_2 sensor with ultra-high response (~556/50 ppm) in smallest response time of 0.4 s under a highly humid atmosphere is a great finding for ethanol marker detection for breath analysis. The very low detection limit (2.94 ppb) of sensor towards ethanol makes it highly applicable for breath analysis application. In breath analysis the long-term stability is essential for reliability of the sensor and $SrTiO_3$-TiO_2 sensor showed excellent stability with negligible attenuation in sensos signal. The sensing performance was slightly unstable in different humid atmospheres (20%-80% RH). The highly stable sensing properties and up to mark humidity resistant nature of TiO_2 nanotubes after the $SrTiO_3$ addition gives an indication to explore $SrTiO_3$ in more detail to develop it an exceptionally good humidity tolerant sensing material for breath analysis application.

References

[1] S. Das and M. Pal, “Review — Non-Invasive Monitoring of Human Health by Exhaled Breath Analysis : A Comprehensive Review Review — Non-Invasive Monitoring of Human Health by Exhaled Breath Analysis : A Comprehensive Review,” 2020, doi: 10.1149/1945-7111/ab67a6.

[2] J. D. Fenske, S. E. Paulson, J. D. Fenske, and S. E. Paulson, “Human Breath Emissions of VOCs Human Breath Emissions of VOCs,” vol. 2247, no. 1999, 2011, doi: 10.1080/10473289.1999.10463831.

[3] D. Wang, D. Zhang, and Q. Mi, “A high-performance room temperature benzene gas sensor based on $CoTiO_3$ covered TiO_2 nanospheres decorated with Pd nanoparticles,” *Sensors Actuators B Chem.*, vol. 350, no. June 2021, p. 130830, 2022, doi: 10.1016/j.snb.2021.130830.

[4] D. Wang, D. Zhang, and Q. Mi, “A high-performance room temperature benzene gas

sensor based on $CoTiO_3$ covered TiO_2 nanospheres decorated with Pd nanoparticles," *Sensors Actuators B Chem.*, vol. 350, no. June 2021, p. 130830, 2022, doi: 10.1016/j.snb.2021.130830.

[5] T. Gakhar and A. Hazra, "Oxygen vacancy modulation of titania nanotubes by cathodic polarization and chemical reduction routes for efficient detection of volatile organic compounds," *Nanoscale*, vol. 12, no. 16, pp. 9082–9093, 2020, doi: 10.1039/c9nr10795a.

[6] V. S. Shinde, K. H. Kapadnis, A. P. Patil, and P. B. Koli, "Designing of $LaCrO_3 - TiO_2$ nanocomposites p: n heterojunction-based sensor material for the selective detection of volatile petrol vapors (PV) and CO_2 gas vapors," *J. Indian Chem. Soc.*, vol. 99, no. 3, p. 100367, 2022, doi: 10.1016/j.jics.2022.100367.

[7] S. Yan *et al.*, "Chemiresistive ethanol sensors based on $In_2O_3/ZnSnO_3$ nanocubes," *Sensors and Actuators Reports*, vol. 4, no. February, p. 100099, 2022, doi: 10.1016/j.snr.2022.100099.

[8] M. Ahmadipour *et al.*, "Detection of breath acetone by semiconductor metal oxide nanostructures-based gas sensors: A review," *Mater. Sci. Semicond. Process.*, vol. 149, no. November 2021, p. 106897, 2022, doi: 10.1016/j.mssp.2022.106897.

[9] A. K. Pathak *et al.*, "Recent Advances in Sensing Materials Targeting Clinical Volatile Organic Compound (VOC) Biomarkers: A Review," *Biosensors*, vol. 13, no. 1, 2023, doi: 10.3390/bios13010114.

[10] W. Pan, Y. Zhang, and D. Zhang, "Self-assembly fabrication of titanium dioxide nanospheres-decorated tungsten diselenide hexagonal nanosheets for ethanol gas sensing application," *Appl. Surf. Sci.*, vol. 527, no. April, p. 146781, 2020, doi: 10.1016/j.apsusc.2020.146781.

[11] X. Tian, Z. Hu, T. Wang, H. Wang, Q. Zhang, and X. Wei, "Influence of multi-layer TiO_2/SnO_2 heterojunctions on fast and sensitive ethanol detection," *Vacuum*, vol. 207, no. May 2022, 2023, doi: 10.1016/j.vacuum.2022.111620.

[12] K. G. Kumar, B. S. Avinash, M. Rahimi-Gorji, and J. Majdoubi, "Photocatalytic activity and smartness of TiO_2 nanotube arrays for room temperature acetone sensing," *J. Mol.*

Liq., vol. 300, p. 112418, 2020, doi: 10.1016/j.molliq.2019.112418.

[13] B. Bhowmik, K. Dutta, A. Hazra, and P. Bhattacharyya, “Low temperature acetone detection by p-type nano-titania thin film: Equivalent circuit model and sensing mechanism,” *Solid. State. Electron.*, vol. 99, pp. 84–92, 2014, doi: 10.1016/j.sse.2014.04.023.

[14] L. L. Deng, C. X. Zhao, Y. Ma, S. S. Chen, and G. Xu, “Low cost acetone sensors with selectivity over water vapor based on screen printed TiO_2 nanoparticles,” *Anal. Methods*, vol. 5, no. 15, pp. 3709–3713, 2013, doi: 10.1039/c3ay40373d.

[15] H. Bian *et al.*, “Characterization and acetone gas sensing properties of electrospun TiO_2 nanorods,” *Superlattices Microstruct.*, vol. 81, pp. 107–113, 2015, doi: 10.1016/j.spmi.2015.01.022.

[16] Y. Saffary, C. N. Christensen, A. Tripathy, M. Jeppson, K. Carlson, and S. K. Mohanty, “Synthesis of Tetracosane Functionalized Titanium Dioxide Sensor for Detecting Heptane as Pneumonia Breath Biomarker,” *IEEE Sens. J.*, vol. 22, no. 16, pp. 15724–15732, 2022, doi: 10.1109/JSEN.2022.3189595.

[17] S. Shao, H. W. Kim, S. S. Kim, Y. Chen, and M. Lai, “NGQDs modified nanoporous TiO_2/graphene foam nanocomposite for excellent sensing response to formaldehyde at high relative humidity,” *Appl. Surf. Sci.*, vol. 516, no. November 2019, p. 145932, 2020, doi: 10.1016/j.apsusc.2020.145932.

[18] T. To *et al.*, “Sensors and Actuators : B . Chemical Hierarchically structured $LaFeO_3$ with hollow core and porous shell as efficient sensing material for ethanol detection,” *Sensors Actuators B. Chem.*, vol. 354, no. November 2021, p. 131195, 2022, doi: 10.1016/j.snb.2021.131195.

[19] D. Kuang *et al.*, “Facile hydrothermal synthesis of $Ti_3C_2T_x$-TiO_2 nanocomposites for gaseous volatile organic compounds detection at room temperature,” *J. Hazard. Mater.*, vol. 416, no. December 2020, p. 126171, 2021, doi: 10.1016/j.jhazmat.2021.126171.

[20] H. Trabelsi, M. Bejar, E. Dhahri, M. P. F. Grac, and M. A. Valente, “Applied Surface Science Raman , EPR and ethanol sensing properties of oxygen-Vacancies $SrTiO_{3-\,1}$

compounds," vol. 426, pp. 386–390, 2017, doi: 10.1016/j.apsusc.2017.07.128.

[21] N. Y. Chan *et al.*, "Highly sensitive gas sensor by the $LaAlO_3/SrTiO_3$heterostructure with Pd nanoparticle surface modulation," *Adv. Mater.*, vol. 26, no. 47, pp. 5962–5968, 2014, doi: 10.1002/adma.201401597.

[22] E. Cao, Z. Chu, H. Wang, W. Hao, L. Sun, and Y. Zhang, "Effect of film thickness on the electrical and ethanol sensing characteristics of $LaFeO_3$ nanoparticle-based thick film sensors," *Ceram. Int.*, vol. 44, no. 6, pp. 7180–7185, 2018, doi: 10.1016/j.ceramint.2018.01.163.

[23] X. Wang, M. Li, B. Ding, Y. Liu, and T. Chen, "UV-enhanced ethanol-sensing properties of TiO_2-decorated $ZnSnO_3$ hollow microcubes at low temperature," *J. Mater. Sci. Mater. Electron.*, vol. 28, no. 17, pp. 12399–12407, 2017, doi: 10.1007/s10854-017-7060-x.

[24] X. Wang *et al.*, "Synthesis of 3D flower-like $ZnSnO_3$ and improvement of ethanol-sensing properties at room temperature based on nano-TiO_2 decoration and UV radiation," *Sensors Actuators, B Chem.*, vol. 264, pp. 119–127, 2018, doi: 10.1016/j.snb.2018.02.178.

[25] Y. Hu, O. K. Tan, W. Cao, and W. Zhu, "A low temperature nano-structured $SrTiO_3$ thick film oxygen gas sensor," *Ceram. Int.*, vol. 30, no. 7, pp. 1819–1822, Jan. 2004, doi: 10.1016/j.ceramint.2003.12.068.

[26] A. M. Schultz, T. D. Brown, M. P. Buric, S. Lee, K. Gerdes, and P. R. Ohodnicki, "High temperature fiber-optic evanescent wave hydrogen sensors using La-doped $SrTiO_3$ for SOFC applications," *Sensors Actuators, B Chem.*, vol. 221, pp. 1307–1313, 2015, doi: 10.1016/j.snb.2015.07.046.

[27] X. Zhou, T. Smensen, and Y. Xu, "Defect structure and oxygen sensing properties of Mg-doped SrTiO , thick film sensors," vol. 41, pp. 177–182, 1997.

[28] M. Zhang, S. Wei, W. Ren, and R. Wu, "Development of high sensitivity humidity sensor based on gray $TiO_2/SrTiO_3$ composite," *Sensors (Switzerland)*, vol. 17, no. 6, pp. 1–6, 2017, doi: 10.3390/s17061310.

[29] R. Tao, X. Li, X. Li, C. Shao, and Y. Liu, "$TiO_2/SrTiO_3/g\text{-}C_3N_4$ ternary heterojunction nanofibers: gradient energy band, cascade charge transfer, enhanced photocatalytic

hydrogen evolution, and nitrogen fixation," *Nanoscale*, vol. 12, no. 15, pp. 8320–8329, 2020, doi: 10.1039/D0NR00219D.

[30] H. Che *et al.*, "Construction of $SrTiO_3/Bi_2O_3$ heterojunction towards to improved separation efficiency of charge carriers and photocatalytic activity under visible light," *J. Alloys Compd.*, vol. 688, pp. 882–890, 2016, doi: 10.1016/j.jallcom.2016.07.311.

[31] N. Y. Chan *et al.*, "Palladium nanoparticle enhanced giant photoresponse at $LaAlO_3/SrTiO_3$ two-dimensional electron gas heterostructures," *ACS Nano*, vol. 7, no. 10, pp. 8673–8679, 2013, doi: 10.1021/nn4029184.

[32] P. Performance, J. Zhang, J. H. Bang, C. Tang, and P. V Kamat, "Tailored $TiO_2/SrTiO_3$ Heterostructure Nanotube Arrays for Improved," vol. 4, no. 1, pp. 387–395, 2010.

[33] V. R. Mastelaro *et al.*, "Ozone gas sensor based on nanocrystalline $SrTi_{1-x}FexO_3$ thin films," *Sensors Actuators B Chem.*, vol. 181, pp. 919–924, May 2013, doi: 10.1016/j.snb.2013.02.068.

[34] X. Yuan *et al.*, "Self-Assembly of Three-Dimensional $SrTiO_3$ Microscale Superstructures and Their Photonic Effect," *Inorg. Chem.*, vol. 52, no. 5, pp. 2581–2587, Mar. 2013, doi: 10.1021/ic302585g.

[35] H. Amani Hamedani, J. A. Khaleel, K. H. Dahmen, and H. Garmestani, "Surface controlled growth of thin-film strontium titanate nanotube arrays on silicon," *Cryst. Growth Des.*, vol. 14, no. 10, pp. 4911–4919, 2014, doi: 10.1021/cg500374m.

[36] A. Hazra, A. Tripathi, A. Jan, S. Kundu, and P. K. R. Boppidi, "Multiple nano-filaments based efficient resistive switching in TiO_2 nanotubes array influenced by thermally induced self-doping and anatase to rutile phase transformation," *Nanotechnology*, vol. 32, no. 11, p. 115201, Mar. 2021, doi: 10.1088/1361-6528/abd05c.

[37] A. Hazra, B. Bhowmik, K. Dutta, P. P. Chattopadhyay, and P. Bhattacharyya, "Stoichiometry, length, and wall thickness optimization of TiO_2 nanotube array for efficient alcohol sensing," *ACS Appl. Mater. Interfaces*, vol. 7, no. 18, pp. 9336–9348, 2015, doi: 10.1021/acsami.5b01785.

[38] Y. Xin, J. Jiang, K. Huo, T. Hu, and P. K. Chu, "Bioactive $SrTiO_3$ Nanotube Arrays :

Osteoporotic Bone Implants," *ASC Nano*, vol. 3, no. 10, pp. 3228–3234, 2009.

[39] M. Y. A. Rahman, S. A. M. Samsuri, and A. A. Umar, "TiO_2–$SrTiO_3$ composite photoanode: effect of strontium precursor concentration on the performance of dye-sensitized solar cells," *Appl. Phys. A Mater. Sci. Process.*, vol. 125, no. 1, p. 0, 2019, doi: 10.1007/s00339-018-2344-4.

[40] G. Panchal, D. K. Shukla, R. J. Choudhary, V. R. Reddy, and D. M. Phase, "The effect of oxygen stoichiometry at the interface of epitaxial $BaTiO_3$/$La_{0.7}Sr_{0.3}MnO_3$ bilayers on its electronic and magnetic properties," *J. Appl. Phys.*, vol. 122, no. 8, p. 085310, Aug. 2017, doi: 10.1063/1.5000133.

[41] J. Liu *et al.*, "In situ green oxidation synthesis of Ti 3+ and N self-doped $SrTiO_xN_y$ nanoparticles with enhanced photocatalytic activity under visible light," *RSC Adv.*, vol. 8, no. 13, pp. 7142–7151, 2018, doi: 10.1039/C7RA13523H.

[42] J. Y. Baek, L. T. Duy, S. Y. Lee, and H. Seo, "Aluminum doping for optimization of ultrathin and high-k dielectric layer based on $SrTiO_3$," *J. Mater. Sci. Technol.*, vol. 42, no. April, pp. 28–37, 2020, doi: 10.1016/j.jmst.2019.12.006.

[43] Z. Saroukhani, N. Tahmasebi, and S. M. Mahdavi, "Effect of working pressure and annealing temperature on microstructure and surface chemical composition of barium strontium titanate films," vol. 38, no. 6, pp. 1645–1650, 2015.

[44] P. Wang *et al.*, "ZnO nanosheets/graphene oxide nanocomposites for highly effective acetone vapor detection," *Sensors Actuators B Chem.*, vol. 230, pp. 477–484, Jul. 2016, doi: 10.1016/j.snb.2016.02.056.

[45] B. Szafraniak and Ł. Fu, "Semiconducting Metal Oxides: $SrTiO_3$, $BaTiO_3$ and $BaSrTiO_3$ in Gas-Sensing Applications: A Review," pp. 1–22, 2021.

[46] J. Li *et al.*, "Ultrafast response and high-sensitivity acetone gas sensor based on porous hollow Ru-doped SnO_2 nanotubes," *Sensors Actuators B Chem.*, vol. 352, no. P2, p. 131061, 2022, doi: 10.1016/j.snb.2021.131061.

[47] N. wang *et al.*, "Ultra-fast and low detection limit of H_2S sensor based on hydrothermal synthesized Cu_7S_4-CuO microflowers," *Sensors Actuators B Chem.*, vol. 350, no. May

2021, p. 130847, 2022, doi: 10.1016/j.snb.2021.130847.

[48] X. Wang *et al.*, “Carbon modification endows WO3 with anti-humidity property and long-term stability for ultrafast H_2S detection,” *Sensors Actuators B Chem.*, vol. 350, no. August 2021, p. 130884, 2022, doi: 10.1016/j.snb.2021.130884.

[49] G. Zhang, W. Jiang, S. Hua, H. Zhao, L. Zhang, and Z. Sun, “Constructing bulk defective perovskite $SrTiO_3$ nanocubes for high performance photocatalysts,” *Nanoscale*, vol. 8, no. 38, pp. 16963–16968, 2016, doi: 10.1039/c6nr04859e.

[50] C. Qin *et al.*, “Metal-organic framework-derived highly dispersed Pt nanoparticles-functionalized ZnO polyhedrons for ppb-level CO detection,” *Sensors Actuators, B Chem.*, vol. 331, no. January, p. 129433, 2021, doi: 10.1016/j.snb.2021.129433.

[51] Y. Wang, X. ning Meng, and J. liang Cao, “Rapid detection of low concentration CO using Pt-loaded ZnO nanosheets,” *J. Hazard. Mater.*, vol. 381, no. April 2019, p. 120944, 2020, doi: 10.1016/j.jhazmat.2019.120944.

[52] C. Wen, Q. Ye, S. L. Zhang, and D. Wu, “Assessing kinetics of surface adsorption-desorption of gas molecules via electrical measurements,” *Sensors Actuators, B Chem.*, vol. 223, pp. 791–798, 2016, doi: 10.1016/j.snb.2015.10.019.

[53] N. Sarin, M. Mishra, G. Gupta, I. P. Parkin, and V. Luthra, “Elucidating iron doping induced n- to p- characteristics of Strontium titanate based ethanol sensors,” *Curr. Appl. Phys.*, vol. 18, no. 2, pp. 246–253, 2018, doi: 10.1016/j.cap.2017.11.007.

[54] Z. Liu *et al.*, “A 2D/2D/2D $Ti_3C_2T_x$ @TiO_2 @MoS_2 heterostructure as an ultrafast and high-sensitivity NO_2 gas sensor at room-temperature,” *J. Mater. Chem. A*, 2022, doi: 10.1039/D1TA09369J.

Chapter-5

$SrTiO_3$ perovskite nanostructures and its Pd nanoparticle modification for humidity-tolerant and selective ethanol Sensing

5.1 Introduction

A real-time sensor for breath VOC detection requires great sensing characteristics with minimum influence of real-time obstacles. The main factors which significantly raise a concern about the reliability of the breath VOC sensors are (i) temperature variation, (ii) ambient humidity and (iii) the presence of cross-interfering VOCs [1-4]. Among them, humidity is one of the most concerning factors, especially for breath analysis where sensors need to detect traces of gases/volatile organic compounds (VOCs) in the presence of more than 80% humidified ambient [1]. In a humid environment, water molecules are attached to the interacting sites of the sensor. As a result, the number of active sites to adsorb the target analyte(s) gets reduced and eventually influences baseline resistance, limits the sensor response, response/recovery speed, and ultimately deteriorates the long-term stability of the sensors [3,5-7].

In this regard, $SrTiO_3$ (STO) can be a preferred material for robust breath volatile organic compounds (VOCs) detection due to its tunable semiconducting bandgap and porous morphology and long-term sensor performance, good thermal, chemical and microstructural stability, high reliability, and low processing cost [8-11]. $SrTiO_3$ also provides a high-density defect state at its interface and can easily be modified by controlling the oxygen stoichiometry [8,9,11-13]. $SrTiO_3$ and its composites have been successfully employed in sensing different VOCs and gases such as H_2 [10, 14], ethanol [8,9,12], O_2[15], ozone [16] and NO_2 [17]. Trabelsi et al. reported oxygen vacancy modulated $SrTiO_3$ for effective ethanol sensing at room temperature. The data concluded that sensors with optimized oxygen vacancy content showed good semiconducting and ethanol sensing properties [8].

Additionally, many researchers are focusing on the development of various morphological nanostructures to achieve improved specific surface area, variated surface properties (porosity, surface roughness) and defect density for better gas sensing characteristics [18,19]. A variety of synthesis routes like sol-gel, mechanochemical, combustion, etc. have also been reported for the $SrTiO_3$ but they were lacking in significant morphological variation and specific surface area [13]. Hydrothermal route is the best alternative way which provides different morphologies by modulating reaction parameters like; temperature, reaction time etc. [13,19,20]. Hydrothermal $SrTiO_3$ prepared by reacting TiO_2 powder (rutile or anatase) with a soluble Sr salt ($SrCl_2$, $Sr(NO_3)_2$, $Sr(OH)_2$ [19-22]. The [13,20,22,23]. Dong et al. synthesized different type of $SrTiO_3$ nanocrystals by varying alcohols like ethanol, 1,4-butanediol, ethylene glycol, 1,2-propanediol, etc. [20]. A wide variety of morphologies of $SrTiO_3$ like nanocubes, nanoparticles, nanosphere, nanofiber, nanotubes, etc. are developed by hydrothermal treatment [21,22,24,25].

To further minimize the effect of environmental humidity, many strategies such as the conductivity modulation of sensing materials [7,26,27], surface functionalization [28, 29], noble metals addition [30-32], operating temperature [32], enhancement of porosity/roughness [6,28,33,34] have been introduced. A few research groups found that the use of metal functionalization (Ag [30], Pd/Sn [32]) or the addition of overlayer (CeO_2 on CuBr) [29] on sensing material that blocks the interaction between moisture and sensing layer to improve the robustness of the sensors towards humidity. Apart from this noble metal nanoparticles (Au [9], Pd [35], Pt [36]) functionalization in sensing material improves the sensing properties through electronic and chemical sensitization effects. These sensitization effects increase the sensitivity, improve selectivity and decrease the overall operating temperature of the sensors [35].

In this chapter, we revealed a general strategy to comprehensively manipulate the morphologies of $SrTiO_3$ semiconductor perovskite, evolving from 1-D nanoforms to 0-D morphology by a facile one-pot hydrothermal synthesis at 180 °C for different reaction times. The underlying factors, that caused the dimensional evolution are insightfully investigated. The elemental growth mechanisms, dimensional breaking, crystal structure transformations and surface property modulations are extensively studied for the developed $SrTiO_3$ nanostructures. With this new understanding, high quality $SrTiO_3$ thin films are synthesized with various controlled morphologies like nanobush, nanograss, nanorods, nanospheres and nano-hollow spheres. Detailed morphology-dependent VOC sensing behaviors of $SrTiO_3$ nanoforms are carefully studied. 1D branched $SrTiO_3$ nanograss and hollow spheres showed impressive sensing activity towards low ethanol concentrations in 80% relative humidity. Later on, the ethanol sensing performance of the STO-hollow sphere sensor was improved with the addition of Pd nanoparticle catalyst. To the best of our knowledge, there are no such reports on high-performance perovskite gas sensors with a high gas response, ultrafast response/recovery speed and selectivity regardless of the atmospheric humidity for breath analysis application.

5.2 $SrTiO_3$ perovskite nanostructures

5.2.1 Synthesis

The schematic representation in Fig. 5.1 summarizes the synthesis steps for the morphology evolution of $SrTiO_3$ nanostructures. In a typical route, $Sr(OH)_2{\cdot}8H_2O$ was dispersed in 75 mL of deionized water under a stirring state and when the solution became transparent anatase-TiO_2 nanoparticles solution was added dropwise in the above solution under stirring. $Sr(OH)_2{\cdot}8H_2O$ and TiO_2 solution were added to arrange the mole ratio as 1 and 2. The pH of the mixed solution was adjusted to about 9.0 using 1M NaOH solution. The hydrothermal method can actively control the size and morphology of produced nanostructures by varying reaction parameters like precursors, concentration, temperature and reaction time [13]. In this direction, we have developed different $SrTiO_3$ morphologies by varying only the reaction time of hydrothermal. The resulting suspension was transferred to a 100 mL Teflon-lined stainless-steel autoclave and heated to 180 ˚C for various desired periods 10, 14, 18, 20, 24 h, respectively. After the completion of the reactions, the reactor was cooled to room temperature and the final precipitated material was collected. The contents were then washed multiple times with absolute ethanol and deionized water to remove

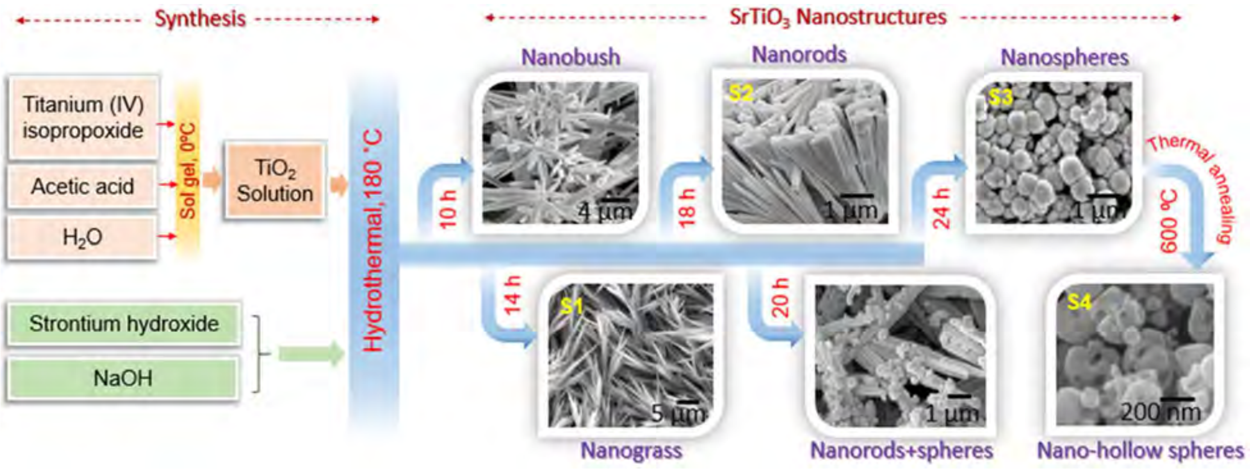

Fig. 5.1. Schematic representation of the experimental procedure used to synthesize various $SrTiO_3$ nanostructures.

excess NaOH and other impurities until the pH value of the liquid reached 7. The solid precipitates were dried in an oven for 14 h at 80 °C. When the reaction was performed for the shortest time (10 h), nanobushes of $SrTiO_3$ were obtained showing the incomplete growth of the nanograss structure. When the reaction time increased to 14 h fully grown nanograss was obtained. Later, the nanorods were obtained at a high reaction time (18 h). On the other side, as the reaction time was 22 h the nanorods started to convert into nanospheres as both the morphologies were observed. The longest reaction time (24 h) showed the fully grown nanospheres of $SrTiO_3$. After 24 h, increase in reaction time did not show any change in the morphology after nanosphere formation. Thermal annealing was performed for all the resulting materials at two different temperatures, 300 ˚C and 600 ˚C for 6 h to enhance the mechanical and electrical stability as well as to enhance the functionalization of $SrTiO_3$ with oxygen species. After the annealing at 600 ˚C, the morphology and distribution of all nanostructures get deteriorated except the nanospheres. The nanospheres were converted into hollow spheres after the high temperature (600 ˚C) annealing (Fig. 5.1). Additionally, the morphologies obtained from reaction times 10 h and 22 h are marked as intermediate growth stages of $SrTiO_3$ and not carried out for further studies.

5.2.2 Crystallization mechanism of $SrTiO_3$

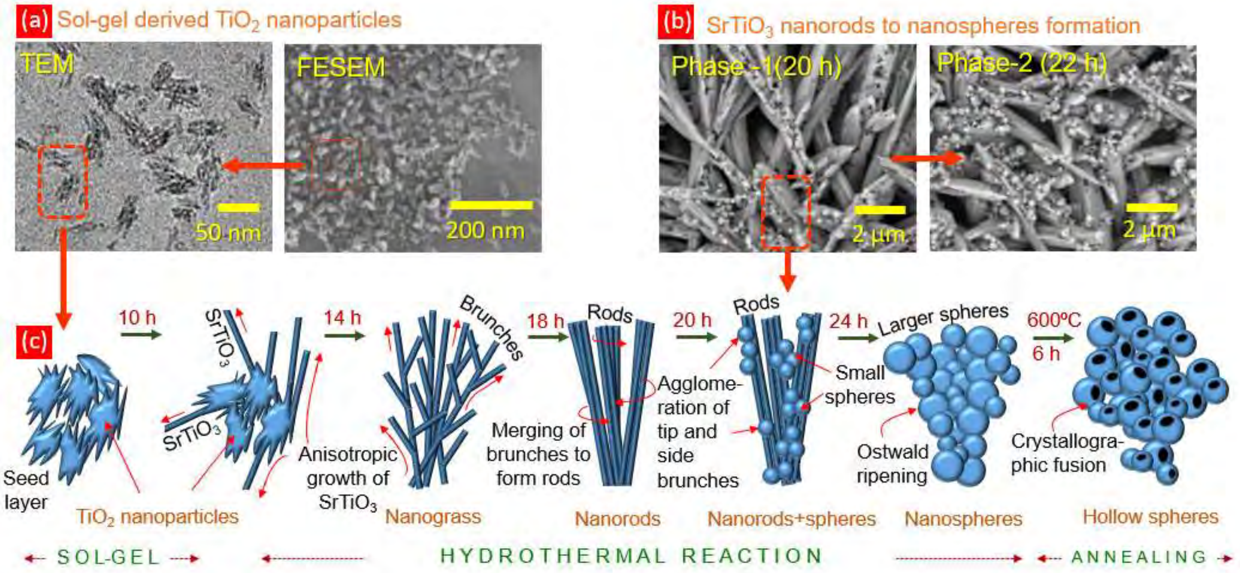

Fig. 5.2. (a) TEM and FESEM image of sol-gel derived TiO_2 nanoparticles, (b) formation of $SrTiO_3$ nanospheres from nanorods, (c) step by step synthesis mechanism of $SrTiO_3$ morphologies at different reaction conditions.

The synthesis conditions were carefully analysed to elucidate the synthesis mechanism of these massive structural and crystal transformations of $SrTiO_3$ nanostructures as given in Fig. 5.2. The synthesis of $SrTiO_3$ from anatase-TiO_2 and $Sr(OH)_2 \cdot 8H_2O$ is the combined involvement of dissolution and precipitation. Titania precursor (TiO_2) is dissolved in the highly alkaline medium as pH plays a significant role in the dissolution and determines the crystallinity of the perovskite by homogenous nucleation in the liquid phase [13, 23]. TiO_2 is not only a Ti precursor but also acts as a skeleton or seed layer for the growth of $SrTiO_3$ as shown in Fig. 5.2 [37]. In the first step, Ti-O bonds in titania are broken by a hydrolytic attack that results in a soluble hydroxytitanium $[Ti(OH)_6]^{2-}$ complex [37,38]. The respective reaction is given below.

$$TiO_2(aq) + 2OH^-(aq) + 2H_2O(I) \rightarrow [Ti(OH)_6]^{-2}\,(aq) \qquad (5.1)$$

The highly alkaline NaOH medium (pH> 10) enables the rapid solubility and the formation of $[Ti(OH)_6]^{2-}$ which is capable of reaction with strontium ions and consequently determines the crystallization rate of the final product [13]. In the presence of a mineralizer (NaOH) at an optimum temperature, the dissolution of precursors is fast and a high nucleation rate leads to the formation of more regular aggregates at a comparatively small reaction time (Fig. 5.2). Later, the precipitation of $SrTiO_3$ perovskite occurs as per the following reaction.

$$Sr^{+2}(aq) + [Ti(OH)_6]^{-2}(aq) \rightarrow SrTiO_3\,(s) + 3H_2O \qquad (5.2)$$

$[Ti(OH)_6]^{-2}$ species are supposed to be highly active which react with Sr^{+2} and form new nucleus for $SrTiO_3$ formation according to the nucleation process shown in equation 2 [37]. The nucleation process was further carried out and the growth of large nuclei continued in the vicinity of the TiO_2 surface as shown in Fig. 5.2. The early growth after the initial surface nucleation is mostly determined by the surface density of nuclei [13].

In the hydrothermal process, phase transformation of the materials occurs and a series of stable intermediate nanostructures are formed (Fig. 5.2) depending on the solubility of the nanocrystals, which are strongly influenced by synthesis conditions such as mineralizers concentration, reaction time, temperature, etc. [13,39]. As shown in Fig. 5.1, the evolution of nanostructures may follow the four-stage model i.e., dissolution–crystallization–aggregative growth–recrystallization [40]. After the dissolution, crystallization and nucleation process, the aggregative growth of nuclei is taken place due to the Van Der Waals forces. These aggregates are seen to have more regular shapes after the structural rearrangements (Fig. 5.2(c)). Sol-gel derived TiO_2 nanoparticles, as shown in Fig. 5.2(a), acted as the seed layer in the hydrothermal reaction. The anisotropic growth of $SrTiO_3$ from the TiO_2 seed layer was then transformed into nanograss morphology after 14 h of reaction time (Fig. 5.2(c)). Later on, an increase in reaction time up to 18 h leads to merging branches to form solid rods like morphology (Fig. 5.2). As the reaction proceeds, recrystallization occurs at a higher reaction time, leading to a more regular shape of the particles of $SrTiO_3$ (nanospheres). The formation of nanospheres was started by breaking or shredding nanorods, which worked as a growth point of small spheres, as shown in FESEM images in Fig. 5.2(b). At 20 h reaction time, the small nanospheres started to grow but still, the rods were the dominant morphology as shown in Fig. 5.2(b). Similar morphological evolution has also been reported in the hydrothermal growth of lead zirconate titanate nanostructures [41]. The large nanospheres (Fig. 5.1 and 5.2(c)) formation takes place by the Ostwald ripening process where reduction in surface energy is the primary driving force for the crystal growth and the evolution of large nanospheres, which is due to the difference in solubility between larger and smaller particles [13,25]. Nanospheres containing many small nanopores and annealing at higher temperature promote the crystallographic fusion and coalesce of nanopores by forming larger nanocavities or mesopores as shown in Fig. 5.1 and 5.2(c) [13]. These mesopores formation introduced a new hollow sphere morphology with further improved surface properties of $SrTiO_3$.

5.2.3 Characterization

Morphological characterization

Fig. 5.1 summarizes the morphological evolutions in $SrTiO_3$ nanostructures at different operating times of hydrothermal reaction. Four significant morphologies i.e., nanograsses (S1), nanorods (S2), nanospheres (S3) and nano-hollow spheres (S4) are described in detail in Fig. 5.3. A solution of 1M $Sr(OH)_2 \cdot 8H_2O$+NaOH and 2 M TiO_2 was treated with hydrothermal reaction at 180 ˚C for 14 hours and the resulting $SrTiO_3$ was further annealed at 300 ˚C for 6 hours. The synthesized $SrTiO_3$ showed uniform grass-like morphology with needle-shaped laterally distributed brunches (Fig. 5.3 (a, b)). The average diameter of the individual needle was measured as ~300 nm (inset of Fig. 5.3 (b)). With the increase of hydrothermal reaction time up to 18 hours, the lateral branches merge and promote the formation of wider and thicker nanorods (S2) as shown in Fig. 5.3(c, d). The branches are preferably agglomerated at the top/tip portion

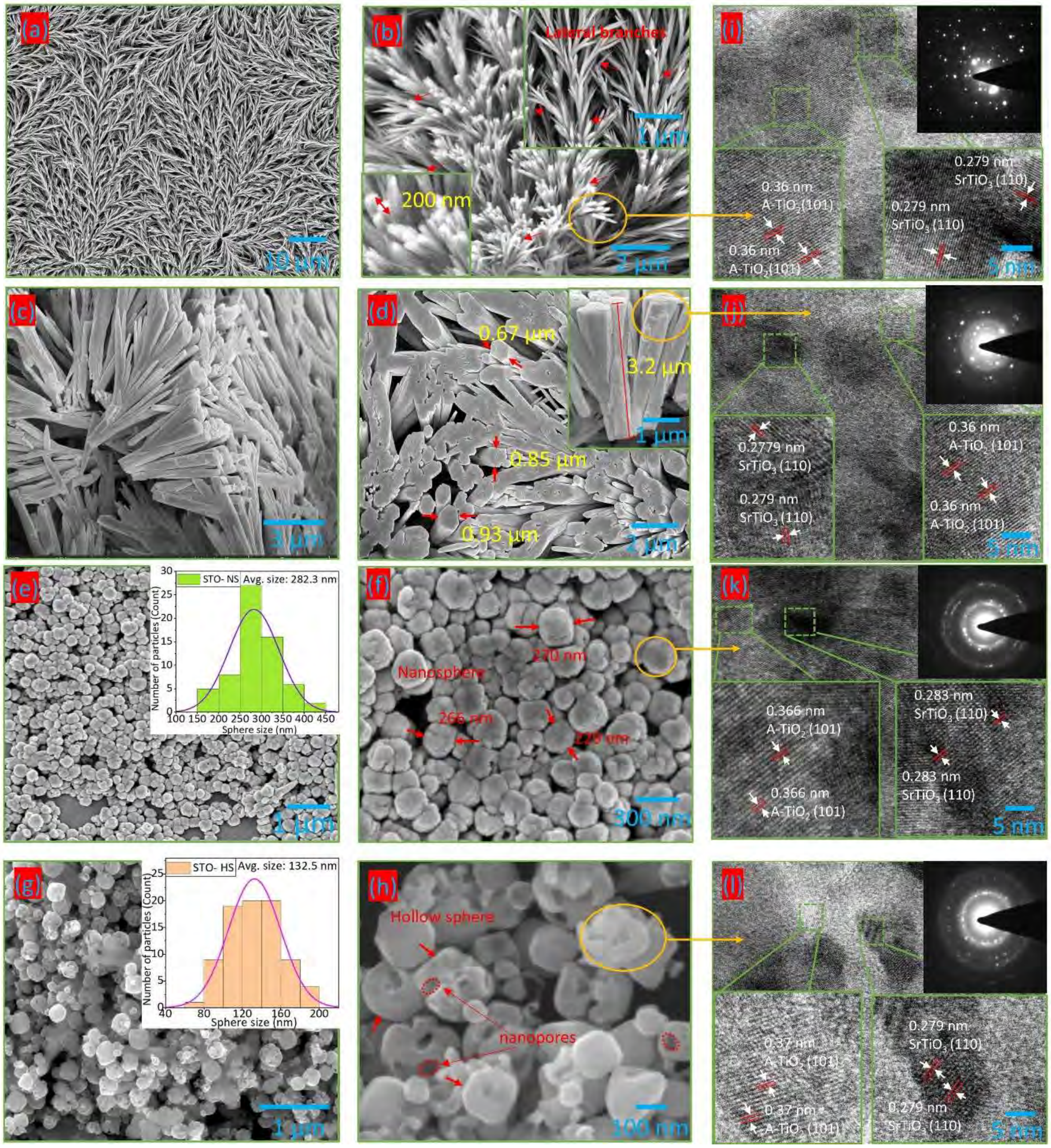

Fig. 5.3. FESEM images of (a, b) Nanograss (S1), (c, d) Nanorods (S2), (e, f) Nanospheres (S3) and (g,h) Hollow sphere (S4), respectively; HRTEM images and SEAD patterns (inset of figure) of (i) Nanograss (S1), (j) Nanorods (S2), (k) Nanospheres (S3) and (l) Hollow sphere (S4) samples.

which eventually made the nodes and the blade part of the nanorods wider than the remaining parts (Fig. 5.3(d)). After the transformation of grasses into rod-like morphology, the average diameter was increased up to 700 nm (figure 3d). The effective length of the nanorod was 3.2 μm (inset of Fig. 5.3(d)). The highest reaction or nucleation time resulted in the transformation of nanorods into nanospheres morphology (S3) of $SrTiO_3$ (Fig. 5.3(e, f)). The intermediate stage, after 20 h reaction time exhibited a partial and discrete formation of nanospheres decorated over the nanorods (Fig. 5.1 and 5.2). The nanorods started to vanish at the longest hydrothermal reaction time of 24 h and final nanospheres (S3) morphology was originated. The uniform, compact, and stable distribution of nanospheres was observed in the FESEM image in Fig. 5.3(e, f). The inset of Fig. 5.3(e) shows the size distribution analysis (using ImageJ software) where the average diameter of nanospheres is measured as 282.3 nm. Later on, due to the consequence of high annealing temperature nanospheres were converted into the hollow spheres (S4) of $SrTiO_3$ as shown in Fig. 5.3(g, h). The high annealing temperature resulted in the formation of mesopores on nanospheres and the size of these nanopores is in the range of 40-50 nm (Fig. 5.3(h)). Interestingly, the average size of nanospheres gets reduced significantly after its transformation to hollow spheres and the resulting average size is calculated as 132.5 nm (Fig. 5.3(g)). These nanocavities effectively improved the surface area to volume ratio of the $SrTiO_3$ nanospheres.

In order to give more insight into the structural details, high-resolution transmission electron microscopy (HRTEM) was performed for all four samples i.e., S1-S4 (Fig. 5.3(i-l)). HRTEM images of nanorods, nanosphere and hollow spheres clearly show the parallelism of the lattice fringes throughout the crystallite for the cubic phase of $SrTiO_3$ and the anatase TiO_2 in Fig. 5.3(j), (k) and (l), respectively. Two types of lattice fringes attributed to (101) and (110) are observed, which have a respective interplanar spacing of 0.353 and 0.277 nm corresponding to the (anatase) A-TiO_2 and cubic-$SrTiO_3$ for all $SrTiO_3$ submicron/nanostructures (Fig. 5.3(i-l)), respectively. Moreover, it can be seen in Fig. 5.3(i-l) that there is a clear interface between $SrTiO_3$ and TiO_2 that signifies the existence of TiO_2 in the final product which is further confirmed by the XRD analysis. The selected area electron diffraction (SAED) patterns are recorded and shown in the inset of HRTEM data. The diffraction rings consisted of numerous diffraction spots, which are the characteristics of a multi-crystalline structure [21]. The SEAD pattern consisted of numerous spots and clear rings signifying the highly crystalline nature of the resulting nanostructures correlated with the XRD data (inset (Fig. 5.3(i-l)). The clear pattern of several rings with good intensity indicates that the area comprises more than one crystalline phase. The pattern was indexed to mix crystallites of Cubic- $SrTiO_3$, anatase (A) and rutile (R) as seen in the diffraction rings.

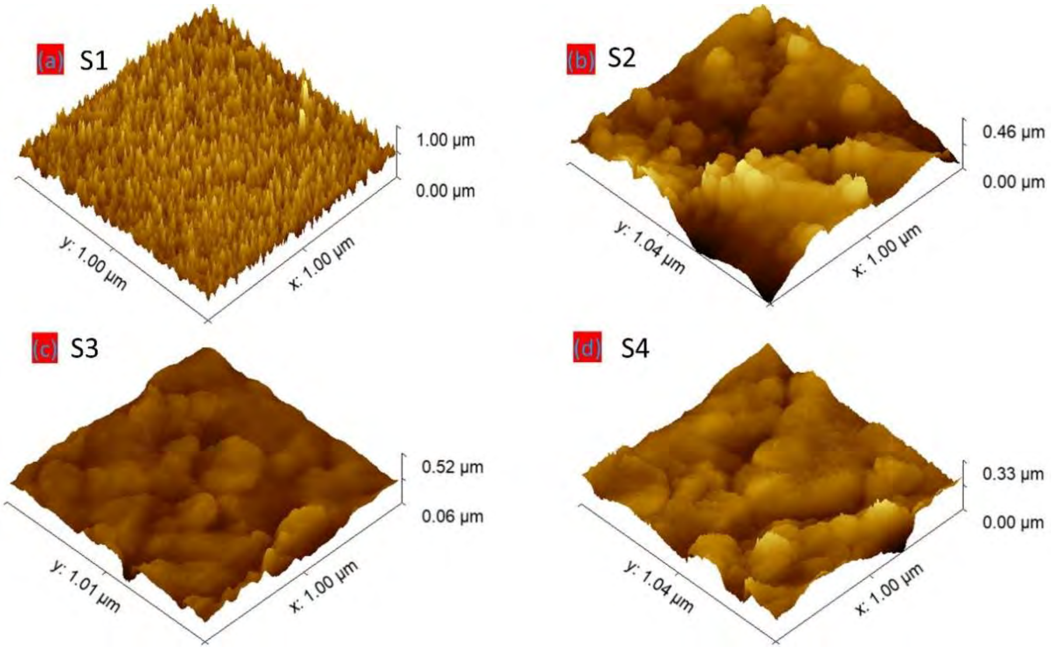

Fig. 5.4. AFM 3D topography images of (a) Nanograss (S1), (b) Nanorods (S2), (c) Nanospheres (S3) and (d) Hollow sphere (S4) samples.

The surface roughness of the prepared morphologically variated samples was studied with atomic force microscopy. The topographic images (Fig. 5.4) revealed the top surface properties of the S1-S4 samples. 1 µm × 1 µm area was considered for the surface scan of all the samples and the statistical parameters like RMS surface roughness (Sq) and mean roughness (Sa) were measured with Gwyddion software and listed in Table 1. The data reveals that the S1 (Fig. 5.4(a)) sample with the more pronounced RMS value with the hydrophobic nature has the highest irregularity in nanograss morphology than other variations in the nanometer range. In the case of nanorods (S2) (Fig. 5.4(b)) the RMS is quite high but uniformity on the top surface leads to a decrease in surface roughness (Table 5.1). On the other hand, 0D nanospheres (S3) (Fig. 5.4(c)) with the highest continuity led to the lowest RMS value but hollow spheres (S4) (Fig. 5.4(d)) lead to irregular surface topography and improved RMS value possibly due to the existence of mesopores which resulted in rough and porous topology at nanometer scale [6,28]. Moreover, all the morphologies of $SrTiO_3$ developed in the current study showed higher surface roughness than the previously reported $SrTiO_3$ nanoforms [16,34].

Table 5.1 Surface property measurement of S1-S4 samples from AFM topographic images.

Sample	RMS surface roughness (S_q)-nm	Mean roughness (S_a)-nm

S1	100.8	79.4
S2	72.6	58.4
S3	25.2	19.3
S4	28.9	22.3

Table 5.2 BET analysis of S1-S4 samples.

Sample	a_s, BET (m^2/g)	Pore volume (cm^3/g)
S1	3.0993	1.4786
S2	6.4902	3.7585
S3	5.9138	8.9862
S4	6.7981	9.1952

Further, a nitrogen adsorption-desorption study was carried out to obtain information about the specific surface area (m^2/g) and porosity (cm^3/g) of all four morphologies listed in Table 5.2. The BET surface area was found to be maximum in hollow sphere morphology (S4) due to the availability of mesopores and lowest in grass morphology (S1). Nanorods (S2) and nanospheres (S3) also showed appreciably high surface areas comparable to hollow spheres (S4). Additionally, the average pore volume was found to increase gradually from S1-S4 samples (Table 5.2) which are also helpful in the diffusion of gaseous analytes during the interaction.

Structural characterization

X-ray diffraction (XRD) patterns of the $SrTiO_3$ nanostructures with four different morphologies are shown in Fig. 5.5. The significant XRD peaks correspond to both $SrTiO_3$ and TiO_2.

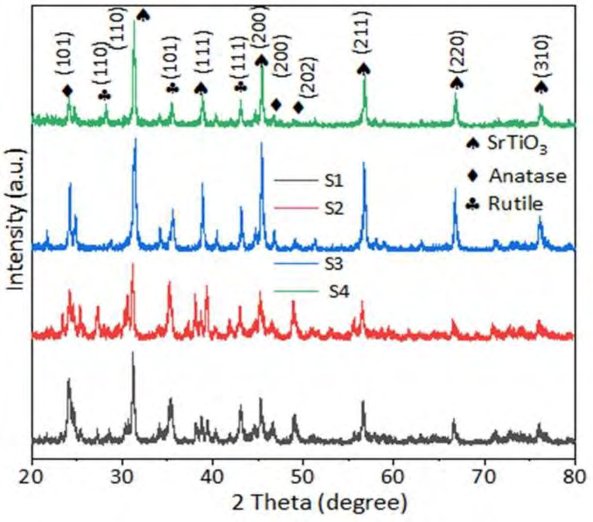

Fig. 5.5. XRD patterns of Nanograss (S1), Nanorods (S2), Nanospheres (S3) and Hollow sphere (S4).

Diffraction patterns match well with the cubic $SrTiO_3$ phase (JCPDS No. 35-0734) that correspond crystal faces like (110), (111), (200), (211), (220) and (310) [21,42]. The highest intensity peak at $2\theta = 31.7°$ for the (110) crystal plane of $SrTiO_3$ was observed in all four samples and correlated with HRTEM results (Fig. 5.3(i-l)). The peaks corresponding to the anatase (JCPDS No. 21-1272) and rutile phases (JCPDS No. 88-1175) of TiO_2 were identified and labeled in XRD spectra (Fig. 5.5) [43-44]. At lower reaction times (14 h and 18 h), the relative intensity, peak area and the number of diffraction peaks for anatase and rutile crystal structure of TiO_2 were very much significant (Fig. 5.5). 24 h hydrothermal reaction followed by thermal annealing at 600 ˚C (S4) exhibited the highest peak intensities for $SrTiO_3$ along with the highly crystalline behavior of the resulting material. Most of the TiO_2 peaks almost disappeared in the case of the S3 and S4 samples (Fig. 5.5). Moreover, in S4, almost all the diffraction peaks in the patterns could be indexed to a pure cubic phase of $SrTiO_3$.

Chemical characterization

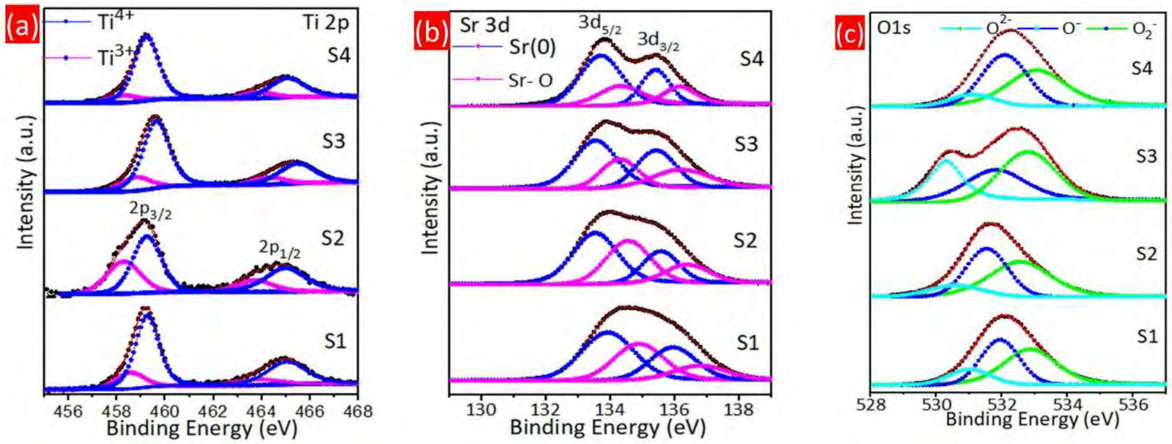

Fig. 5.6. (a) Ti 2p, (b) Sr 3d and (c) O 1s XPS spectra of Nanograss (S1), Nanorods (S2), Nanospheres (S3) and Hollow sphere (S4), respectively.

High-intensity binding energy Ti(2p) peaks for S1–S4 were recorded with a high-resolution scan to observe the change in doublet peaks, i.e., $Ti(2p)_{3/2}$ and $Ti(2p)_{1/2}$ (Fig. 5.5(a)). Additionally, the Ti 2p peaks are well de-convoluted into four peaks as Ti^{3+} $2p_{3/2}$, Ti^{4+} $2p_{3/2}$, Ti^{3+} $2p_{1/2}$ and Ti^{4+} $2p_{1/2}$, which clearly demonstrates the existence of Ti_2O_3 (Ti^{3+}) and TiO_2 (Ti^{4+}) oxidation states [45,46]. The detailed Ti $(2p)_{3/2}$ and Ti $(2p)_{1/2}$ area of peaks is summarized in Table 5.3 from Fig. 5.5(a). S1-S4 showed a relatively higher peak area for the Ti^{+4} oxidation state compared to the Ti^{+3} showing the highly oxygen-functionalized surface of the samples (Table 5.3). The Sr 3d spectrum of $SrTiO_3$ samples (S1-S4) showed two main peaks i.e., Sr $3d_{5/2}$ and Sr $3d_{3/2}$ (Fig. 5.5(b)). The two metallic peaks i.e. Sr(0) $3d_{5/2}$ and Sr(0) $3d_{3/2}$ correspond to the bonding of Sr-atoms in the perovskite materials and two other oxidation peaks i.e. Sr-O $3d_{5/2}$ and Sr-O $3d_{3/2}$ indicate the possible existence of Sr-OH, $Sr-CO_3$, Sr-Sr, and Sr-O bonds to the surface of the samples [47,48]. In Fig. 5.5(b), the area of the defect components is comparatively more pronounced than the peak area of metallic Sr, which eventually shows the high surface activeness of the $SrTiO_3$ samples. The corresponding area distribution is summarized in Table 5.4. Fig. 5.5(c) shows the high-resolution O(1s) spectra of S1 to S4 samples. O(1s) spectra were deconvoluted in three sub-peaks located at the binding energy near 530.5±0.3 eV (O^{2-}), 531.6±0.2 (O^-) and 532.5±0.3 eV (O_2^-) (Fig. 5.5(c)). The peak at the lowest binding energy corresponds to chemically bonded lattice oxygen (O_L), the middle one is associated with unsaturated oxygen vacancies or surface defects (O_V) and the highest binding energy peak corresponds to weakly bonded physiosorbed or chemisorbed (O_C) surface oxygen species.

Table 5.3 Area distribution measurement of S1-S4 samples from Ti 2p and Sr 3d spectra of XPS results.

Sample	**Ti^{3+} (Area %)**	**Ti^{4+} (Area %)**	**Sr(0) (Area %)**	**Sr-O (Area %)**
S1	28.2	71.8	58.2	41.8
S2	35.6	64.4	62.1	37.9
S3	13.6	86.4	67.9	32.1
S4	7	93	65.9	34.1

Table 5.4 Area distribution measurement of S1-S4 samples from O1s spectra of XPS results.

Sample	**O^{2-} (O_L)**	**O^- (O_V)**	**O^-_2 (O_C)**
S1	14.4	37.9	47.7
S2	12	39.4	48.6
S3	27.7	32.7	39.6
S4	9.9	43.5	46.6

The area of fitted peaks for S1 to S4 is summarized in Table 5.3. Due to having a significantly high surface area, the overall surface oxygen was found to be very high in the case of all the $SrTiO_3$ samples which was considered beneficial for gas sensing [49]. Oxygen vacancy type defects (43.5%) were increased in the hollow sphere (S4) sample possibly due to the high temperature (600 ºC) thermal annealing.

Surface wettability study

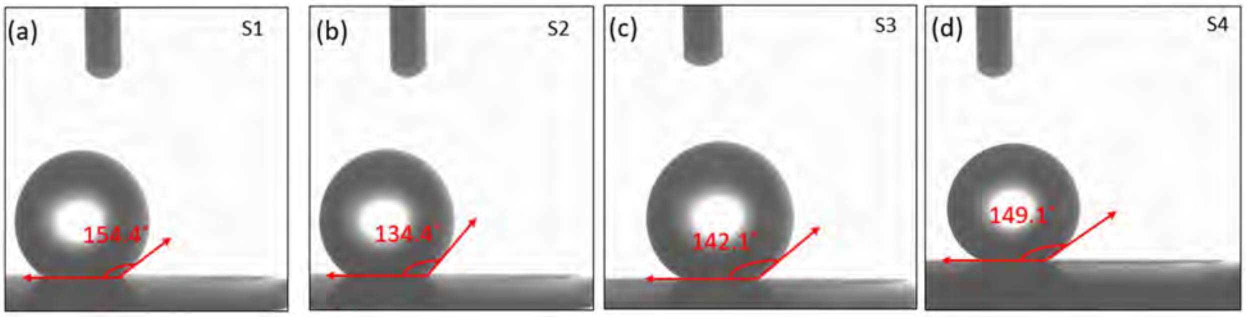

Fig. 5.7. The static water contact angles of the sensing film of S1-S4 samples.

In particular, we examined the surface wettability of all four (S1-S4) sensing films to understand their anti-humidity properties (Fig. 5.7). The surface wettability is the measurement of the water droplet contact angle where hydrophobic materials show high contact angle (90°< θe < 150°) [27,50]. A contact angle measurement device measured the static water contact angles (CAs) of a deionized water droplet (8 µl) on the surface STO film.

The static contact angle of all four sensing layers was measured (Fig. 5.7(a-d)) and found to be 154.4°, 134.4°, 142.1° and 149.1° for S1-S4, respectively. However, the results confirm the superior hydrophobic nature of the prepared STO films and are in agreement with the previously reported works [27,50]. The high contact angle makes the water molecules harder to adsorb to the surface of the STO films and the hindrance of sensing performance due to humidity is minimized. Moreover, the water contact angle of STO films was found to be significantly high as compared to a few popular hydrophobic materials such as polymethyl methacrylate (PMMA), CeO_2, etc. [51,52].

5.2.4 Sensor study

VOC sensing

The VOC sensing performance of four evaluated morphologies (S1-S4) was examined. The previously reported $SrTiO_3$ nanostructures showed an incompetent response at an extremely high operating temperature [9, 14]. However, the working temperature of a sensor influences the surface state of the sensing layer and contact behavior during the sensing process [53]. All four sensors were tested at a temperature range varying from 100- 200 °C, under exposure to 50 ppm ethanol in 80% RH (Fig. 5.8). The initial sensing performance of all four sensors was

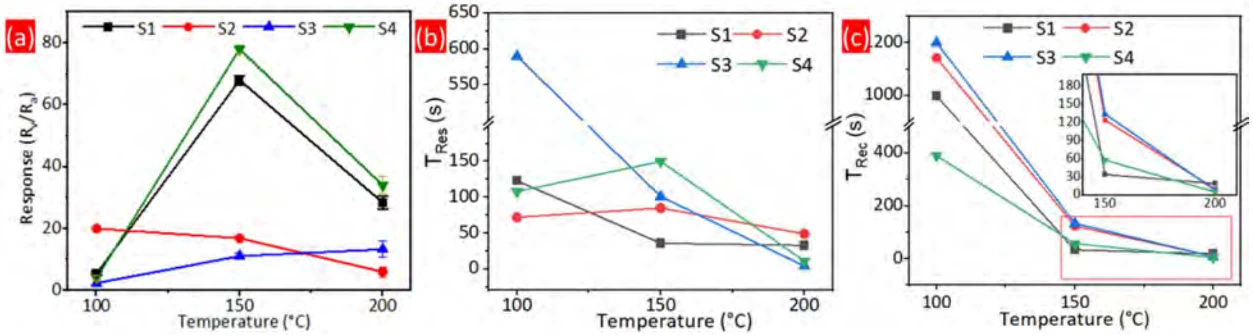

Fig. 5.8. (a) Response magnitude; (b) response time; (c) recovery time; as a function of temperature for S1-S4 sensors in 50 ppm of ethanol and 80% constant RH.

compared with three sensing properties, i.e., response magnitude, response time and recovery time, as a function of operating temperature (150–250 °C) and shown in Fig. 5.8(a)–(c). The change in morphologies showed a significant influence on sensing properties. S1 and S4 exhibited a very high response throughout the temperature range (100 °C–250 °C). All four sensors showed the highest responses i.e., 69, 16.9, 11.1 and 78 for S1, S2, S3 and S4, respectively at 150 °C. All the sensors showed a gradual increase of response from 100 °C to 150 °C and decreasing tendency exceeding 150 °C (at 200 °C). The study indicates that 150 °C is an optimized temperature (Fig. 5.8(a)). However, the small electronegativity of $SrTiO_3$ influenced the easy formation of ionic bonds with oxygen atoms and then VOC analytes even at relatively low temperature exhibited quite a high response (150 °C). Exceptionally, S2 exhibited a high response (20) at 100 °C and showed monotonic decrement towards higher temperatures (Fig. 5.8(a)).

The response time (T_{Res}) and the recovery time (T_{Rec}) are two important parameters highly influenced by the operating temperature. T_{Res} and T_{Rec} were measured for all four sensors and then represented as a function of temperature (150 and 200 °C) in Fig. 5.8(b, c). All the sensors became faster with an increase in temperature. Two sensors i.e., S1 and S4 with a highly activated sensing surface provided the highest sensitivity and very fast response (36 s and 150 s, respectively) and recovery (34 s and 58 s, respectively) at 150 °C (Fig. 5.8(b, c)). After studying the overall performances in Fig. 5.8(a-c), 150 °C was considered to be the optimized temperature for all the sensors. Moreover, the fast response/recovery speed and high sensitivity of $SrTiO_3$ nanostructured samples are attributed to the significantly high concentration of defects (such as oxygen vacancies) and chemisorbed oxygen are found in XPS results (Fig. 5.8(d)).

The real-time ethanol sensing was performed for all four morphologically variated $SrTiO_3$ nanostructured based at 150 °C in the presence of 80% RH. In Fig. 5.9(a-d), all the sensors responded in a positive direction of the Y-axis unfolding the p-type semiconducting behavior of the $SrTiO_3$ nanostructures [54]. The p-type conductivity of the $SrTiO_3$ nanoforms possibly originated from the p-TiO_2 nanoparticles used in hydrothermal synthesis [55]. The higher concentration of Ti vacancy (Ti^{+4}) compared to the oxygen vacancy is responsible for the p-type behavior of undoped TiO_2 [55,56]. In the transient measurement (Fig. 5.9(a-d)), ethanol concentration varied from 0.5 to 200 ppm. In minimum ethanol concentration i.e., 0.5 ppm, all four sensors i.e., S1-S4 offered responses like 12.4, 3.15, 4.25 and 15.1, respectively (Fig. 5.9(e)). However, it was noted that the response of the sensor was a near-linear relationship with ethanol concentration varying from 0.5 to 200 ppm (Fig. 5.9(e)). The linear regression equations for S1, S2, S3 and S4 are shown in Figure 7e with R^2 values > 0.92, 0.91, 0.89 and 0.933, respectively [57]. The theoretical detection limit was calculated by using the slope of the logarithmic plot (Fig. 5.9(e)) and the standard deviation from the baseline of Fig. 5.9(a-d) at 150 °C [58]. Therefore, the calculated detection limit of S1, S2, S3 and S4 sensors are 78 ppb, 88.1 ppb, 152 ppb and 57 ppb, respectively at 150 °C in the presence of 80% RH.

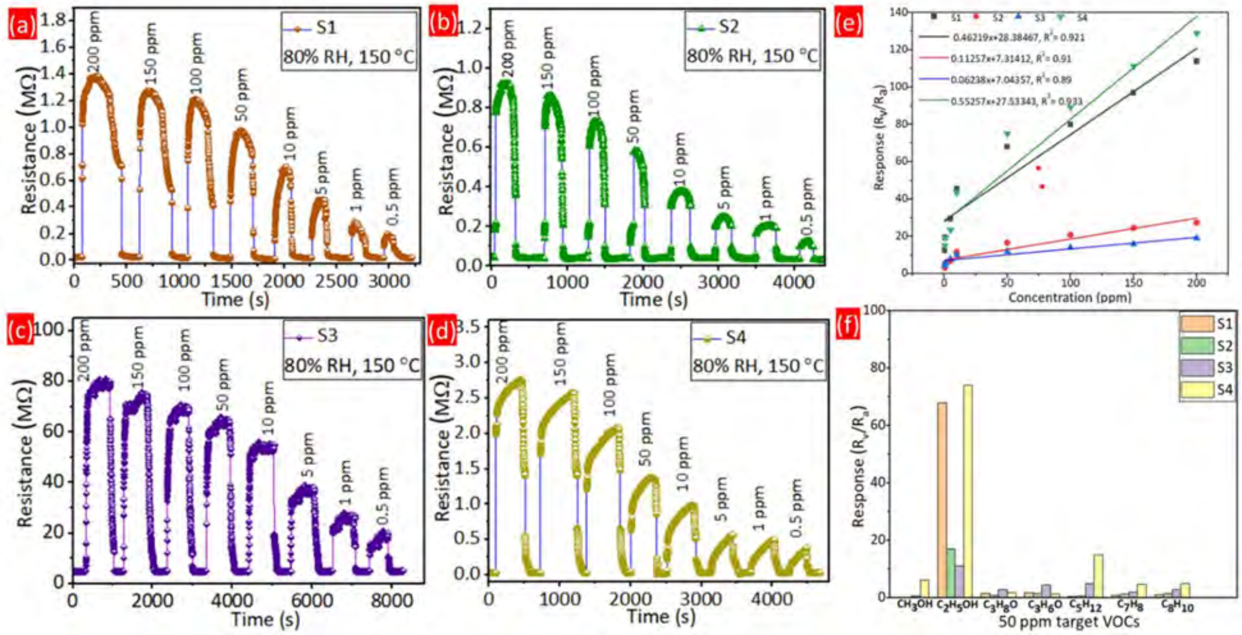

Fig. 5.9. (a-d) Dynamic response of nanograss (S1), nanorods (S2), nanospheres (S3) and nano-hollow sphere (S4) to different concentrations of ethanol varying from 500 ppb to 200 ppm; (e) Sensor responses as a function of gas concentration; (f) selectivity behavior of all the four sensors towards various volatile organic compounds at 150 °C in 80% RH.

To study the influence of interfering VOCs, all four sensors were tested with a different group of VOCs like methanol (CH_3OH), ethanol (C_2H_5OH), 2-propanol (C_3H_8O), acetone (C_3H_6O), formaldehyde (HCHO), n-pentane (C_5H_{12}), toluene (C_7H_8) and xylene (C_8H_{10}) of 50 ppm at 150 °C. All four $SrTiO_3$ sensors (S1-S4) yielded a unique and significant response to ethanol compared to other VOC analytes tested (Fig. 5.9(f)). Among all the sensors, S4 showed the highest response toward ethanol as compared to other sensors, the sensitivity of S4 was relatively high for the analytes like methanol (6) and pentane (15) but significantly smaller than the ethanol (Fig. 5.9(f)). The response of the sensing layer towards different analyte gases depends on their adsorption and desorption kinetics and for better understanding, we have conducted the DFT simulation study for (110) $SrTiO_3$ system for all interactive VOCs. The repeatability was investigated by measuring five successive sensing cycles of the S1-S4 sensors toward 50 ppm of ethanol (Fig. 5.10(a)). Furthermore, the sensing response of the S1-S4 sensors toward ethanol was stable with less than 1.5% signal fluctuation during successive sensing cycles (Fig. 5.10(a)).

Humidity study

The relative humidity is an unavoidable parameter because it changes according to weather, season and location. In a typical application like breath analysis, relative humidity is found to be very high (RH >80%) in exhaled breath and it drastically influences the sensing performance of a gas/VOC sensor to detect any targeted breath component(s) [59-60]. This may be attributed to the water vapor interactions with the negatively charged surface oxygen active sites on the surface of the sensor, where they create chemical bonds in certain atomic sites and form a layer of hydroxyl groups. The competitive adsorption of water molecules with other reacting analytes leads to substantial changes in gas response. The typical water poisoning mechanism of the oxide semiconductor is given by the following reaction: $H_2O + O_{ads}^{-}\ or\ O_{ads}^{-2} \leftrightarrow 2OH + e^{-}(2e^{-})$ [29,30].

The responses of the morphologically varied $SrTiO_3$ sensors are represented to detect 50 ppm ethanol at 150 °C where the relative humidity levels vary from 0 to 80% (Fig. 5.10(b)). The baseline sensors resistance was increased slightly with increased humidity from dry to 80% RH as depicted in Fig. 5.10(b). The high porosity and mean surface roughness (Fig. 5.4(a-d)) of $SrTiO_3$ morphologies were in favour of the elimination of the effect of humidity (Fig. 5.10(b)). Overall, the response to ethanol in humid air decreased slightly with an increase in relative humidity level (bar charts of Fig. 5.10(b)). The influence of humidity on VOC sensing is partially evidenced in S2 and S3 where sensor response was decreased with an increase in the humidity level (Fig. 5.10(b)). Probably, highly porous morphology significantly improved the humidity-tolerant capabilities of those sensors. The hollow sphere morphology with a large number of mesopores provided an irregular surface and gas molecules could easily diffuse easily through these mesopores thus showing a negligible influence on humidity [6,28]. Moreover, the $SrTiO_3$ sensors with different morphologies exhibited p-type conductivity that greatly enhanced their anti-humidity ability and was optimal for sensing performance in harsh environments.

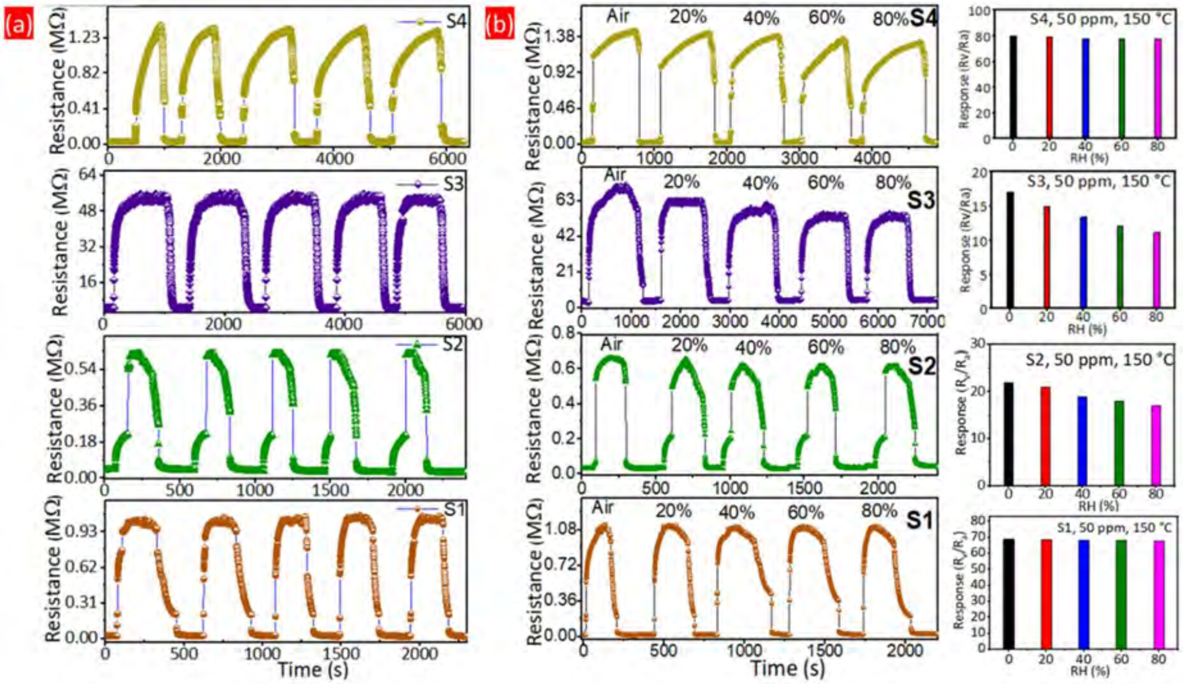

Fig. 5.10. (a) Reproducibility of the sensor on successive exposure to 50 ppm ethanol pulses for all four sensors at 150 °C in 80% RH; (b) dynamic response curves of sensors in the exposure of 50 ppm ethanol at 150 °C under various humidity conditions (0—80% RH) and corresponding bar chart presentation of the response characteristic of the S1-S4 sensors upon exposure to 50 ppm ethanol from dry air to 80% RH at 150 °C.

After the careful evaluation of the sensing characteristics of all four sensors, the S4 sensor showed the best highest sensing response (R_v/R_a: 78 for 50 ppm ethanol) with significant humidity-independent behavior. Undoubtedly, the STO hollow spheres sensors have exceptionally good ethanol sensing properties and selectivity compared to the other reported ones.

5.3 Pd modified $SrTiO_3$ (STO) hollow spheres

5.3.1 Synthesis

Pd modified STO hollow spheres

Hollow spheres were modified with Pd nanoparticles. Pd salt solution was prepared by emerging 17 mg of palladium chloride ($PdCl_2$, Molychem) salt in 100 mL DI water and stabilized by the dropwise addition of dilute HCl with continuous sonication. Later, the hollow sphere powder (0.2 mmol) was first dispersed in a 2 mL aqueous solution of $PdCl_2$ under stirring and then 5 mL of ascorbic acid (AA, 0.1 M) and 5 ml of PEG (polyethylene glycol) were added (1:1). Then suspension undergoes mechanical stirring for 4 h at room temperature the precipitate of Pd modified hollow spheres was collected and washed multiple times with absolute ethanol and DI water multiple times and dried at 80 °C in a vacuum oven. The sensor was marked with Pd-STO-600 sample throughout the study. The schematic representation of synthesis procedure in given in Fig. 5.11.

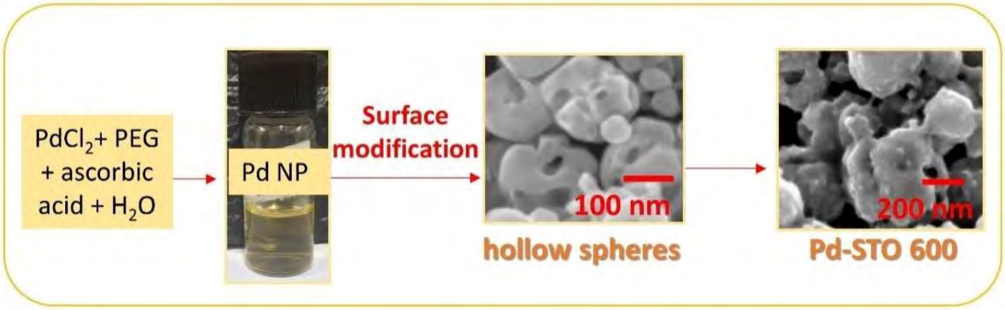

Fig. 5.11. Schematic representation of the experimental procedure used to prepare the Pd modified $SrTiO_3$ hollow spheres-based sensing material.

5.3.2 Characterization

Morphological characterization

The texture of the hollow spheres was changed due to the decoration of Pd nanoparticles (Pd-STO-600, Fig. 5.12(a)). The average size of the Pd-STO-600 hollow sphere (148.8 nm) (Fig. 5.12(b)) was increased as compared to the STO-600 (132.5 nm) possibly due to the dense growth of Pd nanoparticles on its surface (Fig. 5.12(a)). The TEM image in Fig. 5.12(c) exhibited uniform decoration of Pd nanoparticles on the STO hollow sphere. Not only the size but also the catalytic properties during gaseous interaction were increased in the case of Pd-STO-600 [35,36]. The individual and discrete Pd nanoparticles are identified in TEM images (Fig. 5.12(d)) with an average size of 3.75 nm. The high-resolution TEM (HRTEM) image of Pd-STO-600 in Fig. 5.12(e) revealed tausonite (110) crystallinity with a lattice spacing of 0.278 nm. The discrete and high-resolution spots in the selected area electron diffraction (SAED) pattern in the inset of Fig. 5.12(e) confirmed the highly crystalline nature of the STO hollow spheres. The Pd crystallite of (111) with a lattice spacing of 0.24 nm is evident on the tausonite (110) crystal plane of STO (inset in Fig. 5.12(e)). Additionally, the lattice fringe of 0.35 nm agrees well with the (101) plane of anatase

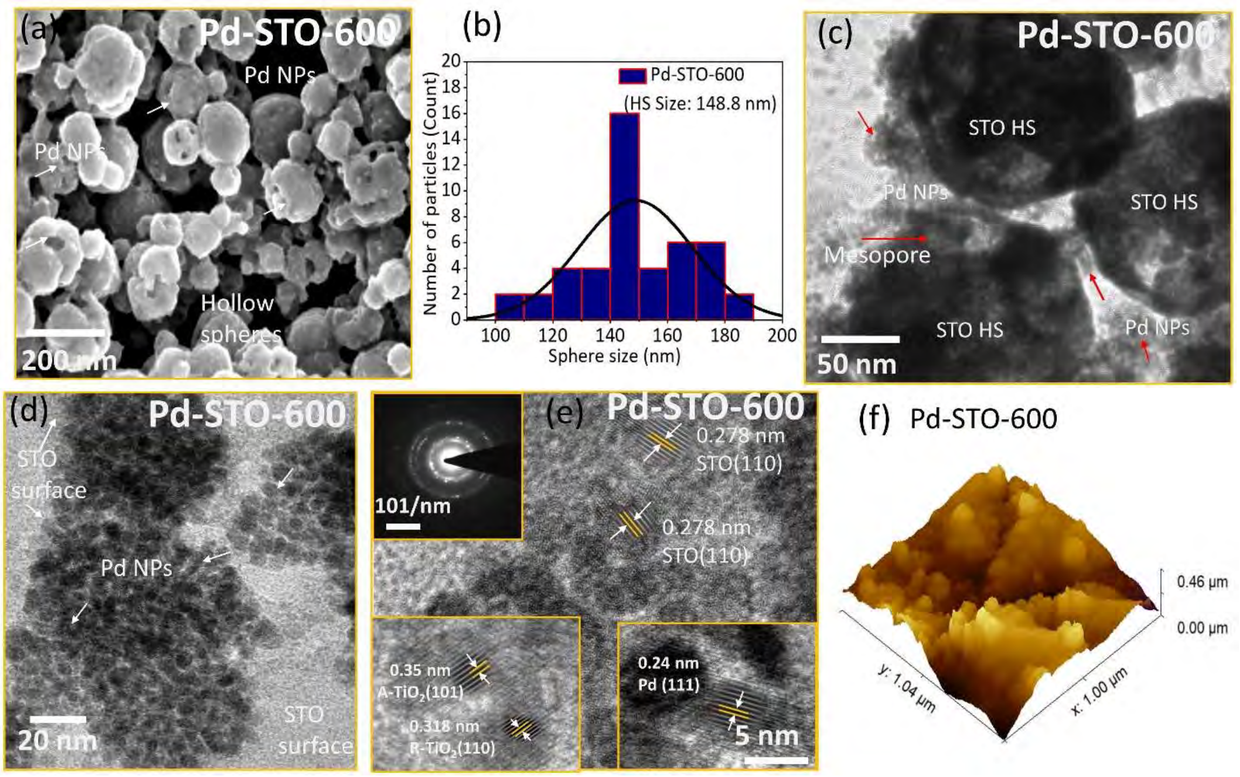

Fig. 5.12. FESEM images of (a) Pd-STO-600 hollow spheres, (b) Size distribution analysis by ImageJ software, (c, d) TEM images at different magnifications; (e) HRTEM images and the inset is showing SEAD pattern and (f) AFM 3D topography images of Pd-STO-600 hollow spheres.

TiO_2, whereas the lattice fringe of 0.318 nm corresponds to the (110) plane of rutile TiO_2 (inset of Fig. 5.12(e)). All the crystal planes evidenced in the HRTEM image are well supported by the XRD spectra in Fig. 5.13.

The topographic image in Fig. 5.12(f) taken from the atomic force microscopy (AFM) revealed the top surface properties of the Pd-STO-600 sample. The mean surface roughness (Sa) for Pd-STO-600 was 58.6 nm which is significantly high compared to the previously reported data [16,34]. Functionalization with Pd metal nanoparticles was also responsible for the enhanced surface roughness [28, 30,3 1].

Structural characterization

The XRD spectra in Fig. 5.13 show the strongest peak at around 2θ = 32° that confirming the existence of the tausonite phase of STO and the crystal plane of (110) for all three samples (JCPDS File No. 35-0734) [21,42]. A few other standard peaks at 39°, 47°, 52°, 57°, 67°, and 76° are assigned to the (111), (200), (211), (220) and (310) planes of STO, respectively [21,42]. A few low-intensity anatase and rutile peaks in Fig. 5.13 confirm that the TiO_2 is not fully converted into STO [43,44]. The most significant peak in all three samples is observed at 2θ = 24.2° which corresponds to anatase (101) crystallinity (JCPDS File No. 21-1272) [44]. STO-600 and Pd-STO-600 showed a low intensity peak at around 2θ = 27.8° indicating rutile (110) crystallinity (JCPDS File No. 88-1175).

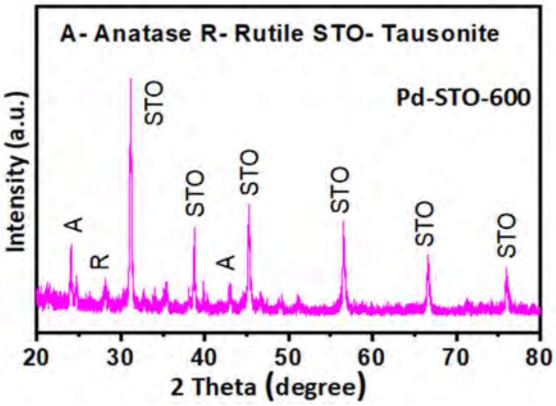

Fig. 5.13. XRD pattern of Pd-STO-600 sensor.

Chemical characterization

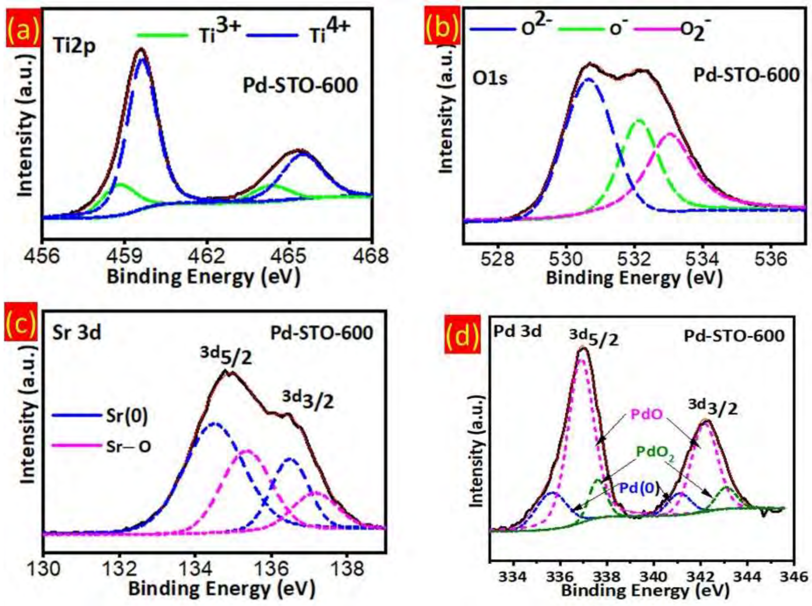

Fig. 5.14. XPS spectra of Pd-STO-600 (a) Ti 2p, (b) O 1s, (c) Sr 3d and (d) Pd 3d.

The high-resolution XPS spectrum of Ti 2p (Fig. 5.14(a)) shows two peaks at the binding energies 459.1± 0.3 eV and 464.40± 0.4 eV, which can be ascribed to Ti $2p_{3/2}$ and Ti $2p_{1/2}$ respectively. Ti 2p peaks are de-convoluted into four peaks as Ti^{3+} $2p_{3/2}$ (457.98 eV), Ti^{4+} $2p_{3/2}$ (458.55 eV), Ti^{3+} $2p_{1/2}$ (463.46 eV) and Ti^{4+} $2p_{1/2}$ (464.45 eV) [45, 46]. The Ti^{4+} state with a peak area of 81.5 % in Pd-STO-600 confirms a highly oxidized surface. The fitted O1s spectra were a combination of three peaks found at 530.4± 0.4 eV, 531.9± 0.1 eV, and 532.9± 0.2 eV (Fig. 5.14(b)) which indicates the lattice oxygen, unsaturated oxygen vacancies and chemisorbed oxygen species, respectively [49]. The Sr 3d spectra of the STO samples (Fig. 5.14(c)) showed two main peaks of Sr $3d_{5/2}$ and Sr $3d_{3/2}$ at 133.7 eV and 135.3 eV, respectively. The presence of other two minor peaks at 134.3 and 136.2 eV, attributed to the non-perovskite bonding (Sr-OH, Sr-Sr, and Sr-O) of $SrTiO_3$ showing the surface sensitivity of the STO towards the interactive analytes [47,48]. Therefore, the non-perovskite bonding peak area was increased in Pd-STO-600. The Pd 3d spectrum of Pd-STO-600 (Fig. 5.14(d)) was deconvoluted into three doublets. The doublets correspond to Pd $3d_{5/2}$ and Pd $3d_{3/2}$ states that appear around (335.5 and 341.0 eV), (336.9 and 342.2) and (337.9 and 343.1) are attributed to the species of Pd(0), PdO and PdO_2 respectively which directly interpret that the highly oxygen functionalized surface due to Pd modification in Pd-STO-600 [61].

Further, a nitrogen adsorption-desorption study of the Pd-STO-600 sample was carried out to obtain information about the specific surface area (m^2/g) and porosity (cm^3/g). Pd-STO-600 sensor exhibited a specific surface area of 13.422 m^2/g and porosity of 7.8365 cm^3/g. The highest surface area for Pd-STO-600 was attributed to the decoration of Pd nanoparticles on STO-600 hollow spheres, which could provide more surface-active sites and available space for the adsorption of gas molecules resulting in excellent sensitivity. Average pore volume was found to be a little less in Pd-STO-600 compared to STO-600 possibly due to the dense decoration of Pd nanoparticles on the STO-hollow sphere surface. But Pd nanoparticles on the STO surface catalyzed the removal of hydroxyls further improving the robustness of the materials towards humidity [28].

Surface wettability study

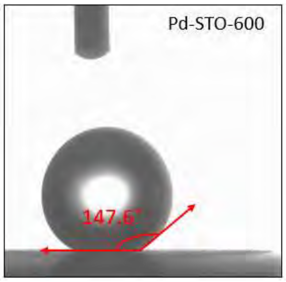

Fig. 5.15. The static water contact angles of Pd-STO-600 sensing film.

In particular, we examined the surface wettability of the Pd-STO-600 sensing film to understand its anti-humidity properties (Fig. 5.14). Pd-STO-600 showed a 147.6° contact angle of the sensing film. However, the results confirm the intact hydrophobic nature of the prepared STO After the Pd modification. The contact angle of Pd-STO-600 was slightly lesser than hollow spheres (Fig. 5.14) but the addition of noble metals minimized the influence of humidity significantly as discussed above [28,30,31].

5.3.3 Sensor study

VOC sensing

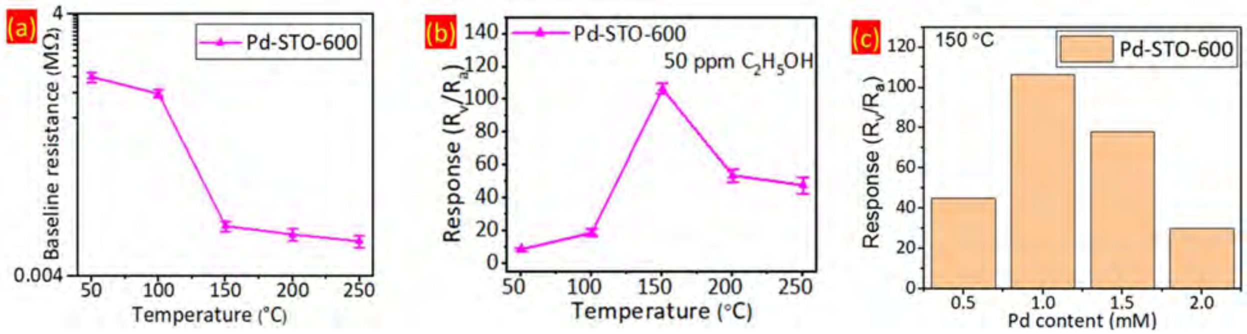

Fig. 5.16. (a) Baseline resistance of the Pd-STO-600 sensor, (b) response of Pd-STO-600 sensor to 50 ppm ethanol at different operating temperatures in 80% RH (generated at 35 ˚C), (c) Response of sensors with different Pd content.

Fig. 5.16(a) is showing the change in the baseline resistance under different operating temperatures. The results show that the resistance of the sensor decreased as the operating temperature increased because thermal excitation energy induced more carriers to the conduction band, thus leading to high conductivity and low resistance [2]. In the case of Pd-modified STO (Pd-STO-600) baseline resistance (~15 kΩ) was lowest due to uniform coverage of metallic Pd nanoparticles to the STO hollow sphere surface which was confirmed by the TEM results (Fig. 5.12(c)).

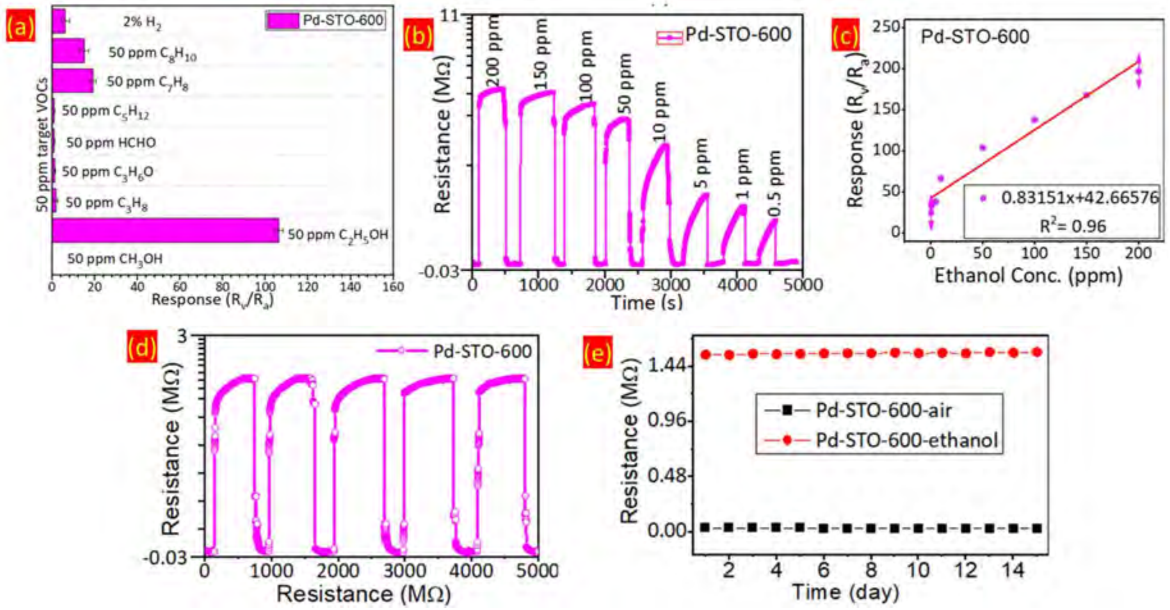

Fig. 5.17. (a) selectivity behavior of all the three sensors towards various volatile organic compounds, (b) Dynamic response to different concentrations of ethanol varying from 500 ppb to 200 ppm, (c) Sensor responses as a function of gas concentration, (d) Reproducibility of the

sensor on successive exposure to 50 ppm ethanol pulses, (e) long-term stability of the Pd-STO-600 sensor at 150 ˚C operating temperature in 80% RH (generated at 35 ˚C).

To evaluate VOC sensing performance, the sensor was tested at different operating temperatures varying from 50 to 250 ˚C in the exposure of 50 ppm ethanol (Fig. 5.16(b)). 150 ˚C was the optimized temperature where all the sensors exhibited the highest response (Fig. 5.16(b)) [27]. The Pd loading effect on ethanol sensing was studied on STO hollow spheres. The most efficient sensing performance was observed for a 1 mM solution of $PdCl_2$. Apart from 1 mM solution, three other $PdCl_2$ solutions were prepared i.e., 0.5 mM, 1.5 mM, and 2 mM and used to functionalize STO hollow spheres. The response towards 50 ppm ethanol was tested for all four samples at 150 °C and represented in the form of a bar chart plot in Fig. 5.16(c). The result concluded that 0.5 mM Pd concentration is not enough for effective sensitization and 2 mM Pd concentration results in a higher metallic sensing surface which also diminishes the sensing response. The intermediate 1 mM and 1.5 mM both were most suitable for Pd functionalization but at 1 mM sensor showed the highest response which was later used in further sensing studies of the Pd-STO-600 sensor. On the other hand, Pd-STO-600 was most interactive with the target analytes exhibiting the highest response (106.4± 2.5 at 150 ˚C) among all the three sensors (Fig. 5.16(b)). Pd-STO-600 with the highest response even at all temperatures might be due to the catalytic properties of Pd nanoparticles which improved the sensing performance of the STO layer [35,36]. To investigate the selectivity of the Pd-STO-600 sensor, the dynamic sensing responses were tested for 50 ppm concentration of a variety of VOCs under 80% RH (generated at 35 ˚C) at 150 ˚C of sensor operating temperature (Fig. 5.17(a)). As Pd is a well-known sensing material for efficient H_2 detection, the selectivity of the sensors was tested in the presence of 2% H_2. Pd-STO-600 exhibited 6 response value in 2% H_2 which is 16 times lower than the response towards 50 ppm ethanol (Fig. 5.17(a)). Pd-STO-600 sensor showed the natural selectivity towards ethanol. Interestingly, methanol and formaldehyde were the most inactive VOCs during the study (Fig. 5.17(a)). Pd-STO-600 with a highly active sensing surface was found to be partially active towards aromatic VOCs (toluene (4) and Xylene (3.4)) (Fig. 5.17(a)). The reason behind the high ethanol selective behavior of STO sensors was probably attributed to the various oxidation states involved in distinctive catalytic activities of STO which promoted the oxidation of ethanol vapor as it shows an affinity with oxygen and multivalent characteristics [62]. Apart from this, the high reactivity of anionic oxygen, the controlled morphology of STO also supported the selective detection of ethanol [62,63]. Additionally, the lowest selectivity towards the smaller molecular size VOCs i.e. methanol and formaldehyde may be due to their less electron-donating capabilities compared to ethanol [64]. On the other hand, poor selectivity towards the VOCs like 2-propanol, n-pentane, toluene and xylene may be attributed to their large molecular size which causes hindrance in the entering and diffusion of analytes molecules through the STO mesopores [62].

The transient response of the Pd-STO-600 sensor was measured in varied ethanol concentrations in 80% RH (generated at 35 ˚C) at an operating temperature of 150 °C (Fig. 5.17(b)). Pd-STO-600 showed a much higher response than STO hollow spheres for all concentrations of ethanol (Fig. 5.17(b)). Additionally, the Pd-STO-600 sensor exhibited the fastest adsorption and desorption of ethanol molecules indicating the chemical sensitization properties of Pd nanoparticles [10,35,36]. Sensing responses were in a near-linear relationship within the ethanol concentration range of 0.5 to 200 ppm. The correlation coefficient (R^2) of the fitting result was calculated as 0.93 for Pd-STO-600 which supports the appreciably good linearity of the sensor (Fig. 5.17(c)).

To evaluate the reproducibility, the Pd-STO-600 sensor was exposed to 50 ppm ethanol for multiple consecutive cycles, purging ethanol for a fixed duration under an 80% RH environment (generated at 35 ˚C) (Fig. 5.17(d)). For long-term stability testing, the Pd-STO-600 sensor was exposed to 50 ppm ethanol at an interval of one day for 15 days (Fig. 5.17(e)). The response magnitude during the test was found relatively stable with a negligible attenuation of 3% which further indicates the promising stability of the STO hollow sphere sensors.

Humidity study

The anti-humidity property of the Pd-STO-600 sensor was carefully evaluated and shown in Fig. 5.18(a, b). The Pd-STO-600 sensors were tested in different humidity conditions (dry air to 80% RH) for 50 ppm of ethanol as shown in Fig. 5.18(a). However, the baseline resistance and response characteristics were almost constant with the increase in relative humidity for all two sensors. A negligibly small decrement in the baseline resistance was observed while changing the ambient from dry air to 80% RH air. Pd-STO-600 was the most humidity-insensitive sensor and exhibited the highest response among the three sensors in the presence of 80% RH (Fig. 5.18(a)). Pd nanoparticles act as a hydroxyl absorber drastically decreasing the response toward humidity

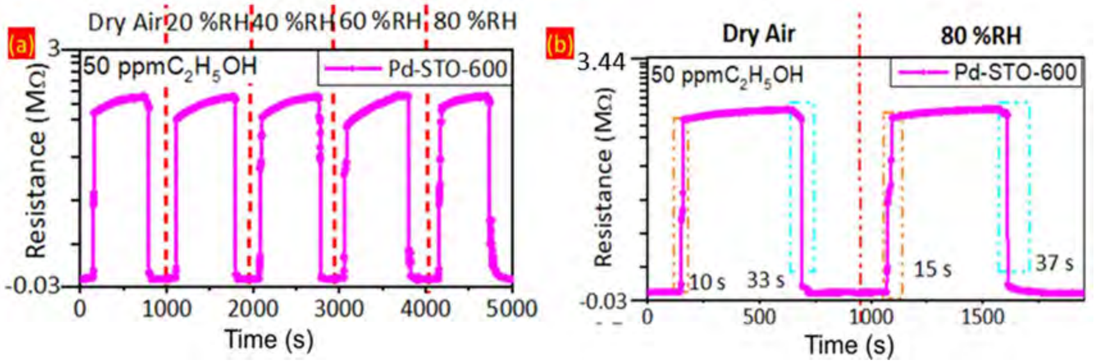

Fig. 5.18. (a) Dynamic response curves of sensor in the exposure of 50 ppm ethanol at 150 ˚C under various humidity conditions, (b) The response and recover characteristics of the Pd-STO-600 sensor upon exposure to 50 ppm ethanol in dry air in 80% RH (generated at 35 ˚C) at 150 ˚C sensor operating temperature.

[32]. Additionally, Pd nanoparticles in Pd-STO-600, dominate the electronic exchange between STO and the ambient by generating new O^{2-} adsorption sites and preventing the adsorption of OH^{-} to the STO surface [30-32].

Fig. 5.18(b) shows the comparative analysis of response–recovery characteristics of STO-based sensors in dry and 80% humid ambient with 50 ppm ethanol at 150 ˚C sensor operating temperature. A negligible attenuation was observed in response and recovery characteristics of sensors in 80% RH. The response/recover times are 15 s/ 37 s for Pd-STO-600 in Air and 80% RH, respectively.

Table 5.5. Comparative sensing performance analysis of $SrTiO_3$ nanostructures for 50 ppm ethanol in 80% RH at 150 °C.

Sensor	**Morphology**	**Sensitivity (Rv/Ra)**	**T_{res}/T_{rec} (s)**	**LOD (ppb)**	**R^2**
S1	Nanograss	69	36/34	78	0.91
S2	Nanorods	16	85/124	88.1	0.89
S3	Nanospheres	12	101/134	152	073
S4	Hollow spheres	75	150/58	57	0.95
Pd-STO-600	Hollow spheres	106.4	15/37	50	0.96

Table 5.5 shows a comparative analysis of the ethanol sensing performance of $SrTiO_3$ based nanostructures at 150 °C and 80% RH. Among all prepared nanostructures, STO hollow spheres showed highly sensitive nature towards ethanol and significant humidity independent behavior with superior hydrophobic properties. Further, Pd modification of the sensor results in improved sensing properties like response, response/recovery time and humidity tolerant nature.

5.3.4 Sensing mechanism of Pd-STO-600 hollow spheres

In the case of unmodified STO sensors, hole transport was conducted through the Schottky barrier formed between two consecutive SrTiO$_3$ hollow spheres (S-S junctions) as shown in Fig. 5.19(a). On the other hand, Pd/SrTiO$_3$ Schottky junctions (M-S junctions) were introduced in the hole transport path that improved the VOC sensing behavior of Pd-STO-600 significantly (Fig. 5.19(b)).

Fig. 5.20(a, b) are showing the Schottky junctions between p-SrTiO$_3$/p-SrTiO$_3$ and p-SrTiO$_3$/Pd/p-SrTiO$_3$, respectively. The schematic in Fig. 5.20(a, b) are well supported by the TEM image shown Fig. 5.12(c) where two distinct cases are visible i.e. (i) direct contact between two STO hollow spheres, and (ii) the connection between two STO hollow sphere through Pd nanoparticles are clearly visible. In the air, oxygen functionalized groups (O^{2-}, O-, O_2^-) are adsorbed to both the inner and outer sides of the sphere through the mesopores and engaged the free dangling bonds lowering the free electron concentration to the STO surface. As a result, the majority carrier holes are accumulated on the STO hollow sphere surface forming a surface potential ($qV_{b\text{-}air}$) as shown in the energy band diagram in Fig. 5.20(c). Ethanol is a strong reducing agent and is considered to form a surface donor state on p-SrTiO$_3$. In the case of p-type SrTiO$_3$, the release of electrons by the surface donor state is expected to lead to a decrease in the effective hole concentration as well as the surface potential ($qV_{b\text{-}VOC}$). As a result, thickness of the hole accumulation region near the STO surface is diminished limiting the overall conductivity of the sensor (Fig. 5.20(c)) [65,66]. However, in hollow sphere structure, both inner and outer surfaces are exposed to the gaseous ambient leading towards a significant modulation of conductivity influenced by target species.

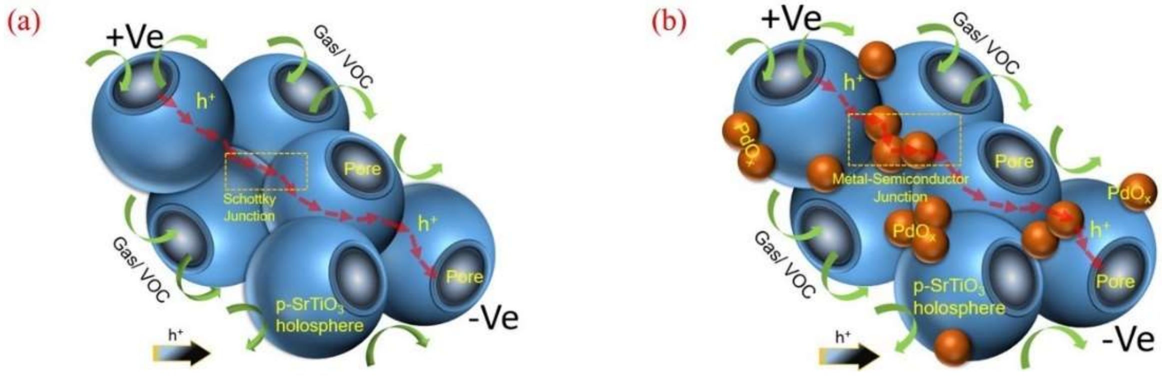

Fig. 5.19. Possible hole transport through the (a) p-SrTiO$_3$ hollow spheres, and (b) Pd nanoparticle decorated p-SrTiO$_3$ hollow spheres.

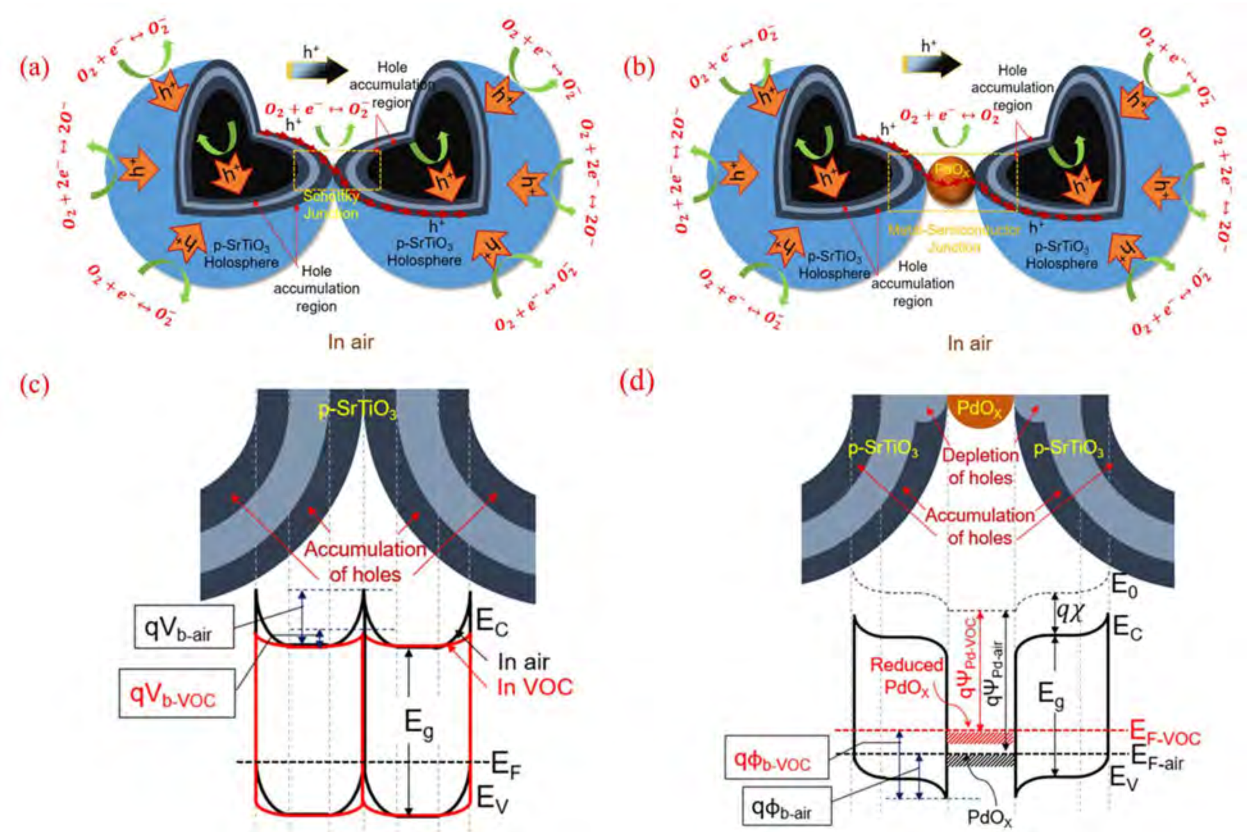

Fig. 5.20. (a) Schematic of intergranular junction between two adjacent hollow spheres, (b) junction between PdO_x and STO hollow sphere, corresponding energy band of (c) STO-STO (S-S) junction and (d) PdO_x-STO (M-S) junction in air and VOC ambient.

To model the current through STO-hollow spheres, Eq. 5.3 is written by considering I_0 as the current in flat band condition (i.e., inert ambient) and $qV_{b\text{-air}}$ and $qV_{b\text{-VOC}}$ as the developed surface potential in the exposure of air and ethanol, respectively. Therefore, k is the Boltzmann's constant and T is the temperature [65]. As the $qV_{b\text{-air}} > qV_{b\text{-VOC}}$ in p-type sensor, current must be higher in air compared to the VOC ambient.

$$I_{air/VOC} = I_0 exp\left(\frac{qV_{b-a\ \ /VOC}}{kT}\right) \tag{5.3}$$

By using Eq. 5.3, response magnitude (RM) in VOC ambient for intergranular S-S junctions of $p\text{-}SrTiO_3$ hollow spheres can be written as in Eq. 5.4.

$$RM \approx exp\left[\frac{(qV_{b-air} - qV_{b-VOC})}{kT}\right] \tag{5.4}$$

In case of surface modification with Pd metallic nanoparticles, two types of mechanisms are mainly involved i.e. (i) "electronic sensitization" which involves the formation of discrete

Schottky junctions and attributes the improved sensing performance to the modulation of the nano-Schottky barriers (Fig. 5.20(b, d)) and (ii) "chemical sensitization" where the catalytic activity of Pd nanoparticles make faster the dissociation of target analytes [56,67,68]. The various oxidation states of Pd (Fig. 5.14(d)) not only enhanced the chemical sensitization but also influenced the electronic sensitization expanding the work function (5.12 eV) of Pd in air. The formation of various oxidation states (PdO_x) increased the work function of Pd ($q\Psi_{Pd-air}$) and decreased the barrier height ($q\varphi_{b-air}$) of the M-S junction in air (Fig. 5.20(d)) [67]. A hole-depleted region is also created in p-$SrTiO_3$ due to the work function difference between PdO_x and p-$SrTiO_3$. In exposure to the VOC (ethanol), PdO_x are reduced fractionally decreasing the work function of Pd ($q\Psi_{Pd-VOC}$) that eventually increase the barrier height ($q\varphi_{b-air}$) of the M-S junction. So, Pd-STO-600 exhibits larger increment in resistance due to extended barrier height ($q\Psi_{Pd-VOC} > q\Psi_{Pd-air}$) in VOC ambient. The barrier height of M-S junction (with p-type $SrTiO_3$) in air/VOC can be represented by the Eq. 5.5, where E_g is the bandgap, $q\chi$ is the electron affinity of semiconductor and $q\Psi$ is the work function of material.

$$q\varphi_{b-air/VOC} = E_{g-SrTiO3} + q\chi_{SrTi} \quad - q\Psi_{Pd\;\frac{air}{VOC}} \tag{5.5}$$

Considering, the modulation of barrier height of M-S junction in air and VOC ambient, response magnitude (RM) can be estimated in Eq. 5.6.

$$RM \approx exp\left[\frac{(q\varphi_{b-VOC} - q\varphi_{b-air})}{kT}\right] \tag{5.6}$$

So, the above discussion confirmed that the variation in built-in potential of S-S junction was principally responsible for the VOC sensing in pure STO-hollow sphere sensor. Whereas, the dual effects i.e. (i) variation in built-in potential of S-S junction and (ii) the change in barrier height of M-S junction simultaneously responsible for the VOC sensing in Pd- STO-600. So, the Pd-modified p-$SrTiO_3$ hollow sphere sensor showed better sensitivity in ethanol.

5.4 Conclusion

In summary, morphology of the $SrTiO_3$ was transformed gradually from nanobush, nanograss, nanorods and nanospheres after 10, 14, 18 and 24 h of hydrothermal reactions, respectively.

Nanospheres were further annealed at 600 ºC and transformed into nano-hollow spheres morphology. The exhaled breath contains a large amount of humidity and become a critical factor in chemiresistive sensors for breath VOC detection. The high surface roughness and hydrophobic surface of $SrTiO_3$ nanoforms motivated us to fabricate the robust sensors for reliable breath VOC detection. All of the $SrTiO_3$ nanoforms showed superior humidity tolerant sensing of the VOCs. The $SrTO_3$ nanoforms showed negligible deviation in ethanol sensing in the range (20%- 80% RH) of humid environment. The highly stable and ethanol sensitive properties of $SrTO_3$ nanoforms sensors were a great achievement in case of breath analysis application. The superior hydrophobicity and moisture resistance behaviour of STO which confirmed by the surface wettability measurement. Among them, hollow sphere was highly sensitive (R_v/R_a of 78) towards ethanol at 150 °C and 80% RH.

Later on, Pd nanoparticles were functionalized on the STO-hollow sphere layer (Pd-STO-600) by chemical route. The Pd-STO-600 sensor with excellent selectivity and ultra-high sensitivity (106.4/ 50 ppm) towards ethanol with fast response /recovery time (38 s/47 s) is highly suitable for breath ethanol sensing. Thereafter, the advanced sensing characteristics of the mesoporous p-type $SrTiO_3$ hollow sphere along with Pd modifications were principally controlled by Schottky barrier model.

Moreover, perovskite materials can be a preferred for robust and humidity tolerant volatile organic compounds (VOCs) detection for breath analysis application. This material is highly applicable for breath ethanol detection with excellent reliability in sensing data at different humidity from RH 20% to RH 80% (generated at 35 ◦C).

References

[1] Y. Jung *et al.*, "Humidity-Tolerant Single-Stranded DNA-Functionalized Graphene Probe for Medical Applications of Exhaled Breath Analysis," vol. 1700068, pp. 1–9, 2017, doi: 10.1002/adfm.201700068.

[2] S. Yang, C. Jiang, S. Wei, S. Yang, C. Jiang, and S. Wei, "Gas sensing in 2D materials," vol. 021304, 2017, doi: 10.1063/1.4983310.

[3] D. Zhang, Z. Yang, S. Yu, Q. Mi, and Q. Pan, "Diversiform metal oxide-based hybrid nanostructures for gas sensing with versatile prospects," *Coord. Chem. Rev.*, vol. 413, p. 213272, 2020, doi: 10.1016/j.ccr.2020.213272.

[4] N. Yamazoe, “Toward innovations of gas sensor technology,” *Sensors Actuators, B Chem.*, vol. 108, no. 1-2 SPEC. ISS., pp. 2–14, 2005, doi: 10.1016/j.snb.2004.12.075.

[5] W. Yan, X. Zeng, H. Liu, C. Guo, M. Ling, and H. Zhou, “Highly reliable and selective ethanol sensor based on α-Fe_2O_3 nanorhombs working in realistic environments,” *Chinese Phys. B*, vol. 28, no. 10, p. 106801, Sep. 2019, doi: 10.1088/1674-1056/ab3af1.

[6] K. D. Esmeryan, T. A. Yordanov, L. G. Vergov, Z. G. Raicheva, and E. I. Radeva, “Humidity Tolerant Organic Vapor Detection Using a Superhydrophobic Quartz Crystal Microbalance,” vol. 15, no. 11, pp. 6318–6325, 2015.

[7] H.-R. Kim, A. Haensch, I. Kim, N. Barsan, U. Weimar, and J. Lee, “The Role of NiO Doping in Reducing the Impact of Humidity on the Performance of SnO_2-Based Gas Sensors: Synthesis Strategies, and Phenomenological and Spectroscopic Studies,” *Adv. Funct. Mater.*, vol. 21, no. 23, pp. 4456–4463, Dec. 2011, doi: 10.1002/adfm.201101154.

[8] H. Trabelsi, M. Bejar, E. Dhahri, M. P. F. Grac, and M. A. Valente, “Applied Surface Science Raman , EPR and ethanol sensing properties of oxygen-Vacancies $SrTiO_{3-1}$ compounds,” vol. 426, pp. 386–390, 2017, doi: 10.1016/j.apsusc.2017.07.128.

[9] Z. Meng *et al.*, “Au nanoparticle modified single-crystalline p-type $LaRhO_3/SrTiO_3$ heterostructure for high performing VOCs sensor,” *Ceram. Int.*, vol. 46, no. 14, pp. 22140–22145, Oct. 2020, doi: 10.1016/j.ceramint.2020.05.290.

[10] N. Y. Chan *et al.*, “Highly sensitive gas sensor by the $LaAlO_3$/ $SrTiO_3$ heterostructure with Pd nanoparticle surface modulation,” *Adv. Mater.*, vol. 26, no. 47, pp. 5962–5968, 2014, doi: 10.1002/adma.201401597.

[11] B. Szafraniak and Ł. Fu, “Semiconducting Metal Oxides: $SrTiO_3$, $BaTiO_3$ and $BaSrTiO_3$ in Gas-Sensing Applications: A Review,” pp. 1–22, 2021.

[12] Hp. E. : L. S. and N. O. giant permittivity and ethanol sensing response in Trabelsi, M. Bejar, E. Dhahri, M. A. Valente, and M. P. F. Graça, “Physica E : Low-dimensional Systems and Nanostructures Oxygen-vacancy-related giant permittivity and ethanol sensing response in $SrTiO_{3-\delta}$ ceramics,” *Phys. E Low-dimensional Syst. Nanostructures*, vol. 108, no. December 2018, pp. 317–325, 2019, doi: 10.1016/j.physe.2018.12.025.

[13] G. Canu, “Hydrothermal synthesis of strontium titanate : thermodynamic considerations , morphology control and crystallisation mechanisms morphological and structural,” pp. 3867–3891, 2017, doi: 10.1039/c7ce00834a.

[14] A. M. Schultz, T. D. Brown, M. P. Buric, S. Lee, K. Gerdes, and P. R. Ohodnicki, “High temperature fiber-optic evanescent wave hydrogen sensors using La-doped $SrTiO_3$ for SOFC applications,” *Sensors Actuators, B Chem.*, vol. 221, pp. 1307–1313, 2015, doi: 10.1016/j.snb.2015.07.046.

[15] X. Zhou, T. Smensen, and Y. Xu, “Defect structure and oxygen sensing properties of Mg-doped SrTiO , thick film sensors,” vol. 41, pp. 177–182, 1997.

[16] V. R. Mastelaro *et al.*, “Ozone gas sensor based on nanocrystalline $SrTi_{1-x}FexO_3$ thin films,” *Sensors Actuators B Chem.*, vol. 181, pp. 919–924, May 2013, doi: 10.1016/j.snb.2013.02.068.

[17] K. Kacem, J. Casanova-Chafer, S. Ameur, M. F. Nsib, and E. Llobet, “Gas sensing properties of graphene oxide loaded with $SrTiO_3$ nanoparticles,” *J. Alloys Compd.*, vol. 941, p. 169011, 2023, doi: 10.1016/j.jallcom.2023.169011.

[18] L. Ji, Y. Jin, K. Wu, C. Wan, N. Yang, and Y. Tang, “Analytica Chimica Acta Morphology-dependent electrochemical sensing performance of metal (Ni , Co , Zn) - organic frameworks,” *Anal. Chim. Acta*, vol. 1031, pp. 60–66, 2018, doi: 10.1016/j.aca.2018.06.008.

[19] V. Kalyani *et al.*, “Hydrothermal Synthesis of $SrTiO_3$: Role of Interfaces,” *Cryst. Growth Des.*, vol. 15, no. 12, pp. 5712–5725, 2015, doi: 10.1021/acs.cgd.5b00770.

[20] L. Dong, H. Shi, K. Cheng, Q. Wang, W. Weng, and W. Han, “Shape-controlled growth of $SrTiO_3$ polyhedral submicro / nanocrystals,” vol. 7, no. 9, pp. 1311–1318, 2014, doi: 10.1007/s12274-014-0495-y.

[21] T. Cao, Y. Li, C. Wang, C. Shao, and Y. Liu, “A facile in situ hydrothermal method to $SrTiO_3/TiO_2$ nanofiber heterostructures with high photocatalytic activity,” *Langmuir*, vol. 27, no. 6, pp. 2946–2952, 2011, doi: 10.1021/la104195v.

[22] X. Yuan *et al.*, “Self-assembly of three-dimensional $SrTiO_3$ microscale superstructures

and their photonic effect," *Inorg. Chem.*, vol. 52, no. 5, pp. 2581–2587, 2013, doi: 10.1021/ic302585g.

[23] H. Amani Hamedani, J. A. Khaleel, K. H. Dahmen, and H. Garmestani, "Surface controlled growth of thin-film strontium titanate nanotube arrays on silicon," *Cryst. Growth Des.*, vol. 14, no. 10, pp. 4911–4919, 2014, doi: 10.1021/cg500374m.

[24] H. Che *et al.*, "Construction of $SrTiO_3/Bi_2O_3$ heterojunction towards to improved separation efficiency of charge carriers and photocatalytic activity under visible light," *J. Alloys Compd.*, vol. 688, pp. 882–890, 2016, doi: 10.1016/j.jallcom.2016.07.311.

[25] M. N. Ha *et al.*, "Morphology-controlled synthesis of $SrTiO_3/TiO_2$ heterostructures and their photocatalytic performance for water splitting," *RSC Adv.*, vol. 6, no. 25, pp. 21111–21118, 2016, doi: 10.1039/c6ra03472a.

[26] H. Trabelsi, M. Bejar, E. Dhahri, M. A. Valente, and M. P. F. Graça, "Physica E : Low-dimensional Systems and Nanostructures Oxygen-vacancy-related giant permittivity and ethanol sensing response in $SrTiO_{3-\delta}$ ceramics," *Phys. E Low-dimensional Syst. Nanostructures*, vol. 108, no. December 2018, pp. 317–325, 2019, doi: 10.1016/j.physe.2018.12.025.

[27] L. Qiu *et al.*, "Sensors and Actuators : B . Chemical Enhanced , stable , humidity-tolerant xylene sensing using ordered macroporous NiO/ZrO_2 nanocomposites," *Sensors Actuators B. Chem.*, vol. 324, no. February, p. 128648, 2020, doi: 10.1016/j.snb.2020.128648.

[28] F. Qu *et al.*, "Surface Functionalized Sensors for Humidity-Independent Gas Detection," *Angew. Chemie - Int. Ed.*, vol. 60, no. 12, pp. 6561–6566, 2021, doi: 10.1002/anie.202015856.

[29] H. Li, C. Lee, D. H. Kim, and J. Lee, "Flexible Room-Temperature NH_3 Sensor for Ultrasensitive , Selective , and Humidity-Independent Gas Detection," 2018, doi: 10.1021/acsami.8b09169.

[30] Y. Qin, X. Wang, and J. Zang, "Sensors and Actuators : B . Chemical Ultrasensitive ethanol sensor based on nano-Ag & ZIF-8 co-modified SiNWs with enhanced moisture resistance," *Sensors Actuators B. Chem.*, vol. 340, no. 92, p. 129959, 2021, doi:

10.1016/j.snb.2021.129959.

[31] G. Rahamim *et al.*, “Sensors and Actuators B : Chemical Hydrogen sensors with high humidity tolerance based on indium-tin oxide colloids,” *Sensors Actuators B. Chem.*, vol. 310, no. December 2019, p. 127845, 2020, doi: 10.1016/j.snb.2020.127845.

[32] K. Suematsu, M. Sasaki, M. Yuasa, and K. Shimanoe, “Antimony-Doped Tin Dioxide Gas Sensors Exhibiting High Stability in the Sensitivity to Humidity Changes,” 2016, doi: 10.1021/acssensors.6b00323.

[33] P. Zhu, S. Li, C. Zhao, Y. Zhang, and J. Yu, “3D synergistical rGO / Eu (TPyP)(Pc) hybrid aerogel for high-performance NO_2 gas sensor with enhanced immunity to humidity,” *J. Hazard. Mater.*, vol. 384, no. October 2019, p. 121426, 2020, doi: 10.1016/j.jhazmat.2019.121426.

[34] R. L. Wilson *et al.*, “Humidity-Tolerant Ultrathin NiO Gas-Sensing Films,” 2020, doi: 10.1021/acssensors.0c00172.

[35] J. H. Lee, A. Mirzaei, J. Y. Kim, J. H. Kim, H. W. Kim, and S. S. Kim, “Optimization of the surface coverage of metal nanoparticles on nanowires gas sensors to achieve the optimal sensing performance,” *Sensors Actuators, B Chem.*, vol. 302, no. September 2019, p. 127196, 2020, doi: 10.1016/j.snb.2019.127196.

[36] M. S. Barbosa, P. H. Suman, J. J. Kim, H. L. Tuller, and M. O. Orlandi, “Investigation of electronic and chemical sensitization effects promoted by Pt and Pd nanoparticles on single-crystalline SnO nanobelt-based gas sensors,” *Sensors Actuators, B Chem.*, vol. 301, no. May, p. 127055, 2019, doi: 10.1016/j.snb.2019.127055.

[37] L. Qi, B. I. Lee, P. Badheka, D. Yoon, W. D. Samuels, and G. J. Exarhos, “Short-range dissolution – precipitation crystallization of hydrothermal barium titanate,” vol. 24, pp. 3553–3557, 2004, doi: 10.1016/j.jeurceramsoc.2003.12.007.

[38] Y. Zhang, L. Zhong, and D. Duan, “Author ’ s Accepted Manuscript from crystalline anatase titanium dioxide,” *Ceram. Int.*, 2015, doi: 10.1016/j.ceramint.2015.07.145.

[39] J. Zeng, H. Wang, Y. Zhang, M. K. Zhu, and H. Yan, “Hydrothermal Synthesis and Photocatalytic Properties of Pyrochlore $La_2Sn_2O_7$ Nanocubes,” pp. 11879–11887, 2007.

[40] S. Zhang, J. Liu, Y. Han, B. Chen, and X. Li, “Formation mechanisms of $SrTiO_3$ nanoparticles under hydrothermal conditions,” vol. 110, pp. 11–17, 2004, doi: 10.1016/j.mseb.2004.01.017.

[41] S. Cho, M. Oledzka, and R. E. Riman, “Hydrothermal synthesis of acicular lead zirconate titanate (PZT),” vol. 226, pp. 313–326, 2001.

[42] S. Tonda, S. Kumar, O. Anjaneyulu, and V. Shanker, “Synthesis of Cr and La-codoped SrTiO3 Nanoparticles for Enhanced,” *Phys. Chem. Chem. Phys.*, vol. 16, no. September, pp. 23819–23828, 2014, doi: 10.1039/C4CP02963A.

[43] I. Morad, M. H. Wasfy, and A. F. Mansour, “Synthesis , structural and electrical properties of PVA/TiO_2 nanocomposite films with different TiO_2 phases prepared by sol – gel technique,” *J. Mater. Sci. Mater. Electron.*, 2020, doi: 10.1007/s10854-020-04313-7.

[44] R. A. C. Amoresi *et al.*, “Electrosteric colloidal stabilization for obtaining $SrTiO_3$/TiO_2 heterojunction: Microstructural evolution in the interface and photonics properties,” *J. Eur. Ceram. Soc.*, vol. 38, no. 4, pp. 1621–1631, 2018, doi: 10.1016/j.jeurceramsoc.2017.10.056.

[45] G. Panchal, D. K. Shukla, R. J. Choudhary, V. R. Reddy, and D. M. Phase, “The effect of oxygen stoichiometry at the interface of epitaxial $BaTiO_3$/$La_{0.7}Sr_{0.3}MnO_3$ bilayers on its electronic and magnetic properties,” *J. Appl. Phys.*, vol. 122, no. 8, p. 085310, Aug. 2017, doi: 10.1063/1.5000133.

[46] J. Liu *et al.*, “In situ green oxidation synthesis of Ti^{3+} and N self-doped $SrTiO_xN_y$ nanoparticles with enhanced photocatalytic activity under visible light,” *RSC Adv.*, vol. 8, no. 13, pp. 7142–7151, 2018, doi: 10.1039/C7RA13523H.

[47] J. Y. Baek, L. T. Duy, S. Y. Lee, and H. Seo, “Aluminum doping for optimization of ultrathin and high-k dielectric layer based on $SrTiO_3$,” *J. Mater. Sci. Technol.*, vol. 42, no. April, pp. 28–37, 2020, doi: 10.1016/j.jmst.2019.12.006.

[48] Z. Saroukhani, N. Tahmasebi, and S. M. Mahdavi, “Effect of working pressure and annealing temperature on microstructure and surface chemical composition of barium strontium titanate films,” vol. 38, no. 6, pp. 1645–1650, 2015.

[49] A. Subramanian and S. Appukuttan, "Sol-gel synthesis and characterization of microencapsulated strontium titanate-myristic acid phase change material for thermal energy storage," *J. Sol-Gel Sci. Technol.*, vol. 94, no. 3, pp. 573–581, Jun. 2020, doi: 10.1007/s10971-019-05084-2.

[50] D. Ahmad, I. Van Den Boogaert, J. Miller, and R. Presswell, "Environmental Effects Hydrophilic and hydrophobic materials and their applications," *Energy Sources, Part A Recover. Util. Environ. Eff.*, vol. 40, no. 22, pp. 2686–2725, 2018, doi: 10.1080/15567036.2018.1511642.

[51] K. R. Wee *et al.*, "Stabilization of ruthenium(II) polypyridyl chromophores on nanoparticle metal-oxide electrodes in water by hydrophobic PMMA overlayers," *J. Am. Chem. Soc.*, vol. 136, no. 39, pp. 13514–13517, 2014, doi: 10.1021/ja506987a.

[52] T. An, X. Deng, Y. Gao, S. Liu, C. Dou, and J. Ju, "Preparation of highly hydrophobic CeO_2 films using glancing angle deposition," *Mater. Lett.*, vol. 216, pp. 147–149, 2018, doi: 10.1016/j.matlet.2018.01.006.

[53] Y. He, D. Li, W. Gao, H. Yin, F. Chen, and Y. Sun, "High-performance NO_2 sensors based on spontaneously functionalized hexagonal boron nitride nanosheets: Via chemical exfoliation," *Nanoscale*, vol. 11, no. 45, pp. 21909–21916, 2019, doi: 10.1039/c9nr07153a.

[54] J. Wang *et al.*, "Regulation of oxygen vacancies in $SrTiO_3$ perovskite for efficient photocatalytic nitrogen fixation," *J. Alloys Compd.*, vol. 902, no. 0001, p. 163865, May 2022, doi: 10.1016/j.jallcom.2022.163865.

[55] A. Hazra, S. Member, K. Dutta, S. Member, B. Bhowmik, and S. Member, "Highly Repeatable Low-ppm Ethanol Sensing Characteristics of p-TiO_2 -Based Resistive Devices," vol. 15, no. 1, pp. 408–416, 2015.

[56] A. Hazra, S. Das, J. Kanungo, C. K. Sarkar, and S. Basu, "Studies on a resistive gas sensor based on sol–gel grown nanocrystalline p-TiO_2 thin film for fast hydrogen detection," *Sensors Actuators B Chem.*, vol. 183, pp. 87–95, Jul. 2013, doi: 10.1016/j.snb.2013.03.113.

[57] A. S. Bittner, E. S. Cross, D. H. Hagan, C. Malings, E. Lipsky, and A. P. Grieshop, "Performance characterization of low-cost air quality sensors for off-grid deployment in rural Malawi," *Atmos. Meas. Tech.*, vol. 15, no. 11, pp. 3353–3376, 2022, doi: 10.5194/amt-15-3353-2022.

[58] M. Wu *et al.*, "Ti_3C_2 MXene-Based Sensors with High Selectivity for NH_3 Detection at Room Temperature," *ACS Sensors*, vol. 4, no. 10, pp. 2763–2770, 2019, doi: 10.1021/acssensors.9b01308.

[59] C. Liu *et al.*, "Sensors and Actuators : B . Chemical Local Gaussian process regression with small sample data for temperature and humidity compensation of polyaniline-cerium dioxide NH_3 sensor," *Sensors Actuators B. Chem.*, vol. 378, no. December 2022, p. 133113, 2023, doi: 10.1016/j.snb.2022.133113.

[60] Z. Yuan, Q. Zhao, Z. Duan, C. Xie, X. Duan, and S. Li, "Sensors and Actuators : B . Chemical Ag 2 Te nanowires for humidity-resistant trace-level NO_2 detection at room temperature," *Sensors Actuators B. Chem.*, vol. 363, no. 2, p. 131790, 2022, doi: 10.1016/j.snb.2022.131790.

[61] J. X. Tang *et al.*, "Screw-like PdPt nanowires as highly efficient electrocatalysts for methanol and ethylene glycol oxidation," *J. Mater. Chem. A*, vol. 6, no. 5, pp. 2327–2336, 2018, doi: 10.1039/c7ta09595c.

[62] A. Kolmakov, D. O. Klenov, Y. Lilach, S. Stemmer, and M. Moskovits, "Enhanced Gas Sensing by Individual SnO_2 Nanowires and Nanobelts Functionalized with Pd Catalyst Particles," 2005.

[63] H. Kim and J. Lee, "Highly sensitive and selective gas sensors using p-type oxide semiconductors: Overview," *Sensors Actuators B Chem.*, vol. 192, pp. 607–627, Mar. 2014, doi: 10.1016/j.snb.2013.11.005.

[64] R. Khatoon *et al.*, "Design of highly sensitive and selective ethanol sensor based on α-Fe_2O_3 /Nb_2O_5 heterostructure," *Nanotechnology*, vol. 32, no. 19, p. 195503, May 2021, doi: 10.1088/1361-6528/abdd5e.

[65] Q. Sun *et al.*, "Increased Active Sites and Charge Transfer in the SnS_2/TiO_2

Heterostructure for Visible-Light-Assisted NO_2 Sensing," *ACS Appl. Mater. Interfaces*, vol. 13, no. 45, pp. 54152–54161, Nov. 2021, doi: 10.1021/acsami.1c16095.

[66] T. Gakhar and A. Hazra, "p -TiO_2/GO heterojunction based VOC sensors : A new approach to amplify sensitivity in FET structure at optimized gate voltage," vol. 182, no. January, pp. 0–2, 2021.

[67] D. Zhang, C. Jiang, and X. Zhou, "Talanta Fabrication of Pd-decorated TiO_2/MoS2 ternary nanocomposite for enhanced benzene gas sensing performance at room temperature," *Talanta*, vol. 182, no. February, pp. 324–332, 2018, doi: 10.1016/j.talanta.2018.01.064.

[68] P. Bindra and A. Hazra, "Electroless deposition of Pd/Pt nanoparticles on electrochemically grown TiO_2 nanotubes for ppb level sensing of ethanol at room temperature," *Analyst*, vol. 146, no. 6, pp. 1880–1891, 2021, doi: 10.1039/d0an01757d.

Chapter-6

$SrTiO_3$ passivated MXene ($Ti_3C_2T_x$) for efficient acetone detection

6.1 Introduction

Mxene is a new-age 2D material that attracted wide attention from researchers due to its plenty of excellent physicochemical, electronic and mechanical properties. A variety of applications such as; supercapacitors [1], photocatalytic degradation [2], hydrogen evolution [3], Li-ion batteries [3] and gas sensing [4] are employed with MXenes and achieve marvelous outcomes and benefits. In general, MXene is a carbide and nitride of transition metal with a general formula of $M_{n+1}X_nT_x$, here T_x representing the surface terminations, such as -O, -OH, -F, etc. which are bonded to the outer M layers [3]. Mxenes originated from their parental MAX phase where the 'A' element (Al, Si, P, S, Ga, etc.) is selectively etched using a suitable etchant such as HF, LIf/HCl, etc. [5,6]. The extremely high specific surface area, miscellaneous chemical and electronic properties, improved surface properties, integrability with planar electronic devices and good hydrophilicity make the MXenes appropriate as promising gas sensing material [7,8]. Most interestingly, MXenes can adsorb many terminations functional groups on its surface, and by modulating these surface groups, MXene can change its semiconducting properties which are highly favorable in gas/VOC sensing [5,6]. Pristine MXenes such as $Ti_3C_2T_x$ [9,10], Ti_3C_2 [5,11], $V_4C_3T_x$ [12], and Mo_2CT_x [13] are used for the detection of various gases and VOCs. Mainly, NH_3 [5], acetone [9,12], and toluene [13] are detected by different types of pristine MXenes.

However, low thermal and chemical stability of MXenes, and drift in sensing properties is a highly concerning factor for device fabrication as the fabricated sensors undergo various environmental conditions. To overcome these limitations researchers emphasized to synthesis MXene-based composite for advanced-level detection VOCs like acetone [14-17, 19]. In this scenario, oxidation of MXene is quite easy way to synthesize MXene/TiO_2 composite [7,8]. The partial oxidation increases specific surface area, defects, or oxygen functional groups, formation of multiple Schottky barriers (SB) and stability in the MXene-based sensors [7].

Breath analysis involves the efficient detection of breath VOCs in exhaled breath of humans and gathering considerable attention from researchers. The complexity of exhaled breath is well known and requires a sensor system with high selectivity towards biomarker VOCs at the sub-ppm level to work under extreme physiological environments (saturated humidity, ≥ 50% RH) [18]. Acetone is the prominent breath marker for diabetes mellitus and the concertation of acetone ranges between 300-900 ppb which was increased to ~2.2 and ~1.7 ppm in patients [14]. Researchers have tried to synthesize various MXene composites to make a more compatible sensor for detection and achieving higher selectivity [15], low ppb detection [14,16], higher sensitivity [17] and faster detection rate [19] for breath analysis application. A few researches have been reported on pristine MXene based sensors for breath acetone detection but have not considered the effect of humidity on the sensing performance [14,15]. Majhi et al. reported accordion-like $Ti_3C_2T_x$ based sensors for the detection sub ppb level acetone for breath analysis with a lower detection limit of 250 ppb at room temperature [15].

MXene and its composite-based sensors are highly affected by humidity in which baseline resistance is shifted significantly modulating the sensor response [14,17,19]. Mxene shows hydrophilic properties and a high-humidity interactive nature [20-24]. To achieve humidity stability in MXene, several techniques have been adopted to create a hydrophobic overlayer on hydrophilic material (i.e., Mxenes) [20,25-27]. In this regard, overlayer or coating of perovskite like $SrTiO_3$ on an MXene sensor could be a remarkable approach because $SrTiO_3$ shows highly hydrophobic properties, morphological stability, good thermal and chemical stability, tunable semiconducting properties and porous morphology [28-31]. In our previous chapters, we have found that SrTiO3 is highly humidity tolerant material.

In the current study, we are reporting a novel approach to establish stable MXene-based sensors appropriate to work under highly humid atmospheres. To achieve this, a passivation layer of $SrTiO_3$ was grownup on MXene by using a hydrothermal route. An MXene channel uniformly covered with a thin $SrTiO_3$ overlayer prevented the direct interactions of water molecules. The $SrTiO_3$ coated MXene sensor (STO/MX-12) exhibited excellent humidity-tolerant sensing towards acetone and ensured ultrahigh response, good selectivity, excellent reversibility, and rapid response/recovery at optimized 150 °C. Such unprecedented sensing capabilities in terms of sensing response, baseline resistance, and response/recovery time was well maintained at each humidity level (20 to 80% RH). In addition, the sensor showed a noticeable response (R_v/R_a)

value of 2.2 to the very low concentration (100 ppb) of acetone which confirmed its potentials in breath acetone detection to diagnose the disease like diabetes mellitus.

6.2 Synthesis

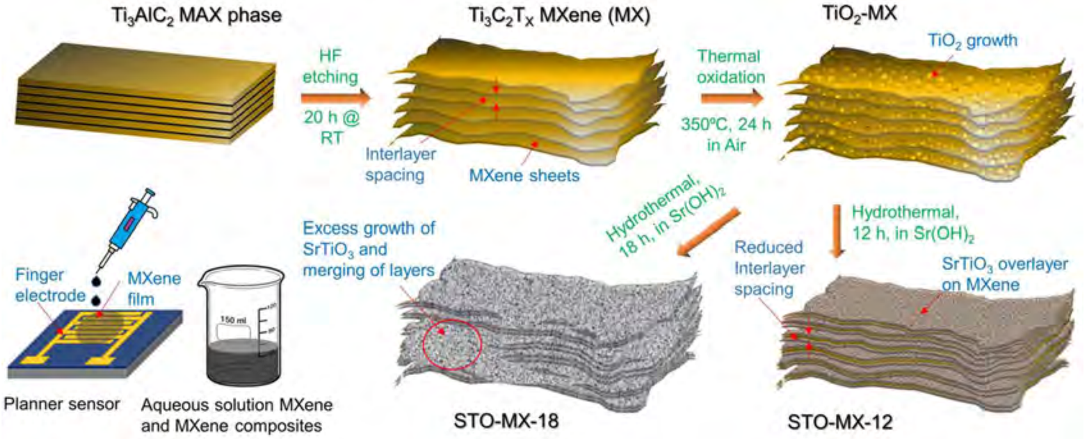

Fig. 6.1. Synthesis flow of MXene and its composites by various routes.

Synthesis of TiO_2/MX

$Ti_3C_2T_x$ MXene powder was first partially oxidized by annealing at 350 °C for 24 h in air ambient. Annealing at such a specific temperature was further encouraged by the results from previous literature, 350 °C was the safest temperature where the maximum of the MXene materials sustain their properties and form a noticeable amount of semiconducting TiO_2 [4,8].

Synthesis of STO/MX

A hydrothermal reaction was carried out where 30 mg of $TiO_2/Ti_3C_2T_x$ powder was dispersed in an 80 mL aqueous solution of 15 mg $Sr(OH)_2\cdot 8H_2O$. The suspension was transferred in a Teflon-lined autoclave and placed inside a hot oven for a hydrothermal reaction to prepare STO/$Ti_3C_2T_x$ hybrid heterostructures. The hydrothermal reaction was done for two different reaction times i.e., 12 h and 18 h, and a constant 180 °C reaction temperature. Later, the resulting precipitate was washed multiple times with water and ethanol to eliminate organic impurities and dried in the air.

The suspension of all four samples (MX, TiO_2/MX, STO/MX-12, and STO/MX-18) was prepared by adding 0.5 mg powder in 1 ml of distilled water followed by sonication for 20 minutes. 5 µL of dispersed suspensions were drop casted onto the 150 nm thick Au interdigitized electrodes. Four sensors, prepared by the above-discussed methods, are marked as; MX, TiO_2/MX, STO/MX-12 and STO/MX-18. The overall flow of synthesis procedure is given in Fig. 6.1.

6.3 Characterizations

Morphological characterizations

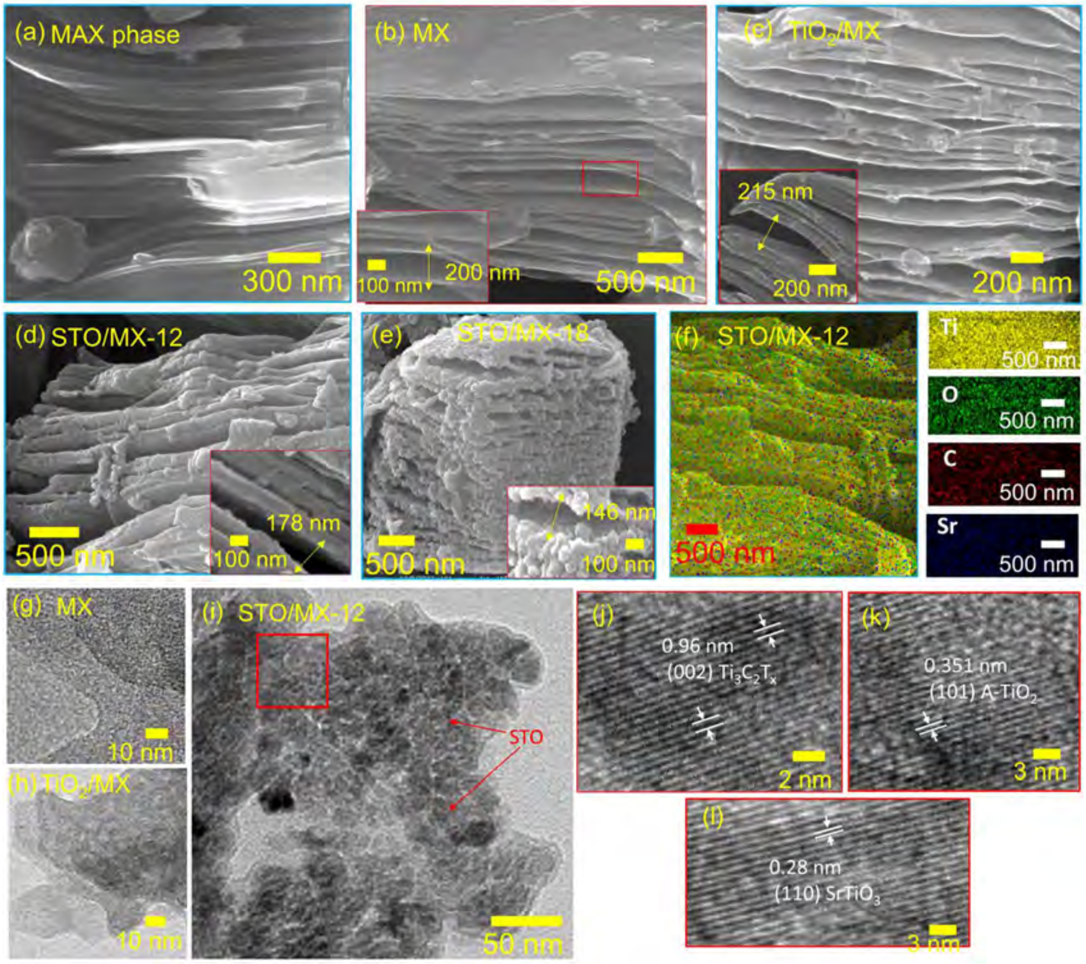

Fig. 6.2. FESEM images of (a) MAX phase before exfoliation; (b) MX; (c) TiO_2/MX; (d) STO/MX-12 and (e) STO/MX-18 nanocomposites; (f) EDX elemental mapping images of Ti, C, O and Sr of STO/MX-12 sample; (g-i) TEM images of MXene; TiO_2/MX; STO/MX-12, respectively and (j-l) HRTEM images of STO/MX-12 sample.

The FESEM analysis was performed to understand the morphological changes in MXene sheets with the different compositional changes (Fig. 6.2(a-e)). Fig. 6.2(a) shows the tightly bounded sheets in the unetched MAX phase (Ti_3AlC_2). The Unetched MAX phase was further treated with suitable etchants and delaminating agents to achieve a typical accordion-like multilayer structure with a smooth surface of $Ti_3C_2T_x$ MXene (Fig. 6.2(a)). The exfoliated sheets with a wide separation indicated the successful removal of Al from the MAX phase as shown in Fig. 6.2(b). The inset image (Fig. 6.2(b)) shows a close view of the spaced layer with average interlamination spacing of 200 nm. Oxidation of MXene at an optimum temperature leads to the formation of TiO_2 into the material which also improves the interlayer spacing between the hierarchical structure (Fig. 6.2(b)). The formation of TiO_2 in MXene sheets resulted in an increased interlayer spacing (inset of Fig. 6.2(b)). The amount of oxidation depends mainly upon oxidation temperature and time [8]. The $Sr(OH)_2.8H_2O$ reaction with TiO_2/MXene for 12 h resulted in the overlayer of $SrTiO_3$ (STO) on MXene sheets and the thickness of the individual sheets was increased simultaneously by decreasing their separation (Fig. 6.2(c)). The inset shows the uniform deposition of STO on sheets with an average inter-sheet spacing of 158 nm (Fig. 6.2(b)). A significant change in the STO decoration was observed when the reaction time was increased up to 18 h and sheets were densely coated with STO nanoparticles (Fig. 6.2(d)). Consequently, the excess STO leads to the lowest spacing between the sheets with an average value of 120 nm (inset of Fig. 6.2(d)). The EDS mapping estimated the chemical distribution in STO/MX-12 sample and confirmed the signals of Ti, C, O and Sr (Fig. 6.2(f)). The distribution of Sr and O elements in the STO/MX-12 composite was homogeneous in the characterized area. The results confirmed the uniform growth of STO on $Ti_3C_2T_x$ sheets (Fig. 6.2(f)).

The detailed analysis of structural changes in MXene and composites was studied with TEM and HRTEM analysis. Fig. 6.2(g) shows the TEM image of MXene sheets lying on each other. TiO_2/MX TEM image (Fig. 6.2(h)) displays some nonuniformity on the top of the sheets. The TEM image of STO/MX-12 shows the clear decoration of STO on a single MXene sheet (Fig. 6.2(i)). Moreover, the HRTEM images of a selected area from the TEM image (Fig. 6.2(i)) showed the coexistence of lattice fringes of all three MXene, TiO_2 and STO (Fig. 6.2(j-l)). The estimated lattice fringes spacing for MXene, TiO_2, and STO were 0.96 nm, 0.35 nm and 0.28 nm attributed to the (002) [22,32], (101) [33] and (110) [28] crystal planes, respectively. These results demonstrate the successful formation of the heterogeneous interface between MXene, TiO_2 and STO in STO/MX-12 nanocomposite to facilitate improved VOC sensing properties [42].

Structural characterizations

To examine the formation of TiO_2 and then STO on the $Ti_3C_2T_x$ MXene in more detail we executed X-ray diffraction (XRD), Raman spectroscopy and X-ray photoelectron spectroscopy (XPS) experiments as shown in Fig. 6.3. The XRD spectra in Fig. 6.3(a) show the diffraction peaks for all four samples. The MX sample has a number of diffraction peaks at 9.34°, 18.6° and 27.9° attributed to (002), (004) and (006) crystallinity in 2D $Ti_3C_2T_x$ MXene which is also a consequence of the Al etching from the Ti_3AlC_2 MAX phase [34, 35]. The series of MXene peaks confirms a layered structure of stacked sheets with an interplanar distance of 0.96 nm [36]. Oxidation of MXene results in the peak of anatase TiO_2 at 24.9° corresponding to (101) anatase plane as visible in Fig. 6.3(a). The broader peak could be due to the formation of the small crystallite size of TiO_2 or plenty of lattice defects during the oxidation process (300 °C) [37]. The STO formation in the remaining two samples leads to the characteristic peaks of cubic symmetry at 32.4° matching with (110) crystal plane as shown in Fig. 6.3(a) [38]. The intensity and sharpness of the peaks were increased in STO/MX-18 sample compared to the 12h sample (Fig. 6.3(a)). The XRD results were completely coincidence with the TEM and HRTEM results (Fig. 6.2).

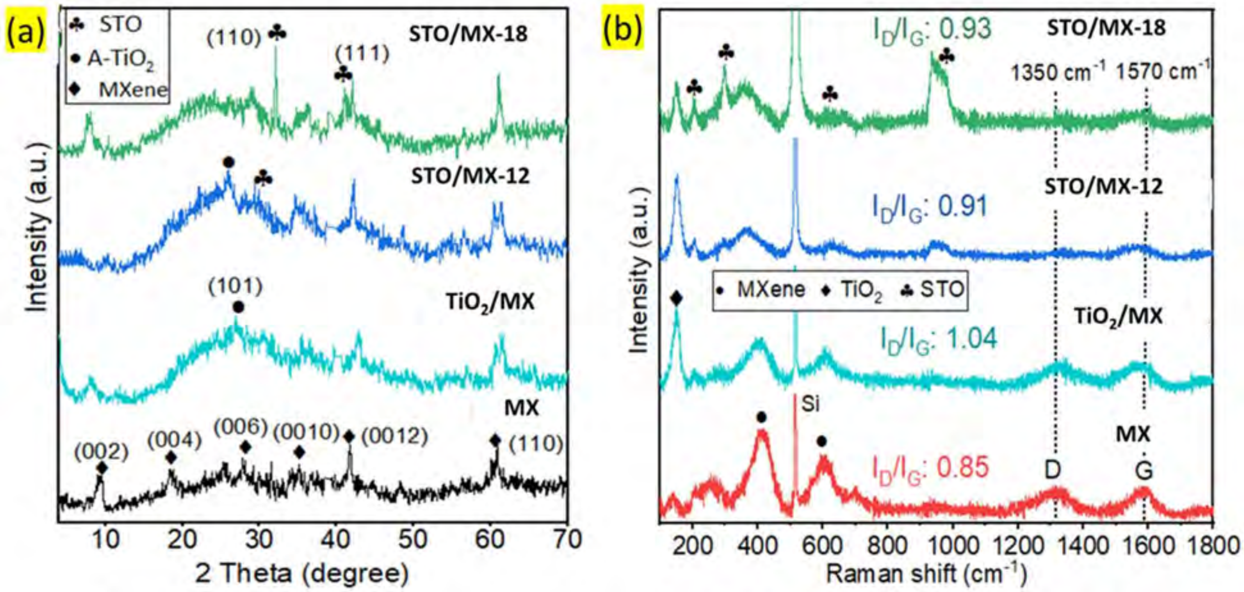

Fig. 6.3. (a) XRD spectra; (b); Raman spectra of MX, TiO_2/MX, STO/MX-12 and STO/MX-18 nanocomposites, respectively.

Raman spectra were recorded to identify the structural modifications in the materials (Fig. 6.3(b)). In pure $Ti_3C_2T_X$, the peaks at 390 and 620 cm^{-1} belong to the A1g signals arising from the presence of –OH, –O, and–F functional groups on the surface. The vibration modes for Ti-Al were missing in the resulting spectrum, confirming the successful etching [39,40]. The two broad peaks at 1350 and 1570 cm^{-1} were observed corresponding to the D and G peaks resulting from the formation of graphitic carbon during the etching process [39,40]. The oxidation process results in a strong band at 149 cm^{-1}, illuminating anatase-TiO_2 as shown in Fig. 6.3(b) [41]. The STO overlayer formation in STO/MX-12 and STO/MX-18 samples, consequences in four bands at 210, 307, 609 and 990 cm^{-1} as shown in Fig. 6.3(b) [38]. The graphitic carbon in MXene acts as an electron channel between the $Ti_3C_2T_x$, TiO_2 and STO as they are closely connected with each other [39]. The Raman spectra of STO/MX-12 and STO/MX-18 samples show the existence of D and G peaks indicating the interaction and coexistence of STO over $Ti_3C_2T_X$. Whereas, the intensity of D and G peaks started decreasing as the formation of TiO_2 and STO proceeded (Fig. 6.3(b)). The I_D/I_G value of TiO_2/MXene composite increased compared with that of pure MXene, indicating slight damage to the graphitized carbon during oxidation (Fig. 6.3(b)). But STO addition leads to a decrease in D peak which consequently decreases the I_D/I_G STO/MXene samples compared to the TiO_2/MX confirming the decreased defect density in the form of surface functional groups in STO-modified samples [39,40]. Moreover, the above results verified strong interaction and boosted charge transfer between the MXene and STO [40].

Chemical characterization

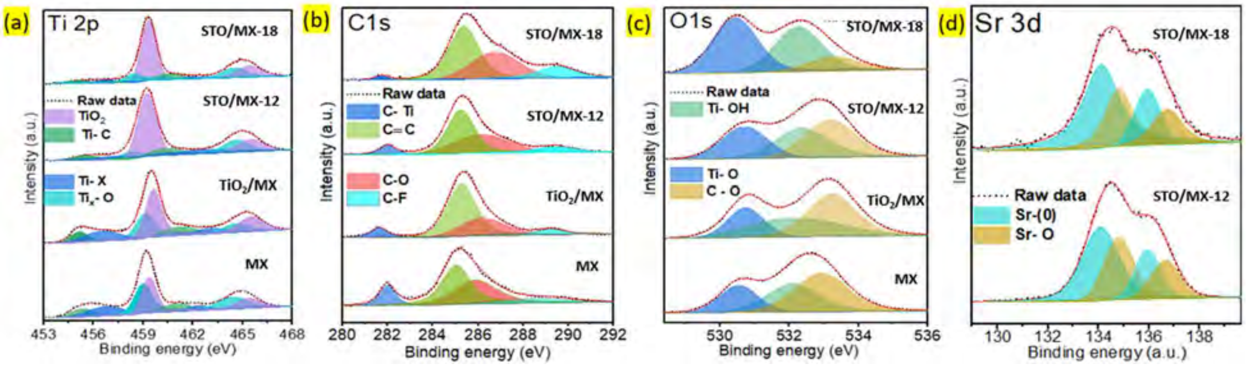

Fig. 6.4. XPS spectra for (a) Ti 2p; (b) C 1s; (c) O 1s and (d) Sr 3d of MX, TiO_2/MX, STO/MX-12 and STO/MX-18 nanocomposites, respectively.

Fig. 6.4(a) shows the Ti 2p peaks for the MX, TiO_2/MX and STO/MX samples with four doublets for Ti $2p_{1/2}$ and Ti $2p_{3/2}$ whereas each doublet is separated by 5.9 eV. The pristine $Ti_3C_2T_x$ was deconvoluted into four peaks corresponding to the Ti−C (Ti^+), Ti−X (Ti^{2+}), Ti_xO_y

(Ti^{3+}), and TiO$_2$ (Ti^{4+}), respectively, where Ti−X corresponds to substoichiometric titanium carbide or titanium oxycarbides (Table 6.1) [6, 42]. In TiO$_2$/MXene, the peak intensity and area of TiO$_2$ was increased and for other peaks were decreased (Table 6.2). The SrTiO$_3$ formation leads to the highest intensity oxidation peak (Ti^{+}) in STO/MX-12 and STO/MX-18 while Ti-C peak is decreased as shown in Fig. 6.4(a) [34]. Fig. 6.4(b) shows the C 1s spectra fitted into four peaks corresponding to the C-Ti, C=C, C-O, and C-F, respectively (Table 6.1). The intensity of the C-Ti peak starts decreasing as the oxidation and Sr modification are progressed because the Ti-C bonds on the surface and edges start breaking and converting into Ti-O and Sr-O bonds as visible in Fig. 6.4(b) [7]. The O 1S spectra (Fig. 6.4(c)) were deconvoluted into three peaks credited to Ti-OH, Ti-O-Ti, and C-OH, respectively (Table 6.1) [22]. In pristine MXene, plentiful oxygen functional groups are present on the surface and edges which are beneficial for gas or VOC sensing. These oxygen functional groups are also sensitive to humidity and significantly modulate the sensing

Table 6.1. Binding energy (eV) of the deconvoluted peaks of MX, TiO$_2$/MX and STO/MX samples.

Sample	**2p$_{3/2}$ (Ti-C, Ti-X, Ti$_x$-O, TiO$_2$)**	**2p$_{1/2}$ (Ti-C, Ti-X, Ti$_x$-O, TiO$_2$)**	**O 1s (Ti-O, Ti-OH, C-O)**	**C 1s (C-Ti, C=C, C-O, C-F)**	**Sr-0 (3d$_{5/2}$, 3d$_{3/2}$)**	**Sr-O (3d$_{5/2}$, 3d$_{3/2}$)**
MX	455.3, 456.7, 458.9, 459.3	461, 462.3, 464.3, 465.3	530.6, 532.3, 533.1	281.9, 285.1, 285.9, 289.2	-	-
TiO$_2$/MX	455.1, 456.5, 459, 459.4	461.2, 462.3, 464.5, 465.4	530.7, 532.1, 533.2	281.9, 285.2, 286.1, 289.4	-	-
STO/MX-12	455.1, 456.7, 458.3, 459.3	460.9, 462.5, 464.4, 465.3	530.5, 532.1, 532.9	281.7, 285.3, 286.1, 289.2	134, 135.9	134.8, 136.6
STO/MX-18	455.2, 456.8, 458.2, 459.2	460.7, 462.5, 464.5, 465.4	530.4, 532.2, 533.3	281.9, 285.3, 286.1, 289.4	134.1, 135.9	134.8, 136.7

Table 6.2. Relative area (%) estimation of the deconvoluted peaks of MX, TiO$_2$/MX and STO/MX samples.

Sample	**2p$_{3/2}$ (Ti-C, Ti-X, Ti$_x$-O, TiO$_2$)**	**2p$_{1/2}$ (Ti-C, Ti-X, Ti$_x$-O, TiO$_2$)**	**O 1s (Ti-O, Ti-OH, C-O)**	**C 1s (C-Ti, C=C, C-O, C-F)**	**Sr-0 (3d$_{5/2}$, 3d$_{3/2}$)**	**Sr-O (3d$_{5/2}$, 3d$_{3/2}$)**
MX	8.2, 15.4, 24.3, 22	6, 3, 12.8, 8.3	28.7, 34.7, 36.2	12.9, 43.1, 36.7, 7.3	-	-
TiO$_2$/MX	7.1, 13.9, 19.5, 30.7	6.7, 3.5, 6.8, 11.8	22.3, 34.3, 43.1	7.9, 49.1, 36.2, 6.8	-	-
STO/MX-12	3.4, 3.4, 11.4, 45.9	6.2, 2.6, 12, 14.7	21.8, 33.7, 44.5	8.7, 60.3, 26.5, 4.5	60.3	39.7
STO/MX-18	5.2, 4.3, 7.7, 46.7	6.4, 5.9, 11.6, 11.8	48.5, 39.7, 11.8	1.8, 50.4, 34.4, 13.4	63.7	36.3

characteristics [24]. But the STO overlayer formation in STO/MX-12 and STO/MX-18 samples result in increasing peak intensity of the Ti-O band and simultaneous decreasing peak intensity for O-H and C-O band that indicates the fractional removal of hydroxyl groups from MXene surface [7,42]. The Sr 3d spectra of STO/MX-12 and STO/MX-18 samples are given in Fig. 6.4(d). The peaks were fitted in two doublets consisting of two peaks which correspond to perovskite (Sr-(0)) and non-perovskites bonding in STO such as Sr-OH, Sr-CO, Sr-Sr, and Sr-O bonds at the surface (Table 6.1) [28,43]. STO/MX-12 exhibited more non-perovskite bonds as compared to the 18h sample (Fig. 6.4(d)).

Surface wettability study

The surface water contact angle of all four MXene-based sensor films was analyzed as shown in Fig. 6.5. After the long hydrothermal treatment, the sensors based on STO/MX-12 and STO/MX-18 composites exhibit obvious humidity-tolerant response properties. From the hydrophilic nature of pure MXene with a contact angle of 43° (Fig. 6.5(a)) [24,47] to achieving an excellent hydrophobic sensing surface by STO coating and achieving a contact angle of 104° and 113° for STO/MX-12 and STO/MX-18 sensors, respectively (Fig. 6.5(c, d)). Pristine MXene disperses in water because of the hydrophilic functional groups (e.g., =O, –OH, and –F) on their surface [27]. Still, water repellent nature of STO@$Ti_3C_2T_x$ could be due to the hydrophobic properties of STO (Fig. 6.5).

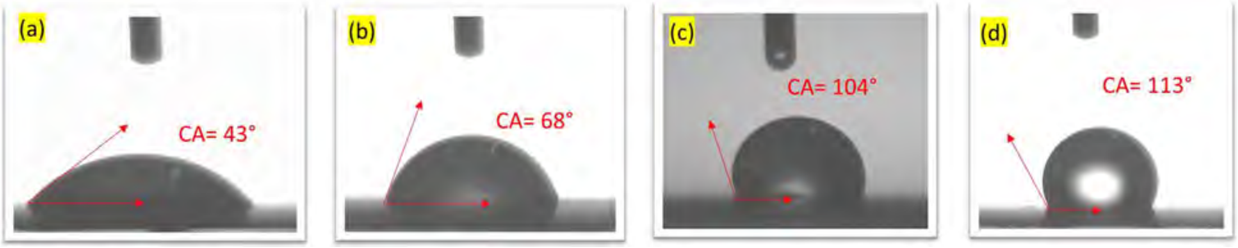

Fig. 6.5. (a-d) Contact angle results of MX, TiO_2/MX, STO/MX-12 and STO/MX-18 nanocomposites, respectively.

6.4 Sensor study

VOC sensing

The VOC sensing characteristics of all the Mxene-based sensors are tested by considering the simulations effect of ambient humidity. The baseline resistance of the sensors was tested in two different ambient i.e., dry air and 80% humid air when the operating temperature varied from 25-200 °C (Fig. 6.6(a)). The treatment of metallic conductive MAX phase in suitable etchant consequences in different functional (–OH, –O, or –F) groups and abundant adsorption sites that exhibited p-type semiconducting properties in MXene [4]. After oxidation, the baseline resistance of MXene was increased from 1.56 MΩ to 1.98 MΩ at 25 °C in the air (Fig. 6.6(a)) [7,8]. $SrTiO_3$ passivation decreases the baseline resistance up to 0.22 and 0.12 MΩ for STO/MX-12 and STO/MX-18, respectively at 25 °C in air (Fig. 6.6(a)). The electrical resistance of sensors was decreased monotonously with an increase in operating temperature from 25 to 200 °C [44]. The baseline resistance of the sensors was deviated in the presence of humidity at different temperatures and summarized in Fig. 6.6(a). The baseline resistance of pure MXene is highly influenced by 80% RH and the value was increased from 1.56 MΩ to 2.4 MΩ at 25 °C. STO passivated MXene-based sensors exhibited a negligible change in baseline resistance in 80% RH compared to the dry air at all temperatures (Fig. 6.6(a)).

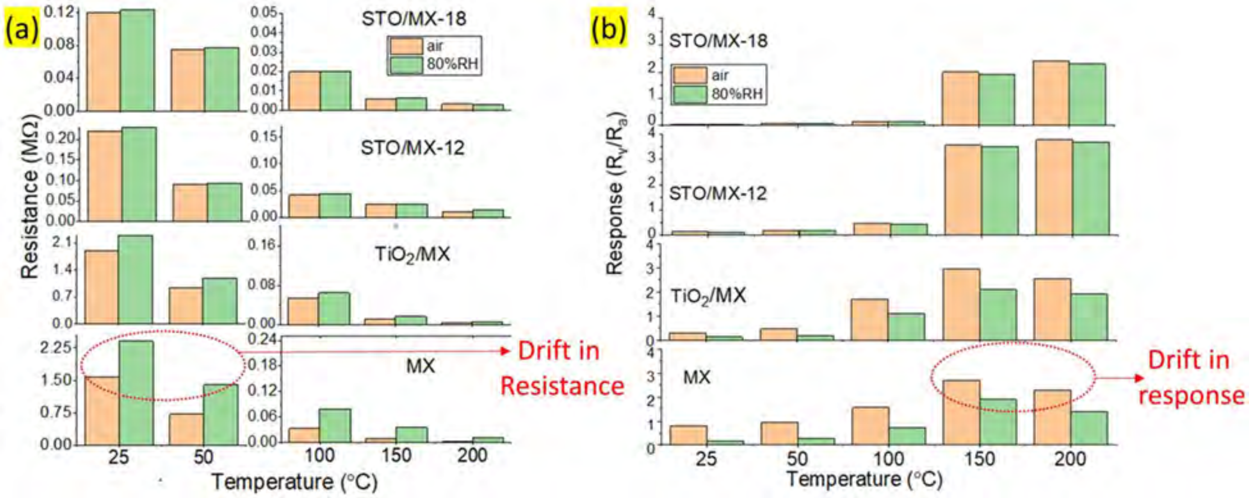

Fig. 6.6. (a) baseline resistance vs temperature curve in air and 80% RH; (b) response vs temperature curve in air and 80% RH for MX, TiO_2/MX, STO/MX-12 and STO/MX-18 nanocomposites, respectively.

The changes in sensor response in air and 80% RH at different operating temperatures were recorded for 50 ppm acetone and summarized in Fig. 6.6(b). MX sensor showed a moderate response at lower temperatures (<100 °C) and a relatively high response (2.7 at 150 °C) at elevated temperatures owing to its highly functionalized surface with improved specific surface area [4]. The response was significantly disturbed (decreased) in the MX sensor in the presence of 80% RH as shown in Fig. 6.6(b). MX sensors are drastically affected by humidity [35, 46] due to the presence of large hydroxyl (OH) and fluorine (F) groups that ultimately enhance the hydrophilic property of $Ti_3C_2T_x$ MXene [23]. After the formation of TiO_2 on MXene, the response was increased further (2.95 at 150 °C) but the influence of humidity was intact (Fig. 6.6(b)) [7,45]. A drastic change in VOC sensing was observed in STO-passivated MXene. STO/MX-12 and STO/MX-18 sensors showed very small responses at lower temperatures (25-100 °C) because the perovskite materials require more activation energy to interact with the VOC molecules [44]. But the response was drastically increased beyond 100 ºC and STO/MX-12 showed the highest response (3.7 at 150 ºC) towards acetone among all four sensors. The response further deteriorated slightly in STO/MX-18. The most important observation was insignificant interference of 80% RH in response to STO passivated MXene sensor (Fig. 6.6(b)).

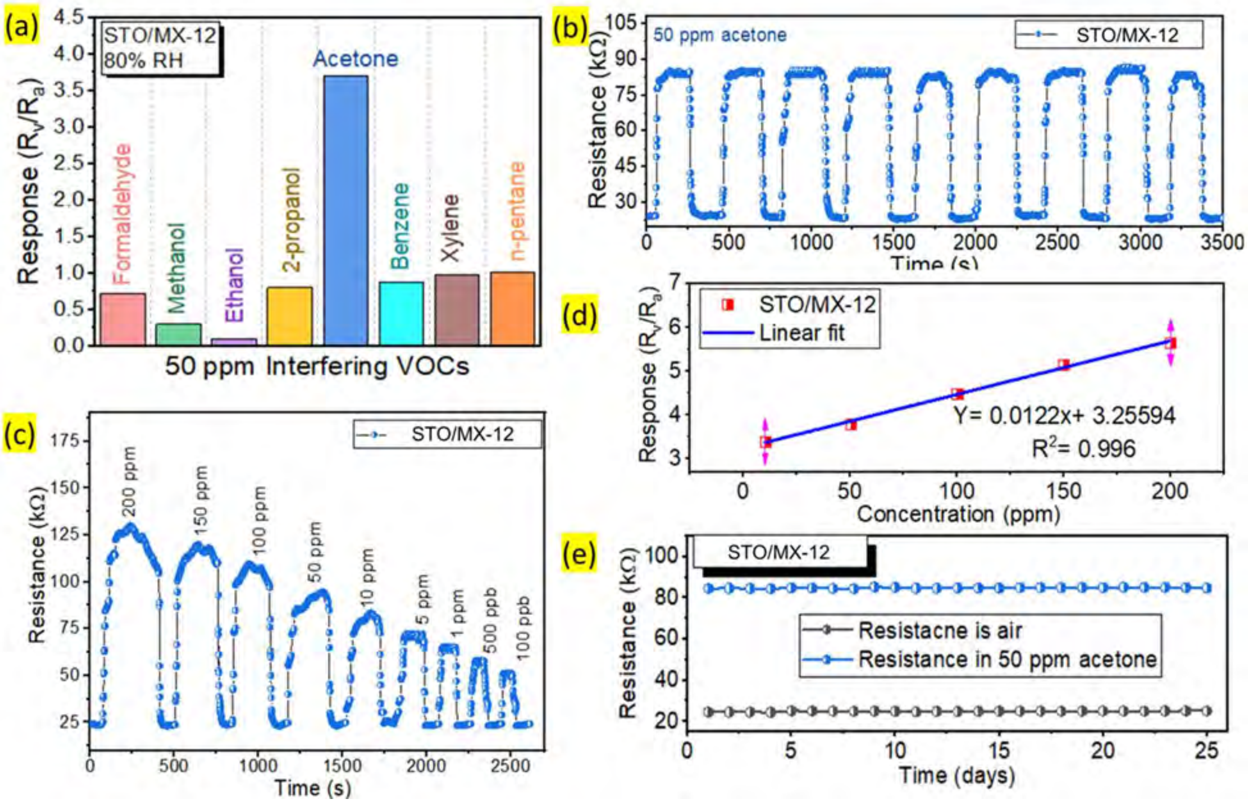

Fig. 6.7. (a) Selective acetone response curve among different interfering VOCs for 50 ppm concertation; (b) repeated cycle study; (c) transient curve for a range of acetone concentrations (200 -0.1 ppm); (d) linear relation between response vs acetone concentration and (e) long term stability curve of STO/MX-12 nanocomposite at 150 °C and 80% RH atmosphere.

Moreover, STO/MX-12 sensor was found to be the best-performing sensor for humidity-tolerant acetone sensing. The transient response, selectivity, long-term stability, and repeatability were tested for STO/MX-12sensor for real-time applications. In order to investigate the cross-sensing response of the STO/MX-12sensor, various VOCs were exposed to the film at 150 °C in the presence of 80% RH ambient. Fig. 6.7(a) displays 0.7, 0.28, 0.1, 0.8, 3.7, 0.88, 0.97, and 1.08 sensing responses for 50 ppm concentration of formaldehyde (HCHO), methanol (CH_3OH), ethanol (C_2H_5OH), 2-propanol (C_3H_7OH), acetone (C_3H_6O), benzene (C_6H_6), xylene (C_8H_{10}), n-pentane (C_5H_{12}), respectively (Fig. 6.7(a)). The sensor showed the highest response toward acetone while the response for HCHO, C_2H_5OH and C_3H_7OH was significantly low. The results indicate that the $Ti_3C_2T_x$ channel in STO/MX-12 sensor has a good responsive behavior towards the hydrogen bonding VOCs and is undoubtedly controlled by the terminal hydroxyl (−OH) groups on the surface [6]. However, $SrTiO_3$ addition helped to achieve acceptable selectivity towards acetone among all hydrogen-bonded reducing VOCs attributed to their less reactive nature towards the methanol and formaldehyde VOCs as the catalytic activities are dependent on oxidation states of STO. Additionally, previous reports claimed that the bond disaggregation energy of acetone is smaller than the maximum participating VOCs providing a superior possibility of interaction with the adsorbed oxygen species [19]. The repeated response recovery characteristics of the sensor were monitored for 50 ppm acetone (Fig. 6.7(b)). The sensor maintained its original response-recovery amplitude without any apparent fluctuations during the eight consecutive cycles, ensuring that the sensor could show excellent reproducibility compared to the previously reported MXene-based sensors [5,6]. The real-time transient sensing characteristics of the STO/MX-12 sensor was further inspected by controlling the acetone concentration from 0.1 to 200 ppm at 150 °C and 80% RH (Fig. 6.7(c)). As expected for the semiconductor sensor, as we increased the acetone concentration, the response increased and the experimental detection limit could be 100 ppb as shown in Fig. 6.7(c). On the basis of the response value at the corresponding acetone concentration, a linear curve of the sensor was plotted and found the linear relationship; $Y = 0.0122x + 3.25594$ (Fig. 6.7(d)). The sensor showed acceptable linearity in response to the broad acetone concentration range and might have numerous real-time applications based on humidity-tolerant acetone sensors. The theoretic limit of detection (LOD) was achieved as 27 ppb. Furthermore, the long-term stability was tested with STO/MX-12 sensor for 25 days on the interval of 1 day and preserved the study parameter constant, as shown in Fig. 6.7(e). This excellent stability may be attributed to the high chemical and thermally stable nature of the $SrTiO_3$ perovskite layer on the MXene channel [28,29].

Humidity study

To evaluate the role of $SrTiO_3$ (STO) passivation on MXene for humidity tolerant sensing, a detailed study was conducted for all four sensors at the different values of RH i.e., 0% (dry air), 20%, 40%, 60%, 80% and shown in Fig. 6.8. Four parameters of the sensors i.e., baseline resistance, response, response time and recovery time were targeted to study in the presence of different levels of RH at their optimum temperature i.e., 150 ºC. For direct visualization of the changes in those parameters in different RH conditions, a radar plot was preferred (Fig. 6.8). In support, the transient response of all four sensors toward 50 ppm of acetone in the presence of

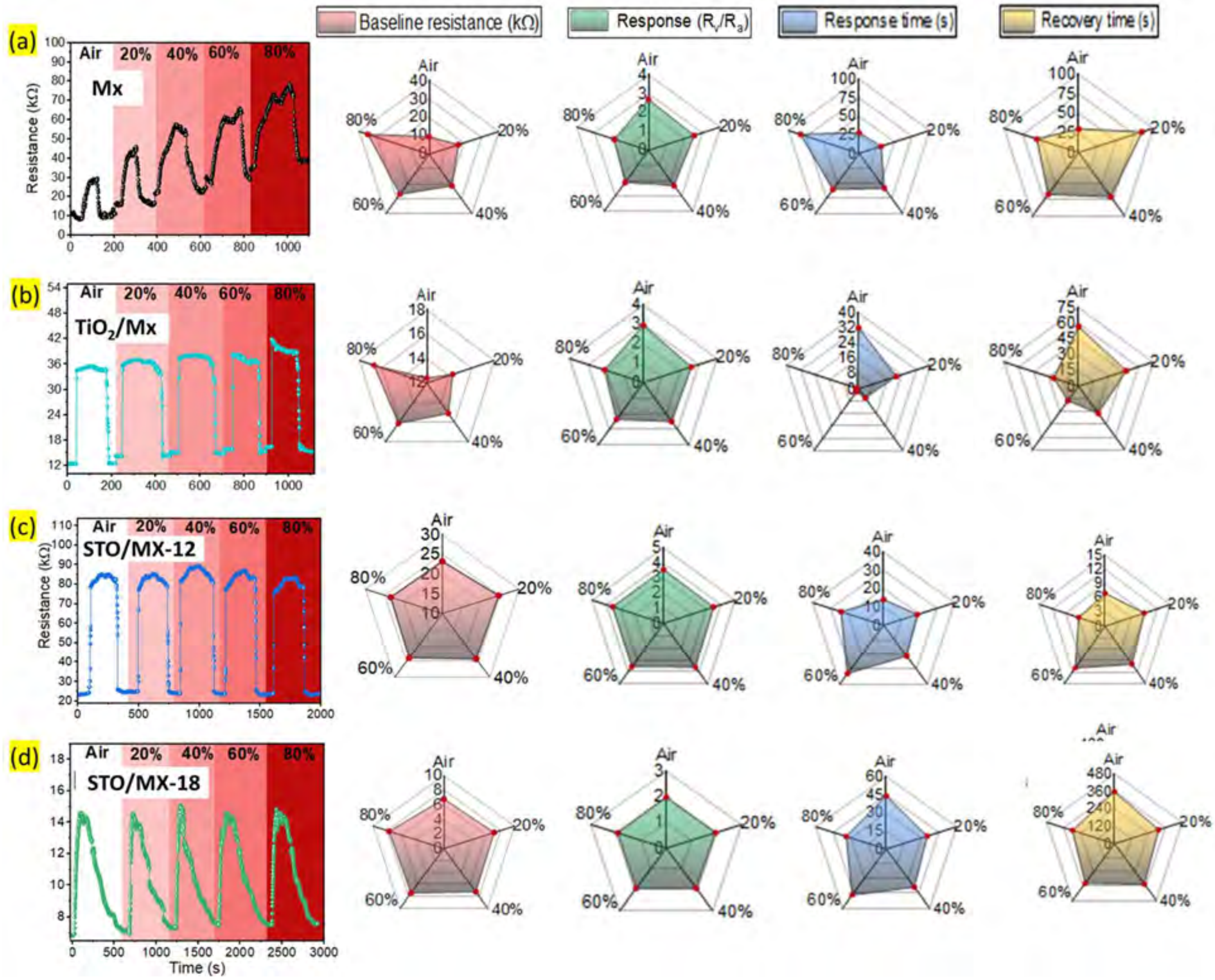

Fig. 6.8. (a-d) showing resistance vs time curve at different humidity levels (air, 20%, 40%, 60% and 80% RH) and the radar plots showing the change in sensing parameters i.e., baseline resistance, response, response/recovery time with a change in humidity for 50 ppm acetone and 150 °C operating temperature.

different humid backgrounds is added to Fig. 6.8. The increase of sensor resistance in the exposure of reducing acetone vapor envisaged the p-type conductivity of all the sensors [4,5,28]. The baseline resistance of MX and TiO_2/MX sensors was greatly influenced by ambient humidity whereas $SrTiO_3$ passivation on MXene worked professionally and the baseline resistance was not even a bit affected by any (0-80%) humidity level in STO/MX-12 and STO/MX-18 sensors (Fig. 6.8(c-d)). Similarly, sensor response was negligibly influenced by a humid background in the case of $SrTiO_3$ passivated MXene sensors that were clearly understood from their uniform radar plot (Fig. 6.8(c, d). The increased humidity prevents the adsorption and desorption of VOC molecules to the sensing layer and consequently response and recovery time get increased [46]. The response/recovery time was increased in a pure MXene sensor as the humidity had a negative impact on the gas/VOC sensing properties (Fig. 6.8(a)). However, TiO_2/MXene was fastest at higher humidity levels (60 and 80% RH) could be attributed to its improved properties which make easy intercalation and desorption of VOCs (Fig. 6.8(b)) [22]. The study confirms that the STO/MX-12 sensor is the best-performing sensor regarding uniform baseline resistance, response towards 50 ppm acetone, and response/recovery time at each humidity level at 150 °C (Fig. 6.8(d)). Moreover, the active participation of the STO layer which not only improved the humidity tolerance but also some of their gaseous adsorption sites (XPS data in Fig. 6.4(d)) help in more VOC interaction (Fig. 6.8(b)) [28,31]. After the long hydrothermal treatment, the sensors based on STO/MX-12 and STO/MX-18 composites exhibit prominent humidity-tolerant response properties. To realize the humidity tolerant property of $SrTiO_3$ passivated MXene, static water contact angle measurement was performed for all four samples and represented in Fig. 6.8. Such humidity tolerant properties are attributed to the following aspects: (i) reduced interlayer distances of MXene induced by overlayer formation of $SrTiO_3$ that facilitate water molecule repulsion from the surface; (ii) super hydrophobic layer of $SrTiO_3$ (Fig. 6.5) blocks the interaction between moisture and MXene nanosheets and repel the adsorption of water molecules to the top surface; (iii) the budlike and rough nanostructure with a good contact angle can provide weaker contacts between the sensing material and water molecules.

6.5 Sensing mechanism

MXene is a semiconducting material having different surface functional groups (-OH, -O, or -F) after the etching of the metallic MAX phase with a suitable etchant [48,49]. Generally, the

$Ti_3C_2T_x$ MXene shows a p-type sensing response where resistance is increased during the interaction with reducing VOCs. Surface groups (=O, -OH) and active defect sites on the MXene react with the VOC analytes during the adsorption process and change the electrical conductivity of MXene [14,17]. When acetone interacted with the adsorbed oxygen species on the MXene layer, the captured electrons were released back to the $Ti_3C_2T_x$ channel causing an increase in electrical resistance [17]. The possible reaction is given in eq. 6.1 [14].

$$CH_3COCH_3 \; + \; 8O^-(adsorbed) \rightarrow 3CO_2 + \; 3H_2O\,(adsorbed) \; + \; 8e^- \qquad (6.1)$$

However, pure MXene is highly reactive with water molecules or humidity, which immobilizes surface reactive sites, resulting in an interference to acetone sensing [50]. Furthermore, the hydrophilic groups on $Ti_3C_2T_x$ MXene can easily be hydrolyzed in a $Ti_xC_y(OH)_z$ (hydroxyl functionalized MXene) as an intermediate compound in a humid environment as shown in eq. 6.2 [51,52]. Even long-term exposure to humidity or bulk water layers on $Ti_3C_2T_x$ leads to the formation of permanent oxide as shown in eq. 6.3 [52].

$$Ti_3C_2T_x + \; H_2O \; \rightarrow Ti_xC_y(OH)_z \qquad (2)$$

$$Ti_xC_y(OH)_z \; \rightarrow TiO_2 \qquad (3)$$

The physical oxidation process led to the formation of semiconducting TiO_2 in the TiO_2/MX sensor. The baseline resistance of the TiO_2/MX sensor was decreased compared to the MX sensor showing the formation of p-n heterojunction between the material [7,8]. The formation of TiO_2 on the MXene surface definitely improves its surface properties by enriching the active site [45]. However, the resistance of the TiO_2/MX sensor was increased during the interaction with reducing vapor that predict the formation of TiO_2 on the top surface and MXene is still the base channel material [7,42]. Lastly, the STO overlayer formation on MXene showed a significant decrease in baseline resistance; 0.22 MΩ and 0.12 MΩ for STO/MX-12 and STO/MX-18 sensors confirming the changes in semiconducting properties of the hybrid material. The STO formation on MXene sheets works in two ways. Firstly, the $SrTiO_3$ formation from the TiO_2 results in the substitution of some Ti^{4+} by Sr^{2+} ions that increase defects in terms of oxygen vacancies in the MXene sheets [53,54]. The increased defects, significantly modulate the activation energy and provide more interaction sites [45]. In the STO/MX-12 sensor, all three materials; MXene, TiO_2, and STO participated in the VOC adsorption as confirmed by the XRD results (Fig. 6.3(a)). The acetone interaction with the MX/STO-12 sensor results in maximum acetone adsorption, and highest resistance variation than MX and TiO_2/MX sensors. Secondly, $SrTiO_3$ was introduced to eliminate the effect of humidity on the MXene sheets and enable easy and fast transportation of VOC analytes. The highly humidity stable (Fig. 6.2(e)) and porous STO is the top layer and reacts with water molecules instead of $Ti_3C_2T_x$, which blocks the interaction between moisture and the MXene layer. It is important to note that the response to 50 ppm acetone decreased from 3.7 (STO/MX-12) to 1.8 (STO/MX-18) with the thickening of the STO overlayer (Fig. 6.5(b)). The thickening of STO on MXene decreases the porosity of the layer and MXene sheets will be less participative in the VOC interaction. The optimum thickness of the STO overlayer on MXene (STO/MX-12) in the present study shows the synergistic effects of a hybrid between MXene, TiO_2, and STO, resulting in high acetone response and humidity independence sensing characteristics.

6.6 Conclusion

In summary, MXene with excellent acetone sensing properties showed limitations of poor signal stability and high humidity influence and requires a solution for reliable and real time breath VOC detection. To achieve the stable acetone sensing properties, MXene was undergone the physical oxidation process to to create a thin TiO_2 layer on MXene sheets (TiO_2/MX) which was further treated with the $Sr(OH)_2$ by hydrothermal route to develop $SrTiO_3$ passivated MXene (STO/MX). We have taken this novel approach to create an overlayer of $SrTiO_3$ on MXene sheets to block the interaction between moisture and hydrophilic MXene sheets. A surface wettability study predicted the improved hydrophobic property of MXene after the $SrTiO_3$ overlayer formation. The STO/MX-12 sensor showed the best sensing performance with a natural selective nature towards acetone. STO/MX-12 sensor exhibited excellent response (2.2 in 100 ppb) towards acetone with 27 ppb of LOD at 150 °C in 80% RH ambient which is completely fulfilling the requirement of breath acetone detection for breath analysis. Additionally, STO/MX sensors successfully achieved stable and humidity-independent sensing of acetone in a wide range of humidity (0–80% RH). These research outcomes make the STO/MX-12 sensor a highly appropriate for real time breath acetone detection.

References

[1] X. Xu *et al.*, “MXenes with applications in supercapacitors and secondary batteries: A comprehensive review,” *Mater. Reports Energy*, vol. 2, no. 1, p. 100080, 2022, doi:

10.1016/j.matre.2022.100080.

[2] P. Kuang, Z. Ni, J. Yu, and J. Low, "New progress on MXenes-based nanocomposite photocatalysts," *Mater. Reports Energy*, vol. 2, no. 1, p. 100081, 2022, doi: 10.1016/j.matre.2022.100081.

[3] Y. Gogotsi and B. Anasori, "The Rise of MXenes," *ACS Nano*, vol. 13, no. 8, pp. 8491–8494, 2019, doi: 10.1021/acsnano.9b06394.

[4] S. Mehdi Aghaei, A. Aasi, and B. Panchapakesan, "Experimental and Theoretical Advances in MXene-Based Gas Sensors," *ACS Omega*, vol. 6, no. 4, pp. 2450–2461, 2021, doi: 10.1021/acsomega.0c05766.

[5] M. Wu *et al.*, "Ti_3C_2 MXene-Based Sensors with High Selectivity for NH_3 Detection at Room Temperature," *ACS Sensors*, vol. 4, no. 10, pp. 2763–2770, 2019, doi: 10.1021/acssensors.9b01308.

[6] S. J. Kim *et al.*, "Metallic $Ti_3C_2T_x$ MXene Gas Sensors with Ultrahigh Signal-to-Noise Ratio," *ACS Nano*, vol. 12, no. 2, pp. 986–993, 2018, doi: 10.1021/acsnano.7b07460.

[7] J. Choi *et al.*, "In Situ Formation of Multiple Schottky Barriers in a Ti_3C_2 MXene Film and its Application in Highly Sensitive Gas Sensors," *Adv. Funct. Mater.*, vol. 30, no. 40, pp. 1–9, 2020, doi: 10.1002/adfm.202003998.

[8] H. Pazniak *et al.*, "Partially Oxidized $Ti_3C_2T_x$ MXenes for Fast and Selective Detection of Organic Vapors at Part-per-Million Concentrations," *ACS Appl. Nano Mater.*, vol. 3, no. 4, pp. 3195–3204, 2020, doi: 10.1021/acsanm.9b02223.

[9] E. Lee, A. Vahidmohammadi, B. C. Prorok, Y. S. Yoon, M. Beidaghi, and D. J. Kim, "Room Temperature Gas Sensing of Two-Dimensional Titanium Carbide (MXene)," *ACS Appl. Mater. Interfaces*, vol. 9, no. 42, pp. 37184–37190, 2017, doi: 10.1021/acsami.7b11055.

[10] Y. Jian *et al.*, "The prior rules of designing $Ti_3C_2T_x$ MXene-based gas sensors," pp. 1–13, 2021.

[11] Y. Chae *et al.*, "An investigation into the factors governing the oxidation of two-

dimensional Ti_3C_2 MXene," *Nanoscale*, vol. 11, no. 17, pp. 8387–8393, 2019, doi: 10.1039/c9nr00084d.

[12] W. N. Zhao, N. Yun, Z. H. Dai, and Y. F. Li, "A high-performance trace level acetone sensor using an indispensable $V_4C_3T_X$ MXene," *RSC Adv.*, vol. 10, no. 3, pp. 1261–1270, 2020, doi: 10.1039/c9ra09069j.

[13] W. Guo *et al.*, "Selective Toluene Detection with Mo_2CT_x MXene at Room Temperature," *ACS Appl. Mater. Interfaces*, vol. 12, no. 51, pp. 57218–57227, 2020, doi: 10.1021/acsami.0c16302.

[14] S. Sun *et al.*, "$W_{18}O_{49}$/ $Ti_3C_2T_x$ Mxene nanocomposites for highly sensitive acetone gas sensor with low detection limit," *Sensors Actuators, B Chem.*, vol. 304, no. August 2019, p. 127274, 2020, doi: 10.1016/j.snb.2019.127274.

[15] A. Rudie, A. M. Schornack, Q. Wu, Q. Zhang, and D. Wang, "Two-Dimensional Ti_3C_2 MXene-Based Novel Nanocomposites for Breath Sensors for Early Detection of Diabetes Mellitus," *Biosensors*, vol. 12, no. 5, pp. 1–10, 2022, doi: 10.3390/bios12050332.

[16] S. M. Majhi, A. Ali, Y. E. Greish, H. F. El-Maghraby, and S. T. Mahmoud, "V_2CT_X MXene-based hybrid sensor with high selectivity and ppb-level detection for acetone at room temperature," *Sci. Rep.*, vol. 13, no. 1, pp. 1–12, 2023, doi: 10.1038/s41598-023-30002-6.

[17] M. Liu, Z. Wang, P. Song, Z. Yang, and Q. Wang, "Flexible MXene/rGO/CuO hybrid aerogels for high performance acetone sensing at room temperature," *Sensors Actuators, B Chem.*, vol. 340, no. April, p. 129946, 2021, doi: 10.1016/j.snb.2021.129946.

[18] G. Konvalina and H. Haick, "Effect of Humidity on Nanoparticle-Based Chemiresistors: A Comparison between Synthetic and Real-World Samples," 2012.

[19] M. Liu, J. Ji, P. Song, M. Liu, and Q. Wang, "α-Fe_2O_3 nanocubes/$Ti_3C_2T_x$ MXene composites for improvement of acetone sensing performance at room temperature," *Sensors Actuators B Chem.*, vol. 349, no. May, p. 130782, 2021, doi: 10.1016/j.snb.2021.130782.

[20] H. Li, C. Lee, D. H. Kim, and J. Lee, "Flexible Room-Temperature NH_3 Sensor for

Ultrasensitive , Selective , and Humidity-Independent Gas Detection," 2018, doi: 10.1021/acsami.8b09169.

[21] Z. Wang, K. Yu, Y. Feng, R. Qi, J. Ren, and Z. Zhu, "Stabilizing $Ti_3C_2T_x$-MXenes with TiOF2 nanospheres intercalation to improve hydrogen evolution reaction and humidity-sensing performance," *Appl. Surf. Sci.*, vol. 496, no. April, 2019, doi: 10.1016/j.apsusc.2019.143729.

[22] J. Wu *et al.*, "High performance humidity sensing property of $Ti_3C_2T_x$ MXene-derived Ti3C2Tx/K2Ti4O9 composites," *Sensors Actuators, B Chem.*, vol. 326, no. September 2020, 2021, doi: 10.1016/j.snb.2020.128969.

[23] N. Li *et al.*, "High-Performance Humidity Sensor Based on Urchin-Like Composite of Ti_3C_2 MXene-Derived TiO2 Nanowires," *ACS Appl. Mater. Interfaces*, vol. 11, no. 41, pp. 38116–38125, 2019, doi: 10.1021/acsami.9b12168.

[24] H. Zhou *et al.*, "Study on contact angles and surface energy of MXene films," *RSC Adv.*, vol. 11, no. 10, pp. 5512–5520, 2021, doi: 10.1039/d0ra09125a.

[25] Z. Gao *et al.*, "A facile PDMS coating approach to room-temperature gas sensors with high humidity resistance and long-term stability," *Sensors Actuators, B Chem.*, vol. 325, no. August, 2020, doi: 10.1016/j.snb.2020.128810.

[26] F. Qu *et al.*, "Surface Functionalized Sensors for Humidity-Independent Gas Detection," *Angew. Chemie - Int. Ed.*, vol. 60, no. 12, pp. 6561–6566, 2021, doi: 10.1002/anie.202015856.

[27] T. E. Song *et al.*, "Vertically Aligned Nanopatterns of Amine-Functionalized Ti_3C_2 MXene via Soft Lithography," *Adv. Mater. Interfaces*, vol. 7, no. 18, 2020, doi: 10.1002/admi.202000424.

[28] T. Cao, Y. Li, C. Wang, C. Shao, and Y. Liu, "A facile in situ hydrothermal method to $SrTiO_3/TiO_2$ nanofiber heterostructures with high photocatalytic activity," *Langmuir*, vol. 27, no. 6, pp. 2946–2952, 2011, doi: 10.1021/la104195v.

[29] H. Trabelsi, M. Bejar, E. Dhahri, M. A. Valente, and M. P. F. Graça, "Physica E : Low-dimensional Systems and Nanostructures Oxygen-vacancy-related giant permittivity and

ethanol sensing response in $SrTiO_{3-\delta}$ ceramics," *Phys. E Low-dimensional Syst. Nanostructures*, vol. 108, no. December 2018, pp. 317–325, 2019, doi: 10.1016/j.physe.2018.12.025.

[30] Z. Meng *et al.*, "Au nanoparticle modified single-crystalline p-type $LaRhO_3/SrTiO_3$ heterostructure for high performing VOCs sensor," *Ceram. Int.*, vol. 46, no. 14, pp. 22140–22145, Oct. 2020, doi: 10.1016/j.ceramint.2020.05.290.

[31] J. Y. Baek, L. T. Duy, S. Y. Lee, and H. Seo, "Aluminum doping for optimization of ultrathin and high-k dielectric layer based on $SrTiO_3$," *J. Mater. Sci. Technol.*, vol. 42, no. April, pp. 28–37, 2020, doi: 10.1016/j.jmst.2019.12.006.

[32] S. N. Shuvo, A. M. Ulloa Gomez, A. Mishra, W. Y. Chen, A. M. Dongare, and L. A. Stanciu, "Sulfur-Doped Titanium Carbide MXenes for Room-Temperature Gas Sensing," *ACS Sensors*, vol. 5, no. 9, pp. 2915–2924, 2020, doi: 10.1021/acssensors.0c01287.

[33] T. Gakhar and A. Hazra, "C 60 -encapsulated TiO_2 nanoparticles for selective and ultrahigh sensitive detection of formaldehyde," 2021.

[34] H. Deng *et al.*, "Nanolayered Ti3C2 and $SrTiO_3$ Composites for Photocatalytic Reduction and Removal of Uranium(VI)," *ACS Appl. Nano Mater.*, vol. 2, no. 4, pp. 2283–2294, 2019, doi: 10.1021/acsanm.9b00205.

[35] A. Hermawan *et al.*, "CuO Nanoparticles/ $Ti_3C_2T_x$ MXene Hybrid Nanocomposites for Detection of Toluene Gas," *ACS Appl. Nano Mater.*, vol. 3, no. 5, pp. 4755–4766, 2020, doi: 10.1021/acsanm.0c00749.

[36] A. Lipatov, M. Alhabeb, M. R. Lukatskaya, A. Boson, Y. Gogotsi, and A. Sinitskii, "Effect of Synthesis on Quality, Electronic Properties and Environmental Stability of Individual Monolayer Ti_3C_2 MXene Flakes," *Adv. Electron. Mater.*, vol. 2, no. 12, 2016, doi: 10.1002/aelm.201600255.

[37] T. Ungár, "Microstructural parameters from X-ray diffraction peak broadening," *Scr. Mater.*, vol. 51, no. 8 SPEC. ISS., pp. 777–781, 2004, doi: 10.1016/j.scriptamat.2004.05.007.

[38] M. Akilarasan *et al.*, "An eco-friendly low-temperature synthetic approach towards micro-

pebble-structured GO@$SrTiO_3$ nanocomposites for the detection of 2,4,6-trichlorophenol in environmental samples," *Microchim. Acta*, vol. 188, no. 3, 2021, doi: 10.1007/s00604-021-04729-w.

[39] T. Su *et al.*, "Sulfur Vacancy and $Ti_3C_2T_x$ Cocatalyst Synergistically Boosting Interfacial Charge Transfer in 2D/2D $Ti_3C_2T_x$/$ZnIn_2S_4$ Heterostructure for Enhanced Photocatalytic Hydrogen Evolution," *Adv. Sci.*, vol. 9, no. 4, pp. 1–16, 2022, doi: 10.1002/advs.202103715.

[40] L. Jin, L. Chai, W. Yang, H. Wang, and L. Zhang, "Two-Dimensional Titanium Carbides ($Ti_3C_2T_x$) Functionalized by Poly (m-phenylenediamine) for E ffi cient Adsorption and Reduction of Hexavalent Chromium."

[41] S. S. Al-Taweel and H. R. Saud, "New route for synthesis of pure anatase TiO_2 nanoparticles via utrasound-assisted sol-gel method," *J. Chem. Pharm. Res.*, vol. 8, no. 2, pp. 620–626, 2016.

[42] D. Kuang *et al.*, "Facile hydrothermal synthesis of $Ti_3C_2T_x$-TiO_2 nanocomposites for gaseous volatile organic compounds detection at room temperature," *J. Hazard. Mater.*, vol. 416, no. December 2020, p. 126171, 2021, doi: 10.1016/j.jhazmat.2021.126171.

[43] J. Y. Baek, L. T. Duy, S. Y. Lee, and H. Seo, "Aluminum doping for optimization of ultrathin and high-k dielectric layer based on $SrTiO_3$," *J. Mater. Sci. Technol.*, vol. 42, pp. 28–37, 2020, doi: 10.1016/j.jmst.2019.12.006.

[44] B. Szafraniak and Ł. Fu, "Semiconducting Metal Oxides: $SrTiO_3$, $BaTiO_3$ and $BaSrTiO_3$ in Gas-Sensing Applications: A Review," pp. 1–22, 2021.

[45] M. Hou *et al.*, "Improvement of gas sensing property for two-dimensional $Ti_3C_2T_x$ treated with oxygen plasma by microwave energy excitation," *Ceram. Int.*, vol. 47, no. 6, pp. 7728–7737, 2021, doi: 10.1016/j.ceramint.2020.11.117.

[46] D. Zhang, Q. Mi, D. Wang, and T. Li, "MXene/Co_3O_4 composite based formaldehyde sensor driven by ZnO/MXene nanowire arrays piezoelectric nanogenerator," *Sensors Actuators B Chem.*, vol. 339, no. April, p. 129923, 2021, doi: 10.1016/j.snb.2021.129923.

[47] K. Zukiene *et al.*, "Wettability of MXene and its interfacial adhesion with epoxy resin,"

Mater. Chem. Phys., vol. 257, no. July 2020, 2021, doi: 10.1016/j.matchemphys.2020.123820.

[48] W. Yuan, K. Yang, H. Peng, F. Li, and F. Yin, “A flexible VOCs sensor based on a 3D Mxene framework with a high sensing performance,” *J. Mater. Chem. A*, vol. 6, no. 37, pp. 18116–18124, 2018, doi: 10.1039/c8ta06928j.

[49] X. Zhan, C. Si, J. Zhou, and Z. Sun, “MXene and MXene-based composites: Synthesis, properties and environment-related applications,” *Nanoscale Horizons*, vol. 5, no. 2, pp. 235–258, 2020, doi: 10.1039/c9nh00571d.

[50] N. Li *et al.*, “High-Performance Humidity Sensor Based on Urchin-Like Composite of Ti_3C_2 MXene-Derived TiO_2 Nanowires,” *ACS Appl. Mater. Interfaces*, vol. 11, no. 41, pp. 38116–38125, 2019, doi: 10.1021/acsami.9b12168.

[51] W. Y. Chen, S. N. Lai, C. C. Yen, X. Jiang, D. Peroulis, and L. A. Stanciu, “Surface Functionalization of $Ti_3C_2T_x$ MXene with Highly Reliable Superhydrophobic Protection for Volatile Organic Compounds Sensing,” *ACS Nano*, vol. 14, no. 9, pp. 11490–11501, 2020, doi: 10.1021/acsnano.0c03896.

[52] J. Azadmanjiri *et al.*, “Prospective advances in MXene inks: Screen printable sediments for flexible micro-supercapacitor applications,” *J. Mater. Chem. A*, vol. 10, no. 9, pp. 4533–4557, 2022, doi: 10.1039/d1ta09334g.

[53] X. Yuan *et al.*, “Self-assembly of three-dimensional $SrTiO_3$ microscale superstructures and their photonic effect,” *Inorg. Chem.*, vol. 52, no. 5, pp. 2581–2587, 2013, doi: 10.1021/ic302585g.

[54] H. Amani Hamedani, J. A. Khaleel, K. H. Dahmen, and H. Garmestani, “Surface controlled growth of thin-film strontium titanate nanotube arrays on silicon,” *Cryst. Growth Des.*, vol. 14, no. 10, pp. 4911–4919, 2014, doi: 10.1021/cg500374m.

Chapter 7

Summary, conclusion and scope of future work

7.1 Summary of the current work

The current study involves the effective detection of VOCs mostly available in human breath by using nanomaterials-based chemiresistive sensor systems. Chemiresistive sensors for breath analysis should possess specific characteristics such as; (i) highly sensitive towards the particular breath marker, (ii) sensors with fast response time and recovery time (iii) sensors providing high selectivity towards a particular VOC among a number of cross-interfering VOCs, (iv) low operating temperature, (v) sensors having the lower detection limit down till ppb level with good response value and (vi) low humidity impact on the sensing properties to meet the criteria of effective breath VOC detection. To achieve these goals a variety of approaches have been employed and among all of them formation of nanocomposites of two highly compatible nanomaterials is the most effective way. Different routes have been employed to synthesize nanocomposites of Titanium oxide, carbide and titanate perovskite materials. Two different types of TiO_2 nanostructures; TiO_2 nanoparticles (0-D) and TiO_2 nanotubes (1-D) have been synthesized by the sol-gel and electrochemical anodization routes, respectively. Anatase TiO_2 nanoparticles and highly oriented TiO_2 nanotubes have distinct semiconducting properties with p-type and n-type semiconducting nature, respectively. Additionally, pure p-type $Ti_3C_2T_x$ MXene was synthesized by the chemical etching route where a suitable etchant was used to exfoliate the MAX phase with a good interlayer spacing.

To achieve high selectivity and stability in terms of the lifetime of the sensor and humidity-tolerant nature at an optimum operating temperature, a significant number of composites with $SrTiO_3$ were synthesized from the pure nanostructures resulting in the formation of different heterojunctions. $SrTiO_3/TiO_2$ nanotube array, $SrTiO_3$ nanostructures, and MXene/$SrTiO_3$ nanosheets-based nanocomposites have been synthesized by a one-step hydrothermal route. Further, the nanomaterial was also functionalized by nanoparticles and quantum dots to enhance the sensing properties.

Different nanostructures and their nanocomposites were taken into account to form discrete Schottky junctions. All the fabricated nanomaterials and their hybrids were subjected to various morphological, structural, and chemical characterization including SEM, TEM or HRTEM, XRD, Raman spectroscopy, XPS, and EDS. Nanoparticles, hollow spheres, nanograss, nanosheets etc. were used to deposited on interdigitated Au finger electrodes to from planner type chemiresistive structure sensors. On the other hand, vertically aligned 1-D structured nanoforms like TiO2 nanotubes are configured into metal-insulator-metal (MIM) type sensors.

It was an attempt to make sensor systems have the synergetic properties of both the participating nanomaterials and results in a significant improvement in the sensing results. The first work mainly involves MoS_2 quantum dots functionalized TiO_2 nanotubes for the selective detection of the xylene VOC marker at a low operating temperature. In another study, a sensor system was designed based on $SrTiO_3$ nanomaterials in different nanoforms derived from the TiO_2 nanoparticles percussor solution. $SrTiO_3$ semiconducting perovskite was utilized to form different nanoforms at different hydrothermal reaction times. The superior physical and chemical stability, tunable defect density and superhydrophobic properties of $SrTiO_3$ make it desirable for highly stable VOC sensing applications. A number of nanoforms such as; nanograss, nanorods, nanospheres and hollow spheres were synthesized and underwent the humidity-tolerant VOC sensing study. Later the best-responded hollow spheres of $SrTiO_3$ were functionalized with Pd nanoparticles to improve the sensitization properties of the material. Lastly, the overlayer of $SrTiO_3$ on hydrophilic $Ti_3C_2T_x$ MXene sheets resulted in humidity-inactive and highly stable acetone sensing properties. Table 6.1 enlists the novel sensors fabricated with their morphology, response magnitude towards target VOC, operating temperature, response/recovery time and deviation in response in a humid environment.

7.2 Conclusion

The main aim of this work was designing of nanomaterial based chemiresistive sensors for breath analysis application. To fulfill the requirements like higher selectivity, lower detection limit, stability and humidity-tolerant for breath VOC detection we have prepared different nanomaterials and their hybrid based chemiresistive sensors. The detailed study involved synthesis and fabrication of titanium oxide, carbide and titanate perovskite nanomaterials and their hybrid based chemiresistive sensors to make them more accurate for breath VOC detection.

Firstly, we have successfully synthesized nanotubes and nanoparticles of titanium oxide, different nanostructures like nanograss, nanorods, nanospheres and hollow spheres of $SrTiO_3$ and

$Ti_3C_2T_x$ MXene sheets by different chemical routes. Further some selective nanomaterials like TiO_2 nanotubes and $SrTiO_3$ hollow spheres were successfully hybridized with MoS_2 quantum dots and Pd nanoparticles, respectively. A detail morphological, structural and chemical characterizations of synthesized nanomaterials and their hybrids were done. Later on, we have successfully fabricated the vertical and planner chemiresistive sensors to testing them for VOCs which are mostly considered as potential marker of a diseases. The sensors were tested in terms of selectivity, lower ppb detection, humidity tolerant sensing with long term stability to make them suitable for breath analysis application. Among various chemiresistive sensor some of them were showed maximum applicability in VOC detection for breath analysis application.

The first one was MoS_2 functionalized TiO_2 nanotube sensor, where we have achieved highly selective sensing of xylene breath marker at low operating temperature. The MoS_2/TiO_2 sensor showed extraordinary selectivity towards xylene over different interfering VOCs. The detection of xylene in chemically similar VOCs like benzene and toluene is the most difficult task but the sensor achieved the excellent xylene selective behavior with lowest response towards these VOCs. Additionally, the sensor responded at low operating temperature of 75 °C which is very difficult in metal oxide-based sensors. In another study of nanotube-based sensor we have achieved very low limit of detection towards ethanol. $SrTiO_3$-TiO_2 heterostructured nanotube array showed the outstanding sensitivity towards ethanol (~556/50 ppm) in the shortest response time of 0.4 s. The sensor showed the lowest detection limit of 2.94 ppb as shown in Table 7.1. The long term stability of the sensor was also exceptional where sensor showed a negligible influence on baseline resistance and response value even after 60 days. To accomplish the humidity tolerant VOC sensing, $SrTiO_3$ perovskite-based sensors were studied. From the $SrTiO_3$ nanograss sensors we have achieved exceptionally high contact angle of 154.4° which is showing the superhydrophobic properties of the material. The $SrTiO_3$ nanograss displayed zero influence of humidity interference on ethanol sensing. Later, Pd modification in $SrTiO_3$ hollow spheres was done to achieve the humidity tolerant ethanol selective sensing at 150 °C. Another interesting outcome was found from the $SrTiO_3/Ti_3C_2Tx$ sensor. The sensor showed the lower ppb (100 ppb) acetone sensing among all of the reported sensors. The hydrophilic properties of Ti_3C_2Tx MXene was minimized by the overlayer of hydrophobic $SrTiO_3$ and sensor achieved minimum interference of humidity on acetone sensing. The detailed sensing performance of all of the sensors are incorporated in Table

7.1. Moreover, we have achieved some of the set goals such as high selectivity, low LOD and humidity tolerant sensing etc. for VOC sensing for breath analysis applications by using various chemiresistive sensors. But we were lacking in the optimization of the sensors mainly in terms of low temperature sensing. Most of the sensors were working at the 150 °C operating temperature. specifically, the long term and humidity stability of MoS_2/TiO_2 sensor was not good enough for the employment in the breath analysis application. $SrTiO_3$/MXene sensor was not very much selective towards acetone.

Table 7.1. The sensing performance of various fabricated devices under different environmental conditions.

S. No.	**Sensor**	**Device**	**Target VOC marker**	**Detection range**	**LOD (ppb)**	**Response (R_v/R_a)/ 50 ppm**	**Op. Temp. (°C)**	**Response/ Recovery time (s)**	**Humidity tolerant**	**Contact angle (°)**
1	MoS_2/TiO_2 nanotubes	MIM	Xylene	0.5-150 ppm	33	2.97	75	38/335	No	68
2	$SrTiO_3/TiO_2$ nanotubes	MIM	Ethanol	0.25-200 ppm	2.94	556	150	0.4/50	yes	84
3	$SrTiO_3$ Nanograss	Planar	Ethanol	0.5-200 ppm	78	69	150	36/34	yes	154.4
4	Pd-$SrTiO_3$ hollow spheres	Planar	Ethanol	0.5-200 ppm	50	106.4	150	15/37	yes	147.6
5	$SrTiO_3/Ti_3C_2T_x$ Nanosheets	Planar	Acetone	0.1-200 ppm	27	3.7	150	17/6	yes	104

7.3 Scope of future work

1. Testing and optimization of sensors in the presence of breath samples of individuals by collaborating with hospitals.
2. Use of sensors array for the prototype development.
3. Use of machine learning approaches to further processing of the sensor data for real-time disease monitoring.

Book chapter

1. ***R. Bhardwaj,*** A. Hazra; Hybridized Graphene Field-Effect Transistors for Gas Sensing Applications. ***Wiley-VCH***, 2023, DOI: **10.1002/9783527843374.ch13**.

List of Publications

1. **R. Bhardwaj,** V. Selamneni, U. N. Thakur, P. Sahatiya, A. Hazra; Detection and discrimination of volatile organic compounds by noble metal nanoparticle functionalized MoS_2 coated biodegradable paper sensors. ***New Journal of Chemistry,*** 44(38), 16613-16625, 2020.
2. ***R. Bhardwaj,** A. Hazra; MXene-based gas sensors. ***Journal of Materials Chemistry C***, 9(44), 15735-15754, 2021.
3. **R. Bhardwaj,** A. Hazra; Realization of ppb-level acetone detection using noble metals (Au, Pd, Pt) nanoparticles loaded GO FET sensors with simultaneous back-gate effect. ***Microelectronic Engineering,*** 256, 111719, 2022.
4. **R. Bhardwaj,** U. N. Thakur, P. Ajmera, R. Singhal, Y. Rosenwaks, A. Hazra; Field-assisted sensitivity amplification in a noble metal nanoparticle decorated WO_3/GO hybrid FET-based multisensory array for selective detection of breath acetone. ***Wiley, ChemNanoMat***, 8(2), e202100448, 2022.
5. ***R. Bhardwaj,** A. Hazra; Pd functionalized $SrTiO_3$ Hollow Spheres for Humidity-Tolerant Ethanol Sensing. ***Sensors and Actuators B: Chemical***, 372, 132615, 2022.
6. ***R. Bhardwaj,** A. Hazra; $SrTiO_3$-TiO_2 Heterostructure Nanotube Arrays for Ultrafast Ethanol Sensing. ***ACS Applied Nano Materials***, 5(10), 15507-15517, 2022.
7. ***R. Bhardwaj,** A. Hazra; Nanostructural evolution of hydrothermally grown $SrTiO_3$ perovskite and its implementation in gaseous phase detection of volatile organic compounds. ***Nanotechnology***, 34(40), 405502, 2023.
8. ***R. Bhardwaj,** A. Hazra; $SrTiO_3$ Passivated MXene ($Ti_3C_2T_x$) for Efficient VOC Detection in Hazardous Humid Ambient, ***Sensors and Actuators B: Chemical,*** 401, 134967, 2024.
9. **R. Bhardwaj,** A. Hazra; Oxygen-functionalized $MoSe_2$ nanoflowers for selective Detection of xylene at Room Temperature, ***Surfaces and Interfaces,*** 43, 103523,

2023.

10. ***R. Bhardwaj,** A. Hazra; MoS_2 Functionalized TiO_2 nanotubes for selective detection of xylene at low temperature **(manuscript under preparation).**
11. U. N. Thakur, **R. Bhardwaj,** P. Ajmera, A. Hazra; ANN based approach for selective
    detection of breath acetone by using hybrid GO-FET sensor array; ***Engineering Research Express**, 4(2), 025008, 2022.*
12. D. Rathore, **R. Bhardwaj,** A. Hazra**;** Surface Adsorption Assisted Visible and NIR Photodetection in $SrTiO_3$ Nanostructures. ***ACS Applied Electronics Materials***, 4(9), 4521-4529, 2022.
13. U. N. Thakur, **R. Bhardwaj,** A. Hazra; A Multivariate Computational Approaches with Hybrid Graphene Oxide Sensor Array for Partial Fulfilment of Breath Acetone Sensing. ***IEEE Sensors***, 22(21), 20207-20215, 2022.
14. A. Hazra**, R. Bhardwaj**; Filamentary resistive switching in an $SrTiO_3/TiO_2$ Heterostructured nanotube array. ***ACS Applied Electronics Materials,*** 5(1), 265-274, 2023.

Note: The publication marked with * are only incorporated into thesis.

Conference papers and proceedings

1. **R. Bhardwaj,** A. Hazra; Efficient acetone sensing by Pd nanoparticle loaded graphene Field Effect Transistor. IEMTRONICS, IEEE, Toronto, Canada, 2021.
2. **R. Bhardwaj,** A. Hazra; Bimetals (Au-Pd, Au-Pt) loaded WO_3 hybridized graphene oxide FET sensors for selective detection of acetone. IEMTRONICS, IEEE, Toronto, Canada, 2022.
3. **R. Bhardwaj,** A. Hazra; $SrTiO_3$-TiO_2 heterostructured Nanotubes Array for Selective Acetone Sensing. APSCON, IEEE, Bengaluru, India, 2023.
4. **R. Bhardwaj,** A. Hazra; Fullerene- $MoSe_2$ nanocomposite-Based Sensor for Selective Detection of Formaldehyde. APSCON, IEEE, Bengaluru, India, 2023.
5. **U. N. Thakur, R. Bhardwaj,** A. Hazra; Statistical Analysis for Selective Identifications of VOCs by Using Surface Functionalized MoS_2 Based Sensor Array. CSAC, 2021.

Brief Biography of the Candidate

Radha Bhardwaj received her integrated B. Tech.-M. Tech. dual degree in nanotechnology from the University of Rajasthan, Rajasthan, India in 2018. She is presently doing her Ph.D. from Birla Institute of Technology and Science, Pilani, India. Her research interests cover the synthesis of advanced nanomaterials, the study of their advanced properties and their gas sensing application. She has also attended three international conferences and presented her research work. She has published eleven research papers and three more have been communicated for publication. She has also been awarded with Prospective Women Researchers Award by Springer Nature-Ministry of Education under G20 Initiative.

Brief Biography of the Supervisor

Arnab Hazra received his M.Tech. and Ph.D. from the Indian Institute of Engineering Science and Technology (IIEST), Shibpur, India, in 2011 and 2015, respectively. Presently, he is an Associate Professor in the Department of Electrical and Electronics Engineering, Birla Institute of Technology and Science (BITS), Pilani, Rajasthan, India. He worked as a visiting scientist at Tel Aviv University, Israel and Sensor Laboratory, University of Brescia, Italy in 2018. His current research interest includes nanoscale materials-based devices for gas sensing, photodetection and memristive applications and 2D materials-based field-effect devices. He has published about seventy research articles in the journals and conferences of international repute, two book chapters, and received two Indian patents. He received the best Ph.D. thesis award from Indian National Academy of Engineering (INAE) and ISSS, India, in 2015 and 2016, respectively. He also received IEI young engineer award from the Institute of Engineers, India, in 2016.